Nanocrystalline Perovskites for Catalytic Combustion and Oxygen Separation

by

Neeraj Sangar

M.S. Chemical Engineering Practice
Massachusetts Institute of Technology, 1998

B. S. Chemical Engineering
Rutgers University, 1996

Submitted to the Department of Chemical Engineering
in Partial Fulfillment of the Requirements for the Degree of

Doctor of Philosophy in Chemical Engineering

at the

MASSACHUSETTS INSTITUTE OF TECHNOLOGY

June 2002

Author:_____
Department of Chemical Engineering
May 15, 2002

Certified by:_____
Prof. Jackie Y. Ying
Professor of Chemical Engineering
Thesis Supervisor

Accepted by:_____
Prof. Daniel Blankschtein
Professor of Chemical Engineering
Chairman, Departmental Committee on Graduate Studies

Nanocrystalline Perovskites for Catalytic Combustion and Oxygen Separation

by

Neeraj Sangar

M.S. Chemical Engineering Practice
Massachusetts Institute of Technology, 1998

B.S. Chemical Engineering
Rutgers University, 1996

Submitted to the Department of Chemical Engineering
On May 15, 2002 in Partial Fulfillment of the
Requirements for the Degree of Doctor of Philosophy in
Chemical Engineering

ABSTRACT

Nanocrystalline perovskites ($La_{1-x}A_xMn_{1-y}B_yO_3$) were successfully synthesized with higher surface area and smaller grain size by chemical co-precipitation compared to solid-state and complexation/combustion synthesis routes. The choice of solvent, base and suspension pH in co-precipitation was found to strongly affect the chemical stoichiometry of the resulting material. Stoichiometric $La_{0.5}Sr_{0.5}MnO_3$ was successfully obtained at a high pH using isopropanol as the solvent and tetraethylammonium hydroxide as the base. $La_{0.5}Sr_{0.5}MnO_3$ was derived with a ultrafine grain size of 13 nm and a high surface area of 43 m^2/g at 650°C, and maintained its nanocrystalline microstructure on heating to 1000°C, with a grain size of 25 nm and a surface area of 19 m^2/g.

The catalytic activity of these perovskites was investigated for different A- and B-site substitutions. Among $LaBO_3$ perovskites, the catalytic activity was found to decrease in the order: Mn > Fe ~ Ni > Co, with $LaMnO_3$ showing the lowest light-off temperature of 420°C. The intrinsic catalytic activity at 650°C decreased in the order: Ni > Co > Fe > Mn. Substitution of Group IIA metals for La^{3+} was found to increase the reaction rate of $La_{1-x}A_xMnO_3$, while higher valency dopants did not change or decreased catalyst activity. In the case of Ca^{2+} and Sr^{2+} dopants, intrinsic activity of $La_{1-x}A_xMnO_3$ was found to increase with doping level until x = 0.4 and 0.6, respectively. $La_{0.4}Sr_{0.6}MnO_3$ exhibited the lowest light-off temperature of 380°C, with a reaction rate that was 2.5 times higher than $LaMnO_3$. Methane TPR experiments showed that methane oxidation over the perovskites occurred by methane adsorption on the catalyst surface via hydrogen abstraction. Substitution of Group IIA metals for La^{3+} enhanced catalytic activity by increasing the rate of methane activation, but lowered activity at high doping levels due to slow carbonate decomposition.

Mixed conducting $Ba_{1-x}Sr_xCo_{1-y}M_yO_{3-\delta}$ perovskite membranes were developed for oxygen separation applications. $Ba_{0.75}Sr_{0.25}Co_{0.8}Fe_{0.2}O_{3-\delta}$ showed a very high oxygen flux of

~ 3.8 cm^3[STP]/min/cm^2 at 900°C. $Ba_{0.25}Sr_{0.75}Co_{0.8}Ti_{0.2}O_{3-\delta}$ exhibited an oxygen flux of ~ 1.4 cm^3[STP]/min/cm^2 at 750°C with excellent stability over time. These oxygen fluxes were ~ 2 times higher than those reported for the best existing membrane materials. High oxygen fluxes were obtained by creating a high oxygen vacancy concentration (~ 15% of oxygen lattice sites) via extrinsic doping, and by increasing the unit cell free volume to allow facile oxide ion hopping. The challenge in developing these membranes was to prevent the phase transformation of the vacancy-disordered perovskite to a poorly conductive vacancy-ordered structure in the desired temperature range of 750-900°C. This was accomplished by doping various cations in place of cobalt at the B site. Iron was found to be the most effective dopant for stabilizing the perovskite phase, followed by titanium and tin.

A novel approach was developed to stabilize the vacancy-disordered perovskite phase of $BaCo_{0.8}M_{0.2}O_3$ on cooling to room temperature, so that significantly higher oxygen fluxes could be achieved at low temperatures with excellent stability. When a single type of dopant cation was introduced at the B site, the vacancy-disordered phase could not be fully stabilized, resulting in phase transformation to an ordered structure and low oxygen fluxes. Dopants that satisfied the selection criteria most closely (i.e. Sn^{4+} and Fe^{3+}) corresponded to smaller heats of transition and lower order-disorder temperatures. A "mixing pot" approach was utilized to stabilize the perovskite phase to room temperature by introducing both Sn^{4+} and Fe^{3+} at the B site. Substituting a mixture of stabilizer dopants created more cationic disorder at the B site, which together with their coordination preferences and valence states, successfully prevented the oxygen vacancies from forming an ordered structure. This resulted in higher oxygen fluxes, and excellent flux stability even at a relatively low temperature of 750°C. The stabilized $BaCo_{1-y-z}Sn_yFe_zO_3$ perovskites exhibited impressive oxygen fluxes of ~ 3.5 and ~ 1.3 cm^3[STP]/min/cm^2 at 900°C and 750°C, respectively, which were substantially higher than those achieved by conventional perovskite membrane compositions.

Thesis Supervisor: Jackie Y. Ying
Title: Professor of Chemical Engineering

Acknowledgements

Table of Contents

List of Figures

12

List of Tables

List of Symbols

a	slope of σ_{ion}-$\ln(P_{O2})$ plot
a	unit cell dimension
b	intercept of σ_{ion}-$\ln(P_{O2})$ plot
D	tracer diffusion coefficient
D_v	vacancy diffusion coefficient
E_a	Arrhenius activation energy
F	Faraday's constant
J_{O2}	oxygen flux
k_1	rate constant for methane activation
k_2	rate constant for conversion of adsorbed methoxy species to surface carbonate
k_s	surface exchange rate
K_3	equilibrium constant for oxygen dissociation
L	membrane thickness
L_c	characteristic membrane thickness with surface exchange limitation
n_i	number of metal cations i in unit cell
P_{O2}	oxygen partial pressure
r_A	molar average radius of A-site cations
r_B	molar average radius of B-site cations
r_O	radius of oxide ion
R	universal gas constant
t_i	ionic transference number
T	temperature
V_i	volume of metal cation i
V_m	perovskite molar volume
V_o	oxygen vacancy
V_{occ}	total volume occupied by metal cations and oxide anions in unit cell
V_{tot}	total volume of unit cell
x	A-site dopant concentration
y	B-site dopant concentration
γ	activity coefficient for oxygen vacancies
δ	oxygen vacancy concentration
ϕ	fuel-to-air stoichiometric ratio
σ_{ion}	oxide conductivity

1 – Background and Research Motivation

1.1 Methane Combustion Catalysts

Combustion of carbon-containing fuels is used extensively today in industry as a means of generating electric energy. Roughly 70% of the total electric power generated in the United States comes from the combustion of coal (54.9%), natural gas (9.4%), and other hydrocarbons (3.9%) [1]. Environmental regulations, recently put into effect both in the United States and the international community, significantly restrict the output of hazardous products from the combustion processes. These include greenhouse gases, acid rain-causing compounds, and ozone-depleting agents. In addition, significant efforts are underway to reduce the worldwide emissions of greenhouse gases (in particular, carbon dioxide), which have been found to adversely affect world climate.

Combustion of methane is an important alternative to combustion of coal or long-chain hydrocarbons in power generation and other processes, since it has the potential to reduce the emission of greenhouse gases. Methane produces twice the amount of energy per unit mass of CO_2 emitted than coal due to its higher hydrogen-to-carbon ratio. However, methane requires a higher flame temperature for its stable combustion than other hydrocarbons, due in part to the absence of carbon-carbon bonds in the molecule, which makes it relatively unreactive.

The elevated temperatures required for methane combustion (> 1400°C) can cause significant production of nitrogen oxide species (NO_x). Formation of NO_x under these conditions occurs through two different mechanisms [2]. The first is direct oxidation of the nitrogen in air (thermal NO_x) [3]. The second mechanism involves reaction of methyl radicals with nitrogen, leading to HCN species that can be further oxidized to NO_x (prompt NO_x) [4]. Exposure to high levels of NO_x may have an immediate impact on human health, such as cyanosis and pulmonary edema. Prolonged exposure to NO_x above the natural ambient levels may lead to bronchitis, pneumonia and alterations to the immune system [5]. Additionally, NO_x contributes to the formation of smog by reacting with unburned hydrocarbons and volatile organic compounds to produce ozone, and also leads to acid precipitation [6]. In addition to NO_x emissions, a substantial amount of unburned or partially oxidized hydrocarbons may be emitted during the initial start-up stages of a methane or natural gas combustor. These compounds can contribute to the formation of smog and have significant greenhouse effects [7].

Catalytic combustion of methane has been studied as an alternative to gas-phase homogeneous combustion [8]. The use of an active catalyst for methane oxidation can stabilize a flame at significantly lower fuel-to-air ratios, thereby decreasing flame temperatures from > 1500°C to ~ 1300°C. This minimizes the formation of thermal NO_x, and avoids the need to quench flame temperatures to ~ 1300°C with fresh air before entering a gas turbine. The use of a catalyst at high levels of excess air also leads to more complete combustion and reduced hydrocarbon emissions [9].

In catalytic combustion, methyl radicals that promote the gas-phase homogeneous combustion are produced on the catalyst surface and are subsequently desorbed. These radicals are presumed to stabilize the flame at temperatures lower than that of a homogeneous adiabatic flame [10]. A reactor that uses this type of catalyst system is known as a catalytically stabilized thermal combustor (CSTC). The volumetric heat output of a CSTC, defined as the heat produced per unit volume of the combustion chamber, is comparable to that of a conventional homogeneous flame combustor [11].

An ideal combustion catalyst should possess the following properties: (1) high activity for methane oxidation at the lowest possible temperature and the leanest fuel-to-air ratio, (2) high stability of catalyst activity in the presence of CO_2 and water at high temperatures under prolonged operation, and (3) high surface area, low pressure drop, and high thermal shock resistance for the catalyst/support system.

Traditional catalysts for methane oxidation can be divided into three categories, namely, noble metal, metal oxide, and complex oxide-based catalysts. Noble metals, such as palladium and platinum, have been extensively used as oxidation catalysts. These expensive catalysts are generally supported on a high surface area oxide (such as alumina and silica) to increase the dispersion of the active metal and provide thermal stability. Supported PdO/Al_2O_3 catalysts exhibit the highest activity for methane oxidation at low temperatures (~ 300°C), which makes them attractive as ignition-stage catalysts in a catalytic combustor. However, at high temperatures (> 700°C), PdO undergoes a phase transformation to Pd metal, rendering it inactive for methane oxidation. This instability of PdO-based catalysts at high temperatures results in exhaust temperature cycling, corresponding to reduction and reoxidation of PdO clusters. In addition, the mobility of PdO clusters on the support surface at high temperatures leads to grain growth and sintering of PdO clusters. The resulting loss of PdO dispersion requires the use of

high palladium loadings to achieve sufficient active surface area for methane oxidation. Moreover, PdO-based catalysts also exhibit poor hydrothermal resistance. In the presence of water, PdO surface gets hydrated to form $Pd(OH)_2$, thereby reducing the catalytic activity of the system [12].

Transition metal oxides, such as Co_3O_4, Mn_2O_3, TiO_2, Fe_2O_3 and NiO, and base metal oxides, such as MgO and SrO, have been studied as alternatives to noble metal systems for catalytic combustion. The main advantage of metal oxide catalysts is their higher thermal stability and lower raw material costs, compared to noble metal systems. However, these oxides have lower specific activity for methane oxidation, requiring higher ignition temperatures. In addition, they undergo rapid grain growth and sintering above 800°C, causing reduction of catalyst activity.

Complex metal oxides, such as barium and strontium hexaaluminates, perovskites and aluminosilicates, have been evaluated as candidates for supports or active washcoats and catalytic particles. The complex crystal structure of barium hexaaluminates imparts high thermal stability and ability to retain relatively high surface areas at elevated temperatures, due to its highly anisotropic crystal properties that suppress grain growth. Additionally, these complex oxides can accommodate a wide variety of structural dopants and surface additives, which can enhance their inherently low catalytic activity. Zarur and Ying [13] have reported that by coating BHA nanoparticles with CeO_2 or MnO_2, light-off temperatures for methane oxidation can be lowered from > 700°C for conventional BHA to ~ 400°C. Supporting the CeO_2 or MnO_2 on BHA suppresses the grain growth of these oxides, and allows operation to > 1000°C without loss of catalytic activity.

Recently, perovskite-based materials have been investigated as potential oxidation catalysts for methane, carbon monoxide and hydrocarbon. Several researchers [14-17] have reported the catalyst activity of $La_{1-x}A_xBO_3$ (A = Sr, Ba, Eu, Ce; B = Cr, Mn, Fe, Co, Ni) for methane oxidation. Although these materials exhibit high specific activity for methane oxidation, conventional synthesis methods (such as solid-state reaction and combustion synthesis) result in powders with low surface areas (< 15 m^2/g) and large grain sizes (> 50 nm) due to the required high-temperature treatment. It has also been found that A- and B-site substitutions have a dramatic effect on catalyst activity, however, an understanding of such effect is still lacking.

1.2 Oxide-Ion Conducting Membranes

Ceramic membranes are of great interest as a means for separating oxygen from air or oxygen-containing gas mixtures. Since oxygen generation ranks among the top five for commodity chemicals production in the U.S., successful development of oxide membranes would have clear economic benefits. However, it must be competitive with more traditional separation processes, such as cryogenic distillation, pressure-swing adsorption (PSA), and polymeric membrane separation [18].

Dense oxide membranes for oxygen separation belong to a class of materials called solid electrolytes. Their history dates back to 1834 when Michael Faraday observed high electrical conductivity of PbF_2 at high temperatures, which was later ascribed to the diffusion of fluoride ions [19]. Solid electrolytes with high conductance for specific ions have been developed. For example, oxide, lithium, silver, copper, proton, sodium and potassium ion-conducting electrolytes are of interest in the development of solid-state batteries, fuel cells, electrochemical sensors, membrane separation, electrocatalysis, electrochemical reactors, and electrochromic devices [20].

Figure 1 shows the transport mechanism through an oxide ion-conducting membrane. The first step is the dissociative chemisorption of gas-phase oxygen molecules on the oxide surface to form oxide ions (O^{2-}). This requires the presence of oxygen vacancies on the membrane surface serving as sites for incorporating "fresh" oxide ions, and the presence of electron/holes or reducible metal cations to convert molecular oxygen to fully reduced O^{2-} species. In the presence of an imposed oxygen concentration gradient, the oxide ions diffuse across the membrane until they lose charge, combine and desorb as oxygen molecules at the other side of the membrane.
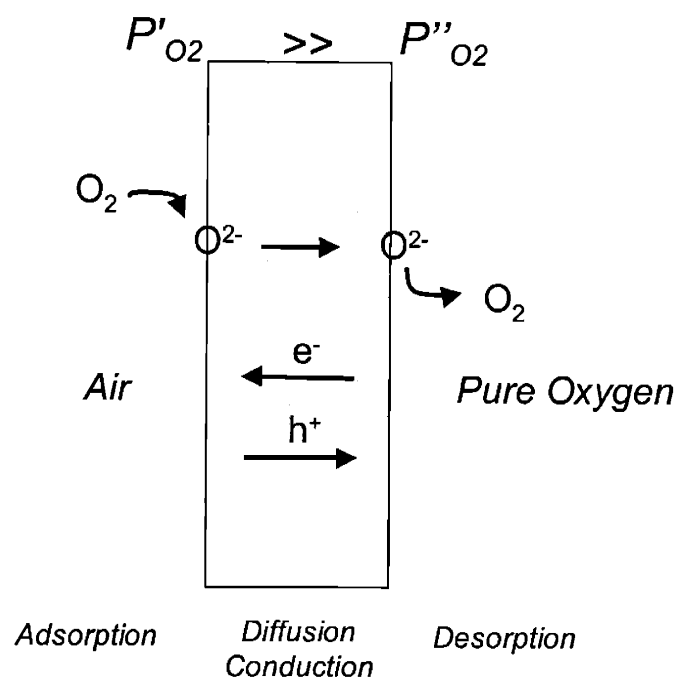
Figure 1.1. Schematic of the surface reactions and transport processes occurring in a mixed oxide-electronic conductor for oxygen separation applications.

Diffusion of oxide ions in the crystal lattice occurs via successive jumps or "hops" of oxide ions from the occupied lattice sites to the neighboring vacant sites. The movement of oxide ions depends greatly on the concentration of these oxygen vacancies, which are positively charged point defects in the crystal lattice, and on the arrangement of these vacancies in the lattice. At low concentrations, oxygen vacancies are randomly arranged, since they do not interact with each other. At higher concentrations, these vacancies begin to interact with each other, and may form ordered arrangements especially at lower temperatures. One structure possessing an ordered arrangement of oxygen vacancies is the brownmillerite structure $(A_2B_2O_5)$, which is derived from the ideal perovskite lattice by regularly removing one-sixth of the oxygen atoms along the cubic [110] direction (Figure 1.2). This results in a layered compound consisting of corner-shared BO_6 octahedra (O) alternating with layers of corner-shared BO_4 tetrahedra (T) stacked in an ...OTOTOTOT... sequence. An ordered vacancy arrangement greatly decreases the oxygen diffusivity because transport is confined to two-dimensional planes consisting of the oxygen vacancies, which cannot escape to adjacent layers. As the temperature is raised, the vacancies begin to invade the adjacent immobile regions, until the entire structure becomes disordered. Although this order-disorder transformation is

energetically unfavorable, it is thermodynamically favorable at high temperatures due to the gain in configurational entropy associated with a random arrangement of oxygen vacancies. Therefore, a sharp increase in oxide conductivity is observed above this transformation temperature.
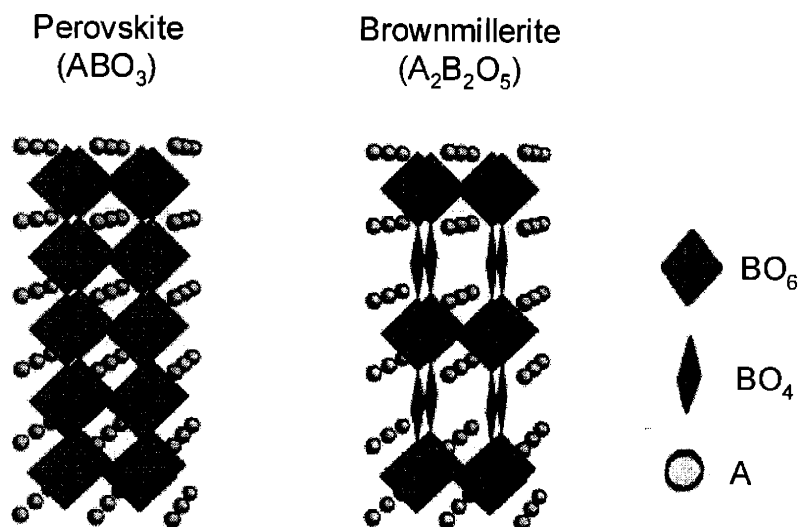
Figure 1.2. Perovskite and brownmillerite crystal structures.

As an oxide ion moves from one lattice site to another by a vacancy jump, it encounters an intermediate saddle point of high energy formed by two A ions and one B ion. The associated activation energy depends strongly on the crystal structure (i.e. lattice free volume, critical radius of migration, atomic sizes, etc.) In general, fluorite-based crystal structures (such as stabilized zirconia and ceria) have a lower activation energy for oxide ion transport, compared to perovskite-based or pyrochlore-based crystal structures, owing to their higher unit cell free volume. Kilner and Brook [21] and Cook and Sammells [22, 23] have proposed empirical relationships for predicting the oxide ion conductivity and activation energy by considering the average metal-oxygen bond strength, lattice free volume, overall lattice polarizability toward anion migration, etc.

Oxide conductors can be divided into two categories, purely ionic or mixed conductor, based on the degree of electronic conduction present in the material. Purely ionic conductors exhibit predominantly oxide ion conduction, possessing oxide ion transference number close to unity ($t_i \sim 1$). Zirconia-based conductors have been extensively studied, and are finding

commercial applications as solid oxide fuel cell electrolytes and oxygen sensors. Ceria and bismuth oxide-based conductors have oxide conductivity higher than yttria-stabilized zirconia (YSZ), but suffer from potential reduction problems at high temperatures and low oxygen partial pressures. The ionic conductivity of YSZ and doped ceria at 900°C are < 0.1 S/cm and ~ 0.1-0.3 S/cm, respectively [1]. Goodenough et al. [24] have reported fast ion conduction in stabilized $Ba_2In_2O_5$ at temperatures as low as 400°C. $Ba_3In_2ZrO_8$ shows oxide ion conductivity of ~ 0.01 S/cm at 400°C, which is twice as high as that reported for calcia-stabilized zirconia at 800°C. Abraham et al. [25] found that the vacancy-disordered, γ phase of $Bi_4V_2O_{11}$ could be stabilized to room temperature by a partial substitution of V by Cu. $Bi_4V_{1.8}Cu_{0.2}V_{11-\delta}$ exhibits remarkably high oxide ion conduction (~ 0.01 S/cm at 350°C). However, maintaining an oxide transference number close to unity, especially under reducing conditions, is challenging due to the presence of reducible metal cations (such as Bi and Cu).

Mixed ionic-electronic conductors (MIEC) exhibit both ionic and electronic (electron or hole) conduction. The conduction of oxide ions across the membrane results in electric charge transport, which is compensated by electron or hole conduction. The type of electronic conduction (n- or p-type) present in the materials depends on the composition, temperature and oxygen partial pressure. In general, most materials are p-type conductors at "high" P_{O2} and n-type conductors at "low" P_{O2}; the oxygen partial pressure range where these transitions occur is composition- and temperature-dependent. Mixed conductors are of interest as oxygen separation membranes, since external circuitry is not required to complete the flow of charge. Initial attempts to create a mixed-conducting membrane utilized internal short-circuiting by forming a composite of a purely oxide conductor (such as YSZ) and an inert metal (such as Pd) [26]. Although high values of oxygen flux have been reported by controlling the amount and dispersion of the metal, the main disadvantages of this approach include: (1) difficulty in sintering these materials to produce dense membranes, (2) potential formation of new phases at interfacial regions, (3) structural integrity of the composite membrane on heating/cooling, and (4) limitation on the highest achievable oxide conductivity determined by the pure oxide conductor.

Iwahara et al. [27] were the first to report a fast oxide conductor with appreciable electronic conductivity. The oxide conductivity of $CaTi_{0.8}Fe_{0.2}O_{3-\delta}$ was ~ 0.1 S/cm at 1000°C with an oxide transference number of ~ 0.6. Teraoka et al. [28-31] investigated the influence of

22

A- and B-site substitution on oxygen permeation through $La_{0.6}A_{0.4}Co_{0.8}Fe_{0.2}O_3$ (A = La, Na, Ca, Sr, Ba) and $La_{0.6}Sr_{0.4}Co_{0.8}B_{0.2}O_3$ (B = Cr, Mn, Fe, Co, Ni, Cu). The oxygen permeability in the two series was found to increase in the respective orders of La < Na < Sr < Ca < Ba and Mn < Cr < Fe < Co < Ni < Cu. $La_{0.6}Sr_{0.4}Co_{0.8}Cu_{0.2}O_3$ was reported to have a flux ~ 2 cm^3[STP]/min/cm^2 at 900°C. Oxygen transport in these materials was not limited by electronic conductivity, in contrast to doped-$CaTiO_3$ or composite systems, but by the intrinsic oxide ion mobility in the crystal lattice. The high electronic conductivity in these materials was attributed to the hopping transport of mobile charge carriers (electrons or holes) between neighboring transition metal cations at the B site, owing to their ability to adopt different oxidation states.

In the $La_{1-x}Sr_xCo_{1-y}Fe_yO_3$ series, Teraoka et al. [28-31] found that the oxygen flux increased with Co and Sr content, the highest flux being achieved with $SrCo_{0.8}Fe_{0.2}O_3$. Kruidhof et al. [32] showed for the first time that in $SrCo_{0.8}Fe_{0.2}O_3$, a change in permeation mechanism corresponding to an order-disorder transition occurs at ~ 790°C. Results from thermal analysis and X-ray diffraction confirmed a phase transition from the vacancy-ordered brownmillerite phase to a vacancy-disordered perovskite phase at high temperatures. It is known that the parent compound $SrCoO_3$ transforms reversibly from a brownmillerite-like structure to a defective perovskite at ~ 930°C in air. The oxygen flux below the transition temperature is very small, as expected for an ordered arrangement of oxygen vacancies, but is found to increase sharply (by 5 to 6 orders of magnitude) at the onset of the phase transition. The perovskite phase in $SrCoO_3$ seems to be stabilized to lower temperatures by partial substitution of Co by Fe.

Thus far, it was assumed that the rate-limiting step in the transport of oxygen through the membrane is the solid-state diffusion of oxide ions. The surface exchange of oxygen between the oxide surface and the gas phase is believed to involve a series of reactions, each of which may be rate-determining. In the design of membranes with high oxygen fluxes, it is critical to understand conditions under which surface-exchange kinetics become rate-limiting. By experimentally measuring the surface-exchange rate with O^{18}-O^{16} isotopic labeling and the oxide diffusion coefficient, a number of researchers [33-35] have proposed the concept of a characteristic thickness (L_c), which is a ratio of the diffusion coefficient (D) and the surface-exchange coefficient (k_s). When the actual membrane thickness (L) is much larger than the characteristic thickness, oxygen transport is predominantly controlled by solid-state diffusion of oxide ions. However, when $L \ll L_c$, oxygen flux is controlled predominantly by oxygen-

exchange kinetics. The characteristic thickness for a number of perovskite compositions has been reported at different temperatures and oxygen partial pressures. For example, $La_{0.6}Sr_{0.4}Co_{0.8}Ni_{0.2}O_3$ has a characteristic thickness of 0.05 cm at 800°C [35]. The characteristic thickness does not represent an intrinsic material property, but may depend on the roughness and porosity of the membrane surface through the value of k_s. Thorogood *et al.* [36] and Deng *et al.* [37] have shown that the oxygen flux can be significantly improved if the thin dense membrane is coated with a porous layer. Therefore, as technological challenges in the fabrication of dense, defect-free, thin perovskite films are resolved, it is important to consider ways to overcome surface-exchange limitations on oxide ion transport.

Although substantial progress has been made in the development of mixed-conducting perovskites as dense, ceramic membranes for oxygen separation, significant research needs to be conducted to address the following technical challenges: (1) designing materials with higher oxide ion conductivity, (2) tailoring material composition to increase membrane stability under reducing conditions, (3) manipulating material composition to allow operation at lower temperatures by suppressing ordering of oxygen vacancies, (4) production of thin, dense, defect-free perovskite films using low-cost fabrication techniques, and (5) overcoming the limitations of surface-exchange kinetics on oxygen flux. These issues are critical to the successful application of perovskite materials for oxygen delivery applications, such as in membrane reactors for selective partial oxidation.

1.3 Research Motivation and Approach

The primary challenge in developing catalysts for natural gas combustion is to achieve (1) high activity for methane oxidation, comparable to noble metal systems, while maintaining high stability in the presence of CO_2 and water, and (2) high thermal stability to prevent catalyst deactivation by grain growth and sintering. Our approach to realizing these goals involves the synthesis of multicomponent perovskite catalysts with nanocrystalline microstructure, high surface area, phase purity and chemical homogeneity. Alternatives to solid-state and combustion synthesis routes will be explored to achieve perovskite nanoparticles with superior phase homogeneity and ultrafine microstructure. The specific catalytic activity of methane oxidation will be optimized through the introduction of various dopants at the A and B sites. The relationship between perovskite composition and catalytic activity will be explored to elucidate

the role of surface oxygen species in activating methane at low temperatures. The nature and amount of active oxygen species on the catalyst surface will be investigated, and related to the defect chemistry of the perovskite.

The primary challenge in the application of perovskite-based membranes for oxygen delivery is to develop novel materials and processing techniques to achieve stable, high oxygen fluxes in the desired temperature range of 700-950°C. Increasing the oxygen flux through these membranes decreases the required exchange area needed to produce a specified oxygen flow rate, thereby decreasing capital and operating costs. Moreover, high stability of the oxygen flux is needed to increase membrane lifetime and decrease process downtime associated with membrane regeneration.

Our approach in developing novel perovskite compositions with *high* and *stable* oxide conductivity is to optimize the concentration of "mobile" oxygen vacancies and the unit cell free volume, without causing phase transformation to a poorly-conductive, vacancy-ordered phase. As the oxygen vacancy concentration is increased, the oxide conductivity is expected to increase due to an increase in the number of carriers available for transporting oxygen. However, interactions between these vacancies will also increase, and may lead to the formation of undesired ordered structures. Increasing the unit cell free volume is expected to reduce the activation energy barrier associated with oxide hopping, giving rise to higher oxide conductivity. However, it may destabilize the perovskite structure due to a size mismatch between A- and B-site cations, causing undesired phase transformations. Therefore, at a given set of operating conditions, the perovskite composition needs to be carefully tailored to optimize the concentration of "mobile" oxygen vacancies and the unit cell free volume.

1.4 References

[1]   "Statistical Yearbook," Edison Electric Institute, 1994.

[2]   Taylor, K.C., *Catal. Rev.-Sci. Eng.* **35**, 457 (1993).

[3]   Fenimore, C.P., *Combust. Flame* **26**, 249 (1976).

[4]   Zeldovich, Y.B., *Acta Physicochem. URSS* **21**, 577 (1946).

[5]   Armor, J.N., *Appl. Catal. B: Env.* **1**, 221 (1992).

[6]   Pereira, C.J., Amiridis, M.D., in "Reduction of Nitrogen Oxide Emissions," (U.S. Ozkan, S.K. Agarwal, and G. Marcelin, Eds.), Vol. 587, p. 1. American Chemical Society, Washington, D.C., 1995.

[7]   "Kyoto Protocol to the United Nations Framework Convention on Climate Change." United Nations Organization, 1997.

[8]   Germain, J.E., "Catalytic Conversion of Hydrocarbons." Academic Press, London, 1969.

[9]   Linan, A., Williams, F.A., "Fundamental Aspects of Combustion." Engineering Science Series, Oxford Press, New York, 1993.

[10]   Lunsford, J.H., *Langmuir* **5**, 12 (1989).

[11]   Pfefferle, L.D., Pfefferle, W.C., *Catal. Rev.-Sci. Eng.* **29**, 219 (1987).

[12]   Ciuparu, D., Katsikis, N., Pfefferle, L., *Appl. Catal. A: Gen.* **216**, 209 (2001).

[13]   Zarur, A.J., Ying, J.Y., *Nature* **403**, 65 (2000).

[14]   Marchetti, L., Forni, L., *Appl. Catal. B: Env.* **15**, 179 (1998).

[15]   Saracco, G., Scibilia, G., Iannibello, A., Baldi, G., *Appl. Catal. B: Env.* **8**, 229 (1996).

[16]   Zhong, Z., Chen, K., Ji, Y., Yan, Q., *Appl. Catal. A: Gen.* **156**, 29 (1997).

[17]   Choudhary, V.R., Uphade, B.S., Pataskar, S.G., *Fuel* **78**, 919 (1999).

[18]   Bouwmeester, H.J.M., Burggraaf, A.J., in "The CRC Handbook of Solid State Electrochemistry," (P.J. Gellings and H.J.M. Bouwmeester, Eds.), p. 481. CRC Press, New York, 1996.

[19]   Kudo, T., in "The CRC Handbook of Solid State Electrochemistry," (P.J. Gellings and H.J.M. Bouwmeester, Eds.), p. 195. CRC Press, New York, 1996.

[20]   Kudo, T., Fueki, K., "Solid State Ionics." Kodansha, Tokyo, 1990.

[21]   Kilner, J.A., Brook, R.J., *Solid State Ionics* **6**, 237 (1982).

[22]   Cook, R.L., Sammells, A.F., *Solid State Ionics* **45**, 311 (1991).

[23]   Sammells, A.F., Cook, R.L., White, J.H., Osborne, J.J., MacDuff, R.C., *Solid State Ionics* **52**, 111 (1992).

[24]   Goodenough, J.B., Ruiz-Diaz, J.E., Zhen, Y.S., *Solid State Ionics* **44**, 21 (1990).

[25]   Abraham, F., Boivin, J.C., Mairesse, G., Nowogrocki, G., *Solid State Ionics* **40/41**, 934 (1990).

[26]   Chen, C.S., Boukamp, B.A., Bouwmeester, H.J.M., Cao, G.Z., Kruidhof, H., Winnubst, A.J.A., Burggraaf, A.J., *Solid State Ionics* **76**, 23 (1995).

[27]   Iwahara, H., Esaka, T., Mangahara, T., *J. Appl. Electrochem.* **18**, 173 (1988).

[28]   Teraoka, Y., Zhang, H.M., Furukawa, S., Yamazoe, N., *Chem. Lett.*, 1743 (1985).

[29]   Teraoka, Y., Nobunaga, T., Yamazoe, N., *Chem. Lett.*, 503 (1988).

[30]   Teraoka, Y., Nobunaga, T., Okamoto, K., Miura, N., Yamazoe, N., *Solid State Ionics* **48**, 207 (1991).

[31]   Teraoka, Y., Zhang, H.M., Okamoto, K., Yamazoe, N., *Mater. Res. Bull.* **23**, 51 (1998).

[32]   Kruidhof, H., Bouwmeester, H.J.M., van Doorn, R.H.E., Burggraaf, A.J., *Solid State Ionics* **63-65**, 816 (1993).

[33]   Ishigaki, T., Yamauchi, S., Mizusaki, J., Fueki, K., Tamura, H.J., *J. Solid State Chem.* **54**, 100 (1984).

[34]   Ishigaki, T., Yamauchi, S., Kishio, K., Mizusaki, J., Fueki, K., *J. Solid State Chem.* **73**, 179 (1988).

[35]   Ftikos, Ch., Carter, S., Steele, B.C.H., *J. Eur. Ceram. Soc.* **12**, 79 (1993).

[36]   Thorogood, R.M., Srinivasan, R., Yee, T.F., Drake, M.P., U.S. Patent 5,240,480, 1993.

[37]   Deng, H., Zhou, M., Abeles, B., *Solid State Ionics* **80**, 213 (1995).

2 – Synthesis of Nanocrystalline Perovskites for Catalytic Combustion of Methane

2.1 Introduction

Methane is becoming an increasingly attractive fuel for energy generation, since natural gas is an abundant and inexpensive resource. Moreover, it has the highest energy yield per unit of CO_2 produced, thereby reducing the emissions of greenhouse gases. Homogeneous combustion of methane is stable under fuel-rich conditions, specifically at fuel-to-air stoichiometric ratios (ϕ) greater than 0.48, resulting in high flame temperatures of 1400-1600°C. The combustion stream is then quickly cooled to ~ 1300°C using fresh air, before entering a gas turbine to generate electricity. Significant NO_x is formed in the localized regions of high flame temperatures (> 1400°C) by activating nitrogen molecules present in air with gas-phase oxygen or methyl radicals. Since NO_x is a major environmental pollutant, effluent streams from these combustors are required to undergo expensive NO_x remediation, such as selective catalytic reduction of NO_x by NH_3 using zeolitic catalysts. As environmental regulations are becoming more stringent, alternative technologies are desired to combust methane without the formation of NO_x, and hence, circumventing the need for expensive post-treatment.

Catalytic combustion of methane can stabilize flames under fuel-lean conditions, resulting in adiabatic flame temperatures below 1300°C. Lower flame temperatures would significantly reduce NO_x emissions, and would eliminate the need to cool the combustion stream before entering the gas turbine. A catalyst can stabilize a flame by activating methane and oxygen molecules on its active surface, followed by desorption of methyl radicals and their participation in gas-phase radical reactions. Since methane is a very stable molecule, it is very challenging to develop catalysts that can activate methane at low temperatures (~ 400°C). It is important to develop highly active catalysts for methane oxidation, since this would decrease the pre-heating requirements for a combustion stream, resulting in a higher fuel efficiency. It is also critical to develop catalysts that can maintain their activity at high temperatures (~ 900°C) over long periods of time, even in the presence of H_2O and CO_2.

The primary challenge in catalytic combustion of methane is to develop catalysts possessing (1) high activity for methane oxidation, (2) high thermal stability, and (3) high stability in the presence of high concentrations of H_2O and CO_2. Traditional catalysts for methane oxidation can be divided into three categories: noble metal, metal oxide, and complex

oxide-based catalysts. Supported PdO catalysts are most active for methane oxidation, but are susceptible to decomposition to inactive Pd metal at high temperatures. In addition, these supported metal catalysts undergo rapid sintering at high temperatures, thereby requiring high loadings of expensive metal to achieve adequate surface areas. PdO-based catalysts also exhibit poor hydrothermal resistance. In the presence of water, PdO becomes hydrated to $Pd(OH)_2$, resulting in greatly reduced catalyst activity [1]. Transition metal oxides (such as Co_3O_4, Mn_2O_3, TiO_2, Fe_2O_3 and NiO) and base metal oxides (such as MgO and SrO) have been studied as alternatives to noble metal systems for catalytic combustion. The main advantage of these catalysts is their higher thermal stability and lower raw material costs, compared to noble metal systems. However, these oxides have lower specific activity for methane oxidation, requiring higher ignition temperatures. In addition, they undergo deactivation with rapid grain growth and sintering above $600^{\circ}C$. Complex metal oxides, such as barium and strontium hexaaluminates, perovskites and aluminosilicates have been evaluated as candidates for support or active washcoats and catalytic particles. The complex crystal structure of barium hexaaluminates imparts high thermal stability, with retention of relatively high surface areas at elevated temperatures. These materials, however, demonstrate inherently low catalytic activity except when they are processed with CeO_2 in the form of nanocomposite [2].

The goal of this study is to develop novel nanocrystalline perovskite-based catalysts with high activity for methane oxidation, and high stability under high temperatures and in the presence of water and carbon dioxide. Perovskite crystal structure (ABO_3) can accommodate a wide variety of metals at the A and B cation sites, and can tolerate a high oxygen non-stoichiometry before undergoing phase transformation. Several catalyst characteristics, such as oxide and electronic conductivity, oxygen vacancy concentration, valence states of A and B cations, and metal-oxygen bond strength, can be systematically varied to affect catalyst performance through appropriate doping at the A and B sites. The effect of perovskite composition on the catalytic activity, microstructure, thermal stability and defect chemistry will be investigated.

The synthesis of nanocrystalline multicomponent oxides is quite challenging. To achieve a homogeneous, stoichiometric mixture of different metal ions and simultaneously attain the nanocrystalline microstructure, special processing techniques have to be developed. Several wet-chemical processes have been recently developed for synthesizing high surface area,

nanocrystalline, multicomponent oxides. Traditionally, multicomponent systems are obtained through solid-state routes, but the high temperatures required for atomic level diffusion of the different components result in coarse-grained materials (> 100 nm) with low surface areas (< 1 m^2/g). Nanocrystalline materials can be synthesized through inert gas condensation (IGC) techniques [3-5], however, low yields, high costs and lack of compositional flexibility are limiting factors for commercial applications.

Wet-chemical methods can produce materials with very fine crystallite sizes, and offer excellent compositional homogeneity through room-temperature processing. However, particle agglomeration must be controlled during wet-chemical synthesis to achieve powders with uniform microstructures and very high surface areas. Lanthanum-based perovskites are generally synthesized by complexation/combustion techniques, such as the amorphous citrate process [6, 7] and the Pechini process [8]. Since the different cations are homogeneously mixed at the atomic level during the complexation step, the formation of intermediate oxide phases is minimized and the perovskite phase can be obtained at low calcination temperatures. This complexation technique has been modified by several groups [9, 10] to a rapid, highly exothermic combustion process. The complexing agent, which can also act as a fuel, spontaneously and violently reacts with an oxidant at temperatures above 200°C. The short reaction time prevents segregation of the cations, and the explosive nature of the mixture leads to a very fine ash. In studies carried out by Chick *et al.* [9, 10] on strontium-doped lanthanum manganite, chromite and ferrite systems with nitrate ions as the oxidant and glycine as the complexing agent, the resulting ash was a crystalline perovskite phase that showed excellent compositional homogeneity and grain sizes below 20 nm.

Chemical precipitation has been studied extensively over the last decade for the synthesis of nanocrystalline oxides. In the precipitation process, particle nucleation and growth, as well as agglomerate size, can be controlled by varying processing parameters. The synthesis of multicomponent oxides requires that the homogeneity and stoichiometry of the precursor solution be preserved in the final precipitate. This is challenging due to the different solubilities of various metal cations, sometimes by orders of magnitude. It is also important to ensure simultaneous precipitation of metal cations to obtain a homogenous precipitate, since metal cations may precipitate at different solution pH. The choice of precipitation agent (such as hydroxides, carbonates, or oxalates) is critical to allow for decomposition at low temperatures,

thereby avoiding grain growth and sintering at high calcination temperatures. During calcination, the precursor components must have similar decomposition behavior to prevent phase segregation. The goal of this project is to develop a reverse-strike coprecipitation method to synthesize multicomponent perovskites with the desired phase and stoichiometry, as well as ultrafine grain sizes and high surface areas. The effect of synthesis method, processing parameters and perovskite composition on the resulting powder morphology and catalytic properties will be investigated.

2.2 Experimental

2.2.1 Synthesis

Nanocrystalline lanthanum-based perovskites ($La_{1-x}A_xBO_3$; A = Ca, Sr, Ba, Pr, Eu, Gd, Ce; B = Cr, Mn, Fe, Co, Ni, Cu) were synthesized using reverse-strike coprecipitation method [11]. The nitrate precursors of the various metals were dissolved together in the desired molar ratio to a total concentration of 0.01-1.0 M cation in distilled water. The precursor solution was added to an aqueous or alcoholic solution of an organic base, tetraethylammonium hydroxide (TEAH, 40 wt% in water, Alfa Aesar) or tetra(n-butyl) ammonium hydroxide (TBAH, 55 wt% in water, Alfa Aesar). The concentration of the base solution was varied between 0.01 M and 1.0 M. The amount of base solution used during precipitation was determined by first calculating the theoretical moles of hydroxide ions required to hydrolyze the metal cations to $M^{z+}(OH^-)_z$ species. The actual hydroxide moles were obtained by multiplying the theoretical value by an excess factor, which was varied between 0.5 and 1.5. Different solvents, including distilled water, methanol, ethanol, isopropanol, and 50 vol% water-50 vol% isopropanol solution, were tested to study their effect on the powder stoichiometry and morphology. The solvent concentration in the final precipitate solution was calculated by dividing the added solvent volume by the total volume, and was typically held constant at ~ 80 vol%. Typically, ~ 150 mL of 0.2 M aqueous solution of precursor nitrates were added dropwise to a base solution (~ 500 mL) containing 0.2 M TEAH dissolved in isopropanol with an excess factor of 1.5. The precipitate was aged at 25°C for 2, 24 or 48 hours, and then centrifuged for supernatant removal. Excess base and residual nitrate salts were removed by washing the precipitate with isopropanol

three times. The precipitates were dried overnight in air, and ground in a mortar and pestle to a fine powder. The powders were calcined at 300-1000°C in air for 2 hours.

When hydroxide and carbonate were combined as precipitating agents, potassium carbonate was dissolved in a base solution containing TEAH. Water was used as solvent, due to the low solubility of K_2CO_3 in alcoholic medium. The moles of carbonate added were calculated by multiplying the theoretical moles required for precipitating the metal cations (M^{z+}) to form $M_2(CO_3)_z$, and a carbonate excess factor, which was varied between 0.75 and 1.5. K^+ impurities were removed by washing the precipitate with isopropanol.

Coprecipitated lanthanum-based perovskites were compared to powders prepared via solid-state and combustion synthesis. In solid-state synthesis, metal oxide/carbonate precursors were ground using a mortar and pestle in acetone to form an intimate mixture. After drying, the powder was fired to 1300-1400°C for 6 hours in air. In combustion synthesis, the nitrates of the metal constituents were dissolved together in the desired molar ratio in distilled water. Glycine (99.2%, Mallinckrodt), which played the dual role of complexant and fuel, was added at a fuel:nitrate molar ratio of 0.83:1. Assuming that glycine underwent complete combustion and the nitrate ions decomposed to nitrous oxide under the highly reducing conditions, the fuel-to-oxidant ratio was 50% higher than the stoichiometric ratio of 0.55:1 for this mixture. The solution was stirred at room temperature for $\geq$ 2 hours to ensure complete complexation. The concentration of the mixture was initially 0.4 M. The mixture was heated on a hot plate until all the water was evaporated and the mixture auto-ignited at approximately 200-300°C, producing a fine ash. The resulting powder was calcined at 650-800°C for 2 hours to ensure complete perovskite formation, and was characterized for its structure and stability.

2.2.2 Characterization

Phase identification of these perovskite powders was performed by powder X-ray diffraction (XRD) using a Siemens D5000 θ-θ diffractometer (45 kV, 40 mA, Cu-Kα). Scherrer's analysis of the broadening of <110> diffraction peak was employed to obtain the volume-averaged crystallite size. Surface area was measured using a 5-point BET (Brunauer-Emmett-Teller) method on a Micromeritics ASAP 2000 instrument. The error associated with surface area and crystallite size determinations was estimated to be ~2%, based on duplicated

measurements. Perovskite composition was determined using inductively coupled plasma-atomic emission spectroscopy (ICP-AES), after dissolution of calcined powder in 20 vol% aqua regia at 40°C. Transmission electron microscopy (TEM) was performed on a JEOL 2010 high-resolution microscope at 200 kV. Thermal gravimetric analysis (TGA) and differential thermal analysis (DTA) were performed using Perkin Elmer TGA7 and DTA7 systems, respectively. The surface species adsorbed on the powders were characterized with a MTEC Model 200 photoacoustic cell on a Bio-Rad FTS60A Fourier-transformed infrared (FTIR) spectrometer. Zeta potential measurements were performed on a ~ 0.05 wt% powder suspension containing 0.01 M potassium chloride as the supporting electrolyte. After sonication to break-up large agglomerates and form a stable suspension, solution pH was measured using an Orion model 420A pH meter, and adjusted by addition of KOH or HCl. After stirring for ~15 min, zeta potential was measured using ZetaPALS Zeta Potential Analyzer (Brookhaven Instruments Corporation).

2.2.3 Catalyst Activity

Catalyst activity measurements were performed at atmospheric pressure in a ¼"-O.D. quartz tube reactor with catalyst supported on a porous quartz frit. Type K thermocouple was located below the catalyst bed, and was used in conjunction with an Omega temperature controller and a Lindberg tube furnace to maintain the catalyst temperature within 2°C of the desired operating temperature. High-purity gases (He, 10% CH_4, 1% CH_4 in air, O_2, 10% O_2) were metered into the top of the quartz reactor using up to six independent MKS mass flow controllers. The reactor effluent was analyzed with a Hewlett Packard 6890 gas chromatograph equipped with molecular sieve 5A and Porapak Q chromatographic columns. This allowed oxygen, methane, carbon dioxide and water in the reactor effluent to be separated and quantified. Partially oxidized products (e.g., carbon monoxide) could be separated using these chromatographic columns, but were not observed under reaction conditions. Carbon balances to within 2.5% were achieved in all runs.

Typically, 25 mg of catalyst was loaded into the quartz reactor, and pretreated at 750°C for 1 hour in the reaction stream. A feed of 50 mL(STP)/min of 1% CH_4 in air was passed through the catalyst bed for the initial screening of catalyst activity. A dilute methane feed was used to prevent localized heating within the catalyst bed associated with methane conversion.

This flowrate corresponded to a gas hourly space velocity (GHSV) of 60,000 hour^{-1}, and was representative of industrial application requirements. After catalyst pretreatment at 750°C, the catalyst temperature was slowly decreased at 1.5°C/min to 250°C, while analyzing the reactor effluent at ~10°C intervals. Methane conversion was calculated based on carbon dioxide formation, by dividing the observed carbon dioxide concentration by that expected based on complete methane conversion.

2.2.4 Mechanistic Studies

Temperature-programmed desorption (TPD) of oxygen was performed on various perovskite compositions to determine the nature and amount of chemisorbed oxygen species. The catalyst was pretreated at 750°C in air for 1 hour to remove surface carbonate and hydroxyl species and any organic contaminants. Following cooling to room temperature, samples were exposed to 20 mL(STP)/min of helium to purge gas-phase oxygen and any weakly adsorbed oxygen species. Desorption of adsorbed oxygen species was performed at a ramp rate of 5°C/min in flowing helium at atmospheric pressure, and was measured using a thermal conductivity detector (TCD).

Thermal gravimetric analysis (TGA) was performed using a Perkin Elmer TGA7 to determine whether methane was adsorbed on the catalyst surface. The sample was pretreated at 750°C in air for 1 hour to remove any surface contaminants, and subsequently cooled to room temperature. Adsorption and desorption of CH_x species were quantified by measuring the weight change of the sample upon heating in a stream of 5% CH_4 in helium at 5°C/min. Differences in sample buoyancy in different atmospheres were accounted for at each temperature.

Temperature-programmed reduction (TPR) with methane was performed to determine the intrinsic activity of these perovskites towards activating methane by C-H bond cleavage, and the subsequent conversion of adsorbed methane species to surface carbonate species. The desorption temperature of the hydroxyl and carbonate species generated could be related to their adsorption strength on the catalyst surface. 750 mg of catalyst powder were first pretreated at 750°C in air for 1 hour using a ½"-O.D. quartz tube to remove any surface contaminants. Following cooling to room temperature, 20 mL(STP)/min of 0.5% CH_4 in helium was passed through the catalyst bed at atmospheric pressure. After purging for ~ 2 hours, the catalyst was

heated at 2°C/min to 550°C. Reaction products were analyzed using a Hewlett Packard 6890 gas chromatograph at temperature intervals of 14°C.

Verification of reaction mechanism and determination of kinetic parameters for methane oxidation over the perovskite catalysts were performed by measuring the reaction rate as a function of methane and oxygen concentrations, while operating under steady-state, differential and reaction-limited conditions. Typically, 30-200 mg of catalyst powder were loaded into a ¼"-O.D. quartz tube. 100 mL(STP)/min of feed gas was passed through the catalyst bed with < 3 psi pressure drop. The catalysts were first pretreated at 750°C in air for 1 hour, and subsequently cooled to 350°C. The methane conversion was recorded as a function of varying inlet methane and oxygen concentrations. Since methane conversions were kept < 5%, methane and oxygen concentrations were assumed to remain essentially unchanged throughout the catalyst bed. The methane and oxygen concentrations were varied from 0.5 to 5.0% and from 2.5 to 21%, respectively, to achieve a broad range of methane-to-oxygen stoichiometric ratios (ϕ) of 0.05-2.80, making the resulting model applicable under most operating conditions. The kinetic parameters were determined by non-linear regression of the experimental data using JMP software (SAS Institute Inc., 1995).

2.3 Results and Discussion

2.3.1 Effect of Synthesis Methods

Three methods were investigated for producing $La_{0.5}Sr_{0.5}MnO_3$ perovskites, namely, solid-state synthesis, complexation/combustion synthesis, and reverse-strike co-precipitation. For solid-state synthesis, calcination to 1400°C was required to achieve phase purity, resulting in low surface areas of < 1 m^2/g and large particle sizes of > 1 μm. Under optimal conditions, combustion synthesis and co-precipitation produced phase-pure powders at lower calcination temperatures of > 650°C, due to the intimate mixing of the constituent metal cations. Table 2.1 shows the grain size and surface area of these powders after calcination. Both combustion synthesis and co-precipitation resulted in ultrafine grain sizes of ~ 17 nm after 800°C. Compared to single-component oxides, these multicomponent perovskites retained nanocrystalline grain sizes to high temperatures, due to slow grain growth and superior thermal stability. Although combustion and co-precipitation resulted in similar grain sizes, co-precipitated $La_{0.5}Sr_{0.5}MnO_3$

has almost twice the surface area, indicating significant differences in the degree of particle agglomeration. Glycine-nitrate combustion process occurred at very high temperatures (> 1400°C), leading to partial sintering of the particles and loss in surface area.

Table 2.1. Effect of synthesis method on XRD grain size and BET surface area of $La_{0.5}Sr_{0.5}MnO_3$ perovskites, after calcination at 800°C for 2 hours. Solid-state synthesis required calcination at 1400°C for 6 hours to achieve phase purity.

Method	Grain Size (nm)	Surface Area (m^2/g)
Solid-State Synthesis (1400°C)	>100	< 1
Combustion Synthesis	16.7	13.8
Co-precipitation	17.2	24.1

TEM micrographs of $La_{0.5}Sr_{0.5}MnO_3$ powders prepared via different synthesis routes are shown in Figure 2.1. Solid-state synthesis resulted in micron-sized particles, due to rapid sintering at high temperatures. Co-precipitated powders consisted of lightly agglomerated clusters of 25-nm primary particles, whereas combustion synthesis gave rise to 40-nm particles that appeared to be more heavily agglomerated, as indicated by the larger contact areas between primary particles.
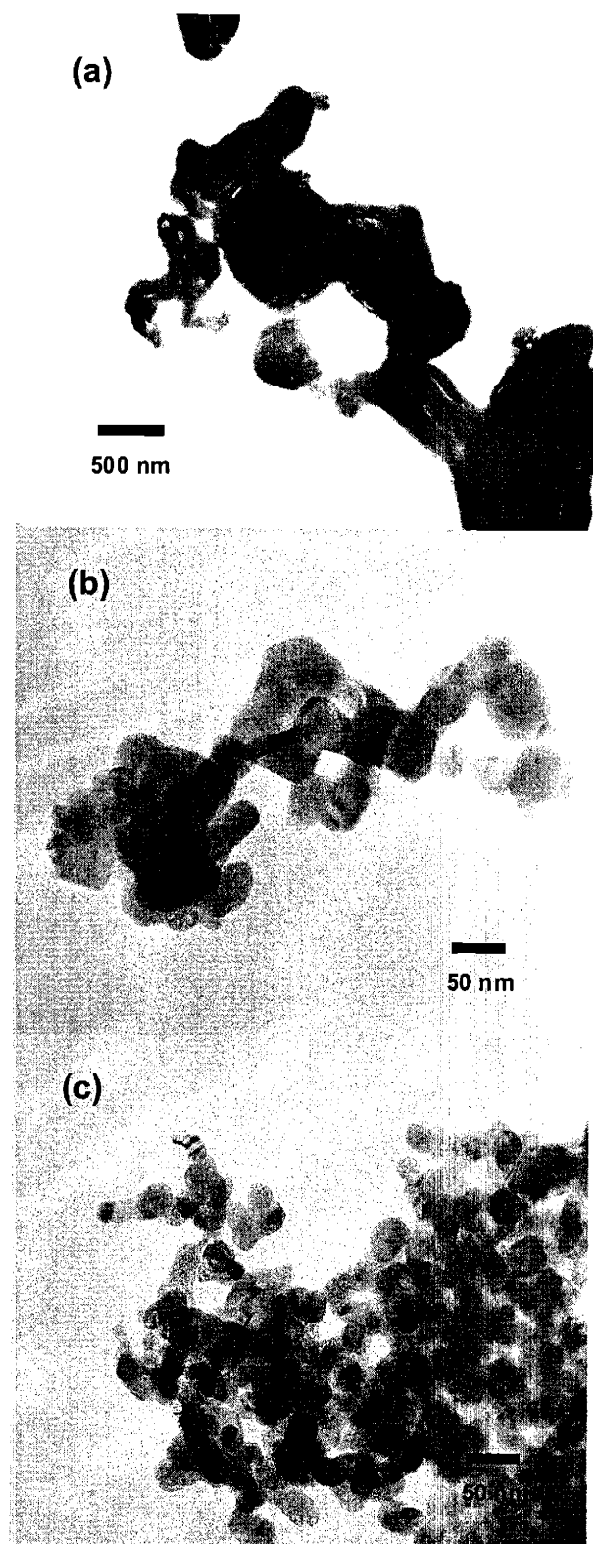
Figure 2.1. TEM micrographs of La$_{0.5}$Sr$_{0.5}$MnO$_3$ powders prepared by (a) solid-state synthesis, (b) complexation/combustion synthesis and (c) chemical co-precipitation, after calcination at 800°C. Powder (a) was calcined to 1400°C to achieve phase purity.

The effect of powder morphology on catalytic performance of $La_{0.5}Sr_{0.5}MnO_3$ is shown in Figure 2.2. Co-precipitated perovskite demonstrated the highest activity for methane oxidation, due to its higher surface area. At 410°C, the reaction rate over the co-precipitated powder is 1.6 times higher than that over the powder derived by combustion synthesis, which is in agreement with the difference in their BET surface areas. This indicates that the intrinsic catalytic activity is independent of synthesis method and powder morphology, as would be expected under reaction-limited conditions. Powder derived by solid-state synthesis showed poor catalytic activity, with light-off temperatures (corresponding to 10% methane conversion) above 550°C, due to its low surface area.
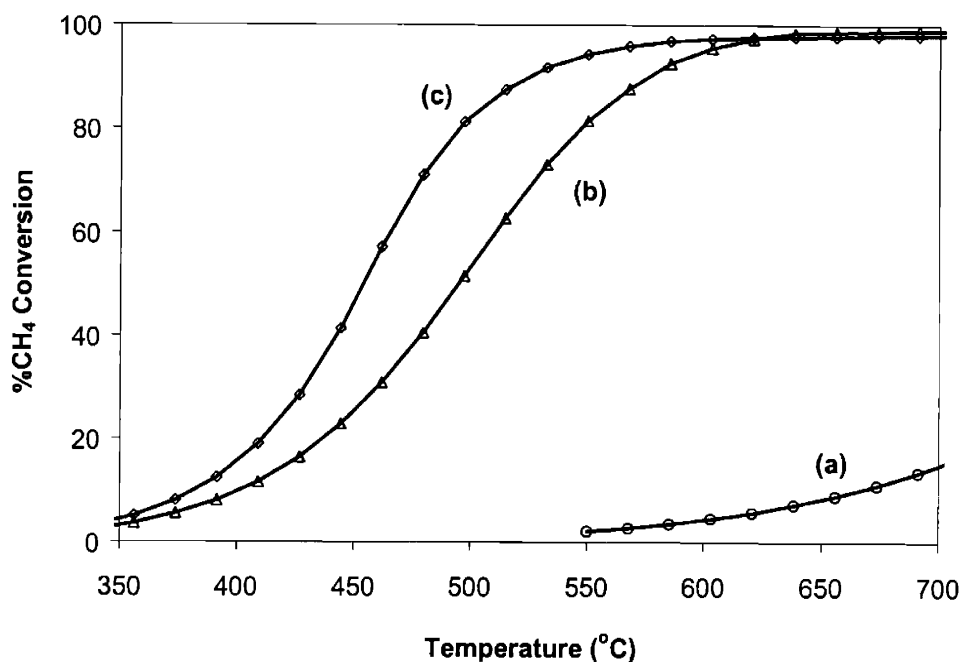
Figure 2.2. Dependence of methane conversion on temperature for $La_{0.5}Sr_{0.5}MnO_3$ derived from (a) solid-state synthesis, (b) complexation/combustion synthesis, and (c) co-precipitation. Catalytic testing was performed over 25 mg of catalyst with a feed of 1% CH_4 in air at 60,000 hour^{-1}.

2.3.2 Optimization of Precipitation Conditions

Chemical stoichiometry, phase purity and powder morphology of precipitated perovskites were found to strongly depend on the synthesis conditions. The choice of precipitation solvent, base and solution pH affects the solubility of metal cations, and therefore, influences the oxide stoichiometry of the precipitate. The grain size and surface area of the resulting powders depend

on the relative rates of nucleation and growth during precipitation, and on the extent of agglomeration from particle recovery, drying and calcination processes.

Table 2.2 shows the effect of solvent on the resulting chemical stoichiometry of $La_{0.5}Sr_{0.5}MnO_3$. Precipitation was carried out at metal and base concentrations of 0.1 M, hydroxide excess of 1.5, solvent concentration of 80 vol%, with tetraethylammonium hydroxide as the base. When water was used as the precipitation solvent, the resulting perovskite was strontium-deficient, due to the relatively high solubility of strontium hydroxide in an aqueous solvent. As the basicity of a metal cation increases, the solubility of its hydroxide increases at a given pH. Among Group IIA elements, solubility increases in the order: Ca < Sr < Ba. The solubility of Group IIA hydroxides can be decreased by increasing pH, however, hydroxides of more acidic metals (such as, Sn, Ga, Mn, In, etc.) become increasingly soluble at high pH. Therefore, the optimal pH for precipitation can vary significantly for different metals in an aqueous solvent, resulting in poor compositional control.

Figures 2.3 (a) and (c) show XRD patterns for 800°C-calcined $La_{0.5}Sr_{0.5}BO_3$ perovskites synthesized using water as the solvent. Due to its strontium deficiency, Co-based perovskite showed phase segregation of excess cobalt as Co_3O_4, and a residual $La_{1-x}Sr_xCoO_3$ phase (Figure 2.3(a)). In contrast, the XRD pattern for Mn-based perovskite does not indicate segregation of excess manganese, indicating that the perovskite phase is retained even with significant A-site deficiency (Figure 2.3(c)).

Perovskites with the desired stiochiometry of the constituent metals were synthesized by substituting alcohols for water as the solvent. The solubility of the various metal hydroxides decreases dramatically on increasing solvent hydrophobicity, resulting in complete precipitation. The dielectric constant, ε, or the ability of the solvent to ionize and thus solvate a compound, is much lower for alcohols (e.g., ε = 24.3 for ethanol) than for water (ε = 78.5). Stoichiometric $La_{0.5}Sr_{0.5}MnO_3$ was prepared using ethanol or isopropanol as solvents, thereby allowing compositional control during multicomponent metal oxide synthesis (see Table 2.2). As seen from Figures 2.3 (b) and (d), $La_{0.5}Sr_{0.5}BO_3$ perovskites synthesized using isopropanol were phase-pure, with no secondary phases. With similar solubilities and precipitation rates, the metal hydroxides formed a stoichiometric and homogeneous precipitate, which crystallized to form a phase-pure perovskite structure at a low calcination temperatures of ~ 650°C.

Table 2.2. Effect of solvent on the $La_{1-x}Sr_xMnO_3$ chemical stoichiometry, XRD grain size and BET surface area, after calcination of nominal $La_{0.5}Sr_{0.5}MnO_3$ at 800°C for 2 hours.

Precipitation Solvent	Stoichiometry with [Mn] = 1.00			Calcination @ 800°C	
	[La]	[Sr]	[La] + [Sr]	Grain Size (nm)	Surface Area (m²/g)
Water	0.47	0.11	0.58	14	49
50% Isopropanol-50% Water	0.51	0.32	0.83	13	43
Methanol	0.47	0.41	0.88	18	31
Ethanol	0.48	0.48	0.96	19	18
Isopropanol	0.49	0.49	0.98	17	24
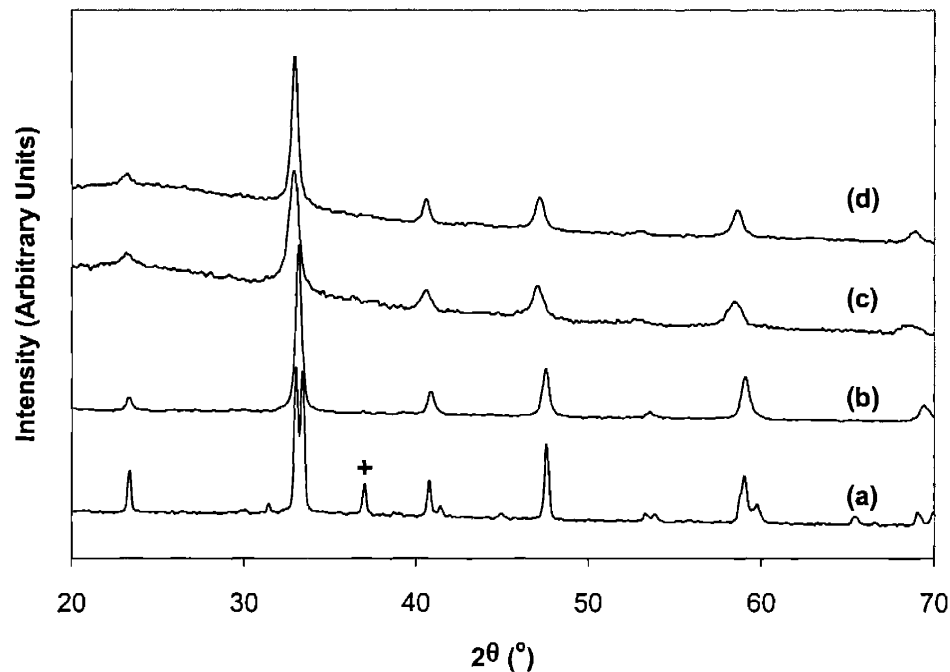
Figure 2.3. XRD patterns for 800°C-calcined $La_{0.5}Sr_{0.5}BO_3$ with (a, b) cobalt or (c, d) manganese at the B site, synthesized using (a, c) water or (b, d) isopropanol as the solvents. XRD peak for Co_3O_4 phase is denoted by "+".

As the Sr deficiency increased, the grain size of $La_{0.5}Sr_xMnO_3$ decreased from 17 to 14 nm with an accompanied increase in surface area from 24 to 49 m²/g (Table 2.2). Although the Sr-deficient perovskites exhibited very high surface areas, methane oxidation rate over $La_{0.47}Sr_{0.11}MnO_{3-\delta}$ was lower by a factor of 7.1 compared to stoichiometric $La_{0.5}Sr_{0.5}MnO_3$ at 350°C, due to the low intrinsic catalytic activity of the former.

The chemical stoichiometry of the precipitated perovskite depended not only on the choice of solvent, but also on the precipitation pH. The final pH of the suspension, after addition of nitrates to the base solution, was varied between 7 and 13 by manipulating the hydroxide excess factor between 0.5 and 1.5, respectively. For the precipitation of $La_{0.5}Sr_{0.5}MnO_3$, the salt and base concentrations were fixed at 0.1 M, tetraethylammonium hydroxide was selected as the base, and the suspension was aged for ~ 1 hour before particle recovery. Figure 2.4 shows the effect of precipitation pH and solvent on La and Sr contents in the calcined perovskite, relative to Mn content. It is interesting that even when isopropanol was used as the solvent, the resulting precipitate showed strontium deficiency on decreasing pH below 12. As expected, perovskites synthesized using 50 vol% isopropanol-50 vol% water showed lower Sr contents at all pH values, due to the higher solubility of strontium hydroxide. In contrast, La content in the precipitate remained stoichiometric on decreasing pH and on using aqueous solvents. Therefore, for the synthesis of stoichiometric perovskites containing Group IIA metal doping, it is necessary to limit the solubility of their respective hydroxides by using a high pH and an alcoholic solvent.
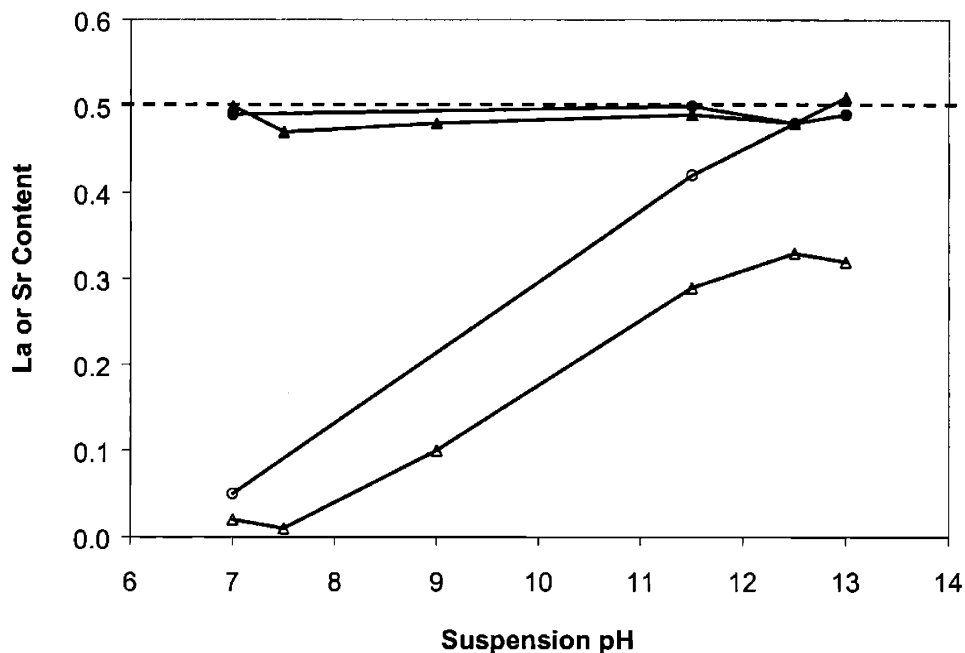
Figure 2.4. La and Sr contents (closed and open symbol, respectively) in 800°C-calcined perovskites synthesized via precipitation of nominal $La_{0.5}Sr_{0.5}MnO_3$ at the final suspension pH indicated, using (○) isopropanol or (△) 50 vol% isopropanol-50 vol% water as the solvent.

The choice of precipitation base was also found to influence chemical stoichiometry through its effect on suspension pH and/or chelation of transition metals. Ammonium hydroxide is the preferred base for precipitation synthesis, since unlike sodium or potassium hydroxides, ammonium cations can be easily removed on calcination, avoiding surface contamination. However, to achieve a high pH of ~ 12 with high NH_4OH concentrations of > 5 M, ammonium ions may chelate and solubilize transition metals resulting in non-stoichiometric perovskites.

Table 2.3 shows the effect of base type on the stoichiometry, grain size and surface area of $La_{0.5}Sr_{0.5}MnO_3$ after calcination at 800°C for 2 hours. Precipitation was performed using isopropanol as solvent, metal and base concentrations of 0.1 M, and a hydroxide excess factor of 2.0. When TEAH or TBAH was used as the bases, the final pH of the suspension was ~ 13, which was considerably higher than ~ 10 for NH_4OH. Therefore, the precipitate formed with NH_4OH was Sr-deficient, due to the relatively high solubility of strontium hydroxide at the lower pH. TEAH or TBAH allowed the use of higher pH due to the increased basicity, while preventing the chelation of transition metals to the alkylammonium ions. TEAH resulted in a smaller grain size of ~ 17 nm and a higher surface area of 24 m^2/g compared to TBAH. Thus, it was preferred over TBAH for use as the organic base for perovskite precipitation.

Table 2.3. Effect of base type on the $La_{1-x}Sr_xMnO_3$ chemical stoichiometry, XRD grain size and BET surface area, after calcination of nominal $La_{0.5}Sr_{0.5}MnO_3$ at 800°C for 2 hours.

Precipitation Base	Stoichiometry with [Mn] = 1.00		Calcination @ 800°C	
	[La]	[Sr]	Grain Size (nm)	Surface Area (m^2/g)
NH_4OH	0.49	0.17	13	50
TEAH	0.49	0.49	17	24
TBAH	0.47	0.47	19	22

Various precipitation agents, such as hydroxides, carbonates and oxalates, have been used to precipitate metal cations from solution. The choice of precipitation agent can greatly affect the stoichiometry, grain size and surface area of the calcined perovskite, due to differences in solubility, particle agglomeration and decomposition temperature of the precipitate. Table 2.4 shows the effect of hydroxide and/or carbonate precipitation agents on the powder morphology of calcined $La_{0.5}Sr_{0.5}MnO_3$. Precipitation was performed using metal and precipitation agent

concentrations of 0.1 M, total hydroxide and carbonate excess factor of 1.5, and aging time of ~ 1 hour. When precipitation was performed using carbonate ions, water was used as the solvent due to the low solubility of potassium carbonate in alcohols. Since the solubility product of strontium carbonate was very small in aqueous solvents, the resulting precipitates were not strontium-deficient. As carbonates were replaced by hydroxides, the BET surface area increased from 11 to 24 m^2/g, while the grain size remained fairly constant at 17-18 nm. This suggested that metal carbonate particles were more agglomerated compared to metal hydroxide particles.

Table 2.4. Effect of precipitation agent on the XRD grain size and BET surface area of 800°C-calcined $La_{0.5}Sr_{0.5}MnO_3$.

Precipitation Agent	Calcination @ 800°C	
	Grain Size (nm)	Surface Area (m^2/g)
Hydroxide	17	24
50% Hydroxide-50% Carbonate	18	15
Carbonate	18	11

In precipitation synthesis, particle agglomeration might be lowered by decreasing the overall metal and base concentration, thereby reducing interparticle interaction via a dilution effect. However, as the metal and base concentrations are decreased, the nucleation rate is expected to decrease due to a reduction in relative supersaturation. Table 2.5 shows the effect of metal cation and base concentrations on the grain size and surface area of $La_{0.5}Sr_{0.5}MnO_3$ after calcination at 650°C for 2 hours. Precipitation was performed using isopropanol and TEAH as solvent and base, respectively, and a hydroxide excess factor of 1.5. It was observed that reducing metal and base concentrations over two orders of magnitude did not affect grain size significantly, and actually decreased the surface area slightly from 41 to 35 m^2/g. The weak dependence of powder morphology on metal and base concentrations indicates that precipitation conditions play a minor role in determining particle agglomeration.

Table 2.5. Effect of metal cation and TEAH concentrations on the resulting XRD grain size and BET surface area of 650°C-calcined $La_{0.5}Sr_{0.5}MnO_3$.

Concentration (M)	Calcination @ 650°C	
	Grain Size (nm)	Surface Area (m^2/g)
0.01	13	35
0.1	13	43
1	12	41

2.3.3 Thermal Evolution

Figure 2.5 shows the TGA and DTA curves of $La_{0.5}Sr_{0.5}MnO_3$ precipitated under optimal conditions. The observed weight loss on heating the precipitate was primarily due to desorption of water during condensation of metal hydroxides to form a metal-oxygen-metal framework. Since the decomposition of these hydroxides required energy, an endothermic peak was observed at ~ 200°C. XRD patterns of $La_{0.5}Sr_{0.5}MnO_3$ precipitate calcined to different temperatures are shown in Figure 2.6. At a low calcination temperature of 300°C, the precipitate was largely amorphous with highly dispersed $SrCO_3$ crystals that formed on the surface of the highly basic precipitate during exposure to air. On heating the precipitate, the XRD peak intensity of $SrCO_3$ phase decreased, indicating its decomposition to form SrO and CO_2. Crystallization of the perovskite phase occurred between 575 and 650°C (see Figure 2.6), which corresponded to a sharp loss in sample weight (see Figure 2.5) associated with the decomposition of residual metal carbonate or hydroxide groups. The XRD pattern of $La_{0.5}Sr_{0.5}MnO_3$ after calcination at 650°C was characteristic of a slightly distorted cubic structure with no evidence of strontium deficiency or phase segregation of SrO. Heating the precipitate above 650°C did not result in significant weight loss, suggesting that the decomposition of hydroxyl and carbonate species was complete.
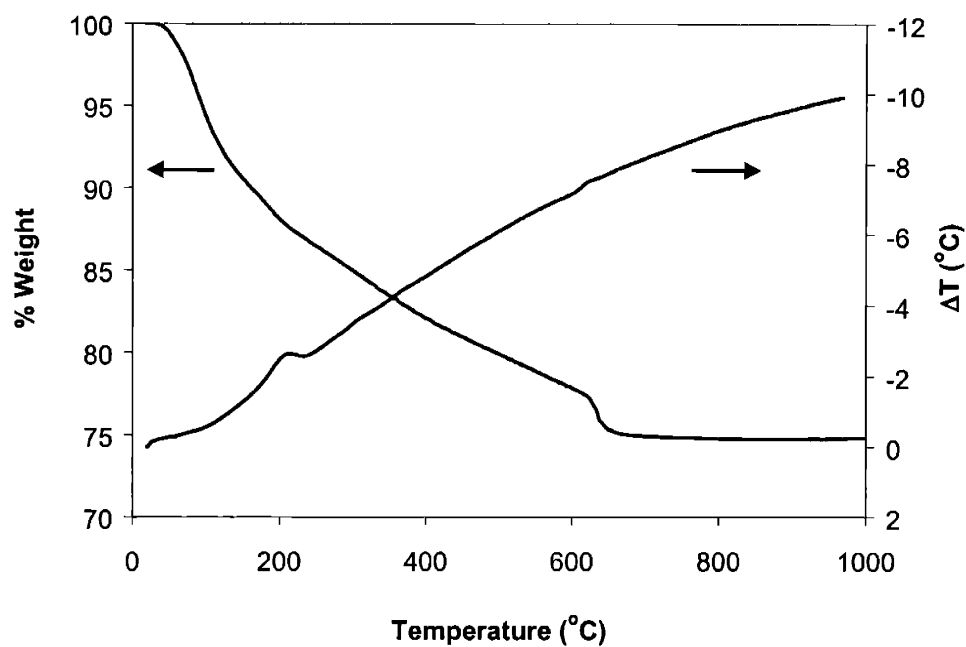
Figure 2.5. TGA and DTA profiles of $La_{0.5}Sr_{0.5}MnO_3$ precipitate in air.
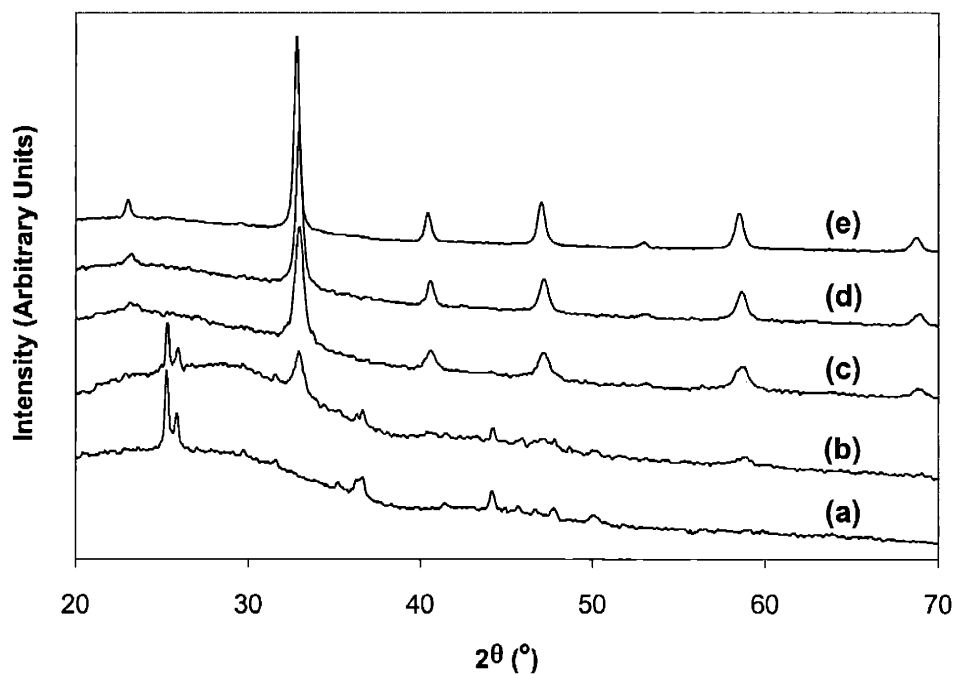
Figure 2.6. XRD patterns for $La_{0.5}Sr_{0.5}MnO_3$ precipitate after calcination at (a) 300°C, (b) 575°C, (c) 650°C, (d) 800°C and (e) 1000°C for two hours in air.

The BET surface area and XRD crystallite size of $La_{0.5}Sr_{0.5}MnO_3$ precipitate on calcination to different temperatures are presented in Figure 2.7. A sharp decrease in surface area was observed during the crystallization of the perovskite phase at ~ 650°C due to an increase in powder density. The sample was composed of perovskite crystallites of ~ 13 nm with a surface area of 43 m^2/g. On further heating to 1000°C, the grain size was found to gradually increase to ~ 25 nm, with an accompanied decrease in surface area to ~ 19 m^2/g. In contrast to single-component metal oxides, $La_{0.5}Sr_{0.5}MnO_3$ showed excellent thermal stability, retaining its nanocrystalline grain size and high surface area to high calcination temperatures. Even at 1000°C, the co-precipitated $La_{0.5}Sr_{0.5}MnO_3$ exhibited a higher surface area than the 800°C-calcined material derived by combustion synthesis (14 m^2/g).
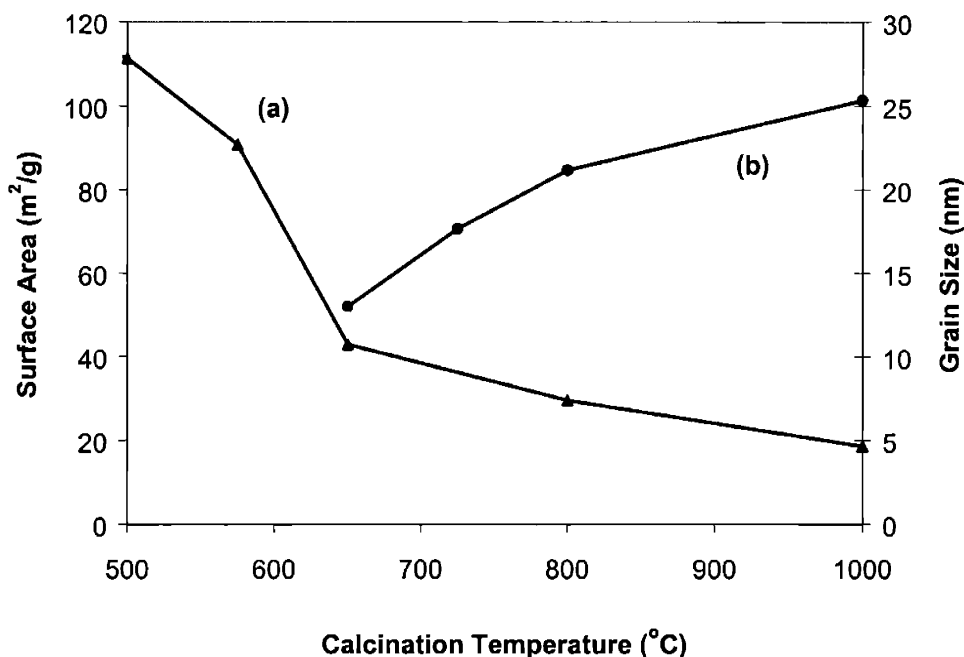
Figure 2.7. (a) BET surface area and (b) XRD grain size of calcined $La_{0.5}Sr_{0.5}MnO_3$.

2.3.4 Characterization and Catalytic Activity of LaBO₃

Figure 2.8 shows XRD patterns of $LaBO_3$ perovskites with different transition metal substitutions at the B site. These 800°C-calcined perovskites have a distorted cubic crystal structure. The size of the unit cell was found to decrease in the following order: $LaFeO_3$ > $LaMnO_3$ > $LaCoO_3$ ~ $LaNiO_3$, which was consistent with the size of their transition metal cations. Fe^{3+} has the largest ionic radius of 0.65 Å, while Co^{3+} and Ni^{3+} have smaller ionic radii

of 0.55 and 0.56 Å, respectively [12]. Depending on the oxygen non-stoichiometry in $LaMnO_{3+\delta}$ at low temperatures [13], Mn could have an average oxidation state between 3+ and 4+, with an average ionic radius between 0.68 and 0.53 Å, respectively [12]. The extent of rhombohedral distortion of the unit cell increased with decreasing transition metal cationic radius. Substitution of Cu at the B site led to the formation of La_2CuO_4 and CuO phases (not shown) due to the larger size and lower valence of Cu^{2+}. Cu-based perovskite could not be stabilized to high temperatures, even after replacement of La^{3+} by Pr^{4+}.
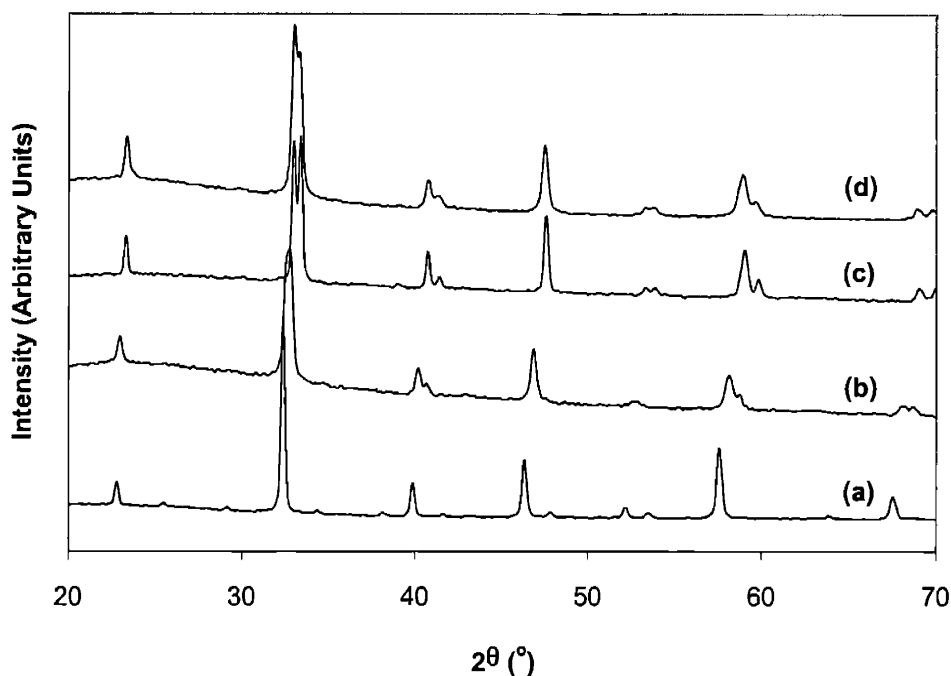
Figure 2.8. XRD patterns of (a) $LaFeO_3$, (b) $LaMnO_3$, (c) $LaCoO_3$ and (d) $LaNiO_3$, after calcination at 800°C in air.

Table 2.6 shows the XRD grain sizes and BET surface areas for $LaBO_3$ perovskites after calcination at 650°C and 800°C for 2 hours. The surface area was strongly dependent on B-site transition metal, and decreased in the order: Mn > Fe > Ni ~ Co. $LaMnO_3$ exhibited the highest surface area of 48 m^2/g at 650°C, and showed superior thermal stability also at 800°C. On crystallization at 650°C, the grain size was found to increase in the order: Ni < Mn < Fe ~ Co.

Table 2.6. XRD grain sizes and BET surface areas of $LaBO_3$ perovskites after calcination at 650°C and 800°C.

B-Site	Calcination @ 650°C		Calcination @ 800°C	
	Grain Size (nm)	Surface Area (m²/g)	Grain Size (nm)	Surface Area (m²/g)
Ni	14	12	34	5
Co	31	10	62	4
Fe	30	20	52	8
Mn	27	48	36	23

Since the observed trends in grain size and surface area did not correlate, significant differences in the degree of particle agglomeration must exist. The degree of particle agglomeration in the $LaBO_3$ perovskites, shown in Figure 2.9, was estimated by comparing their BET surface area to a theoretical value calculated by assuming discrete, spherical grains with no interparticle necking. The degree of particle agglomeration was found to be strongly dependent on the B-site transition metal, and increased in order: Mn < Fe < Co < Ni. The degree of particle agglomeration increased with increasing calcination temperature, due to the sintering of weakly agglomerated particles to form larger particles.
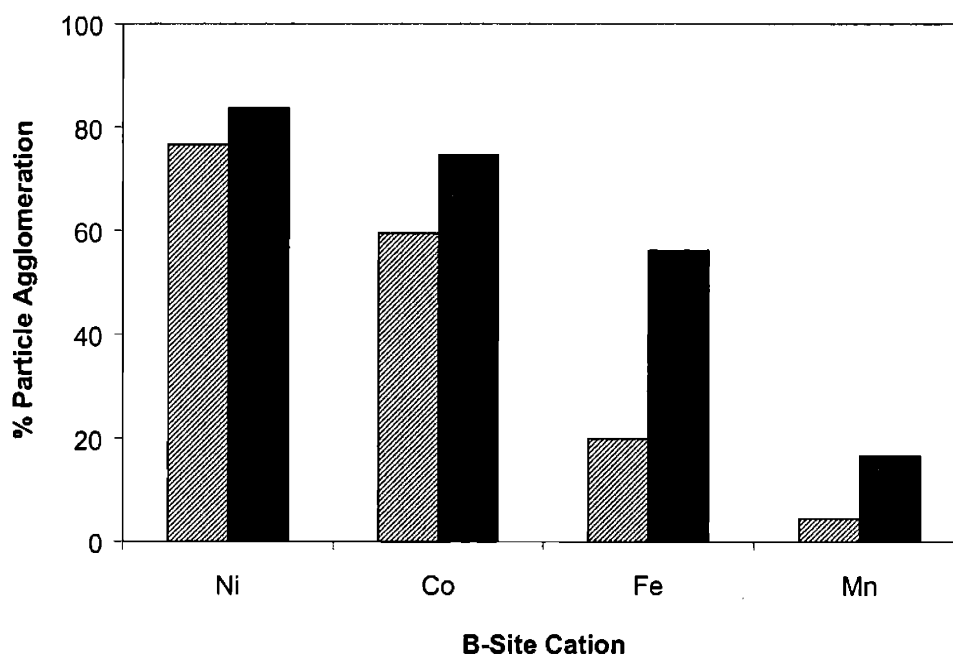
Figure 2.9. Estimated degree of particle agglomeration in $LaBO_3$ perovskites after calcination at 650°C (▨) and 800°C (■) for 2 hours in air.

Figure 2.10 shows TEM micrographs of $LaBO_3$ perovskites after calcination at 650°C for 2 hours. It confirmed that the degree particle agglomeration increased in the order: Mn < Fe < Co < Ni. Although the primary particle sizes were < 50 nm, the grains agglomerated to form larger particles. In $LaMnO_3$, these grains were lightly agglomerated, resulting in high surface area and superior thermal stability. In the case of $LaNiO_3$, the grains were closely packed to form strong agglomerates, which underwent rapid grain growth and sintering at higher temperatures.
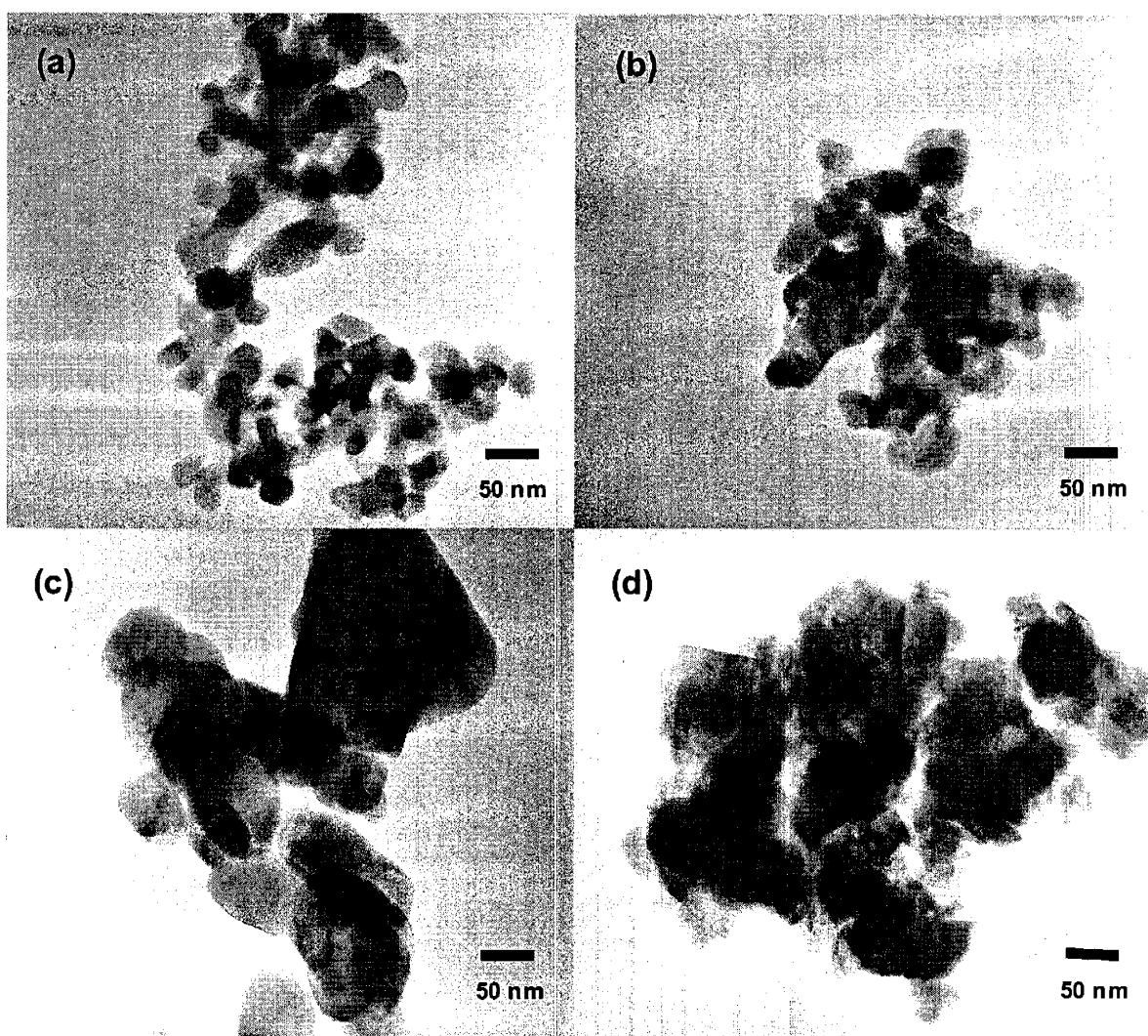
Figure 2.10. TEM micrographs of (a) $LaMnO_3$, (b) $LaFeO_3$, (c) $LaCoO_3$ and (d) $LaNiO_3$, after calcination at 650°C in air.

The observed differences in the degree of particle agglomeration in calcined $LaBO_3$ perovskites could potentially arise from differences in their surface charge during precipitation. Electrostatic repulsion between charged particles was primarily responsible for stabilizing a particle suspension in a non-aqueous solvent (such as, isopropanol) in the absence of surfactants. As-precipitated particles were partially condensed hydrogels, which could have charged surfaces from ionization of surface hydroxides (depending on their pK_a and solution pH), or from adsorption of charged species onto their hydrophilic surfaces.

Figure 2.11 shows the dependence of zeta potential on solution pH for as-precipitated $LaBO_3$. This measurement was performed with water as solvent and 0.01 M KCl as supporting electrolyte. The isoelectric point for these uncalcined samples was strongly dependent on B-site transition metal, and increased in the order: Mn < Fe < Co < Ni, suggesting an increase in the basicity of the corresponding hydrogel. The magnitude of the zeta potential at high pH decreased in the order: Mn > Fe > Co > Ni, indicating a decrease in surface charge. The trend in surface charge was consistent with the observed degree of particle agglomeration. Weak electrostatic repulsion between $LaNi(OH)_x$ particles did not prevent the formation of larger agglomerates, while the more negatively charged $LaMn(OH)_x$ particles remained fairly unagglomerated.

The surface charge of $LaBO_3$ particles was investigated during precipitation and subsequent processing steps, in order to identify synthesis condition(s) that led to significant particle agglomeration. As seen in Table 2.7, as-precipitated particles dispersed in their mother liquor were negatively charged, and have similar zeta potentials. Since isopropanol was used as the solvent, the hydrophilic surfaces of these precipitated particles preferentially adsorbed positively charged cations (such as, tetraethylammonium cations), thereby concealing their intrinsic surface charge. On washing with isopropanol to remove these adsorbed cations, the intrinsic surface charge of the particles was revealed, resulting in differences in particle agglomeration. The surface charge of once washed $LaBO_3$ particles decreased in the order: Mn > Fe > Co > Ni, which was consistent with the increasing degree of particle agglomeration. Further washing of the precipitated powders decreased their zeta potential due to decreasing pH. In fact, Co- and Ni-based perovskites passed through their isoelectric points during the second and third washing steps, resulting in highly agglomerated particles. TEM micrographs of uncalcined $LaBO_3$ precipitates after isopropanol washes are shown in Figure 2.12. The

agglomerate size of LaBO$_3$ precipitates increased in the order: Mn < Fe < Co < Ni, consistent with their decreasing surface charge.

It can be concluded that differences in particle agglomeration arose from differences in their surface charge during the washing steps. Since the samples have similar zeta potentials during precipitation, changing the precipitation conditions will not significantly affect the resulting grain size and surface area. In contrast, modification of the washing steps is expected to have significant effect on the resulting powder morphology.
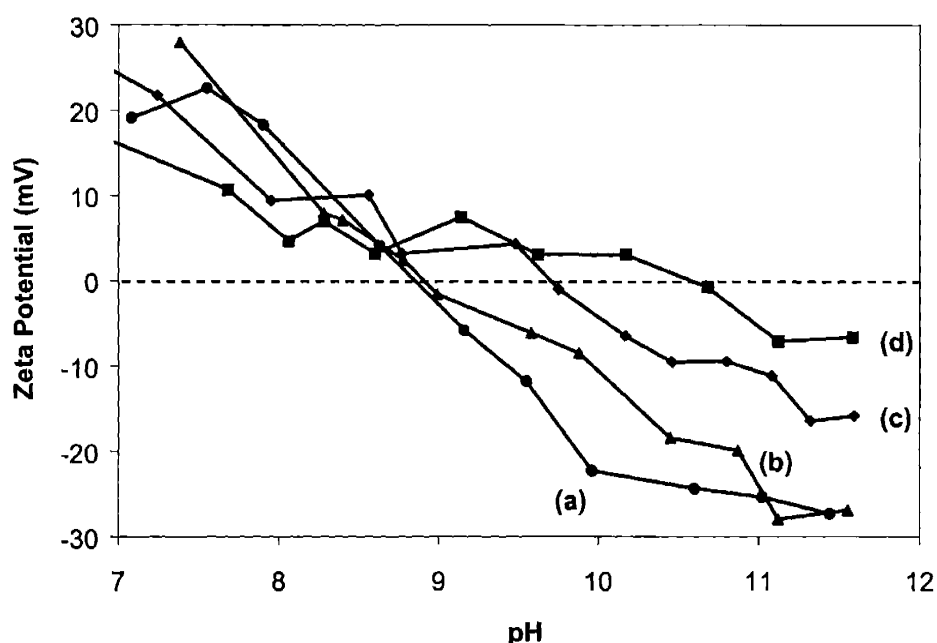
Figure 2.11. Zeta potential profiles for as-precipitated (a) LaMnO$_3$, (b) LaFeO$_3$, (c) LaCoO$_3$ and (d) LaNiO$_3$.

Table 2.7. Zeta potential measurement of LaBO$_3$ particles after precipitation and isopropanol washes.

B-Site Cation	Zeta Potential (mV)			
	As-precipitated	1st wash	2nd wash	3rd wash
Ni	-20	-12	13	12
Co	-27	-17	2	3
Fe	-22	-26	-20	-10
Mn	-18	-39	-35	-30
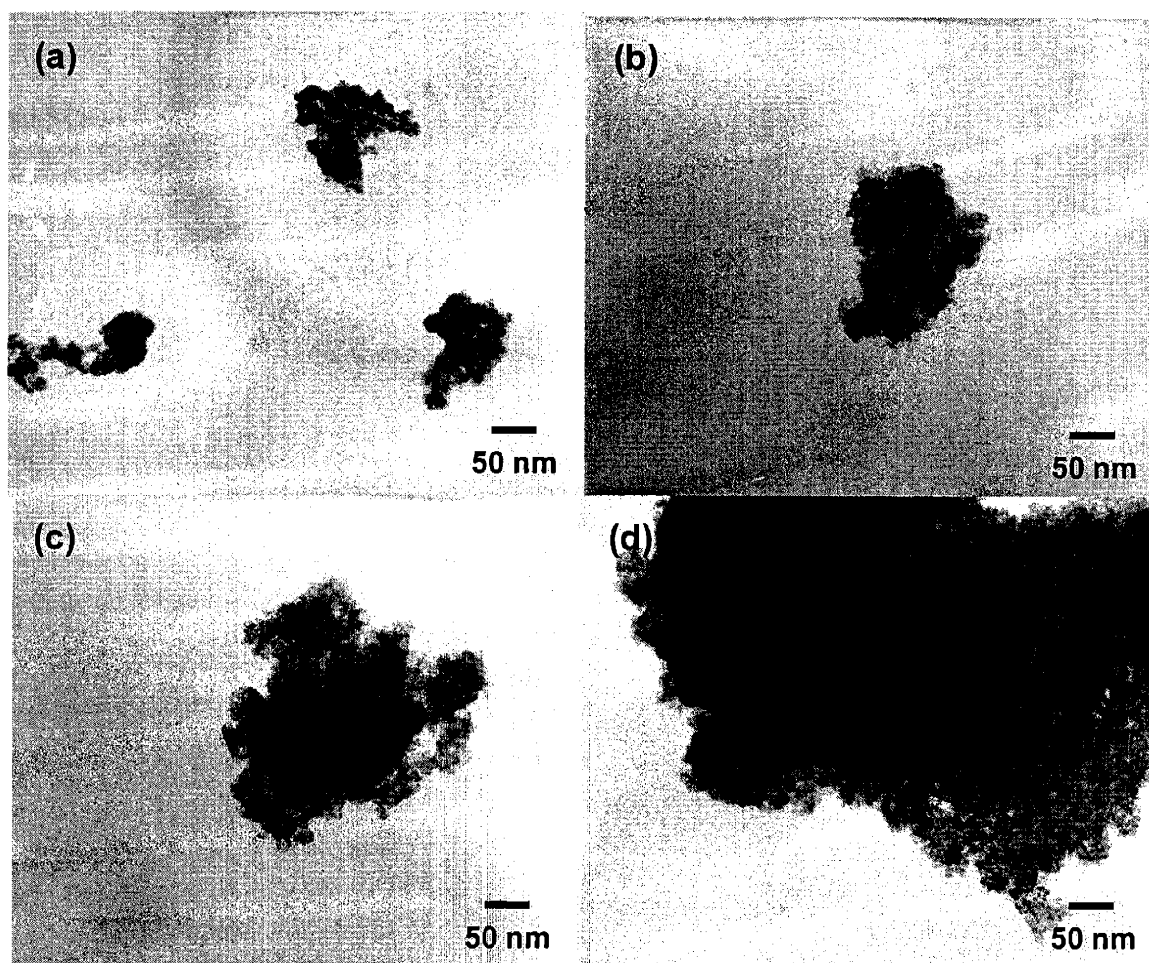
Figure 2.12. TEM micrographs of uncalcined precipitates of (a) $LaMnO_3$, (b) $LaFeO_3$, (c) $LaCoO_3$ and (d) $LaNiO_3$, after isopropanol washes.

Significant differences in the acid/base properties of the precipitated $LaBO_3$ hydrogels strongly affected their surface charge and particle agglomeration. In addition, as the basicity of the metal hydroxide increased, the rate of hydroxide condensation (at a fixed solution pH) to form metal-oxygen-metal bridges was expected to decrease. Hence, owing to its faster rate of hydroxide condensation, hydrogel of $LaMnO_3$ should be less hydroxylated compared to the hydrogel of $LaNiO_3$. TGA profiles for the decomposition of washed, uncalcined $LaBO_3$ on heating in air are shown in Figure 2.13. According to the observed weight loss, hydroxide content of $LaBO_3$ hydrogels depended greatly on B-site transition metal, and increased in the order: Mn < Fe < Co < Ni, which was consistent with increasing basicity.
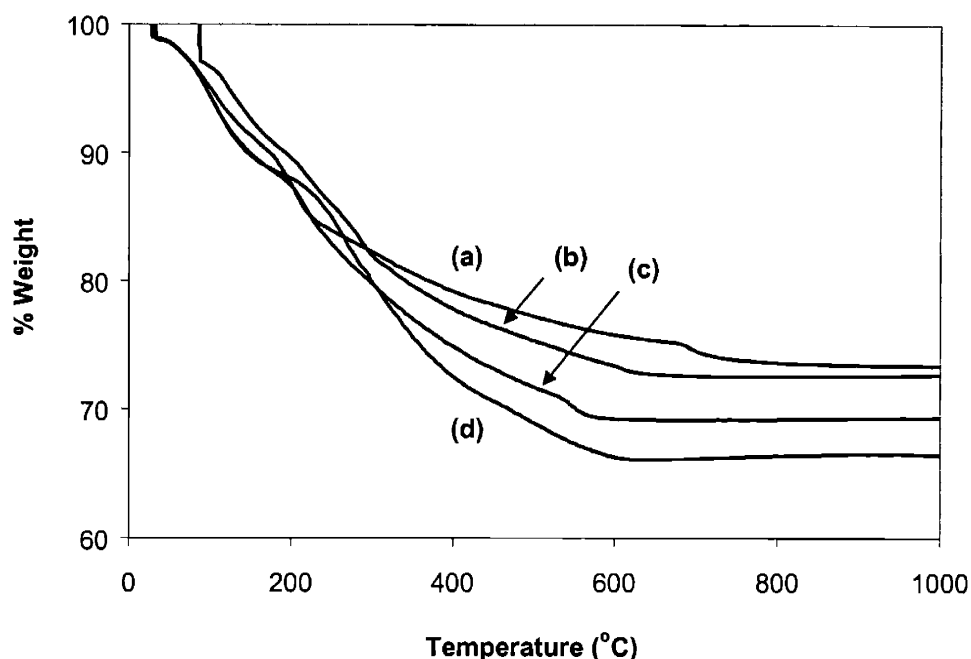
Figure 2.13. TGA profiles for uncalcined (a) $LaMnO_3$, (b) $LaFeO_3$, (c) $LaCoO_3$ and (d) $LaNiO_3$ in air.

The transition metal at the B site greatly affected the perovskite's catalytic activity for methane oxidation [14]. Figure 2.14 shows the methane conversion over various $LaBO_3$ perovskites, after calcination at 650 and 800°C. $LaMnO_3$ was found to be the most active, having a light-off temperature (corresponding to 10% CH_4 conversion) of ~ 420°C, and achieving full conversion by 650°C at 60,000 hour^{-1}. Catalyst activity was found to decrease in the order: $LaMnO_3 > LaFeO_3 \sim LaNiO_3 > LaCoO_3$.

Although the surface area of these perovskites decreased with increasing calcination temperature, the catalytic activity was higher for the 800°C-calcined samples than for the 650°C-calcined samples (Figure 2.14). While these perovskites were fully crystalline and phase-pure after calcination at 650°C, residual hydroxyl and carbonate groups on the catalyst surface might poison some active sites, thereby lowering catalyst activity. Figure 2.15 shows the photoacoustic Fourier-transform infrared (PA-FTIR) spectra for $LaFeO_3$ after calcination at different temperatures. The presence of adsorbed hydroxyl and carbonate species was indicated by a broad M-OH stretch at 3700-2500 cm^{-1}, and a COO$^-$ stretch at 1750-1250 cm^{-1}, respectively. As the calcination temperature was increased to 800°C, the intensities of the hydroxyl and carbonate

peaks decreased, indicating a lower surface coverage of these species. The significant removal of these species by 800°C was also verified by TGA in Figure 2.13.
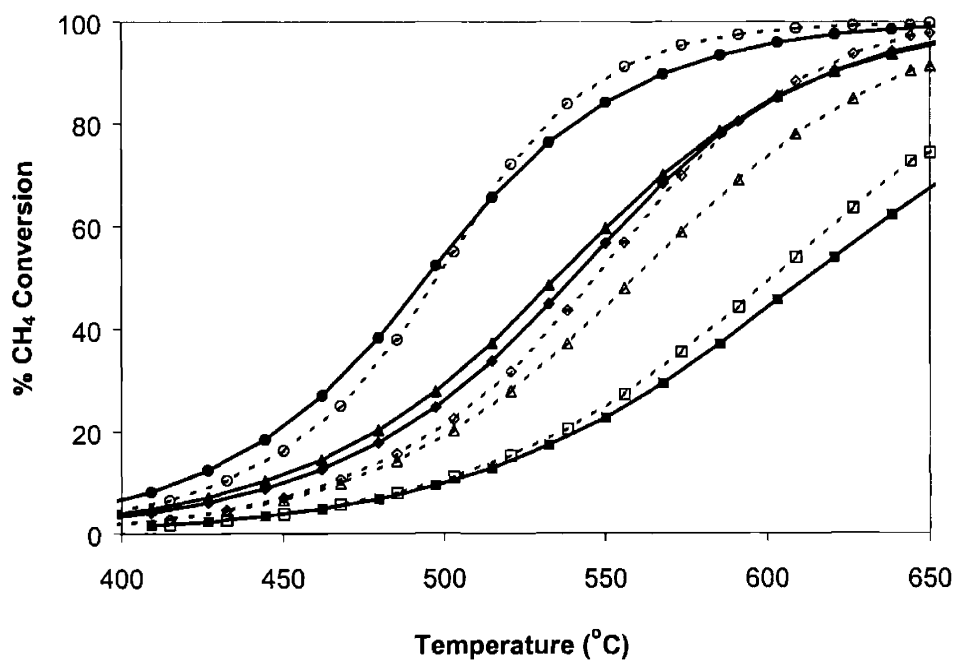
Figure 2.14. Methane conversion as a function of temperature over (•) $LaMnO_3$, (▲) $LaNiO_3$, (♦) $LaFeO_3$ and (■) $LaCoO_3$, calcined to 650°C (open symbols) or 800°C (closed symbols). Catalytic testing was performed with 25 mg of catalyst, and a feed of 1% CH_4 in air at 60,000 hour^{-1}.
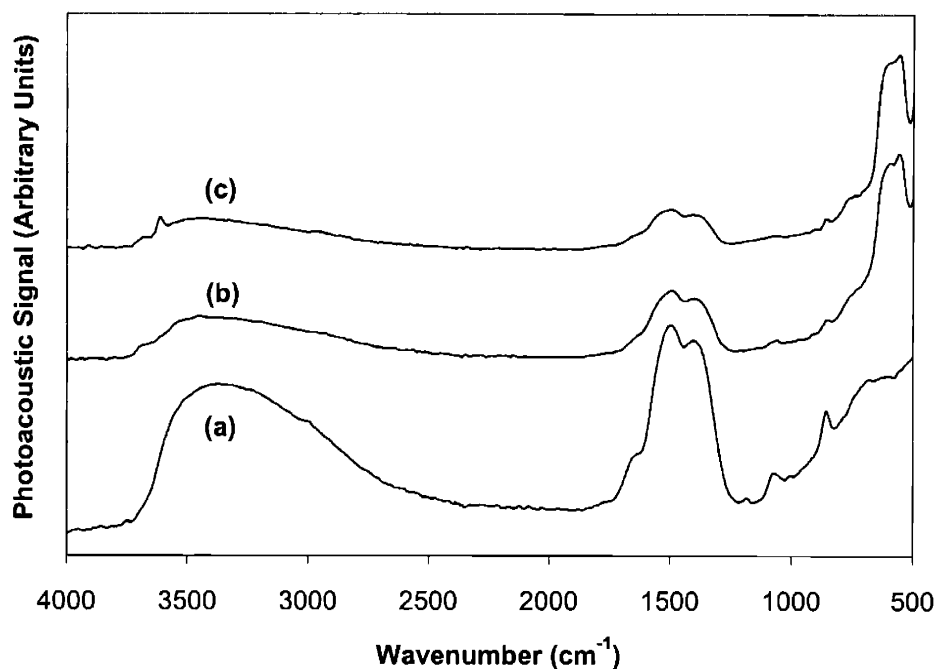
Figure 2.15. PA-FTIR spectra of (a) uncalcined, (b) 650°C-calcined, and (c) 800°C-calcined LaFeO₃.

The observed difference in light-off temperatures for LaBO₃ perovskites could be due to their differences in intrinsic catalytic activity and/or surface areas. Figure 2.16 reports the specific catalytic rate over these perovskites, measured under differential and reaction-limited conditions, after normalizing for BET surface area. LaNiO₃ was found to have the highest specific activity for methane oxidation, followed by LaCoO₃, LaFeO₃ and LaMnO₃. Interestingly, the observed trend in specific activity correlated with their respective positions in the periodic table and their reducibility [15]. Increased catalyst reducibility could result in easier oxygen vacancy creation on the catalyst surface, thereby providing sites for oxygen activation, and easier decomposition of hydroxide/carbonate species to regenerate an active site.

Figure 2.17 shows the apparent activation energies for methane oxidation for these LaBO₃ after calcination at 650°C and 800°C. It was found that increasing the calcination temperature to 800°C resulted in lower activation energies, indicating a change in the surface chemistry of these perovskites. This was consistent with the observed increase in catalytic activity, and change in the surface coverage of hydroxide and carbonate species. At 800°C, the activation energy was found to be invariant of B-site composition.
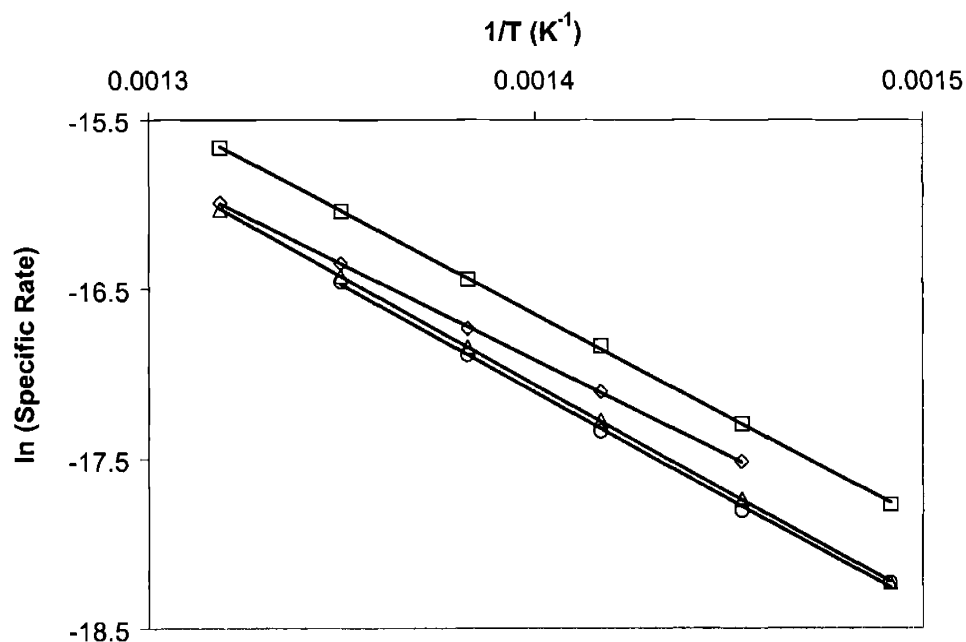
Figure 2.16. The specific catalytic rate (mol/s/m^2) for methane oxidation over (□) LaNiO$_3$ (◇) LaCoO$_3$, (△) LaFeO$_3$ and (○) LaMnO$_3$, after calcination at 650°C. Specific reaction rates were obtained under differential conversions with 25 mg of catalyst, and a feed of 1% CH$_4$ in air at 60,000 hour^{-1}.
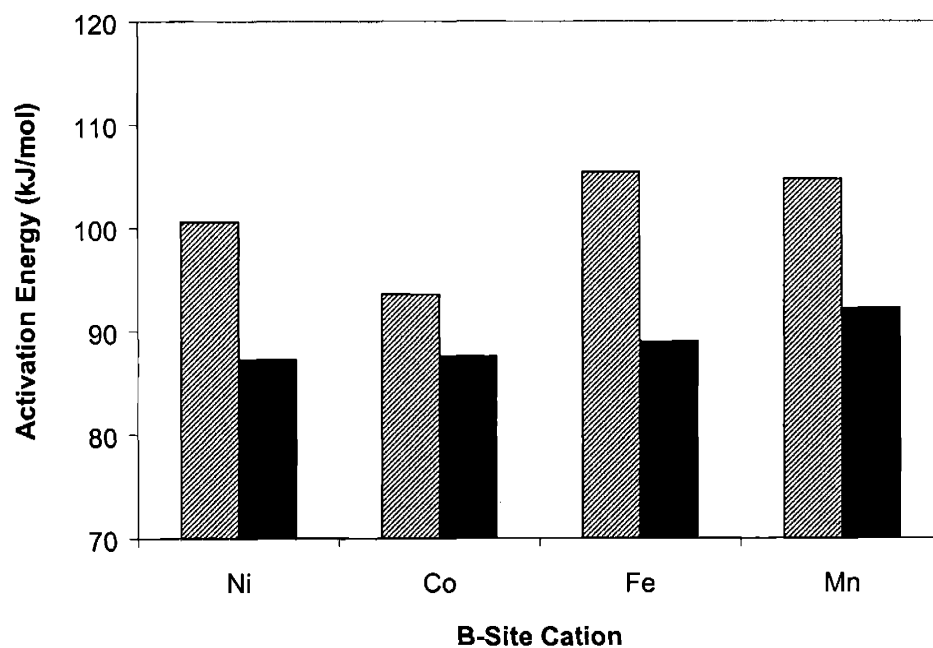
Figure 2.17. Effect of B-site transition metal on the apparent activation energy for methane oxidation over LaBO$_3$ perovskites calcined to (▨) 650°C and (■) 800°C, measured under differential methane conversions at 400-500°C.

2.3.5 Characterization and Catalytic Activity of $La_{0.8}A_{0.2}MnO_3$

Since $LaMnO_3$ showed the highest activity for methane oxidation (Figure 2.14), several dopants were introduced at the A site to investigate their effect on crystal structure, microstructure and catalyst activity for the $La_{0.8}A_{0.2}MnO_3$ perovskite series. Dopants were selected to study the effect of their oxidation state and ionic radius on the catalyst performance.

La^{3+} was substituted by Group IIA cations of lower valence state, such as Ca^{2+}, Sr^{2+} and Ba^{2+}. Doping with these cations resulted in the formation of oxygen vacancies, and/or an increase in Mn oxidation state. In addition, since these dopants are more basic than La^{3+}, their doping may affect the rate of hydrogen abstraction from methane or adsorbed methoxy species, and the stability of adsorbed carbonate/hydroxide species. Since the ionic radius increases in the order $Ca^{2+} \sim La^{3+} < Sr^{2+} < Ba^{2+}$, the size of the unit cell is expected to increase with Sr and Ba doping, leading to potential phase transitions at high concentrations. Rare-earth metals of the same valence state but smaller ionic radius, such as Sm^{3+}, Eu^{3+} and Gd^{3+}, were also substituted for La^{3+}. Although their substitution did not create oxygen vacancies, the perovskite reducibility increased with decreasing ionic radius of the A cation [16]. Replacement of La^{3+} by higher valency dopants, such as Ce^{4+} and Pr^{4+}, was also studied. Their addition could result in oxygen excess and/or a decrease in Mn oxidation state.

Figure 2.18 shows the effect of various A dopants on the XRD patterns of $La_{0.8}A_{0.2}MnO_3$ perovskites, after calcination at 800°C in air. With the exception of Ce^{4+}, these dopants were incorporated into the perovskite structure, resulting in crystalline, phase-pure materials. Ce^{4+} did not replace La^{3+} at the A site, but formed a discrete CeO_2 phase instead. As the Group IIA dopant size increased, increased shifting to lower diffraction angles were noted in the XRD peaks, indicating an expansion of the perovskite lattice.
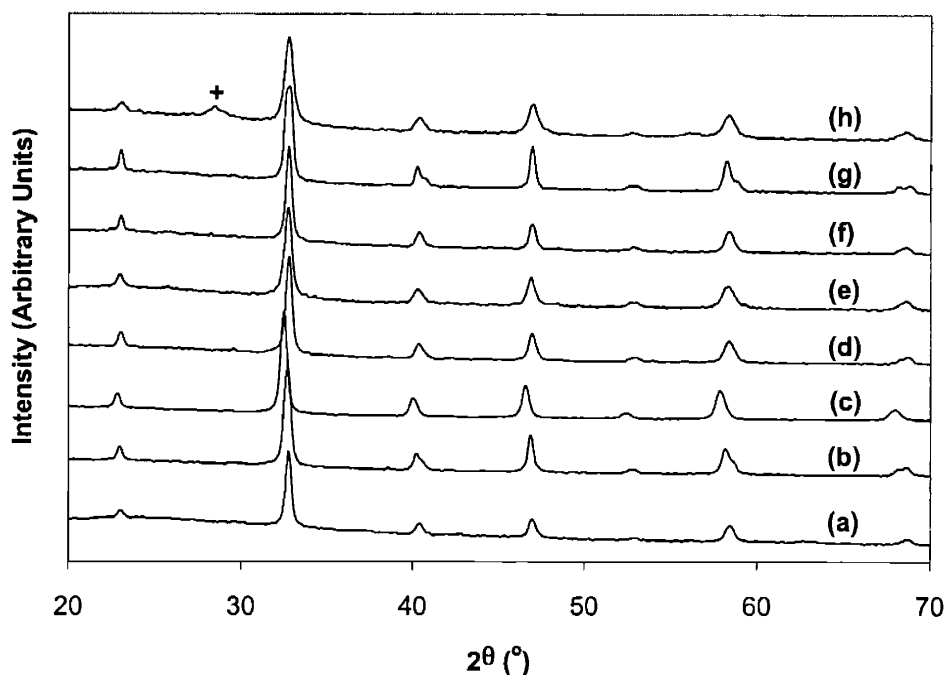
Figure 2.18. XRD patterns of $La_{0.8}A_{0.2}MnO_3$ with various A-site dopants: (a) Ca^{2+}, (b) Sr^{2+}, (c) Ba^{2+}, (d) Eu^{3+}, (e) Gd^{3+}, (f) Sm^{3+}, (g) Pr^{4+} and (h) Ce^{4+}, after calcination at 800°C in air. "+" denotes the presence of a secondary CeO_2 phase.

Table 2.8 reports the XRD grain sizes and BET surface areas for $La_{0.8}A_{0.2}MnO_3$ after calcination at 800°C in air. Substitution of La^{3+} by Group IIA metals did not significantly change the catalyst surface area, although the grain size was significantly reduced for Ca^{2+}- and Ba^{2+}-doped perovskites. As the size of the rare-earth metal dopant was decreased, the grain size was found to dramatically decrease with an accompanied increase in surface area. The formation of a segregated CeO_2 phase suppressed grain growth and sintering of the perovskite phase, resulting in an ultrafine perovskite grain size of 22 nm and a high surface area of 42 m^2/g. Hence, the perovskite thermal stability could be significantly improved through the formation of ceria-perovskite nanocomposite.

Figure 2.19 shows the effect of Group IIA dopants on the catalytic activity of $La_{0.8}A_{0.2}MnO_3$ perovskites. Ca-doped perovskite exhibited the highest activity, with a light-off temperature of ~ 395°C, which was lower than ~ 420°C for $LaMnO_3$. Since these catalysts have similar surface areas, differences in specific catalytic activity suggested differences in their surface chemistry. Doping Group IIA cations at the A site could generate oxygen vacancies on the catalyst surface, thereby providing sites for oxygen chemisorption; the increased basicity

58

associated with Group IIA cations could also affect methane activation and carbonate decomposition.

Table 2.8. XRD grain sizes and BET surface areas for $La_{0.8}A_{0.2}BO_3$ perovskites after calcination at 800°C in air.

A-Site Dopant	Calcination @ 800°C	
	Grain Size (nm)	Surface Area (m²/g)
Ca	34	24
Sr	65	25
Ba	35	24
La	64	23
Sm	39	23
Eu	33	25
Gd	29	31
Ce	22	42
Pr	62	18
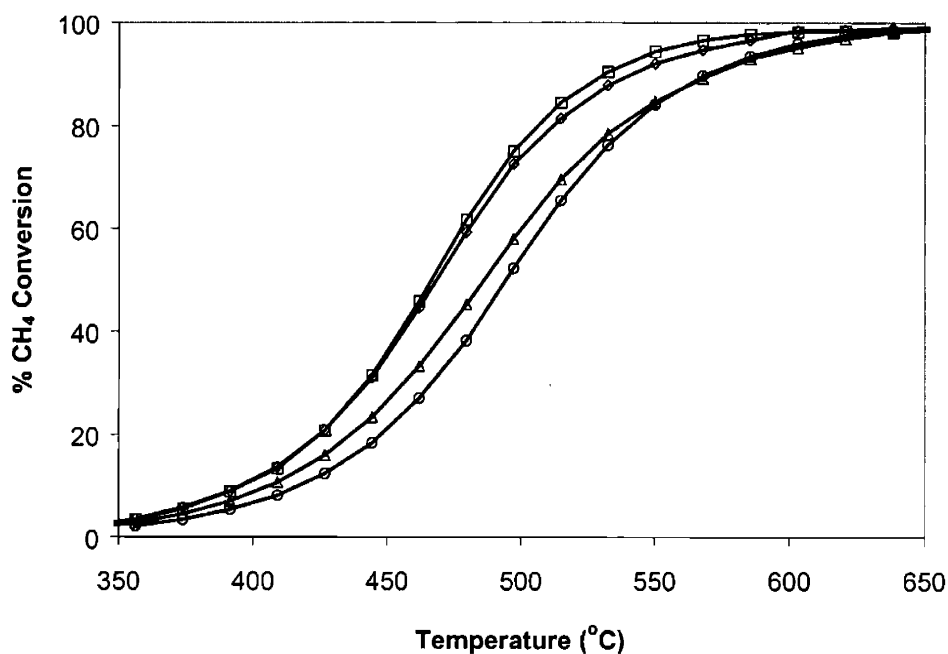
Figure 2.19. Methane conversion over $La_{0.8}A_{0.2}MnO_3$ perovskites containing different A-site dopants: (○) La^{3+}, (△) Sr^{2+}, (◇) Ba^{2+} and (□) Ca^{2+}, after calcination at 800°C. Catalytic testing was performed with 25 mg of catalyst, and a feed of 1% CH_4 in air at 60,000 hour^{-1}.

The effect of rare-earth metal dopants for $La_{0.8}A_{0.2}MnO_3$ perovskites on methane conversion is shown in Figure 2.20. It was found that substitution of A^{3+} dopants for La^{3+} did not significantly alter catalytic activity. The specific activity of these doped catalysts was slightly lower compared to $LaMnO_3$, since they possessed higher surface areas. The replacement of La^{3+} by cations of the same valence did not affect the oxygen vacancy concentration; this suggested that creation of surface oxygen vacancies could be critical towards enhancing catalytic activity.
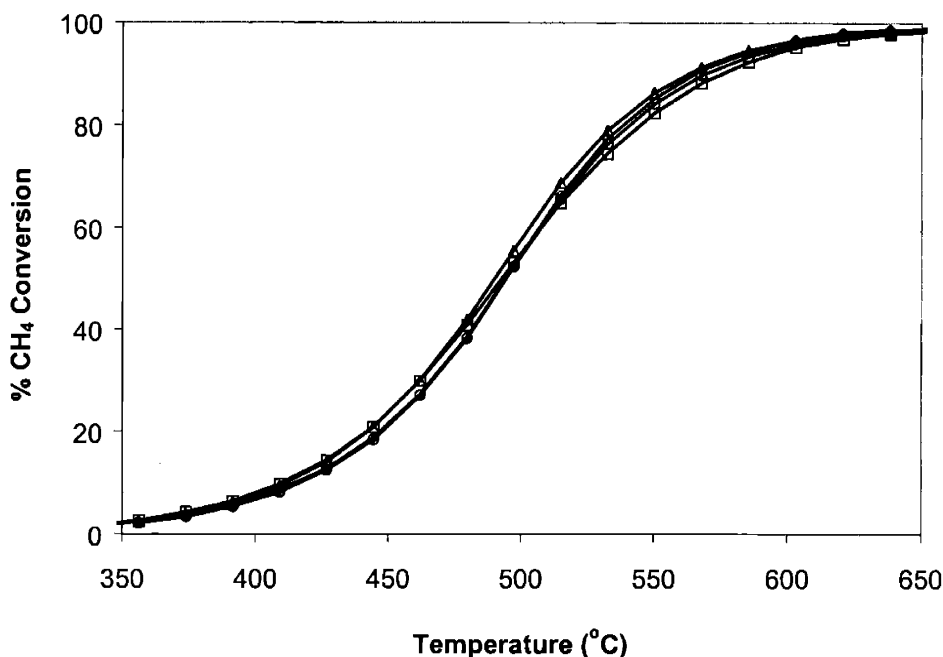
Figure 2.20. Methane conversion over $La_{0.8}A_{0.2}MnO_3$ perovskites containing different A-site dopants: (○) La^{3+}, (△) Sm^{3+}, (◇) Eu^{3+} and (□) Gd^{3+}, after calcination at 800°C. Catalytic testing was performed with 25 mg of catalyst, and a feed of 1% CH_4 in air at 60,000 hour^{-1}.

Figure 2.21 shows the catalytic activity of $La_{0.8}A_{0.2}MnO_3$ perovskites substituted with dopants of higher oxidation state. The addition of Pr^{4+}/Pr^{3+} for La^{3+} resulted in a slight decrease in methane conversion, consistent with an expected decrease in oxygen vacancy concentration. Although the phase segregation of CeO_2 resulted in significantly higher surface area, the addition of Ce^{4+} led to a lower catalytic activity compared to $LaMnO_3$, due possibly to the lower intrinsic activity of ceria. For various dopants examined in this study, it was concluded that the catalytic activity of $La_{0.8}A_{0.2}MnO_3$ was the highest when substituted with Group IIA cations having a lower oxidation state and a higher basicity compared to La^{3+}.
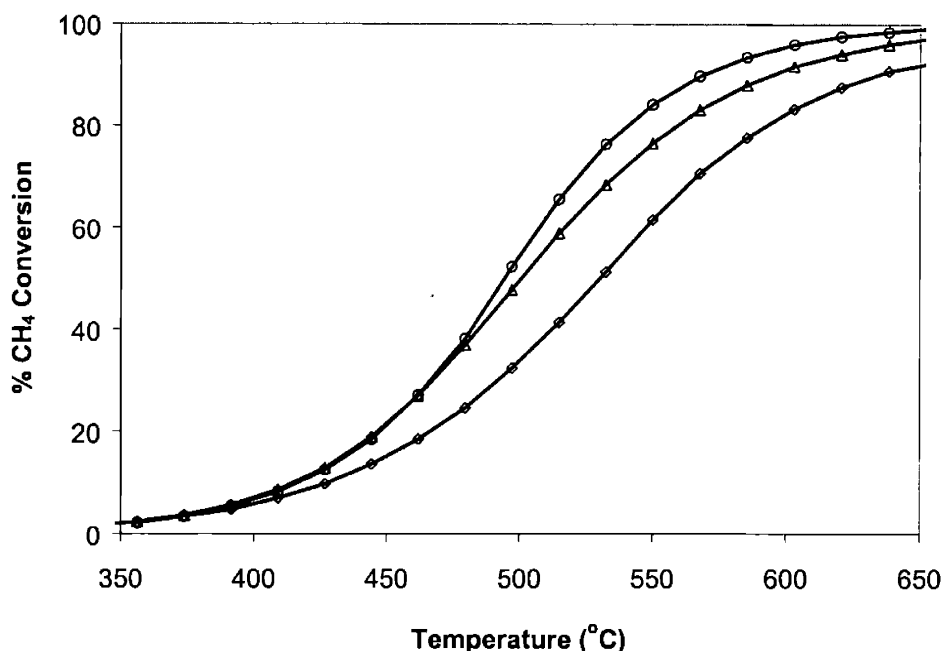
Figure 2.21. Methane conversion over $La_{0.8}A_{0.2}MnO_3$ perovskites containing different A-site dopants: (○) La^{3+}, (△) Pr^{4+} and (◇) Ce^{4+}, after calcination at 800°C. Catalytic testing was performed with 25 mg of catalyst, and a feed of 1% CH_4 in air at 60,000 hour^{-1}.

2.3.6 Characterization and Catalytic Activity of $La_{1-x}A_xMnO_3$

Since the doping of Group IIA metals was found to enhance the catalytic activity of $La_{0.8}A_{0.2}MnO_3$ perovskites, these dopants were further investigated. The substitution of Ca^{2+}, Sr^{2+} and Ba^{2+} for La^{3+} could result in changes in perovskite crystal structure and/or phase transformations, due to their different ionic radius and lower valence state. The effect of doping on the grain size, surface area and morphology of the perovskite particles was also examined.

Figure 2.22 shows the XRD patterns for $La_{1-x}Ca_xMnO_3$ perovskites after calcination at 800°C in air. As Ca^{2+} concentration was increased, there was a noticeable shift in diffraction peaks to higher angles, indicating a reduction in the unit cell partly due to Ca^{2+}'s slightly smaller ionic radius than La^{3+}. The cubic perovskite phase was retained even at high Ca^{2+} concentrations, without the formation of secondary phases or phase transformations.
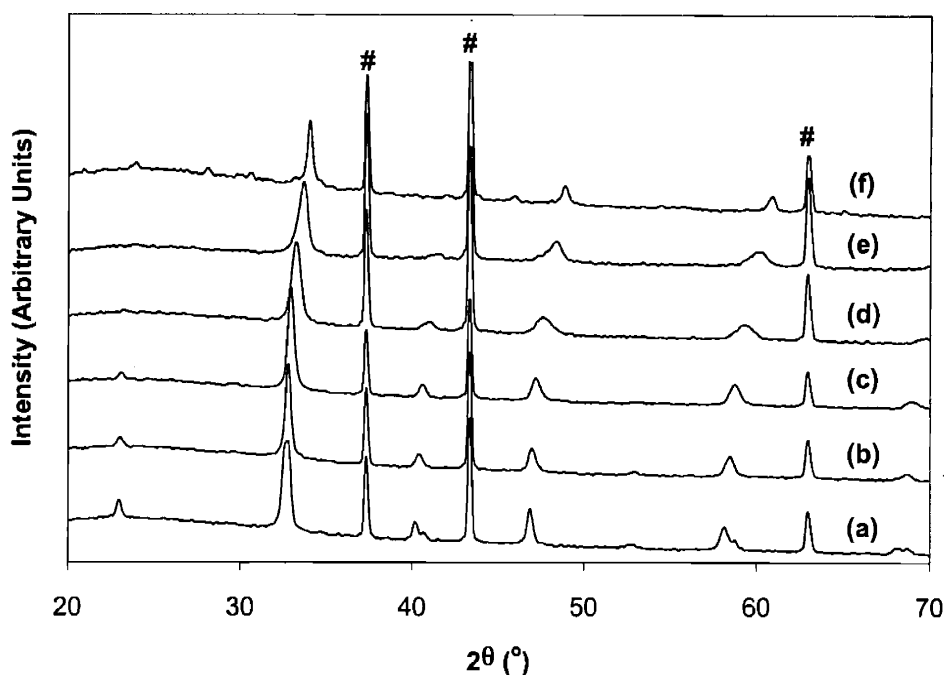
Figure 2.22. XRD patterns of $La_{1-x}Ca_xMnO_3$ perovskites of x = (a) 0.0, (b) 0.2, (c) 0.4, (d) 0.6, (e) 0.8 and (f) 1.0, after calcination at 800°C in air. Peaks for the NiO internal standard are denoted by "#".

The effect of Sr^{2+} doping on the crystal structure of $La_{1-x}Sr_xMnO_3$ perovskites is shown in Figure 2.23. As Sr^{2+} concentration was increased to x = 0.8, the cubic perovskite structure was partially transformed to a hexagonal $SrMnO_3$ phase. Although Sr^{2+} was larger than La^{3+}, the XRD peaks did not shift with strontium doping, indicating that the unit cell size remained essentially constant. X-ray photoelectron spectroscopy (XPS) showed that on increasing Sr^{2+} doping from 0.0 to 0.5, the binding energy separation between the 2p photoelectron peak doublet for manganese at ~ 650 eV increased from 11.40 to 11.48 eV, which was indicative of a higher oxidation state. Thus, as Sr^{2+} dopant concentration was increased, the average oxidation state of manganese cations would increase to maintain charge neutrality, causing a decrease in the average size of the Mn cations. The net result was that the unit cell volume remained unchanged due to the compensating effects of Sr doping and the increase in Mn oxidation state. This was also consistent with the unusually large peak shifts observed with Ca^{2+} doping, although the ionic radius of Ca^{2+} (1.34 Å) was only slightly smaller than La^{3+} (1.36 Å).
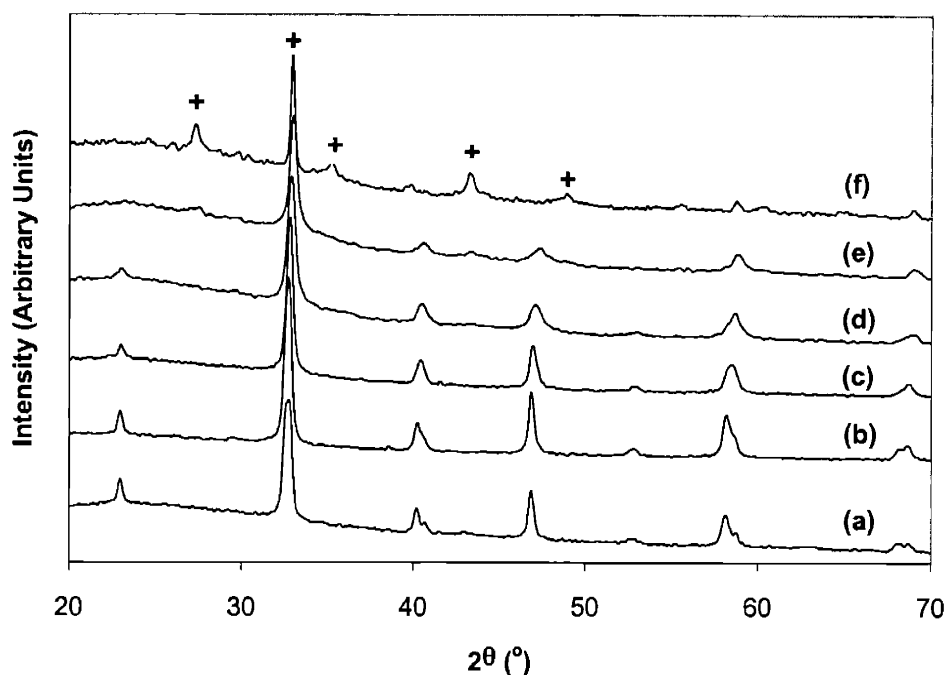
Figure 2.23. XRD patterns of $La_{1-x}Sr_xMnO_3$ perovskites of x = (a) 0.0, (b) 0.2, (c) 0.4, (d) 0.6, (e) 0.8 and (f) 1.0, after calcination at 800°C in air. Peaks for the hexagonal $SrMnO_3$ phase are denoted by "+".

Figure 2.24 shows the effect of barium doping on the phase behavior of $La_{1-x}Ba_xMnO_3$ perovskites after calcination at 800°C. For $0.2 < x < 1.0$, a two-phase mixture of cubic $La_{1-x}Ba_xMnO_3$ and hexagonal $BaMnO_3$ was observed. As Ba^{2+} doping was increased, the hexagonal phase became increasingly dominant; a pure hexagonal $BaMnO_3$ phase was obtained at x = 1.0. XRD peaks corresponding to the perovskite phase were shifted to lower diffraction angles with the incorporation of the larger Ba^{2+} cations, due to an increase in unit cell volume. In contrast, the XRD peaks for the hexagonal $BaMnO_3$ phase did not show similar shifts with increasing barium concentration, indicating that La^{3+} was not present in this segregated phase.
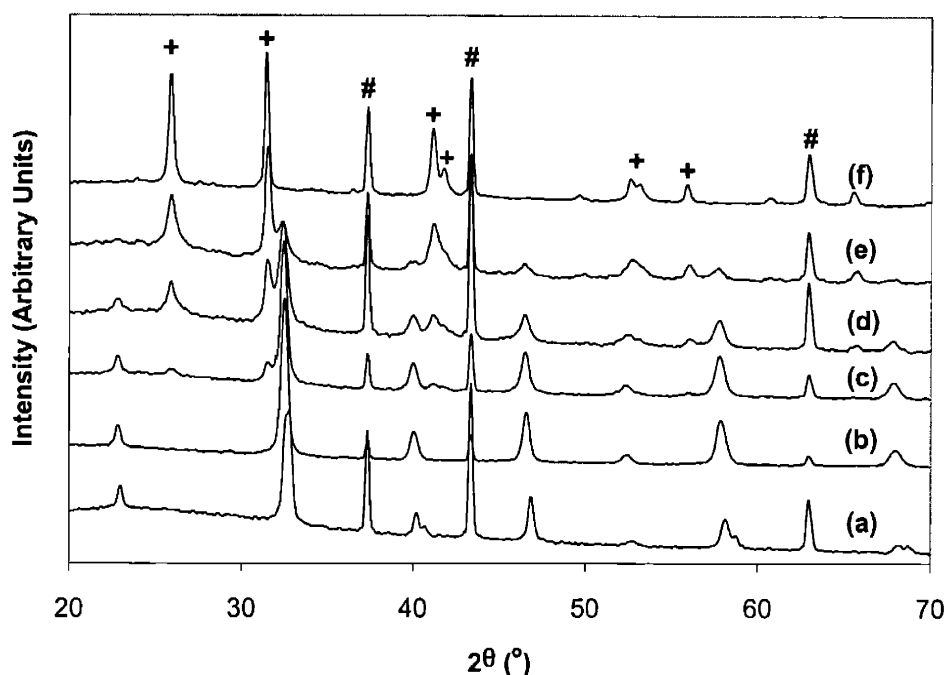
Figure 2.24. XRD patterns of $La_{1-x}Ba_xMnO_3$ perovskites of x = (a) 0.0, (b) 0.2, (c) 0.4, (d) 0.6, (e) 0.8 and (f) 1.0, after calcination at 800°C in air. Peaks for the hexagonal $BaMnO_3$ phase and the NiO internal standard are denoted by "+" and "#", respectively.

The XRD studies illustrated that the stability of $La_{1-x}A_xMnO_3$ perovskites depended greatly on the size of Group IIA dopant. The cubic perovskite phase was stable over the entire compositional range for $A^{2+} = Ca^{2+}$, for x = 0.0 to 0.8 for $A^{2+} = Sr^{2+}$, and for x = 0.0 to 0.2 for $A^{2+} = Ba^{2+}$. As Group IIA dopant size became increasingly larger than La^{3+}, the structural stability of the perovskite phase decreased, resulting in the segregation of a hexagonal $AMnO_3$ phase.

Figure 2.25 shows the XRD grain sizes for $La_{1-x}A_xMnO_3$ perovskites after calcination at 800°C in air for 2 hours. The average grain size decreased as A^{2+} dopant concentration increased, reaching a minimum at x ~ 0.8. At x = 0.8, ultrafine grain sizes of 15, 11 and 17 nm were obtained for Ca-, Sr- and Ba-doped perovskites, respectively. Compared to single-component metal oxides, these perovskites exhibited excellent thermal stability against grain growth at 800°C. For Sr- and Ba-doped materials, both cubic and hexagonal phases had similar grain sizes.
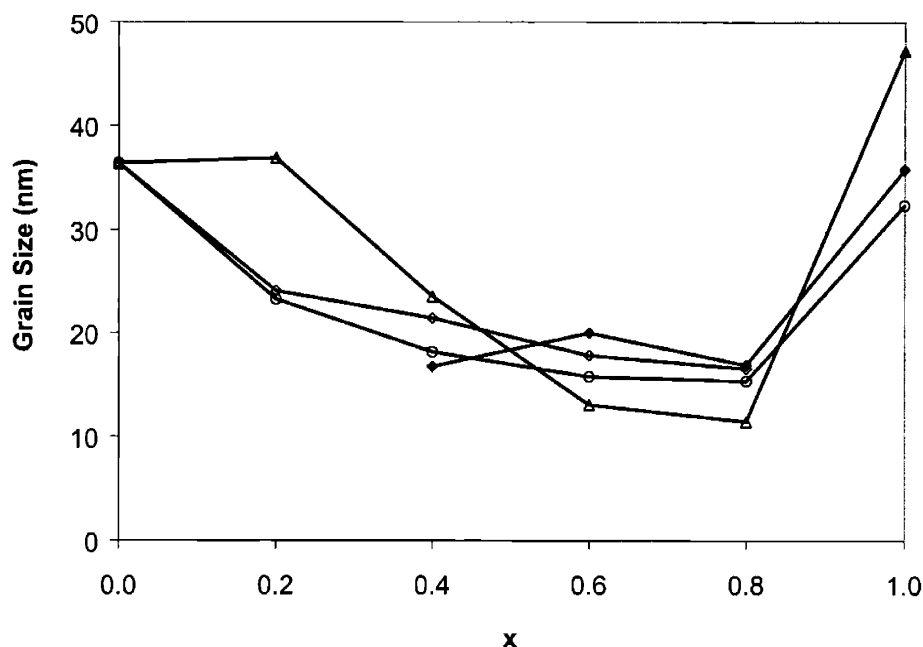
Figure 2.25. XRD grain sizes of $La_{1-x}A_xMnO_3$ containing different A-site dopants: (o) Ca^{2+}, ($\triangle$) Sr^{2+} and ($\diamond$) Ba^{2+}, after calcination at 800°C in air for 2 hours. Open and closed symbols represent the grain sizes for cubic perovskite and hexagonal $AMnO_3$ phases, respectively.

The effect of A^{2+} doping on the BET surface area of $La_{1-x}A_xMnO_3$ perovskites is shown in Figure 2.26. These precipitated perovskites exhibited very high surface areas at 800°C compared to those obtained via combustion or solid-state synthesis. We note that the observed increase in surface area with A^{2+} dopant concentration was relatively small compared to that expected based on the corresponding smaller grain sizes. In fact, Ca-doped perovskites showed a slightly lower surface area compared to undoped $LaMnO_3$, suggesting an increase in particle agglomeration.
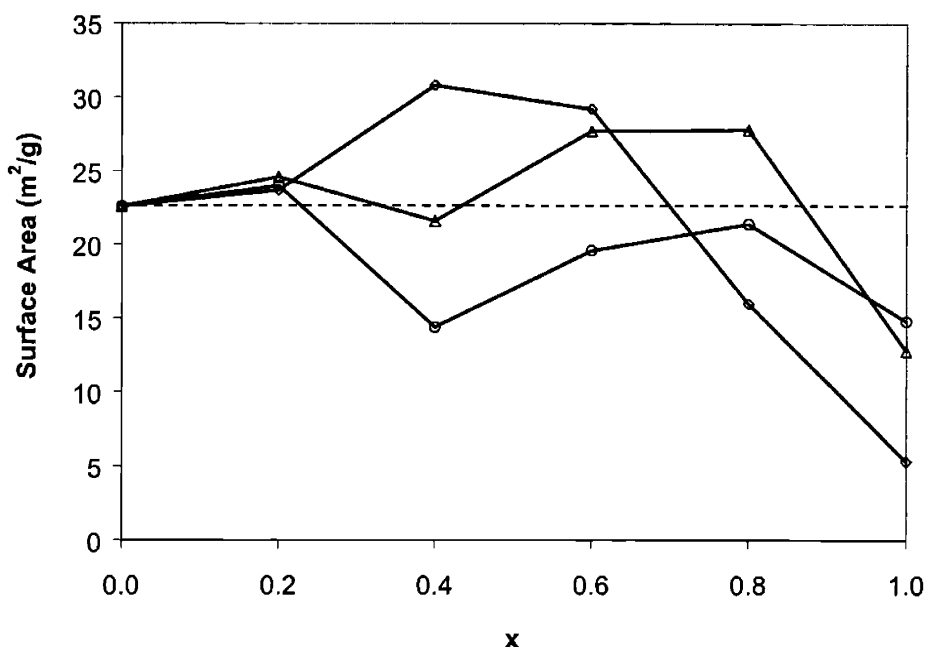
Figure 2.26. BET surface areas of $La_{1-x}A_xMnO_3$ perovskites containing different A-site dopants: (○) Ca^{2+}, (△) Sr^{2+}, and (◇) Ba^{2+}, after calcination at 800°C in air for 2 hours.

TEM micrographs for 800°C-calcined $La_{0.4}A_{0.6}MnO_3$ perovskites are shown in Figure 2.27. The grain size decreased with Sr and Ba doping, in agreement with the XRD results. The degree of particle agglomeration depended greatly on the A-site dopant, and increased in the order: Sr ~ La < Ba < Ca. $La_{0.4}Ca_{0.6}MnO_3$ had large agglomerates, consisting of smaller, densely packed grains. The observed trend in particle agglomeration was found to be consistent with the magnitude of surface charge during the perovskite synthesis (Figure 2.28). Under basic conditions, surface charge (magnitude of zeta potential) of $La_{0.4}A_{0.6}MnO_3$ particles decreased in the order: Sr ~ La > Ba > Ca, resulting in increased particle agglomeration and loss in surface area.
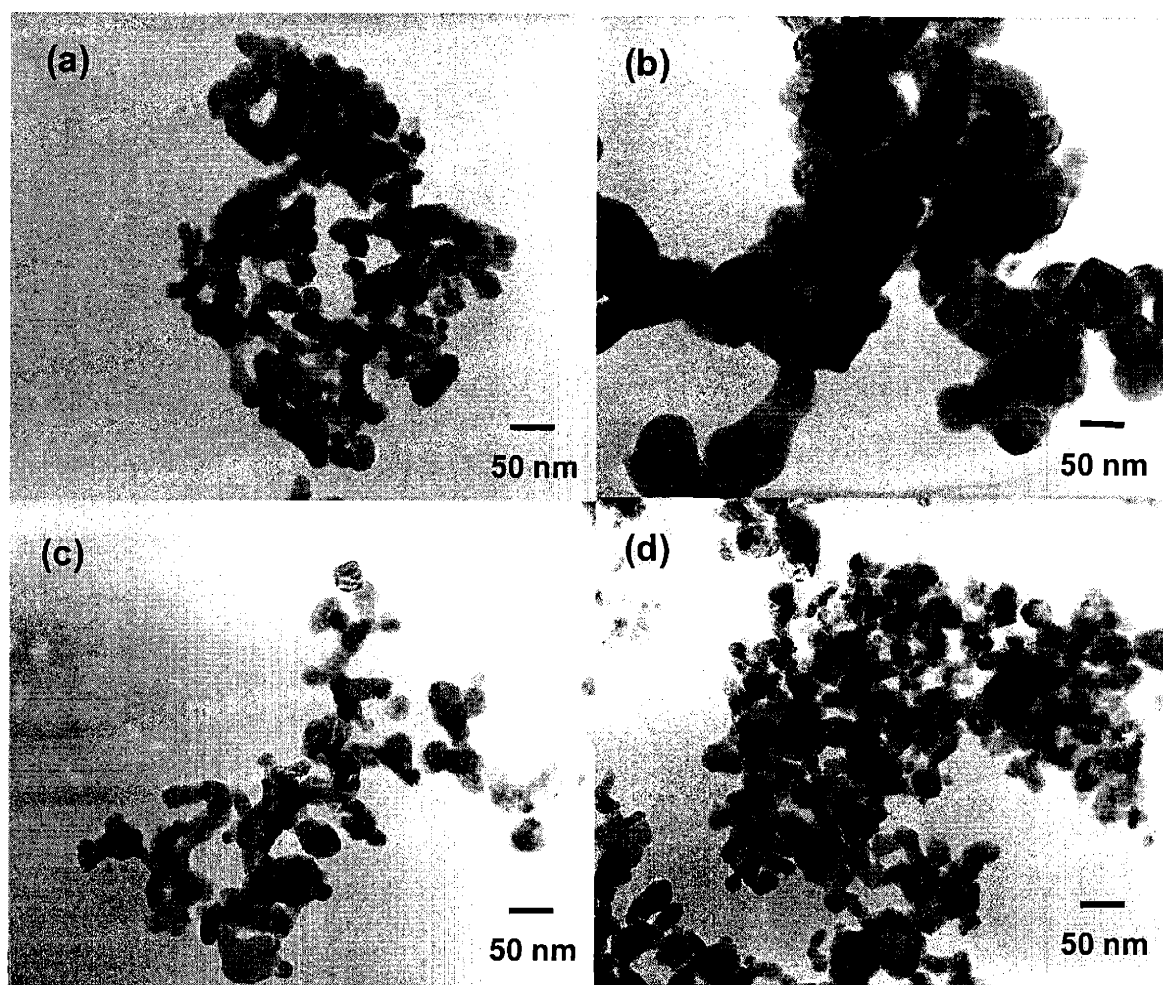
Figure 2.27. TEM micrographs for $La_{0.4}A_{0.6}MnO_3$ perovskites containing different A-site dopants: (a) La^{3+}, (b) Ca^{2+}, (c) Sr^{2+} and (d) Ba^{2+}, after calcination at 800°C for 2 hours.

Figure 2.29 shows the effect of Ca^{2+} doping on the catalytic activity of $La_{1-x}Ca_xMnO_3$ perovskites. Methane conversion was found to be maximized at x = 0.2. The light-off temperature of $LaMnO_3$ was lowered from 420°C to 395°C with 20% Ca doping at the A site, but rose to 445°C for complete Ca^{2+} substitution for La^{3+}. Since these perovskites were phase-pure, the observed decrease in activity at high Ca^{2+} concentrations must be related to their defect chemistry, rather than the formation of inactive secondary phases and/or phase transformations. Moreover, the trend in catalyst activity did not correlate with the observed decrease in grain size with Ca^{2+} doping.
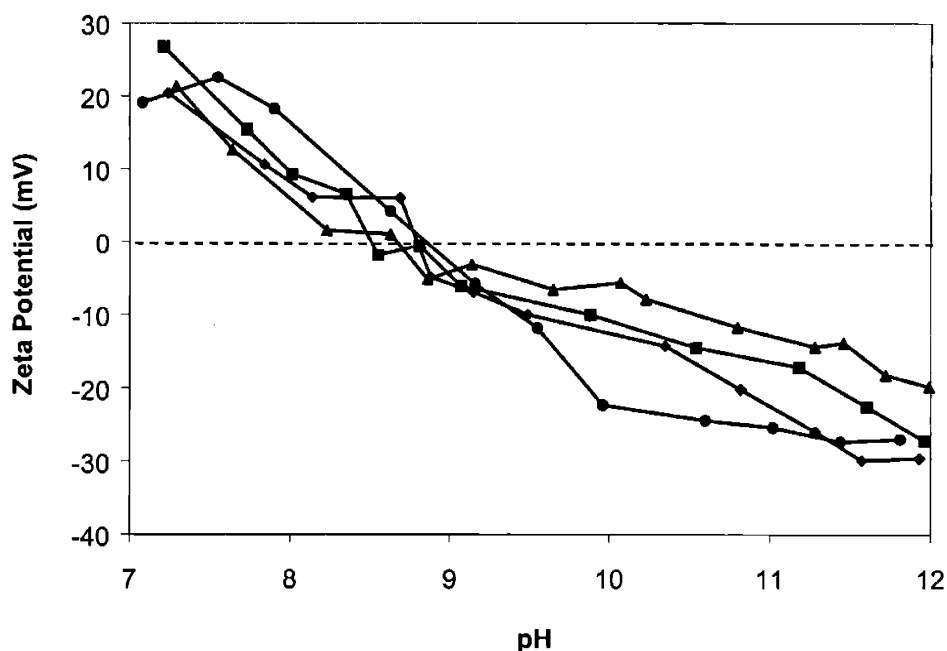
Figure 2.28. Zeta potential profiles for uncalcined $La_{0.4}A_{0.6}MnO_3$ perovskites containing different A-site dopants: (●) La^{3+}, (▲) Ca^{2+}, (◆) Sr^{2+} and (■) Ba^{2+}.

The effect of Sr^{2+} doping on the catalytic activity of $La_{1-x}Sr_xMnO_3$ perovskites is shown in Figure 2.30. Methane conversion was found to reach a maximum at $x = 0.6$. The light-off temperature of $La_{0.4}Sr_{0.6}MnO_3$ was 380°C, which was significantly lower than 420°C for $LaMnO_3$; full methane conversion was achieved by 600°C over $La_{0.4}Sr_{0.6}MnO_3$. The least active $SrMnO_3$ exhibited a higher light-off temperature of 445°C, and achieved full conversion at 725°C. The decrease in catalyst activity for $x > 0.6$ coincided with the appearance of the hexagonal $SrMnO_3$ phase, as seen in Figure 2.23.
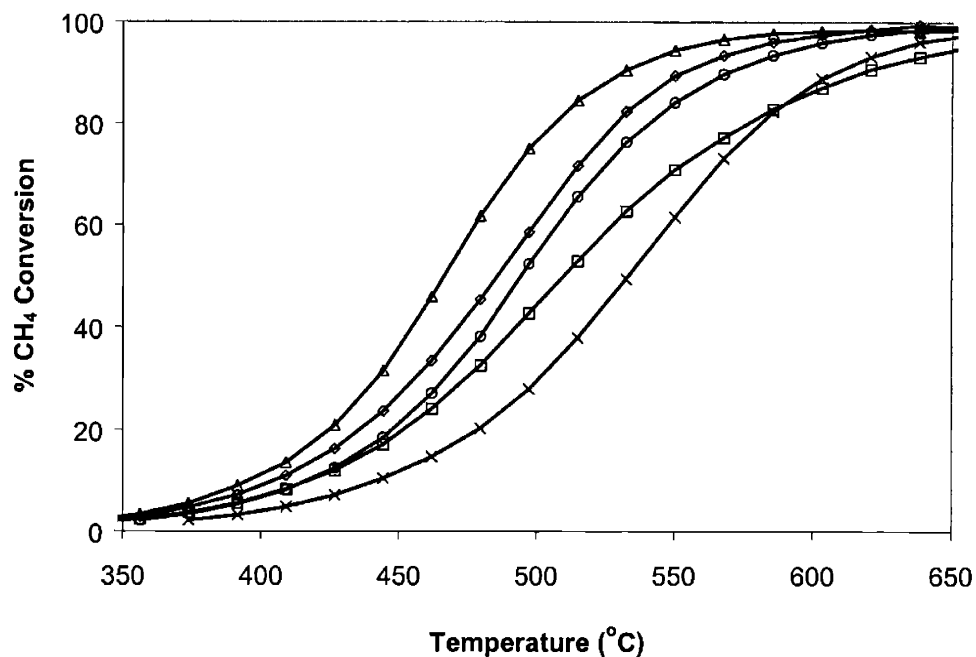
Figure 2.29. Methane conversion over $La_{1-x}Ca_xMnO_3$ perovskites of x = (∘) 0.0, (△) 0.2, (◇) 0.4, (□) 0.6 and (×) 1.0, after calcination at 800°C. Catalytic testing was performed with 25 mg of catalyst, and a feed of 1% CH_4 in air at 60,000 hour^{-1}.
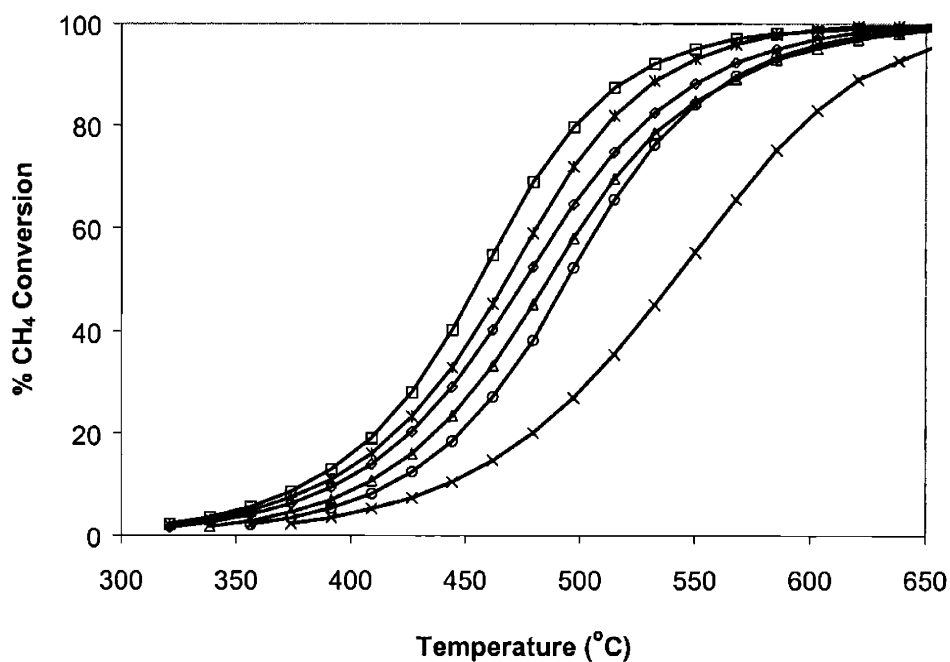
Figure 2.30. Methane conversion over $La_{1-x}Sr_xMnO_3$ perovskites of x = (∘) 0.0, (△) 0.2, (◇) 0.4, (□) 0.6, (∗) 0.8 and (×) 1.0, after calcination at 800°C. Catalytic testing was performed with 25 mg of catalyst, and a feed of 1% CH_4 in air at 60,000 hour^{-1}.

Figure 2.31 shows the effect of Ba^{2+} doping on methane conversion for $La_{1-x}Ba_xMnO_3$ perovskites. Catalyst activity was found to be maximized at x = 0.6 with a light-off temperature of 385°C. In constrast to Sr-doped perovskites, the decrease in catalyst activity for x > 0.6 did not coincide with the appearance of hexagonal $BaMnO_3$ phase at x > 0.2, suggesting that both cubic and hexagonal phases exhibited high activity for methane oxidation.
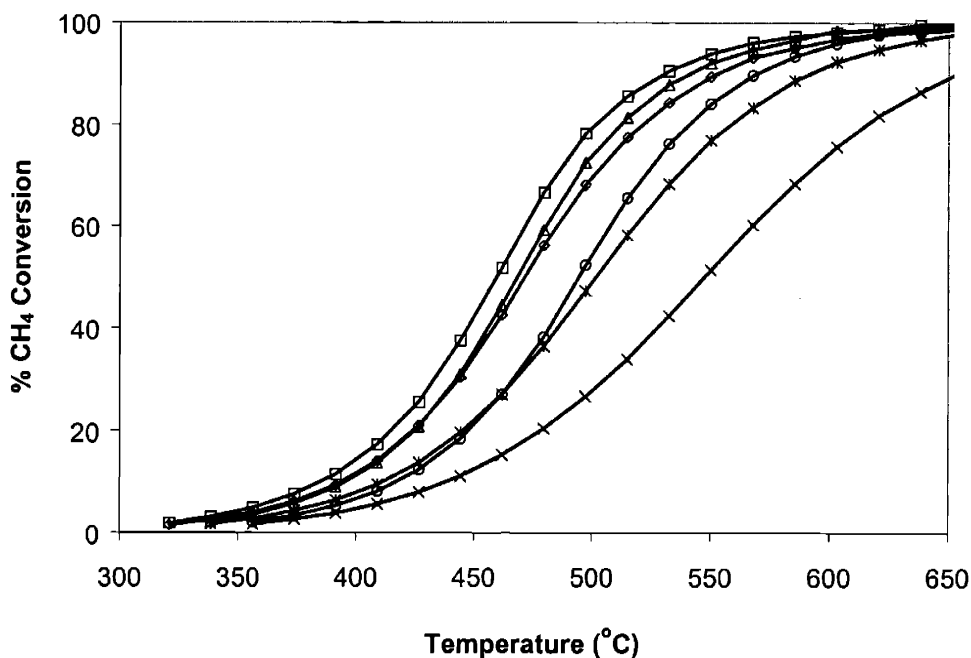
Figure 2.31. Methane conversion over $La_{1-x}Ba_xMnO_3$ perovskites of x = (○) 0.0, (△) 0.2, (◇) 0.4, (□) 0.6, (∗) 0.8 and (×) 1.0, after calcination at 800°C. Catalytic testing was performed with 25 mg of catalyst, and a feed of 1% CH_4 in air at 60,000 hour^{-1}.

Figure 2.32 compares the specific reaction rates for $La_{1-x}A_xMnO_3$ perovskites at 390°C, under differential and reaction-limited conditions. Partial substitution of La^{3+} by Group IIA cations resulted in substantial increases in reaction rate. At an optimal doping level of 0.6, Sr- and Ba-doped perovskites exhibited reaction rates that were higher than undoped $LaMnO_3$ by a factor of 2.5 and 2.2, respectively. At an optimal doping level of 0.2, Ca-doped perovskite gave rise to an increase in reaction rate by a factor of 2.1 compared to undoped $LaMnO_3$.

Figure 2.32. Specific reaction rate (weight-basis) for $La_{1-x}A_xMnO_3$ perovskites containing different A-site dopants: (o) Ca^{2+}, ($\triangle$) Sr^{2+} and ($\diamond$) Ba^{2+}, after calcination at 800°C. Reaction rates were obtained under differential conversions at 390°C with 25 mg of catalyst, and a feed of 1% CH_4 in air at 60,000 hour^{-1}.

Figure 2.33 compares the intrinsic reaction rates of $La_{1-x}A_xMnO_3$ perovskites, which were normalized with respect to BET surface area. The observed increase in methane conversion of perovskites with Group IIA doping predominantly resulted from their higher intrinsic catalytic activity. The intrinsic activities of optimal Ca-, Sr- and Ba-doped perovskites were significantly higher than that of pure $LaMnO_3$ by factors of 2.1, 2.0 and 1.7, respectively. Although the phase purity of perovskite might affect intrinsic activity, the observed trend seemed to correlate with increasing basicity.
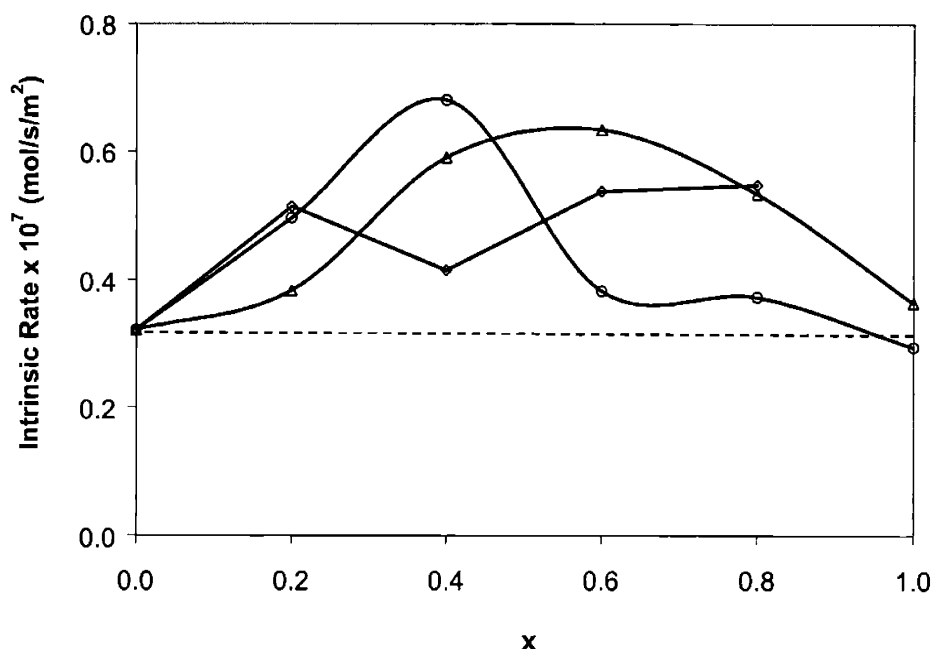
Figure 2.33. Intrinsic reaction rate for $La_{1-x}A_xMnO_3$ perovskites containing different A-site dopants: (○) Ca^{2+}, (△) Sr^{2+} and (◇) Ba^{2+}, after calcination at 800°C. Specific rates were obtained under differential conversions at 390°C with 25 mg of catalyst, and a feed of 1% CH_4 in air at 60,000 hour^{-1}.

2.3.7 Characterization and Catalytic Activity of $La_{1-x}Sr_xBO_3$

Since the substitution of La^{3+} by Sr^{2+} significantly enhanced the methane oxidation rate over Mn-based perovskites, the effect of Sr^{2+} doping on the catalytic activity of Co- and Ni-based perovskites was investigated to further understand the relationship between intrinsic activity and perovskite composition. The effect of Sr^{2+} doping on the crystal structure, phase behavior, grain size, surface area and powder morphology was also examined and related to the catalyst performance.

Figure 2.34 shows the XRD patterns for $La_{1-x}Sr_xCoO_3$ perovskites after calcination at 800°C in air. For x > 0.4, a two-phase mixture comprised of cubic $La_{1-x}Sr_xCoO_3$ perovskite and hexagonal $Sr_2Co_2O_5$ brownmillerite was obtained. The appearance of the hexagonal phase occurred at a lower Sr^{2+} concentration of 0.6 for Co-based perovskites, compared to 0.8 for Mn-based perovskites, indicating a lower stability of the perovskite phase with Co at B site. The rhombohedral distortion of the cubic $LaCoO_3$ structure as observed by the splitting of XRD peaks was significantly reduced with strontium doping.
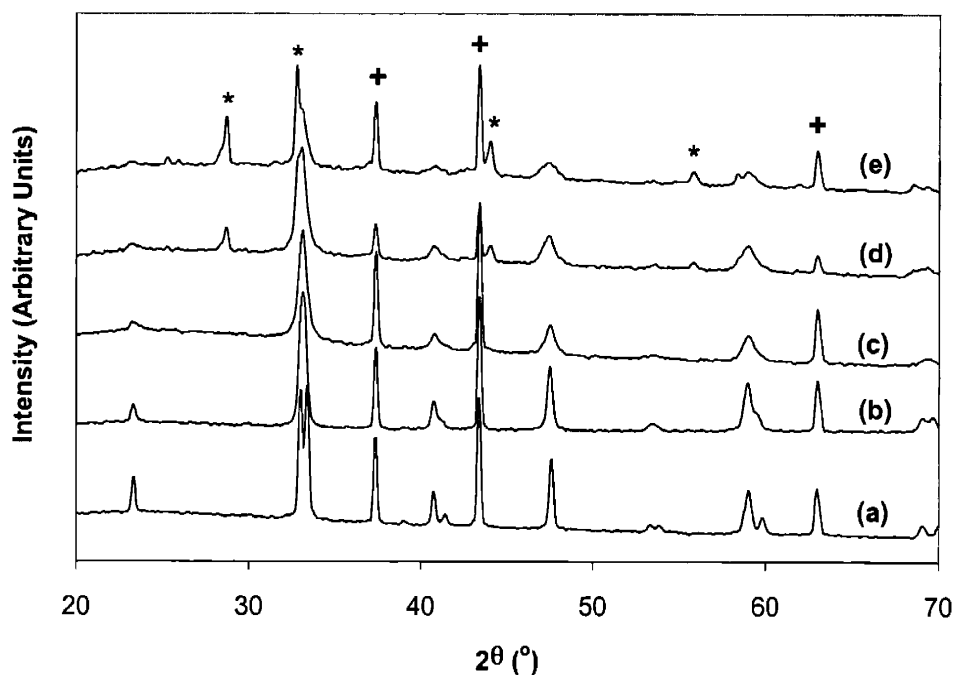
Figure 2.34. XRD patterns of $La_{1-x}Sr_xCoO_3$ perovskites of x = (a) 0.0, (b) 0.2, (c) 0.4, (d) 0.6 and (e) 0.8, after calcination at 800°C in air. XRD peaks for the hexagonal $Sr_2Co_2O_5$ phase and the NiO internal standard are denoted by "*" and "+", respectively.

The effect of Sr doping on the phase behavior of $La_{1-x}Sr_xNiO_3$ perovskites is shown in Figure 2.35. Even at x = 0.2, these perovskites show the segregation of $SrCO_3$ and NiO phases, indicating the low solubility of Sr^{2+} at the A site. The $SrCO_3$ and NiO peaks increased in relative intensity with increasing Sr^{2+} concentration. Unlike Co- and Mn-based perovskites, Sr^{2+} could not be substituted for La^{3+} in the Ni-based perovskites.

The XRD studies showed that the relative stability of $La_{1-x}Sr_xBO_3$ perovskites on strontium doping decreased in the order: Mn > Co > Ni. This trend was consistent with the perovskites' increasing reducibility or preference for lower valence state. The stability of Mn-based perovskites was related to the ability of Mn cations to charge compensate for strontium doping by increasing their average valence above 3+. The resulting lower oxygen vacancy concentration delayed the onset of phase transformation to vacancy-ordered hexagonal phase to a high Sr content. In contrast, the relative preference of Co for 3+ oxidation state resulted in higher oxygen vacancy concentrations in $La_{1-x}Sr_xCoO_3$ perovskites, thereby increasing their tendency to transform to the vacancy-ordered hexagonal phase. The ease of reduction of Ni to

2+ valence state led to perovskite decomposition, since the corresponding oxygen vacancy concentration was too large to be stable.
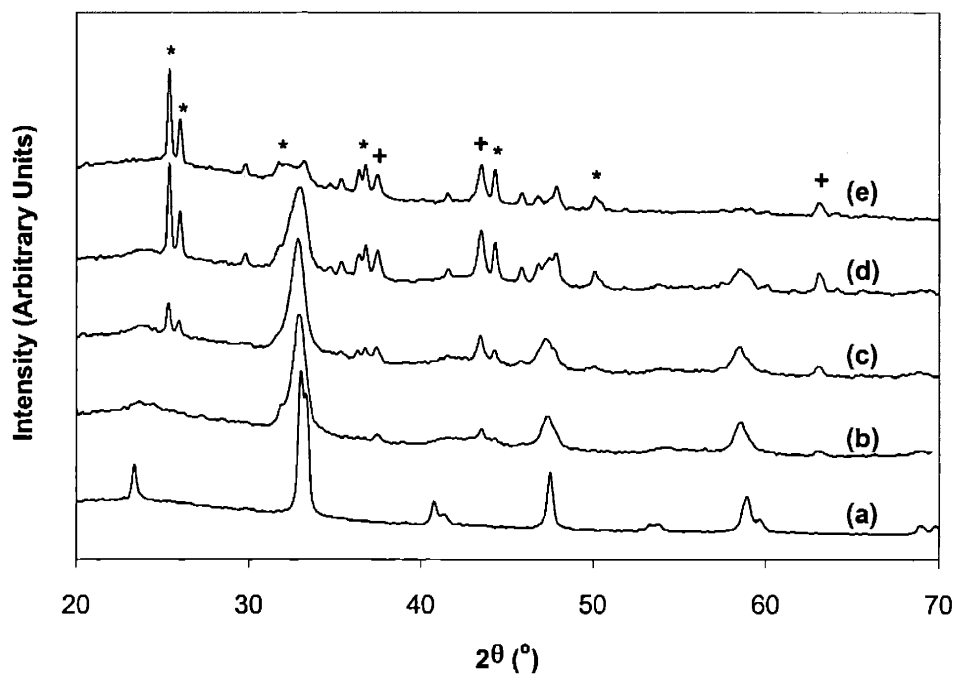
Figure 2.35. XRD patterns of $La_{1-x}Sr_xNiO_3$ perovskites of x = (a) 0.0, (b) 0.2, (c) 0.4, (d) 0.6 and (e) 0.8, after calcination at 800°C in air. XRD peaks for $SrCO_3$ and NiO are denoted by "*" and "+", respectively.

Figure 2.36 shows that as the Sr^{2+} concentration was increased, both Co- and Ni-based perovskites were increased in surface area, reaching a maximum of ~ 18 m^2/g at x ~ 0.4, followed by a decrease in surface area. The increase in surface area was accompanied by a decrease in grain size for the Co-based perovskites, which exhibited an ultrafine grain sizes of 16 nm at x ~ 0.4.
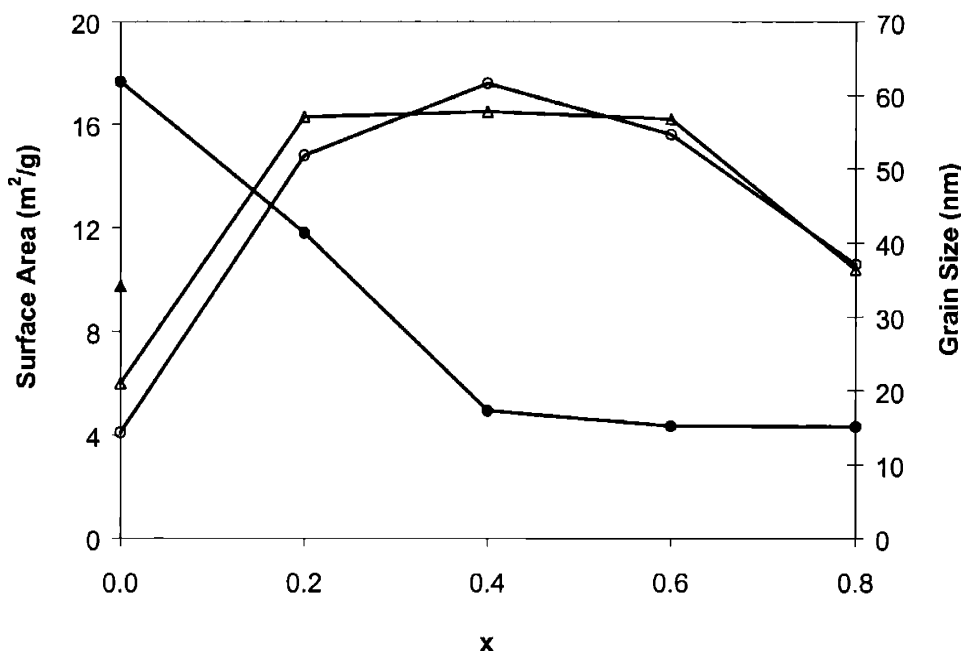
Figure 2.36. BET surface area (open symbols) and XRD grain size (closed symbols) of (○) La$_{1-x}$Sr$_x$CoO$_3$ and (△) La$_{1-x}$Sr$_x$NiO$_3$ perovskites, after calcination at 800°C in air.

The catalytic activity of both Co- and Ni-based La$_{1-x}$Sr$_x$BO$_3$ perovskites was found to reach a maximum at x = 0.2 (Figures 2.37 and 2.38). The light-off temperature of LaCoO$_3$ decreased substantially from 500 to 415°C with 20% Sr^{2+} substitution, but increased on further Sr^{2+} doping to 450°C at x = 0.8. Sr^{2+} substitution had a less pronounced effect on methane conversion for Ni-based perovskites. The light-off temperature of LaNiO$_3$ decreased by only 30°C from 445°C to 415°C on 20% Sr^{2+} doping. At high Sr^{2+} concentrations, the activity of these perovskites was derived from the highly dispersed NiO nanocrystals. At the respective Sr^{2+} concentrations, the activity of La$_{1-x}$Sr$_x$BO$_3$ perovskites decreased in the order: Mn > Ni ~ Co. La$_{0.4}$Sr$_{0.6}$MnO$_3$ has a significantly lower light-off temperature of 380°C, compared to 415°C for La$_{0.8}$Sr$_{0.2}$CoO$_3$ and La$_{0.8}$Sr$_{0.2}$NiO$_3$.
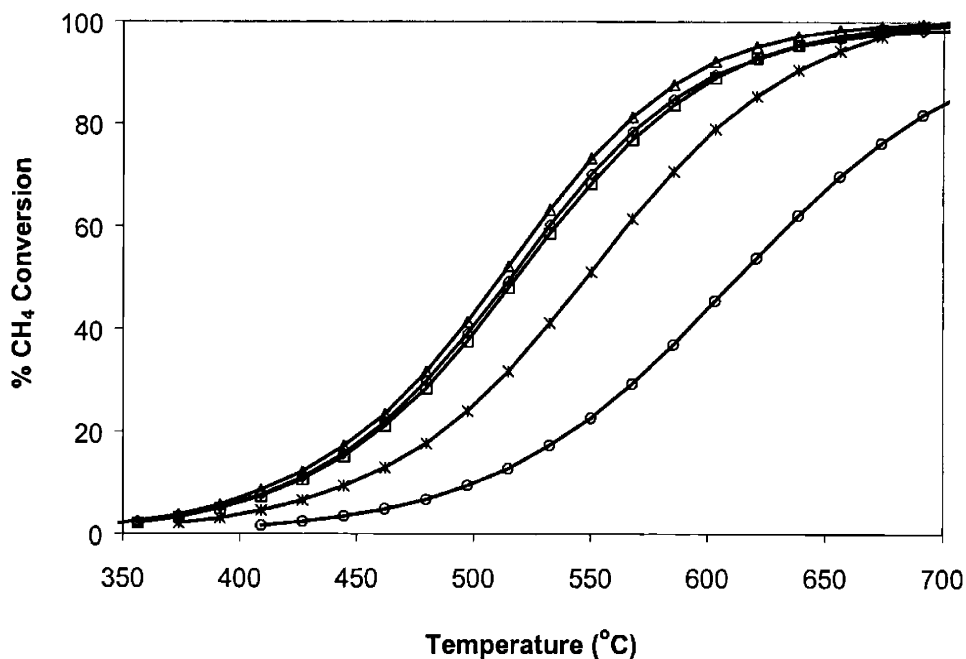
Figure 2.37. Methane conversion over $La_{1-x}Sr_xCoO_3$ perovskites of x = (○) 0.0, (△) 0.2, (◇) 0.4, (□) 0.6 and (*) 0.8, after calcination at 800°C. Catalytic testing was performed with 25 mg of catalyst, and a feed of 1% CH_4 in air at 60,000 hour[-1].
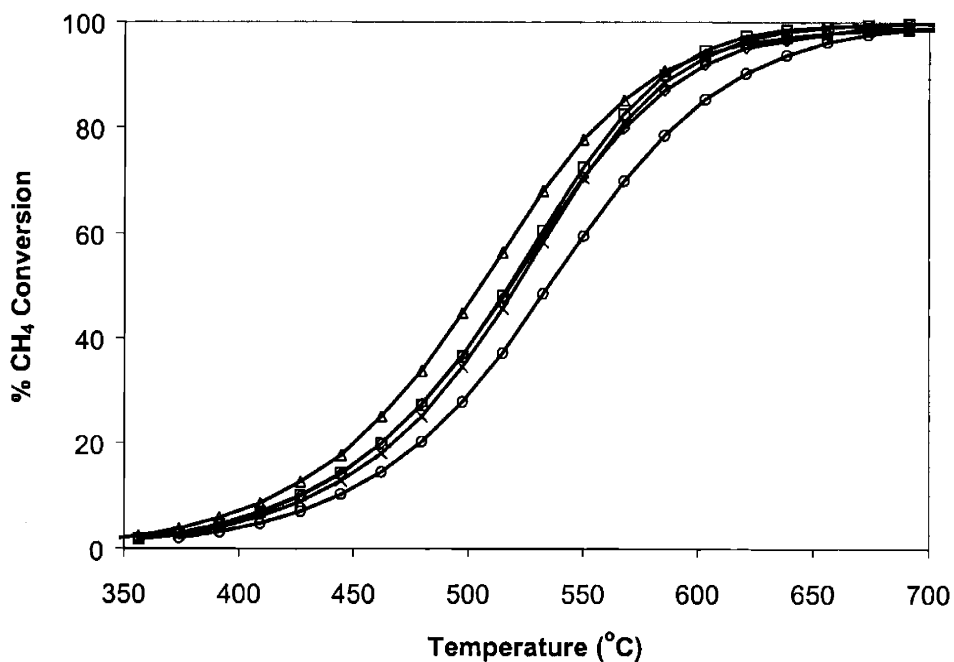
Figure 2.38. Methane conversion over $La_{1-x}Sr_xNiO_3$ perovskites of x = (○) 0.0, (△) 0.2, (◇) 0.4, (□) 0.6 and (×) 0.8, after calcination at 800°C. Catalytic testing was performed with 25 mg of catalyst, and a feed of 1% CH_4 in air at 60,000 hour[-1].

The intrinsic catalytic activity of $La_{1-x}Sr_xBO_3$ perovskites was compared by normalizing the reaction rate, measured at 445°C under differential, reaction-limited conditions, with respect to BET surface area (Figure 2.39). The effect of Sr^{2+} doping on the intrinsic activity of $La_{1-x}Sr_xBO_3$ greatly depended on the B-site transition metal. For $La_{1-x}Sr_xMnO_3$, the intrinsic activity increased with Sr^{2+} concentration until x ~ 0.6. For $La_{1-x}Sr_xCoO_3$, the maximum activity occurred at a lower Sr^{2+} concentration (x ~ 0.2). For $La_{1-x}Sr_xNiO_3$, the addition of Sr^{2+} has a detrimental effect on the intrinsic activity.
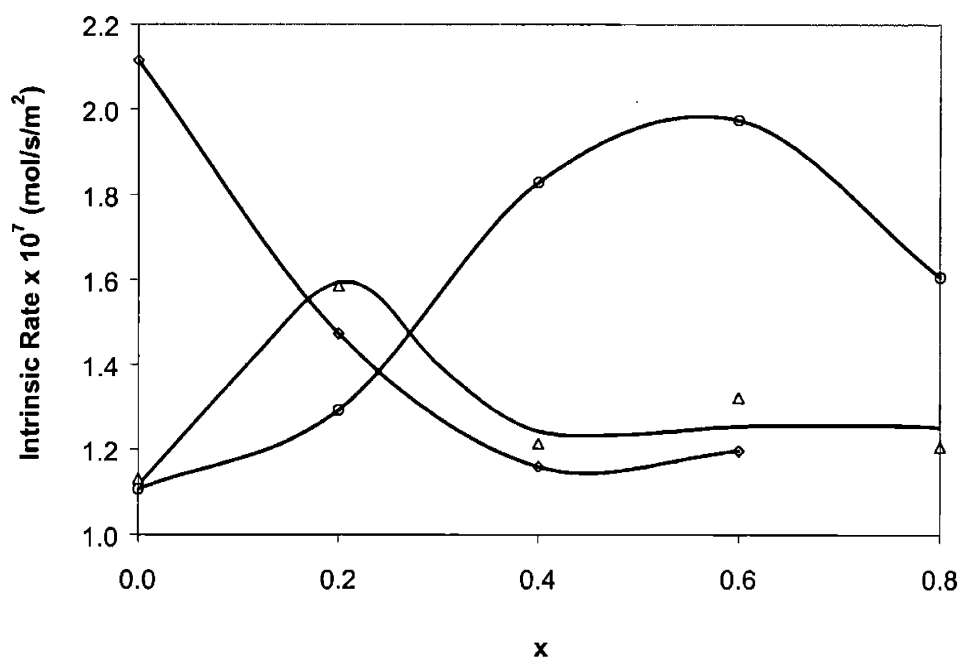
Figure 2.39. Intrinsic reaction rate for $La_{1-x}Sr_xBO_3$ perovskites with different B-site transition metals: (○) Mn, (△) Co and (◇) Ni, after calcination at 800°C. Specific rates were obtained under differential conversions at 445°C with 25 mg of catalyst, and a feed of 1% CH_4 in air at 60,000 $hour^{-1}$.

The enhancement in intrinsic activity on Sr^{2+} doping correlated with the stability of the resulting perovskite. On strontium addition, Ni-based perovskites formed less active, segregated phases of NiO and $SrCO_3$, causing a decrease in intrinsic activity. Compared to Mn-based perovskites, Co-based perovskites underwent transformation to a vacancy-ordered hexagonal phase at a much lower Sr^{2+} concentration. Therefore, to achieve significant enhancement in intrinsic activity with Sr^{2+} doping, it would be important to ensure the stability of the perovskite phase by manipulating the B-site cation(s).

2.3.8 Characterization and Catalytic Activity of $LaMn_{1-y}Ni_yO_3$

The effect of single-component transition metals on the crystal structure, powder morphology and catalytic activity of $LaBO_3$ perovskites was investigated in Section 2.3.4. Intrinsic catalytic activity was found to increase in the order: Mn ~ Fe < Co < Ni, with $LaNiO_3$ exhibiting the highest specific rate. However, methane conversion increased in the order: Co < Ni ~ Fe < Mn, with $LaMnO_3$ showing the lowest light-off temperature due to its high surface area. Therefore, combining the high intrinsic activity of Ni with the high thermal stability of Mn could potentially result in higher catalytic activity. This might be achieved using a mixture of Mn and Ni cations at the B site, as in $LaMn_{1-y}Ni_yO_3$ perovskites.

Figure 2.40 shows that a phase-pure $LaMn_{1-y}Ni_yO_3$ perovskite was obtained at all y values. As the Ni concentration was increased, the XRD peaks shifted to higher diffraction angles, due to the smaller ionic radius of nickel. Figure 2.41 demonstrated that the surface area decreased with Ni addition, but the grain size remained fairly constant at ~ 35 nm. This suggested that the degree of particle agglomeration increased with Ni concentration, which was consistent with the results for $LaBO_3$ perovskites (Figure 2.9).
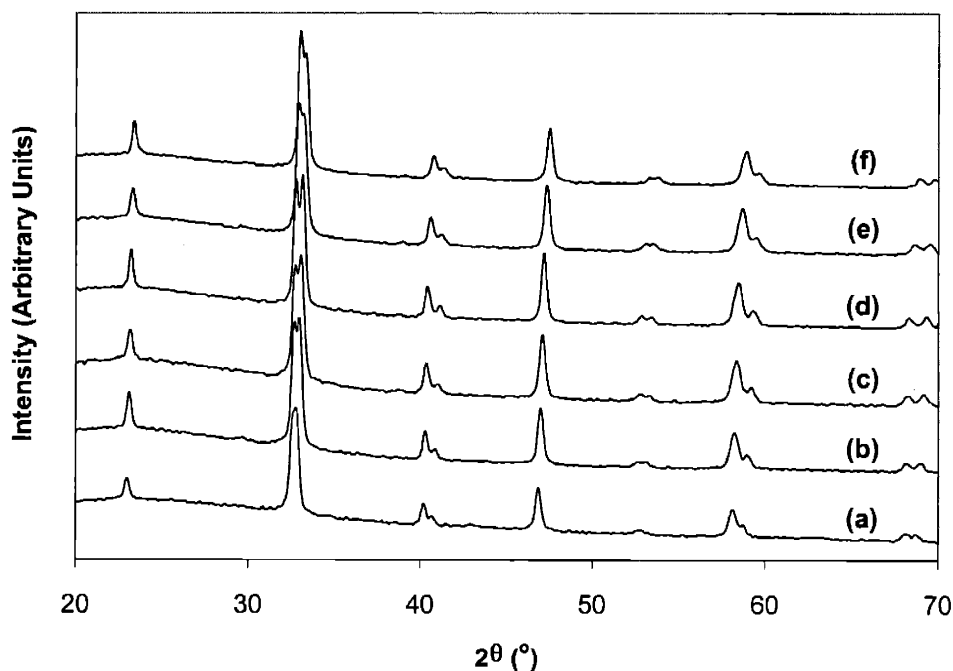
Figure 2.40. XRD patterns of $LaMn_{1-y}Ni_yO_3$ perovskites of y = (a) 0.0, (b) 0.2, (c) 0.4, (d) 0.6, (e) 0.8 and (f) 1.0, after calcination at 800°C in air.
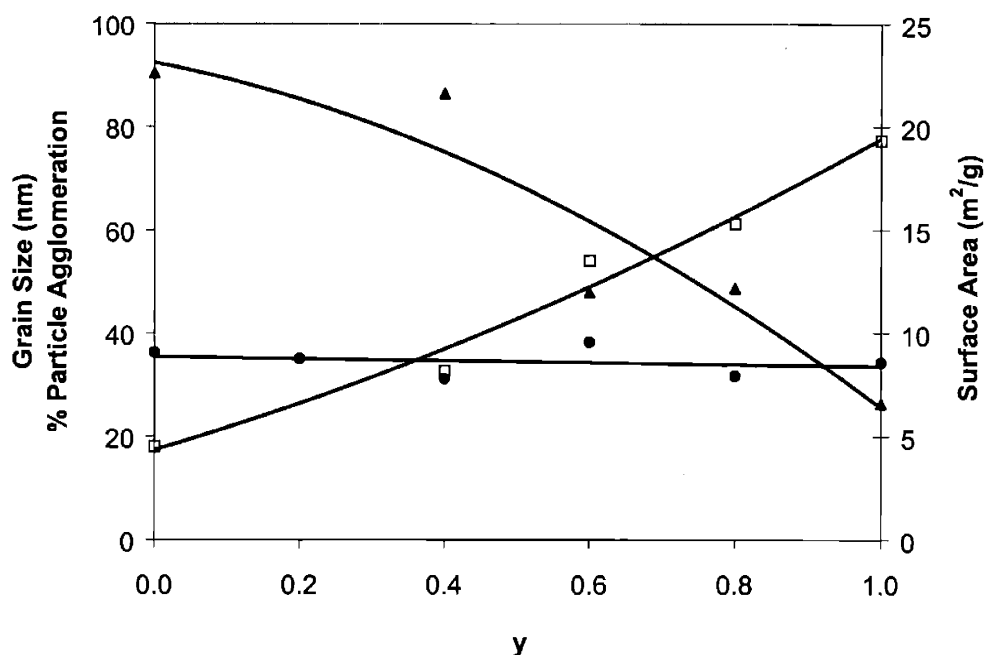
Figure 2.41. XRD grain size (●), BET surface area (▲) and degree of particle agglomeration (□) of LaMn$_{1-y}$Ni$_y$O$_3$ perovskites, after calcination at 800°C for 2 hours.

The effect of B-site composition on the catalytic activity of LaMn$_{1-y}$Ni$_y$O$_3$ is shown in Figure 2.42. As the Ni concentration increased, methane conversion increased until 0.4. Using a 40:60 mixture of Ni and Mn at B site, the light-off temperature was reduced to 390°C, which was significantly lower than 420°C and 445°C required by LaMnO$_3$ and LaNiO$_3$, respectively. Although the perovskite surface area decreased with Ni doping, the accompanied increase in intrinsic activity more than compensated for this loss in surface area, resulting in higher methane conversion for y ≤ 0.4. The specific reaction rate was found to increase by a factor of 2 at the optimal Ni concentration of y = 0.4 (Figure 2.43).

Figure 2.43 shows the intrinsic reaction rates of LaMn$_{1-y}$Ni$_y$O$_3$ perovskites that were normalized with respect to BET surface area. It was interesting to note that intrinsic activity did not vary linearly between the y = 0.0 and y = 1.0 end-points, as would be expected for a physical mixture of LaMnO$_3$ and LaNiO$_3$. Significant interactions occurred between Mn and Ni cations on forming their solid solution at the B site. These interactions seemed to enhance the intrinsic activity of LaMn$_{1-y}$Ni$_y$O$_3$ perovskites.
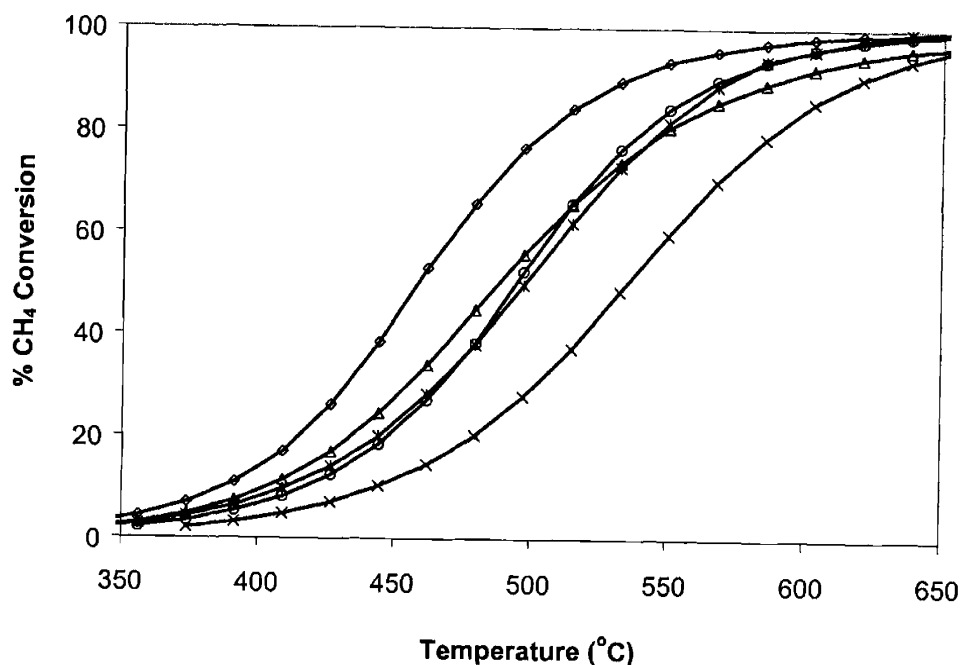
Figure 2.42. Methane conversion over $LaMn_{1-y}Ni_yO_3$ perovskites of y = (○) 0.0, (△) 0.2, (◇) 0.4, (*) 0.8 and (×) 1.0, after calcination at 800°C. Catalytic testing was performed with 25 mg of catalyst, and a feed of 1% CH_4 in air at 60,000 $hour^{-1}$.

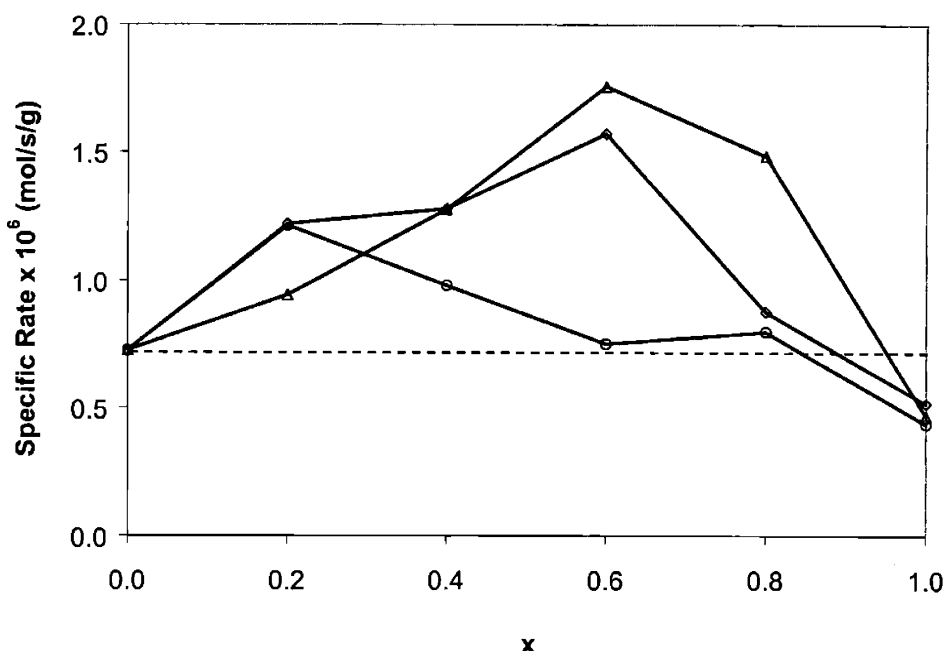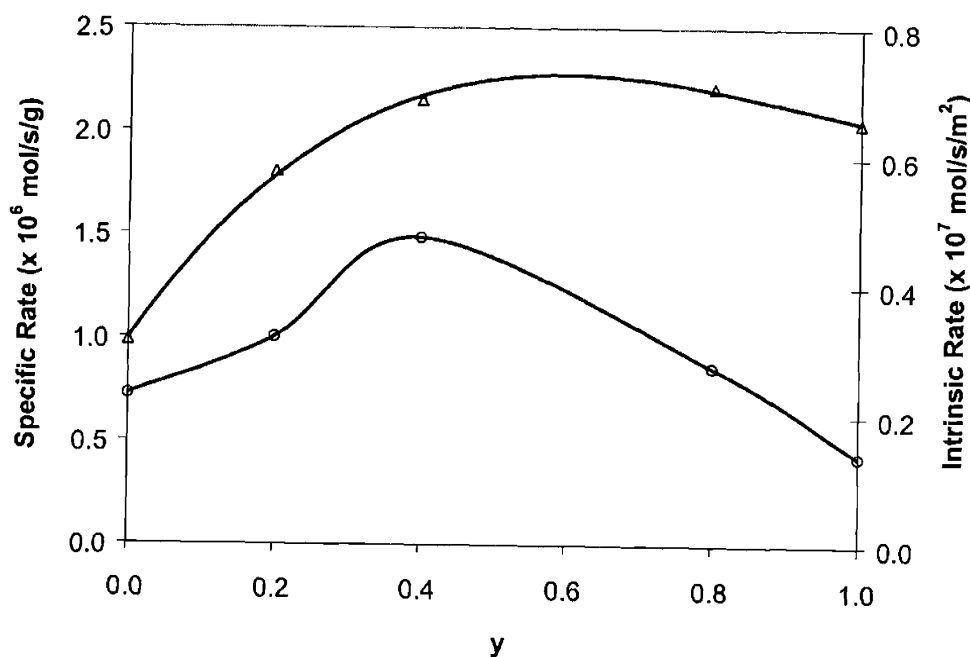**Figure 2.43.** (○) Specific and (△) intrinsic reaction rates of $LaMn_{1-y}Ni_yO_3$, after calcination at 800°C. Reaction rates were obtained under differential conversions at 390°C with 25 mg of catalyst, and a feed of 1% CH_4 in air at 60,000 $hour^{-1}$.

2.3.9 Temperature-Programmed Methane Oxidation over $La_{1-x}A_xMn_{1-y}B_yO_3$

The catalytic oxidation of CH_4 to CO_2 begins with the abstraction of hydrogen from methane, resulting in the formation of activated methane species. At temperatures $> 700°C$, these activated species desorb from the catalyst surface to produce gas-phase methyl radicals. The methyl radicals react with gas-phase oxygen or activated oxygen species on the catalyst surface, leading to the formation of CO_2. At high CH_4-to-O_2 ratios, collisions between methyl radicals may become likely, leading to the formation of ethane through oxidative coupling of methane. Since methane is a very stable molecule, hydrogen abstraction from methane is typically considered to be the rate-limiting step. The activity and selectivity of methane oxidation depend on the nature and amount of oxygen species on the catalyst surface [17-21].

At lower temperatures, the activated methane species may not desorb into the gas phase, but may further react with adsorbed oxygen species leading to carbonate formation. Subsequent desorption of carbonate and hydroxyl species from the catalyst surface regenerates the active site. Therefore, the catalytic mechanism of methane oxidation can be divided into three steps: (1) hydrogen abstraction from methane to form activated methane species, (2) oxidation of adsorbed methane species to surface carbonate, and (3) regeneration of active sites by carbonate and hydroxyl desorption, and oxygen adsorption. To study the individual steps involved in this mechanism, temperature-programmed reduction (TPR) of various perovskites was performed using methane. On heating the catalyst in the presence of methane, the temperature at which methane is activated to form an adsorbed methoxy species can be determined, which can be related to the intrinsic activity for hydrogen abstraction from methane. The desorption temperatures of H_2O and CO_2 indicate the stability of surface hydroxyl and carbonate species, and/or the kinetics of transformation of adsorbed methoxy species to surface carbonate and hydroxyl species.

Figure 2.44 shows methane TPR curves for $800°C$-calcined $LaMnO_3$. Methane activation was found to occur at $\sim 300°C$, with the simultaneous formation of CO_2. This suggested that conversion of adsorbed methoxy species to surface carbonate, and its subsequent desorption as CO_2 were fast reaction steps. Decomposition of surface hydroxyl groups to H_2O occurred at higher temperatures of $\sim 380°C$. Methane conversion was observed to increase at a faster rate on surface regeneration by water desorption, suggesting that hydroxyl decomposition might be partially rate-limiting at low temperatures.
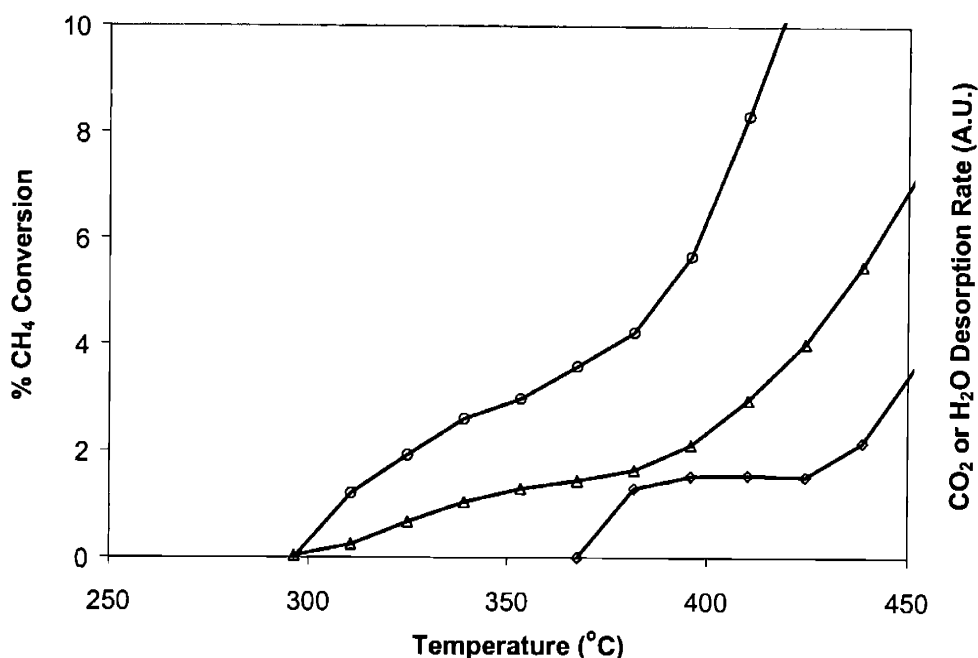
Figure 2.44. Methane TPR curves for $LaMnO_3$ showing (○) methane conversion, and formation rates of (△) CO_2 and (◇) H_2O.

Methane TPR curves for $La_{0.8}Ca_{0.2}MnO_3$ perovskite are presented in Figure 2.45. Activation of methane was found to occur at a lower temperature of ~ 250°C, indicating that substitution of Ca^{2+} for La^{3+} increased the intrinsic activity for hydrogen abstraction from methane. This was consistent with the observed increase in catalytic activity with 20% Ca substitution (Figure 2.19). Although methane activation occurred at low temperatures, CO_2 formation was not observed until ~ 310°C. This confirmed that methane chemisorbed on the catalyst surface as an activated species, in contrast to the Eley-Rideal mechanism applicable at higher temperatures. The observed temperature difference between methane adsorption and CO_2 desorption suggested that the overall reaction rate was partially controlled by the transformation kinetics of the activated methane species to surface carbonate and the subsequent CO_2 desorption. Compared to $LaMnO_3$, hydroxyl decomposition was initiated at a higher temperature of ~ 470°C.
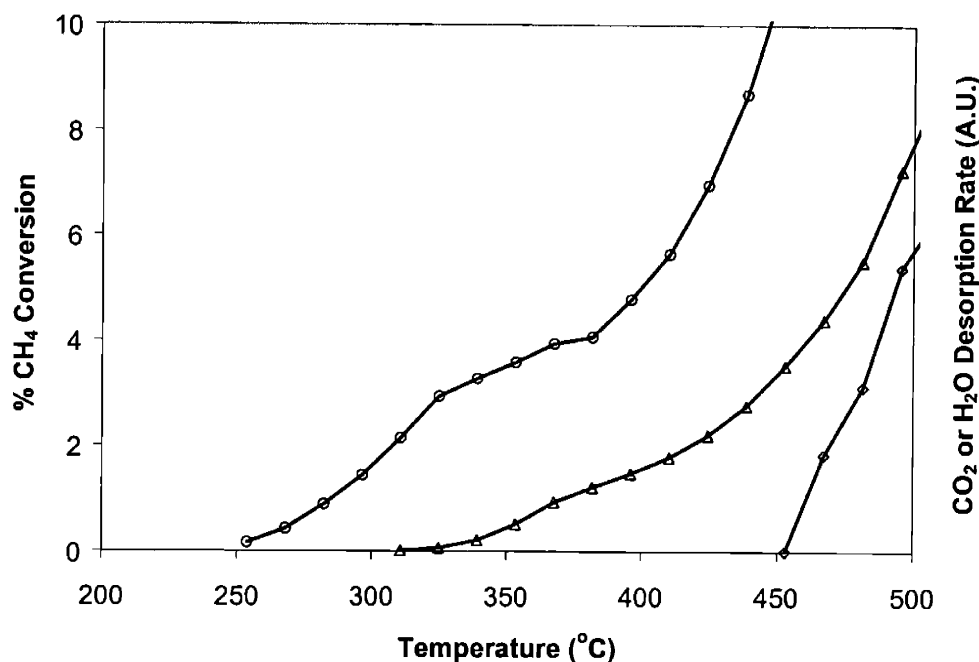
Figure 2.45. Methane TPR curves for $La_{0.8}Ca_{0.2}MnO_3$ showing (o) methane conversion, and formation rates of ($\triangle$) CO_2 and ($\diamond$) H_2O.

As seen from Figure 2.46, $La_{0.8}Ba_{0.2}MnO_3$ activated methane at an even lower temperature of ~ 210°C, indicating its high intrinsic activity for methane adsorption. The simultaneous evolution of water from the catalyst surface during methane adsorption confirmed that methane was adsorbed on the catalyst surface via hydrogen abstraction, resulting in the formation of methoxy and hydroxyl surface species. As basicity increased with A-site doping, the ability of the catalyst to abstract hydrogen from methane increased, hence lowering the temperature required for methane adsorption. Unlike $LaMnO_3$ and $La_{0.8}Ca_{0.2}MnO_3$ perovskites, $La_{0.8}Ba_{0.2}MnO_3$ showed hydroxyl decomposition at a very low temperature of ~ 210°C. Desorption of surface carbonates initiated at a higher temperature of ~ 380°C, consistent with the increased catalyst basicity. As surface sites were regenerated on carbonate removal, the rates of methane oxidation and water evolution were increased dramatically, suggesting that carbonate decomposition might be partially rate-limiting for strongly basic catalysts.
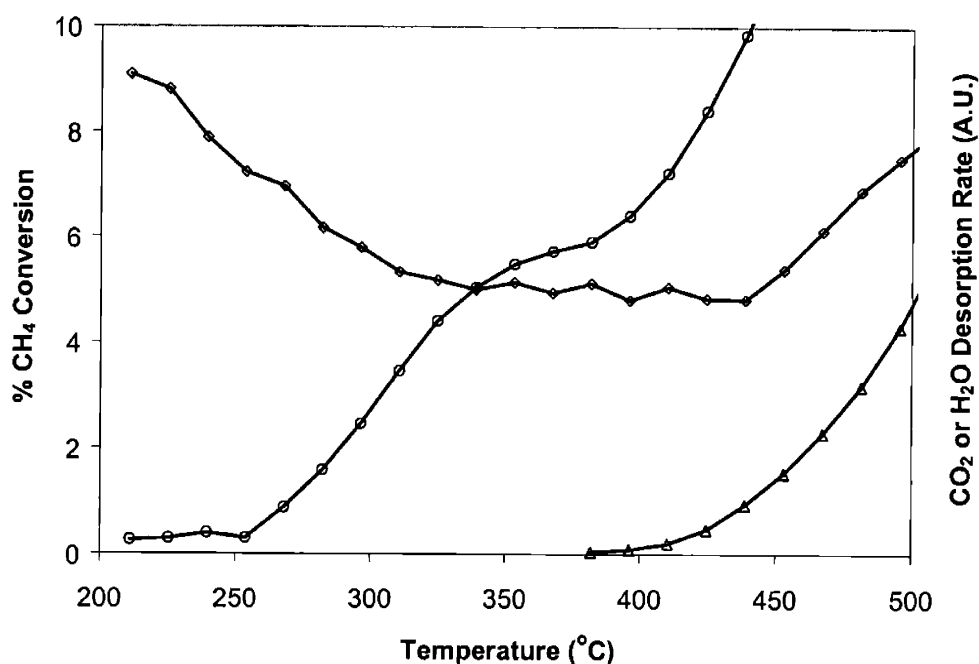
Figure 2.46. Methane TPR curves for $La_{0.8}Ba_{0.2}MnO_3$ showing (○) methane conversion, and formation rates of (△) CO_2 and (◇) H_2O.

Figure 2.47 shows an interesting trend between the ability of the catalyst to adsorb methane by hydrogen abstraction, and the relative stability of the generated carbonate species. As the temperature required for methane adsorption decreased, the carbonate decomposition temperature increased. For $La_{0.8}A_{0.2}MnO_3$, the intrinsic catalyst activity to adsorb methane and the stability of surface carbonate increased in the order: La < Sr < Ca < Ba. Figure 2.48 compares the amount of adsorbed carbon species, in the form of surface methoxy, formate or carbonate groups, for $La_{0.8}A_{0.2}MnO_3$. The surface coverage of these species increased in the order La ~ Sr < Ca < Ba, as expected based on the observed trend in methane activation and carbonate decomposition. Therefore, it could be concluded that increasing methane adsorption rate by increasing catalyst basicity adversely affected catalyst performance by increasing carbonate stability. Moreover, carbonate decomposition might be partially rate-limiting at high concentrations of Group IIA metals.
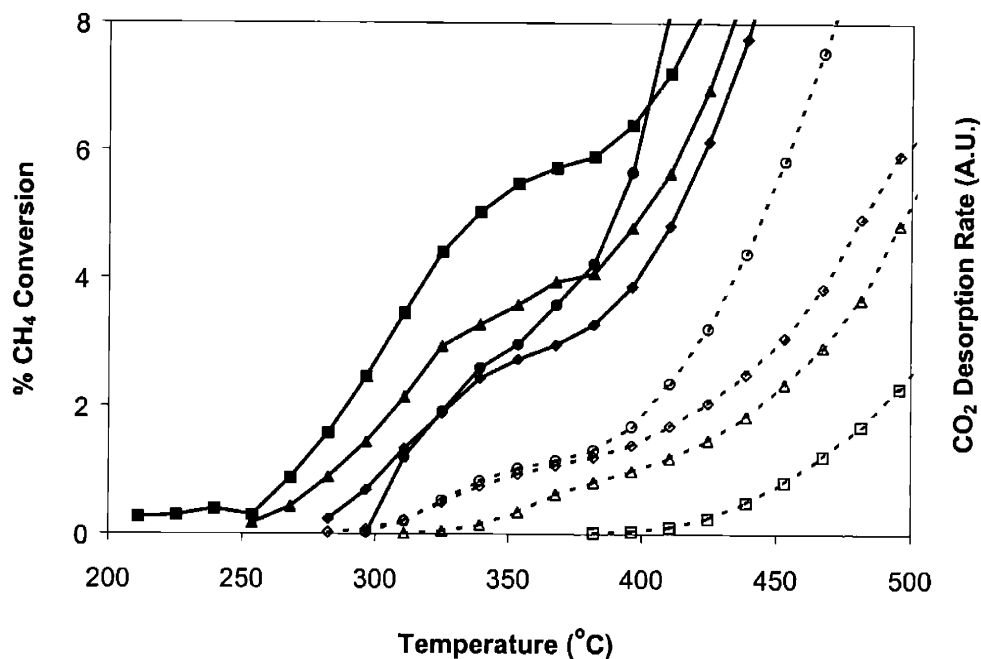
Figure 2.47. Methane TPR curves for $La_{0.8}A_{0.2}MnO_3$ showing methane conversion (closed symbols) and CO_2 formation rate (open symbols) for different A-site dopants: (•) La^{3+}, (♦) Sr^{2+}, (▲) Ca^{2+} and (■) Ba^{2+}.
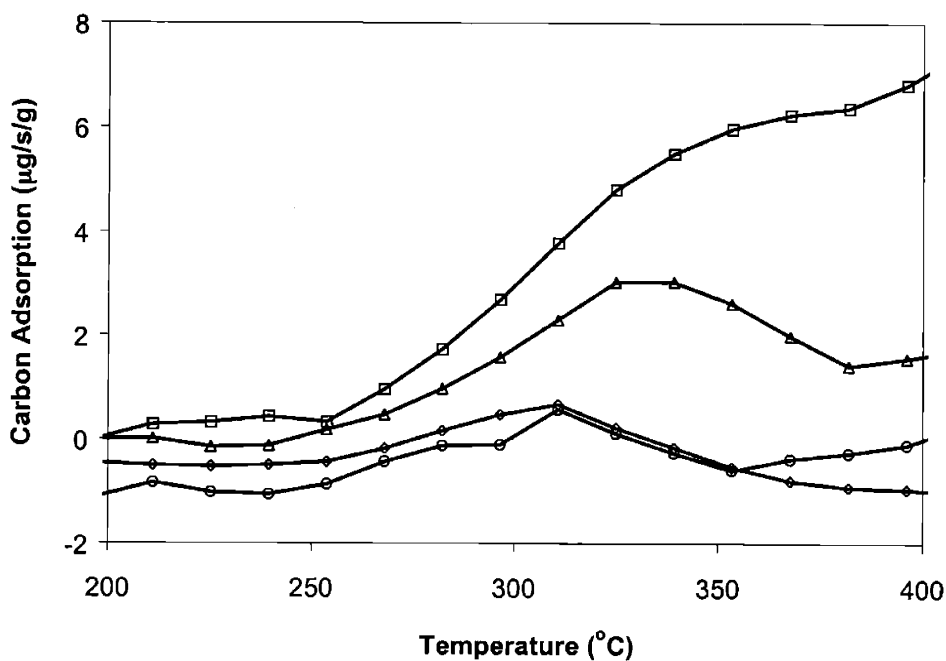
Figure 2.48. Adsorption of carbon species on $La_{0.8}A_{0.2}MnO_3$ perovskites for different A-site dopants: (○) La^{3+}, (◇) Sr^{2+}, (△) Ca^{2+} and (□) Ba^{2+}.

Figure 2.49 shows the effect of strontium concentration in La$_{1-x}$Sr$_x$MnO$_3$ on methane activation and carbonate decomposition. As catalyst basicity was increased with Sr doping, the temperature required for hydrogen abstraction from methane dramatically decreased, however the stability of the resulting carbonate species also increased and hence requiring higher decomposition temperatures. Substitution of Group IIA metals at the A site enhanced catalytic activity by increasing the rate of methane activation, but might lower activity at high dopant concentrations due to slow carbonate decomposition. This was consistent with the observed decrease in intrinsic catalytic activity at high Ca and Sr doping levels (Figure 2.33).
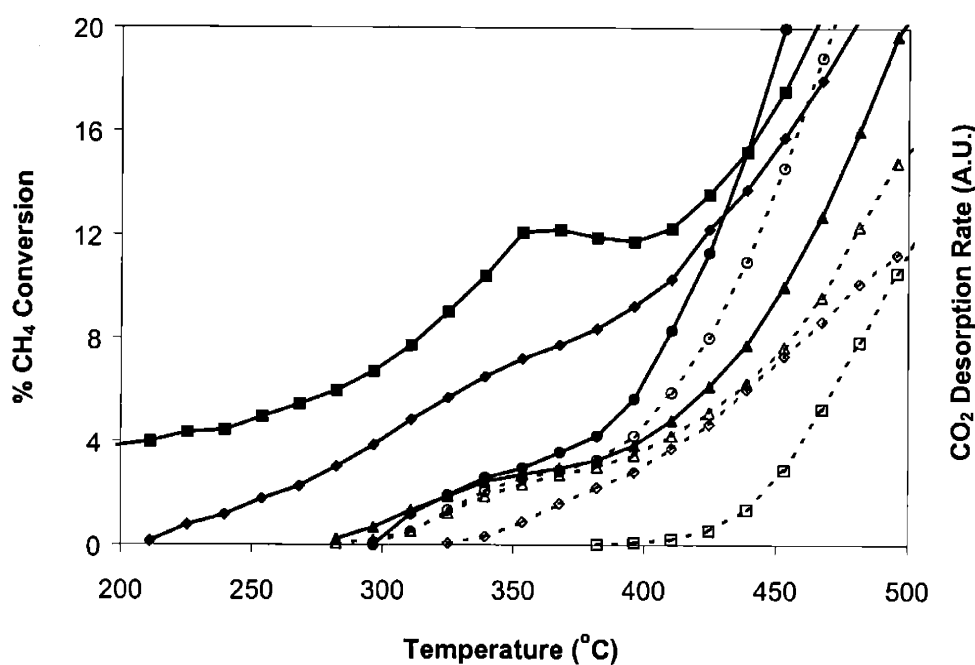
Figure 2.49. Methane TPR curves for La$_{1-x}$Sr$_x$MnO$_3$ showing methane conversion (closed symbols) and CO$_2$ formation rate (open symbols) for x = (●) 0.0, (▲) 0.2, (◆) 0.4 and (■) 0.6.

The activation of methane by hydrogen abstraction resulting in the formation of adsorbed methoxy and hydroxyl species was further confirmed by measuring changes in catalyst weight during methane TPR for several perovskite compositions (Figure 2.50). On heating the catalyst in the presence of methane, catalyst weight was found to increase due to methane adsorption, reaching a maximum, followed by a decrease due to hydroxyl and carbonate decomposition. Strontium substitution at the A site resulted in increased methane adsorption, and shifted the maximum in catalyst weight to higher temperature consistent with slow carbonate decomposition. Methane adsorption was also found to increase with nickel substitution at the B

site, consistent with the observed increase in catalytic activity (Figure 2.43). The measured change in catalyst weight was found to be in good agreement with the calculated weight change based on methane TPR experiments.
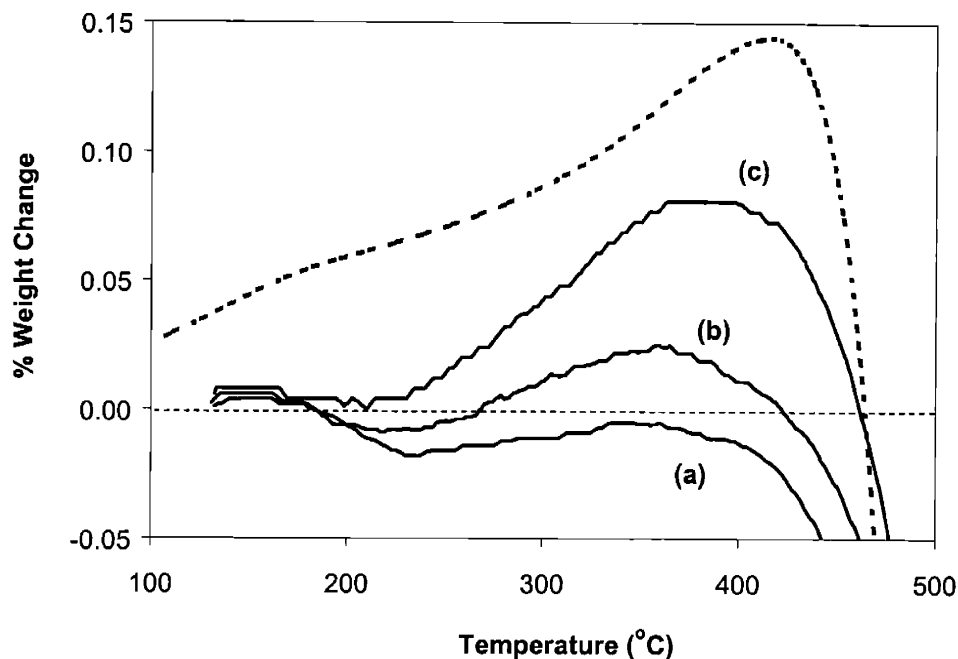
Figure 2.50. TGA profiles for (a) LaMnO$_3$, (b) LaMn$_{0.6}$Ni$_{0.4}$O$_3$, and (c) La$_{0.5}$Sr$_{0.5}$MnO$_3$ during methane TPR. Dashed line shows the calculated weight change for La$_{0.4}$Sr$_{0.6}$MnO$_3$ based on methane TPR data.

2.3.10 Kinetics and Mechanism of Methane Oxidation

The first step in investigating the catalytic mechanism of CH$_4$ oxidation over La$_{1-x}$A$_x$Mn$_{1-y}$B$_y$O$_3$ perovskites was to measure apparent kinetic rate orders for methane and oxygen, and their dependence on the A- and B-site composition. Methane TPR experiments suggested that methane was adsorbed on the catalyst surface via hydrogen abstraction, and was then oxidized to surface carbonate and hydroxyl species. At low oxygen partial pressures, the oxidation of adsorbed methoxy species or carbonate decomposition could be partially rate-controlling, resulting in significant carbon adsorption.

Table 2.9 shows the dependence of methane and oxygen rate orders on B-site transition metal in LaBO$_3$ perovskites under different reaction conditions. The rate order for methane deviated significantly from unity. This indicated that methane was chemisorbed on the catalyst surface, consistent with methane TPR experiments. The Eley-Rideal mechanism, generally

accepted for oxidative coupling of methane [17-19], was not applicable at lower temperatures where surface reactions predominated. Methane and oxygen rate orders were strongly dependent on B-site transition metal. The rate order for methane decreased in the order: Ni > Co > Fe > Mn, while the reverse trend was observed for oxygen rate order. Therefore, adsorption of methane on the catalyst surface, relative to oxygen, decreased in the order: Mn > Fe > Co > Ni. As the surface coverage of adsorbed methane species increased, the rate order for methane should decrease due to gradual saturation of active sites, while the oxygen rate order should increase. On increasing oxygen concentration from 2.5 to 21%, methane rate order was found to increase, since the relative surface coverage of adsorbed methane species decreased due to competitive oxygen adsorption. On raising temperature from 350°C to 400°C, methane rate order increased for Ni and Co-based perovskites, remained unchanged for $LaFeO_3$, and decreased for $LaMnO_3$. Increasing reaction temperature would increase the rate of methane activation and methoxy decomposition on the catalyst surface. Depending on their activation energies, the surface coverage of adsorbed methoxy species could increase or decrease. Moreover, temperature could affect the surface coverage of oxygen species by changing its dissociation equilibrium constant.

Table 2.9. Apparent kinetic rate orders of CH_4 and O_2 for methane oxidation over 800°C-calcined $LaBO_3$ perovskites.

B-Site Cation	CH_4 Rate Order			O_2 Rate Order
	350°C, 2.5% O_2	350°C, 21% O_2	400°C, 21% O_2	350°C, 2.5% CH_4
Ni	0.73	0.76	0.79	0.15
Co	0.72	0.76	0.79	0.19
Fe	0.68	0.74	0.74	0.20
Mn	0.66	0.72	0.60	0.20

The effect of Sr content on the kinetic rate orders for methane and oxygen over $La_{1-x}Sr_xMnO_3$ perovskites is shown in Table 2.10. On increasing Sr^{2+} doping, methane rate order initially decreased reaching a minimum at x ~ 0.4, suggesting increased methane adsorption on the catalyst surface. Partial replacement of La^{3+} by Sr^{2+} was found to increase catalytic activity for hydrogen abstraction from methane (Figure 2.49), which was consistent with the decrease in methane rate order. For x > 0.4, methane rate order was found to increase, indicating a decrease

88

in surface coverage of adsorbed methane. Since Sr^{2+} doping created oxygen vacancies, which might act as sites for oxygen chemisorption, the resulting increase in oxygen adsorption on the catalyst surface would increase the rate order for methane. Increasing the amount of adsorbed oxygen species by increasing the oxygen partial pressure resulted in a similar increase in methane rate order. Since adsorbed CH_4 and O_2 species were predominant under differential conditions, an increase in surface coverage of one species has a reciprocal effect on the other species. Therefore, changes in the rate orders of methane and oxygen were complementary.

Table 2.10. Effect of Sr^{2+} content on CH_4 and O_2 rate orders for methane oxidation over 800°C-calcined $La_{1-x}Sr_xMnO_3$ perovskites.

x	CH_4 Rate Order		O_2 Rate Order
	350°C, 2.5% O_2	350°C, 21% O_2	350°C, 2.5% CH_4
0.0	0.66	0.72	0.20
0.2	0.63	0.69	0.21
0.4	0.62	0.71	0.22
0.6	0.67	0.74	0.21
0.8	0.69	0.74	0.20
1.0	0.70	0.76	0.18

Table 2.11 shows the effect of nickel doping on the apparent rate orders for methane and oxygen over $LaMn_{1-y}Ni_yO_3$ perovskites. At low Ni contents, methane rate order decreased, indicating an increase in surface coverage of adsorbed methane species. TGA in the presence of methane shows greater methane adsorption on $LaMn_{0.6}Ni_{0.4}O_3$ than on $LaMnO_3$ (Figure 2.50). The substitution of Ni for Mn increased the catalyst ability to activate methane, hence increasing methane adsorption and catalytic activity (Figure 2.43). The surface coverage of adsorbed methane species reached a maximum at y ~ 0.4, and decreased with further nickel adidtion. Since nickel was more reducible than manganese, the increase in oxygen vacancy concentration might result in increased oxygen chemisorption at vacant sites. This increase in surface coverage of oxygen species would increase the rate order for methane.

A catalytic mechanism for methane oxidation over $La_{1-x}A_xMn_{1-y}B_yO_3$ perovskites was developed to explain the apparent rate orders for methane and oxygen by considering elementary reaction steps on the catalyst surface. To develop such a mechanism would require knowledge of

key elementary steps and their relative reaction rates, presence of adsorbed species on the catalyst surface, and apparent rate orders for reactant(s) and product(s). Moreover, the proposed catalytic mechanism must be consistent with experimental data, and satisfy any requirements from thermochemistry.

Table 2.11. Effect of nickel content on the apparent kinetic rate orders of CH_4 and O_2 for methane oxidation over 800°C-calcined $LaMn_{1-y}Ni_yO_3$ perovskites.

y	CH₄ Rate Order		O₂ Rate Order
	350°C, 2.5% O₂	350°C, 21% O₂	350°C, 2.5% CH₄
0.0	0.66	0.72	0.20
0.2	0.57	0.66	0.23
0.4	0.58	0.67	0.23
0.6	0.71	0.72	0.18
0.8	0.72	0.72	0.17
1.0	0.73	0.76	0.15

Based on the experimental rate orders for methane and oxygen and the TPR results, methane reacts with the catalyst surface via hydrogen abstraction, forming an adsorbed methoxy species. This elementary step is generally accepted to be rate-determining. It involves the reaction of gas-phase methane with two adsorbed oxygen species, resulting in the formation of adsorbed hydroxyl and methoxy species. Subsequent hydrogen abstractions and oxygen additions convert the adsorbed methoxy to a formate species, leading to the formation of surface carbonate. Since CH_4 has the highest C-H bond energy, activation energy barrier for hydrogen abstraction from methane is higher compared to subsequent hydrogen abstractions from adsorbed methane species. Besides methane, the catalyst surface has adsorbed oxygen, carbonate and hydroxyl species. Oxygen can adsorb on the catalyst surface in various forms (such as O_2^-, O^-, and O^{2-}) with different heats of adsorption. Based on the oxidative coupling of methane literature [17-21], dissociated oxygen species (O^- and O^{2-}) are primarily responsible for methane activation. Although weakly adsorbed oxygen species (such as O_2^-) may be present on the catalyst surface especially at lower temperatures, they do not participate in hydrogen abstraction from methane. However, they may be involved in subsequent transformations of adsorbed

methoxy to surface carbonate. Since the oxygen exchange rates are much higher than the rate of methane activation, the catalyst surface is assumed to be in equilibrium with gas-phase oxygen.

Based on the above arguments, kinetic expression for methane oxidation over $La_{1-x}A_xMn_{1-y}B_yO_3$ perovskites can be developed by considering the following key elementary steps:

$$CH_4 + 2O* \xrightarrow{k_1} CH_3O* + *OH \tag{2.1}$$

$$CH_3O* + 5O* \xrightarrow{k_2} \longrightarrow *CO_3 + 3*OH + 2* \tag{2.2}$$

$$\frac{1}{2}O_2 + * \underset{\xrightarrow{k_3}}{\longleftarrow} O* \tag{2.3}$$

$$*CO_3 \underset{\xrightarrow{k_4}}{\longleftarrow} CO_2 + O* \tag{2.4}$$

$$2*OH \underset{\xrightarrow{k_5}}{\longleftarrow} H_2O + O* + * \tag{2.5}$$
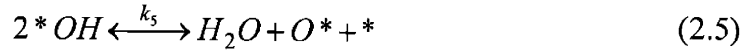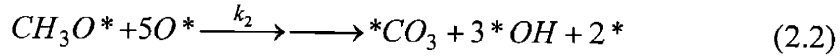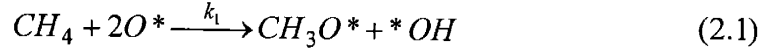
Under differential conditions, the surface coverage of carbonate and hydroxyl species can be neglected. Assuming pseudo- steady state for the concentration of adsorbed methane species, the following rate expression for methane oxidation can be derived,

$$r = \frac{K_3^2 k_1 [CH_4][O_2]}{\left(1 + K_3[O_2]^{1/2} + \dfrac{k_1}{k_2} K_3 [CH_4][O_2]^{1/2}\right)^2} \tag{2.6}$$

where k_1 and k_2 are rate constants for methane activation and subsequent conversion of adsorbed methoxy species to surface carbonate, respectively, and K_3 is the equilibrium constant for oxygen adsorption. These kinetic parameters were obtained by non-linear regression of experimental rate data over a wide range of CH_4 and O_2 concentrations. Figure 2.51 compares the model and experimental reaction rates for $LaMnO_3$ at 350°C, after regression of the kinetic parameters. The proposed mechanism and kinetic expression are consistent with the experimental rate data.
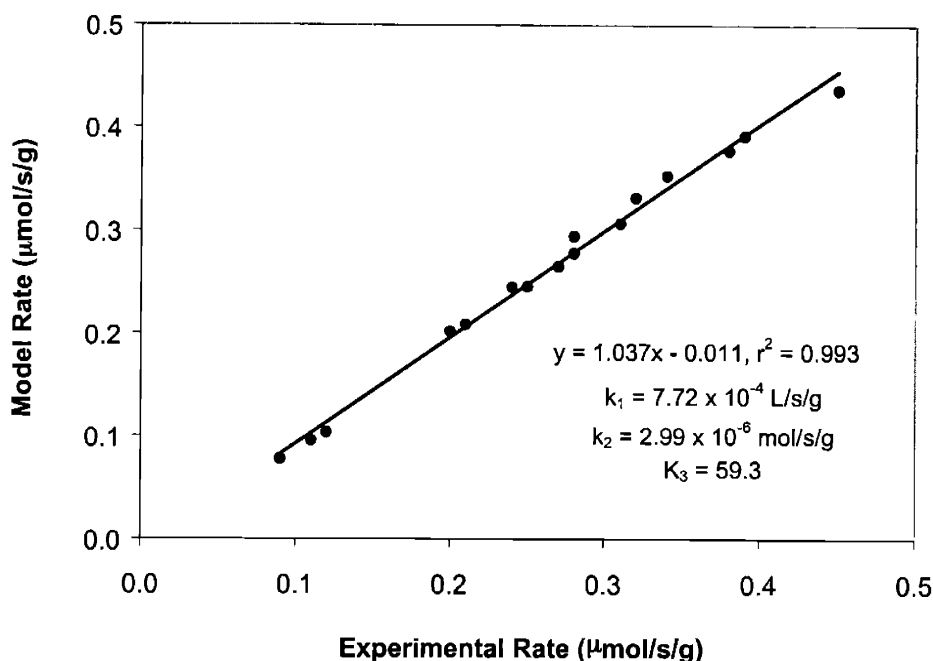
Figure 2.51. Comparison of model and measured rates of methane oxidation over 800°C-calcined LaMnO₃ at 350°C.

Since the kinetic parameters for key elementary steps can be determined, it is interesting to investigate the effect of perovskite composition on these parameters, so as to understand the relationship between composition and elementary surface reactions. Figure 2.52 shows the effect of B-site transition metal in $LaBO_3$ perovskites on the equilibrium constant for oxygen dissociation (K_3). Oxygen dissociation constant was found to increase in the order: Mn < Fe < Co < Ni, indicating an increase in the amount of adsorbed oxygen species, consistent with the observed decrease in the rate order for oxygen in Table 2.9. $LaNiO_3$ has the highest activity to dissociate molecular oxygen and form adsorbed oxygen species on catalyst surface. The increase in oxygen adsorption on the catalyst surface seemed to correlate with the material's bulk reducibility. Since oxygen vacancies might serve as sites for oxygen chemisorption, an increase in oxygen vacancy concentration with catalyst reducibility would be expected to increase oxygen chemisorption.
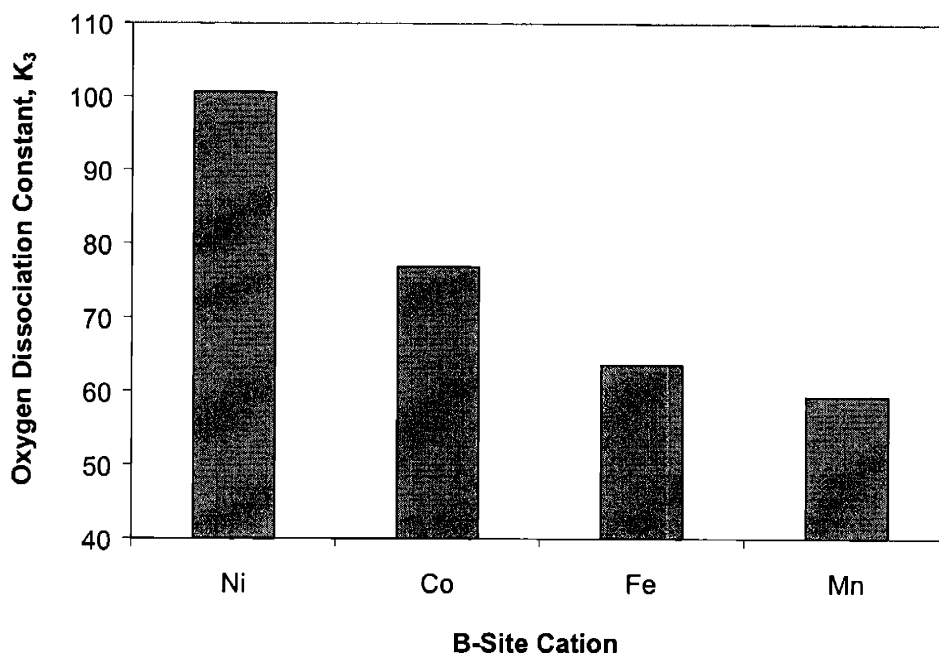
Figure 2.52. Effect of B-site transition metal in $LaBO_3$ on the oxygen dissociation equilibrium constant (K_3) at 350°C.

Temperature-programmed desorption (TPD) of oxygen was performed on $LaBO_3$ perovskites to determine the amount and nature of adsorbed oxygen species on their surfaces (Figure 2.53). Chemisorbed oxygen species would desorb at 100-500°C, while strongly-bound lattice oxygen would be removed at temperatures > 500°C. Figure 2.53 shows that the amount of adsorbed oxygen species on $LaBO_3$ was strongly dependent on the B-site transition metal, and increased in the order: $Mn \sim Fe < Co < Ni$. This increase in the amount of adsorbed oxygen species was consistent with the increase in the equilibrium constant for oxygen dissociation, further providing validity to the proposed catalytic mechanism.

Figure 2.54 shows the dependence of specific rate constants for methane activation and methoxy decomposition on the Sr content in $La_{1-x}Sr_xMnO_3$. These rate constants were found to increase with Sr^{2+} doping until $x \sim 0.6$. This was consistent with methane TPR results, which showed that substitution of Group IIA metals increased the activity for hydrogen abstraction from CH_4. Since elementary steps (2.1) and (2.2) both involved hydrogen abstraction, it was not surprising that k_1 and k_2 demonstrated similar trends. The surface coverage of carbonate species and their decomposition kinetics might not be negligible at high strontium contents, and should be incorporated into the catalytic mechanism.
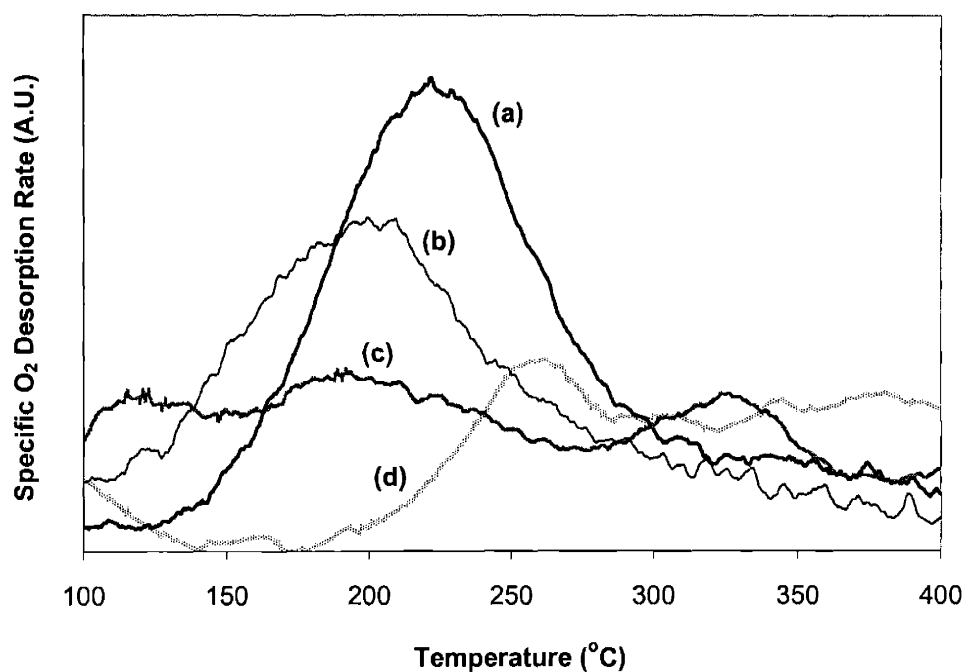
Figure 2.53. Oxygen TPD curves for $LaBO_3$ perovskites with different B-site cations: (a) Ni, (b) Co, (c) Fe and (d) Mn.
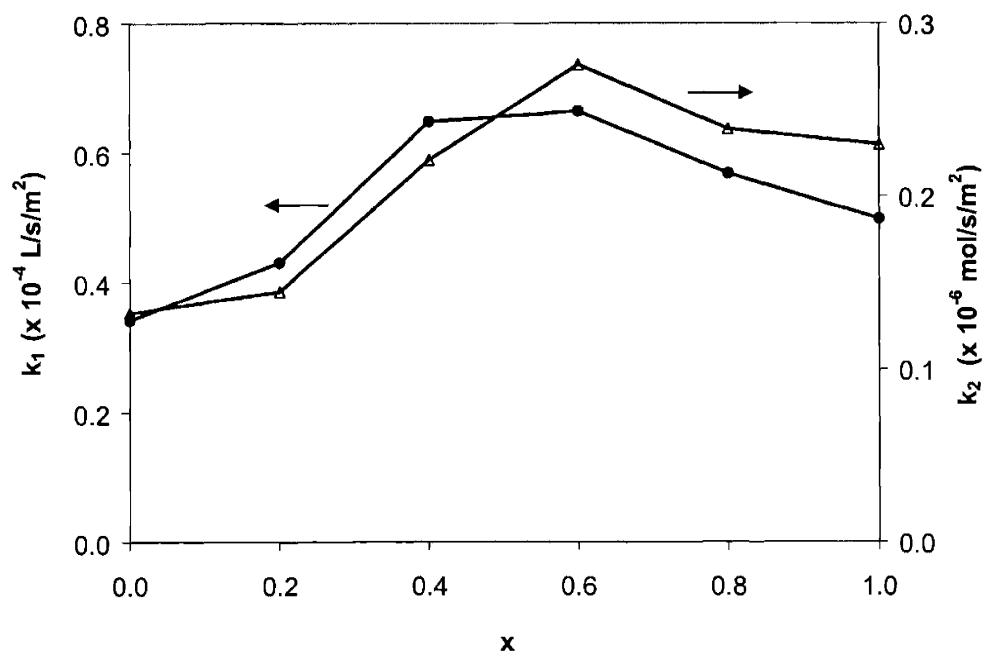
Figure 2.54. Effect of Sr^{2+} content in $La_{1-x}Sr_xMnO_3$ on the rate constants for (•) methane activation (k_1) and ($\triangle$) methoxy decomposition (k_2) at $350^{\circ}C$.

Figure 2.55 shows the effect of Sr^{2+} doping in $La_{1-x}Sr_xMnO_3$ on the equilibrium constant for oxygen dissociation (K_3), and the specific amount of adsorbed oxygen species measured with oxygen TPD. At low Sr^{2+} contents, the amount of adsorbed oxygen species decreased with x, consistent with a decrease in oxygen dissociation constant. According to Berenov et al. [22], oxygen vacancy concentration in $La_{1-x}Sr_xMnO_3$ decreased at low Sr^{2+} contents, reaching a minimum at x ~ 0.25, followed by an increase for x > 0.25. Since oxygen vacancies on the catalyst surface were necessary for oxygen chemisorption, this explained the observed decrease in adsorbed oxygen species. For $0.4 \leq x \leq 0.6$, both the amount and the dissociation constant of adsorbed oxygen species increased, consistent with increasing oxygen vacancy concentration. For x > 0.6, phase transformation from perovskite to the vacancy-ordered hexagonal phase (Figure 2.23) gave rise to a decrease in the amount of adsorbed oxygen species with x.
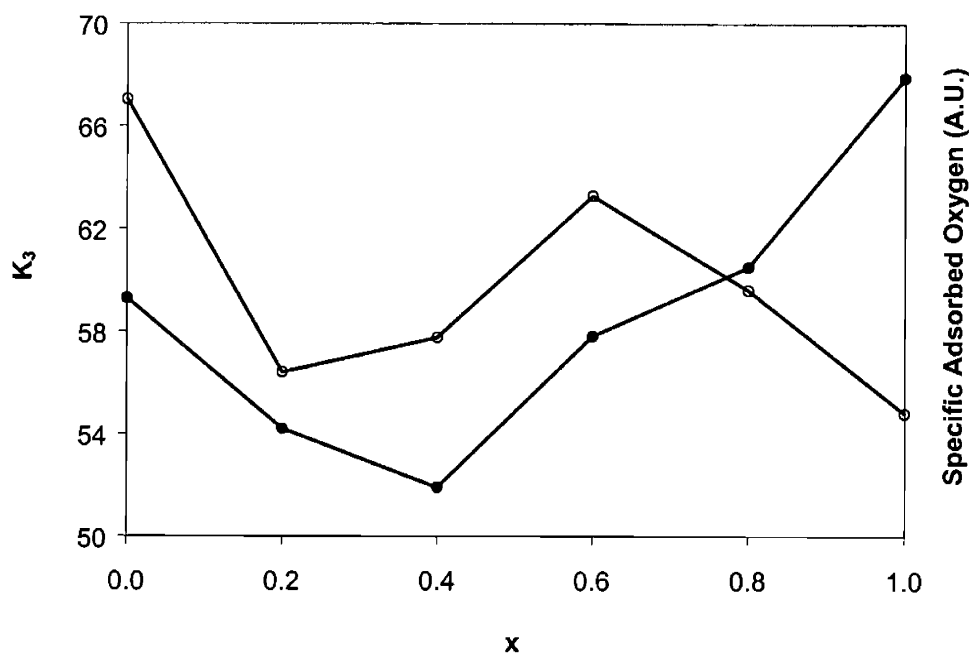
Figure 2.55. Effect of Sr^{2+} content in $La_{1-x}Sr_xMnO_3$ on (•) the equilibrium constant for oxygen dissociation (K_3) at 350°C, and (○) the specific amount of adsorbed oxygen species.

The dependence of k_1, k_2 and K_3 on the B-site composition in $LaMn_{1-y}Ni_yO_3$ perovskites is shown in Figure 2.56. The rate constant for methane activation (k_1) dramatically increased with nickel substitution, reaching a maximum at y = 0.4. This was consistent with methane TPR results that showed greater methane adsorption with nickel substitution (Figure 2.50), resulting in higher intrinsic catalytic activity (Figure 2.43). The rate constant for methoxy decomposition

(k_2) on the catalyst surface showed a similar trend with nickel concentration, but the changes in its magnitude were relatively small. The equilibrium constant for oxygen dissociation (K_3) decreased initially with nickel doping, followed by an increase at $y > 0.4$. The rate constant for methane activation was not directly related to the equilibrium constant for oxygen dissociation. Increasing the amount of adsorbed oxygen did not necessarily result in a higher rate of methane activation. The nature of the adsorbed oxygen species might be more important in determining the methane activation rates.
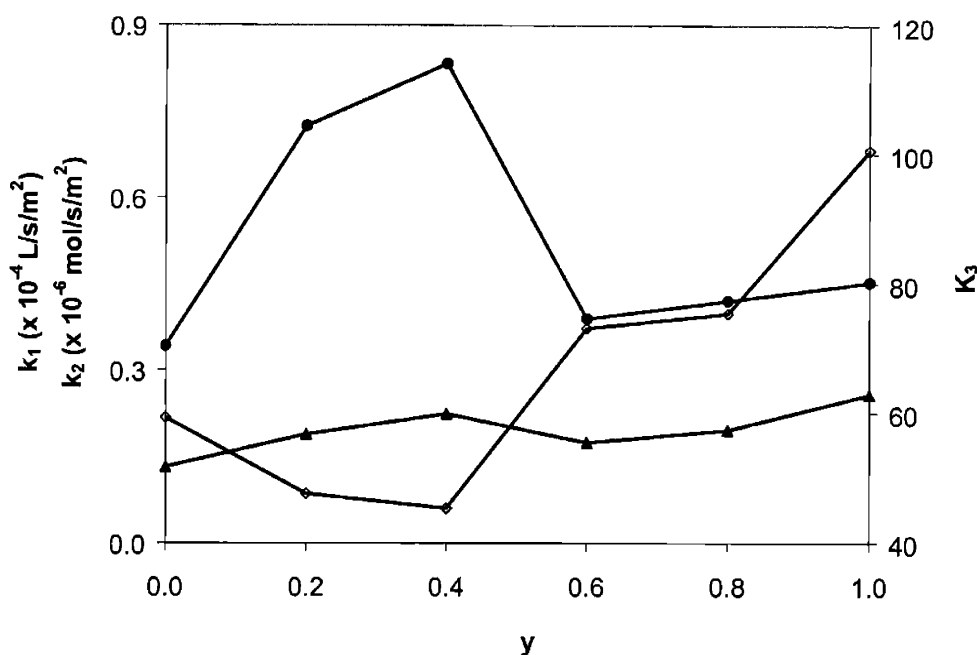
Figure 2.56. Effect of Ni content in $LaMn_{1-y}Ni_yO_3$ on (●) k_1, (▲) k_2, and (◇) the equilibrium constant for oxygen dissociation (K_3) at 350°C.

An interesting relationship existed between the equilibrium constant for oxygen dissociation (K_3), and the ratio of the rate constants for methane activation and methoxy decomposition (k_1/k_2) (see Figure 2.57). As the oxygen dissociation constant increased (indicating an increase in the amount of adsorbed oxygen), the ratio of the rate constants decreased, suggesting that the rate constant for methoxy decomposition increased relative to that for methane activation. Among $LaBO_3$ perovskites, the rate constant for methoxy decomposition (relative to methane activation) decreased in the order: Ni > Co > Fe > Mn (Figure 2.57), which was consistent with their catalytic activity for methanol oxidation [23].
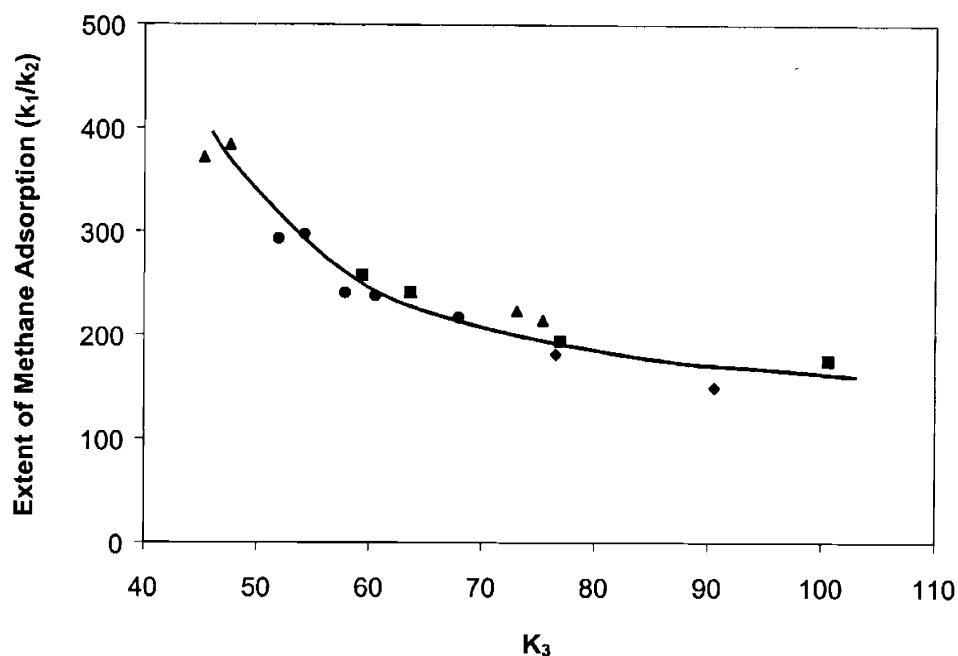
Figure 2.57. Relationship between the extent of methane adsorption (k_1/k_2) and the equilibrium constant for oxygen dissociation (K_3) for various $La_{1-x}A_xMn_{1-y}B_yO_3$ perovskites: (■) $LaBO_3$, (▲) $LaMn_{1-y}Ni_yO_3$, (●) $La_{1-x}Sr_xMnO_3$ and (◆) $La_{1-x}Sr_xCoO_3$.

2.4 Conclusions

Multicomponent, nanocrystalline perovskites were synthesized with ultrafine grain sizes and high surface areas using reverse-strike co-precipitation synthesis. Compared to solid-state and combustion syntheses, chemical co-precipitation produced $La_{0.5}Sr_{0.5}MnO_3$ with smaller grain sizes and superior surface areas, resulting in improved catalytic performance. The choice of solvent, base and suspension pH in co-precipitation was found to strongly affect the chemical stoichiometry of the resulting material. Stoichiometric $La_{0.5}Sr_{0.5}MnO_3$ was successfully obtained at a high pH using isopropanol as the solvent, and tetraethylammonium hydroxide as the base. Intimate mixing of various metal cations during precipitation resulted in the formation of a phase-pure perovskite at a low crystallization temperature of ~ 600°C. $La_{0.5}Sr_{0.5}MnO_3$ was derived with a ultrafine grain size of 13 nm and a high surface area of 43 m^2/g at 650°C, and maintained its nanocrystalline microstructure on heating to 1000°C, with a grain size of 25 nm and a surface area of 19 m^2/g. In contrast, combustion synthesis produced $La_{0.5}Sr_{0.5}MnO_3$ particles of 17 nm and 14 m^2/g, respectively, at 800°C.

The degree of particle agglomeration and surface area of $LaBO_3$ perovskites were found to depend greatly on the acid-base properties of the precipitated hydrogels. As the basicity of the hydrogel increased, the surface charge on the precipitated particles decreased in the order: Mn > Fe > Co > Ni, resulting in increased agglomeration and lower surface areas. The extent of hydroxide condensation to form M-O-M linkages in the precipitate decreased with increasing basicity. Higher hydroxyl concentration and greater agglomeration of precipitated particles in $LaNi(OH)_x$ hydrogel led to the formation of large particles with strong interparticle bonding on calcination. Since the differences in the surface charge of $LaBO_3$ precipitates arose during the washing steps, further improvements in surface area could be achieved by modifying post-precipitation steps instead of varying precipitation conditions. The catalytic activity of $LaBO_3$ perovskites was found to decrease in the order: Mn > Fe ~ Ni > Co, with $LaMnO_3$ showing the lowest light-off temperature of $420^{\circ}C$. The intrinsic catalytic activity at $650^{\circ}C$ decreased in the order: Ni > Co > Fe > Mn, with $LaNiO_3$ showing the highest specific reaction rates.

Since $LaMnO_3$ showed the highest activity for methane oxidation, several dopants were introduced at the A site to investigate their effect on the crystal structure, powder morphology and catalyst activity. Substitution of Group IIA metals for La^{3+} was found to increase reaction rate, while higher valency dopants did not change or decreased catalyst activity. Group IIA metal doping could generate oxygen vacancies on the catalyst surface, resulting in increased oxygen adsorption; their greater basicity could increase the rate of methane activation, resulting in increased methane adsorption. In the case of Ca^{2+} and Sr^{2+}, intrinsic activity of $La_{1-x}A_xMnO_3$ was found to increase with dopant content until x = 0.4 and 0.6, respectively. $La_{0.4}Sr_{0.6}MnO_3$ exhibited the lowest light-off temperature of $380^{\circ}C$, with a reaction rate that was 2.5 times higher than $LaMnO_3$. The degree of particle agglomeration in $La_{0.4}A_{0.6}MnO_3$ perovskites was found to depend greatly on the A-site dopant. Ca-doped perovskites showed the highest degree of particle agglomeration and lower surface areas, since the precipitate particles possessed the lowest surface charge. Although phase transformation from cubic perovskite to hexagonal structure was observed with increasing Sr^{2+} and Ba^{2+} doping, changes in their intrinsic activity did not correlate with phase boundaries, suggesting that both crystal structures were catalytically active for methane oxidation. Substitution of Sr^{2+} for La^{3+} resulted in a small increase in intrinsic activity in $La_{1-x}Sr_xCoO_3$ perovskite at x ~ 0.2, but decreased intrinsic activity in $La_{1-x}Sr_xNiO_3$. Stability of the perovskite phase with increasing Sr^{2+} concentration depended greatly on the B-

site cation, and decreased in the order: Mn > Co > Ni. The decomposition of Ni-based perovskite to form less active, segregated NiO and $SrCO_3$ phases might explain the decrease in intrinsic activity with Sr^{2+} doping.

Apart from A-site modification, the catalytic activity of $LaMnO_3$ could also be increased by nickel substitution at the B site. With $LaMn_{0.6}Ni_{0.4}O_3$, the light-off temperature was decreased to 390°C, with a two-fold increase in reaction rate compared to $LaMnO_3$. Intrinsic catalytic activity did not vary linearly between the pure Mn and Ni end-points, as would be expected for a physical mixture of $LaMnO_3$ and $LaNiO_3$. Rather, an intermediate Ni content was optimal for $LaMn_{1-y}Ni_yO_3$ catalytic performance, suggesting a synergistic interaction between Ni and Mn.

Methane TPR experiments showed that methane oxidation over the perovskites occurred by methane adsorption on the catalyst surface via hydrogen abstraction. Substitution of Group IIA metals for La^{3+} enhanced catalytic activity by increasing the rate of methane activation, but lowered activity at high doping levels due to slow carbonate decomposition. For $La_{0.8}A_{0.2}MnO_3$, the intrinsic catalyst activity to adsorb methane and the stability of the resulting carbonate increased in the order: La < Sr < Ca < Ba. The rate order for methane deviated significantly from unity, confirming the adsorption of methane on the catalyst surface.

Rate orders for methane and oxygen were found to strongly depend on A- and B-site composition. For $LaBO_3$, the rate order for methane decreased in the order: Ni > Co > Fe > Mn, indicating a decrease in the relative surface coverage of oxygen. Substitution of Sr^{2+} in $La_{1-x}Sr_xMnO_3$ resulted in an initial decrease in the methane rate order, consistent with increased methane adsorption due to faster rate of methane activation. However, at higher Sr^{2+} contents, the surface coverage of adsorbed oxygen would increase due to the formation of surface oxygen vacancies, resulting in an increase in methane rate order. Substitution of nickel in $LaMn_{1-y}Ni_yO_3$ led to an initial decrease in methane rate order due to an increase in surface coverage of adsorbed methane, which was verified by TGA under methane TPR conditions. A catalytic mechanism for methane oxidation over $La_{1-x}A_xMn_{1-y}B_yO_3$ perovskites was developed, and shown to be consistent with reaction rate and oxygen TPD data.

2.5 References

[1]   Ciuparu, D., Katsikis, N., Pfefferle, L., *Appl. Catal. A: Gen.* **216**, 209 (2001).

[2]   Zarur, A.J., Ying, J.Y., *Nature* **403**, 65 (2000).

[3]   Gleiter, H., *Prog. Mater. Sci.* **33**, 223 (1989).

[4]   Siegel, R.W., *Annu. Rev. Mater. Sci.* **21**, 559 (1991).

[5]   Ying, J.Y., *J. Aerosol Sci.* **24**, 315 (1993).

[6]   Zhang, H.-M., Teraoka, Y., Yamazoe, N., *Chem. Lett.* 665 (1987).

[7]   Ng, M.F., Reichert, T.L., Schwartz, R.W., Collins, J.P., *Proceedings of the 4th International Conference on Inorganic Membranes*, Gatinburg, TN, July 1996.

[8]   Pechini, M.P., U.S. Patent 3,330,697 (1967).

[9]   Chick, L.A., Maupin, G.D., Graff, G.I., Pedersen, L.R., McCready, D.E., Bates, J.L., *Mater. Res. Soc. Symp. Proc.* **249**, 159 (1992).

[10]   Chick, L.A., Pedersen, L.R., Maupin, G.D., Bates, J.L., *Mater. Lett.* **10**, 6 (1990).

[11]   Sangar, N., Chakravorty, R., Ying, J.Y., to be submitted to *Chem. Mater.*

[12]   Shannon, R.D., *Acta Crystall.* **A32**, 751 (1976).

[13]   Tofield, B.C., Scott, W.R., *J. Solid State Chem.* **10**, 183 (1974).

[14]   Sangar, N., Ying, J.Y., to be submitted to *J. Catal.*

[15]   Bouwmeester, H.J.M., Burggraaf, A.J., "The CRC Handbook of Solid State Electrochemistry," (P.J. Gellings and H.J.M. Bouwmeester, Eds.), p. 481. CRC Press, New York, 1996.

[16]   Tejuca, L.G., Fierro, J.L.G., Tascon, J.M.D., *Adv. Catal.* **36**, 237 (1989).

[17]   Dubois, J.-L., Cameron, C.J., *Appl. Catal.* **67**, 49 (1990).

[18]   Lunsford, J.H., "Natural Gas Conversion II," (H.E. Curry-Hyde and R.F. Howe, Eds.), p. 1. Elsevier, Netherlands, 1994.

[19]   Lunsford, J.H., "Handbook of Heterogeneous Catalysis," (G. Ertl, H. Knozinger, J. Weitkamp, Eds.), p. 1843. VCH, Weinheim, 1997.

[20]   Baerns, M., Ross, J.R.H., "Perspectives in Catalysis," (J.M. Thomas and K.I. Zamaraev, Eds.), p. 315. Blackwell Scientific Publishing, London, 1992.

[21]   Bielanski, A., Haber, J., "Oxygen in Catalysis." Marcel Dekker, New York, 1991.

[22]   Berenov, A.V., MacManus, J.L., Kilner, J.A., *Solid State Ionics* **122**, 41 (1999).

[23]   Weiss, S.E., Ying, J.Y., M.I.T., unpublished results.

3 – Mixed Conducting $Ba_{1-x}Sr_xCo_{1-y}M_yO_3$ Perovskites for Oxygen Separation

3.1 Introduction

Multicomponent perovskites possessing high oxide and electronic conductivity are attractive for oxygen separation applications. As ceramic membranes, they can be utilized as an alternative to cryogenic distillation or pressure-swing adsorption technologies for oxygen production. These materials can also be used in membrane reactors to accomplish oxygen separation and selective hydrocarbon oxidation simultaneously. Researchers have recently investigated perovskite-based and fluorite-based ceramic membranes for oxidative reforming of methane to syngas [1-3] and oxidative coupling of methane to C2 hydrocarbons [4-9]. These membranes deliver a controlled oxygen flux to an active catalytic surface, which performs selective hydrocarbon oxidation. Selectivities achieved in the membrane reactors are typically higher than those obtained in conventional co-feed reactors, since non-selective, gas-phase reactions are minimized and oxygen can be supplied to the catalyst in the form of selective O^{2-} ions. The ceramic membranes are also attractive for zero-emission catalytic combustion technology, where the exclusion of nitrogen from the combustion feedstream results in no NO_x emissions in the effluent stream, and allows for the easy separation of combustion products (CO_2 and H_2O) for storage. The "zero" emission of CO_2 and NO_x makes this technology very attractive, as environmental regulations on greenhouse gases and pollutants have become increasingly stringent.

The primary challenge in the application of ceramic membranes for oxygen delivery is to develop novel materials and processing techniques to achieve high and stable oxygen fluxes in the desired temperature range of 650-950°C. Increasing oxygen flux through these membranes would decrease the required exchange area needed to produce a specified oxygen flow rate, thereby decreasing capital and operating costs. Moreover, high stability of the oxygen flux is desired to increase membrane lifetime and decrease process downtime from membrane regeneration.

The focus of this study is to develop novel perovskite-based membranes with the following objectives: (1) increase the oxygen flux by increasing the intrinsic oxide-ion conductivity, (2) lower the operating temperature range to 750-850°C, which is critical for many partial oxidation reactions, (3) improve the structural and chemical stability of these membranes,

(4) develop compositions with fast oxygen adsorption and desorption kinetics, (5) achieve high electronic conductivity so that electronic conduction is not the rate-limiting step, and (6) develop novel techniques to process micron-thick films without microstructural defects that may reduce separation selectivity.

Several researchers have investigated the oxygen permeation through perovskite-based membranes. Teraoka $et\ al.$ [10-13] investigated the crystal structure and oxide conductivity of $SrCo_{0.8}Fe_{0.2}O_3$ perovskite, which exhibits one of the highest reported oxygen fluxes. At an oxygen gradient of 21% to 1.5%, a 0.8 mm-thick $SrCo_{0.8}Fe_{0.2}O_3$ membrane exhibits an oxygen flux of ~ 1.9 cm^3[STP]/min/cm^2 at 900°C. Several researchers [10-16] have also investigated the oxide conductivity of various doped-lanthanum cobalites ($La_{1-x}A_xCo_{1-y}B_yO_3$: A = Sr, Ca and Ba; B = Fe, Ti, Cr, Al and Cu). These perovskites have oxygen fluxes of 0.3-1.5 cm^3[STP]/min/cm^2 at 900°C, depending on the choice and concentration of A- and B-site dopants. Iwahara $et\ al.$ [17] were the first to develop a mixed oxide-electronic conductor ($BaTi_{1-x}Fe_xO_3$) for oxygen separation. These perovskites have very low oxygen fluxes, typically < 0.1 cm^3[STP]/min/cm^2 at 900°C, due to their low oxygen vacancy concentration and limited electronic conductivity. The objective of this study is to develop novel perovskite membranes with oxygen fluxes exceeding 2.0 cm^3[STP]/min/cm^2 at 900°C, while maintaining stability at a low operating temperature of 750°C. This would address the key bottleneck facing the commercial application of this technology for oxygen separation, and would represent a significant improvement over the current state-of-the-art ceramic membranes.

The oxygen fluxes reported for these perovskites were all measured using the procedures outlined in Section 3.2.1. This allows comparison of the oxygen fluxes obtained for novel perovskite compositions developed in this study with those for conventional materials. This is important because oxygen fluxes reported in the literature for certain similar compositions vary considerably due to differences in membrane synthesis, processing and measurement procedures, etc.

A common problem faced by perovskite compositions is the occurrence of a phase transformation from a highly conductive, vacancy disordered perovskite to a poorly conductive, vacancy ordered structure. Such a phase transition is thermodynamically favored at low temperatures, where the energetically favored ordering of vacancies outweighs the entropically favored random arrangement of vacancies. Such an order-disorder transition is generally

observed at high oxygen vacancy concentrations, whereby vacancies can associate to form complex ordered structures. Oxygen vacancies may exhibit long-range ordering, which can be easily detected by X-ray diffraction (XRD), or short-range ordering to form small ordered domains, which cannot be easily detected by standard diffraction or thermal analysis techniques. It is therefore important to measure the time-dependence of oxygen flux to determine if the oxygen vacancies slowly associate to form ordered domains, which would gradually decrease the oxygen flux. For $SrCoO_{2.5}$, this order-disorder transition occurs at ~930°C, resulting in poor oxygen fluxes below 930°C [18]. A number of researchers have successfully stabilized $SrCoO_{2.5}$ by partially substituting Co^{3+} with Fe^{3+}, Ti^{4+} or Cr^{4+} at the B site [18-20].

The focus of this study is to manipulate the composition of $BaCoO_3$-based perovskites to eliminate the undesired phase transformation. By employing Ba instead of Sr at the A site, the oxygen flux may be increased through lowering the activation energy barrier for oxide ion hopping. Due to its larger size than Sr^{2+}, Ba^{2+} cations can increase the unit cell free volume, thereby decreasing the energy of the transition state during oxide hopping. However, increasing the size of the A cation while keeping the size of the B cation (i.e. Co^{3+}) constant may result in structural instabilities and easier transition to ordered phases. The challenge then is to increase the unit cell free volume (and hence, the oxygen flux) without sacrificing the stability of the perovskite structure. This can be achieved through the careful tailoring of the perovskite composition.

3.2 Experimental

3.2.1 Measurement of Oxygen Flux

Oxygen fluxes were measured at atmospheric pressure under steady state conditions at a fixed gradient in oxygen partial pressure using an oxygen permeation cell (Figure 3.1). The cell consisted of two sealed chambers, one with flowing air (P_{O2} = 0.21 atm) and the second with flowing helium (P_{O2} = 0.015 atm). The oxygen partial pressure on the latter was controlled by adjusting the helium flow rate between 50 and 300 sccm, depending on the temperature, membrane thickness and conductivity. This oxygen partial pressure was set equal to the measured outlet oxygen concentration, assuming a continuous stirred tank reactor (CSTR) model.
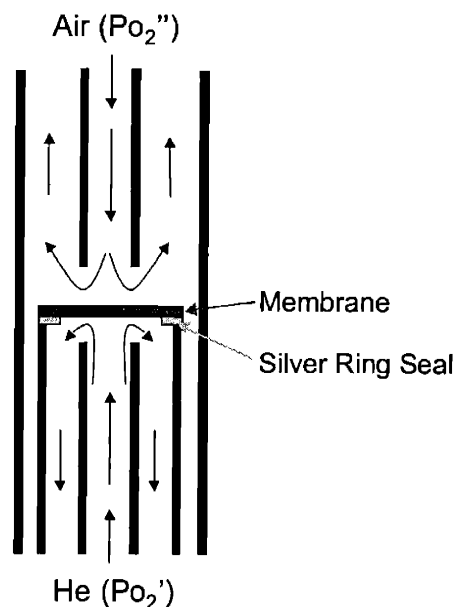
Figure 3.1. Schematic of the oxygen permeation cell.

The air chamber consisted of a 1"-O.D. quartz tube of ~25" long with an inner ½"-O.D. quartz tube supporting a dense membrane. The volume of the air chamber was ~300 cm^3. At air flow rates of < 1 L/min, the measured oxygen flux was found to depend on the air flow rate, indicating external mass transfer resistance. Hence, the air flow rate was set at 2.5 L/min with an average residence time of ~ 7 sec. The helium chamber consisted of a ½"-O.D. quartz tube of ~ 12" long with an inner ¼"-O.D. quartz tube that served as a gas inlet. A dense membrane was sealed at the end of this ½" quartz tube using a silver ring (0.50" O.D. x 0.39" I.D. x 0.02" thickness). To facilitate the adhesion of the silver ring to the ½" quartz tube at high temperatures, a thin layer of silver was coated to the end of the tube. This was achieved by painting silver ink (A3059, Engelhard, NJ) on the quartz surface, followed by firing at ~ 700°C to remove volatile organics and sinter the colloidal silver particles. The distance between the membrane and the inlet ¼" quartz tube was minimized (typically < 5 mm) to ensure good mixing and decrease dead space. The flow pattern in the helium chamber can be characterized as laminar, stagnation flow, with impinging pure helium gas being enriched by oxygen flow from the membrane surface. A type K thermocouple (Omega Engineering, CT) was placed below the membrane surface, and used in conjunction with an Omega 2040 temperature controller (Omega Engineering, CT) and Lindberg Blue-M tube furnace (Lindberg, NC) to maintain the membrane temperature within ±2°C of the desired setpoint.

High-purity (99.999%) gases (He, air, 10% O_2 in He, O_2 and N_2) were metered into the air or helium chambers using up to five independent MKS mass flow controllers. The effluent from the helium chamber was analyzed with a Hewlett Packard 6890 gas chromatograph (GC) equipped with molecular sieve 5A and Porapak Q chromatographic columns, which allowed oxygen and nitrogen to be separated and quantified. The oxygen flux was determined by multiplying the measured oxygen concentration and the effluent flow rate, and normalizing with the exposed membrane surface area.

Before beginning the gas permeation experiments, a ½"-diameter, 0.8 mm-thick perovskite membrane was sealed unto the ½" quartz tube by softening the silver ring at 950-960°C, without exceeding its melting point (963°C). To facilitate the adhesion of the silver ring to the membrane and quartz surface, pressure was applied to the assembly using a quartz plunger, which was later removed from the furnace during the permeation experiments. The presence of oxygen facilitated the adhesion of silver to quartz and membrane surfaces by forming a silver oxide interfacial layer. The gas tightness of the seal was tested by flowing helium in the helium chamber, and measuring the permeated nitrogen concentration in the effluent stream of this chamber. Typically, the leak rate for a successfully sealed membrane was < 2% of the reported oxygen flux. After the membrane has been sealed, it was cooled to 900°C at 1°C/min, and the oxygen flux was measured under steady state conditions at an oxygen gradient of 1.5-21%. A slow cooling rate of 1°C/min was used to prevent the failure of the silver seal from differences in metal and ceramic thermal expansion coefficients. Subsequently, the membrane was cooled to 850°C, 800°C and 750°C to obtain oxygen fluxes at these temperatures. The oxygen flux was monitored for ~ 6 hous at 750°C to investigate any decline in flux over time from potential order-disorder transformations.

3.2.2 Characterization of Crystal Structure and Phase Transitions

The crystal structure of perovskite-based materials was characterized by powder XRD using a Siemens D5000 θ-θ diffractometer (45 kV, 40 mA, Cu-Kα). High-purity NiO (99.99%, Sigma-Aldrich) was used as an internal standard for peak positions.

The transformation from a vacancy-disordered perovskite phase to a vacancy-ordered phase is an exothermic process, since the oxygen vacancies are arranged to form an energetically favorable, ordered configuration. The heat of transition and the order-disorder transition

temperature were characterized by differential thermal analysis (DTA) with Perkin Elmer DTA7 system. About 50 mg each of calcined perovskite and α-Al_2O_3 powders were loaded into the sample and reference alumina crucibles, respectively. The sample was first heated to 1050°C and held for ~ 1 hour in air to ensure the formation of a vacancy-disordered phase, and then slowly cooled at 5°C/min to 600°C. If a phase transition to an ordered structure occurred, an exothermic peak would be observed.

3.2.3 Oxygen Vacancy Concentration

Oxygen vacancy concentration (δ) present in $Ba_{1-x}Sr_xCo_{1-y}M_yO_{3-\delta}$ perovskites was characterized by thermal gravimetric analysis (TGA) with Perkin Elmer TGA7 system. Mizusaki et al. [21-24] measured the oxygen vacancy concentration in $La_{1-x}Sr_xCoO_3$ and $La_{1-x}Sr_xFeO_3$ as a function of temperature and oxygen partial pressure by first determining the equilibrium sample weights under different conditions, followed by reducing the perovskite to its constituent base metal(s) or metal oxide(s) (e.g., La_2O_3, SrO, Co) in hydrogen to determine the equilibrium sample weight at a known oxygen content. The hydrogen reduction step was needed to "calibrate" the TGA measurement to determine the absolute oxygen vacancy concentrations, instead of relative changes in vacancy concentration as a function of temperature and oxygen partial pressure. A major drawback in this approach is that it does not reliably determine the final oxygen content of the reduced product, hence introducing an error in the calculated vacancy concentration. This is because the reduction of a perovskite to its base metal(s) or metal oxide(s) may not be complete, and/or complex intermediate phases may appear with varying oxygen contents. For example, XRD analysis of a $Ba_{0.5}Sr_{0.5}Co_{0.8}Fe_{0.2}O_{3-\delta}$ perovskite that has been reduced in 5% hydrogen in helium at 800°C for 8 hours showed a mixture of phases with broad peaks, making the determination of exact composition and oxygen content very difficult. This approach is also not viable for the more stable perovskite compositions (such as, Fe-, Mn-, or Cr-doped perovskites) that require more severe reducing conditions than that can be achieved *in situ* in the conventional TGA apparatus.

To bypass the above problem, a starting mixture of known oxygen content, typically high-purity metal oxide or metal carbonate precursors was used. This mixture of known stoichiometry was calcined *in situ* to form a pure perovskite phase at high temperatures (1050-1250°C for 4-6 hours). Since the composition of the precursors was known, the absolute oxygen

contents for the subsequent equilibration steps at different temperatures and/or oxygen partial pressures could be accurately determined.

An inherent drawback in using TGA for oxygen vacancy determination is the long equilibration times required at low temperatures (typically $< 600°C$), owing to the slow oxide ion diffusion within the perovskite particles. Therefore, the oxygen vacancy measurements for $Ba_{1-x}Sr_xCo_{1-y}Fe_yO_3$ perovskites were conducted between $600°C$ and $1100°C$, where the equilibration times were relatively short.

Barium carbonate, strontium carbonate, cobalt (II, III) oxide and iron (III) oxide (99.9%, Sigma Aldrich) were ground in acetone using an agate mortar-and-pestle to obtain a homogeneous mixture. The dried powder ($\sim$ 75 mg) was loaded into a platinum pan for TGA. It was first heated to $200°C$, and held for 45 min to obtain the initial weight of the precursors. The powder was then heated to its calcination temperature, typically between $1050°C$ and $1250°C$, and held for 4-6 hours. Samples containing higher iron and strontium levels required the higher calcination temperatures to obtain phase purity. The powder was then cooled to $600°C$ at $-1°C/min$ to obtain the change in sample weight as a function of temperature. The oxygen concentration in the atmosphere was varied between 21% and 1% using two independent MKS mass flow controllers. A gas flow rate of 200 sccm was used with an average residence time of $\sim$ 4 min.

3.3 Results and Discussion

3.3.1 Crystal Structure Analysis of $Ba_{1-x}Sr_xCo_{1-y}Fe_yO_3$

$Ba_{1-x}Sr_xCo_{1-y}Fe_yO_3$ perovskites were synthesized by chemical co-precipitation, according to the procedures outlined in Chapter 2 [25, 26]. Figure 3.2 shows the phase behavior of the mixed oxide with varying Ba:Sr ratio and Co:Fe ratio, after calcination at $900°C$ in air. The vacancy-disordered perovskite was found to transform to a vacancy-ordered phase at high barium and cobalt contents.
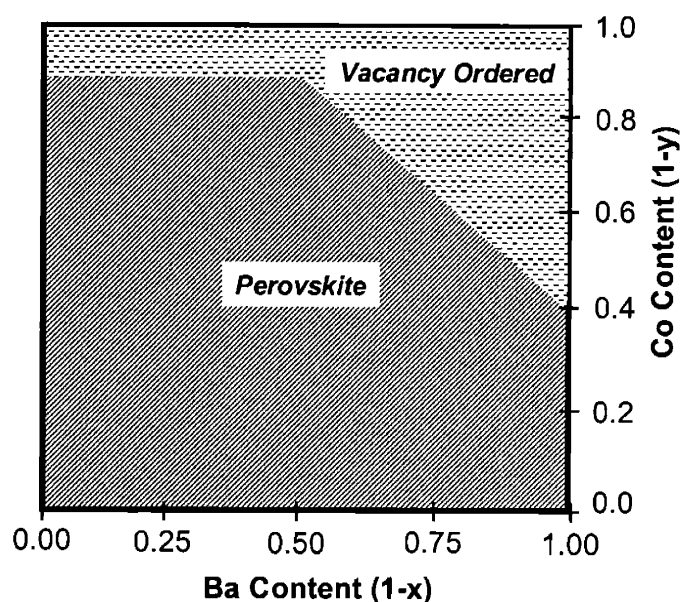
Figure 3.2. Crystal structure of $Ba_{1-x}Sr_xCo_{1-y}Fe_yO_3$ perovskites after calcination at 900°C in air.

Figures 3.3 and 3.4 show the XRD patterns of $BaCo_{1-y}Fe_yO_3$ and $Ba_{1-x}Sr_xCo_{0.8}Fe_{0.2}O_3$ perovskites, respectively, after calcination at 900°C in air. For $BaCo_{1-y}Fe_yO_3$ perovskites, the cubic perovskite phase transformed to an ordered structure at iron contents < 0.6; higher iron substitution at the B site would stabilize the vacancy-disordered cubic phase. In the case of $Ba_{1-x}Sr_xCo_{0.8}Fe_{0.2}O_3$, the cubic phase transformed to an ordered structure at a high barium content of ≥ 0.75. Strontium substitution of ≥ 0.25 at the A site would stabilize the perovskite phase. Increasing barium content resulted in significant peak shifts to lower diffraction angles, indicating substantial lattice expansion without the formation of a separate BaO phase.
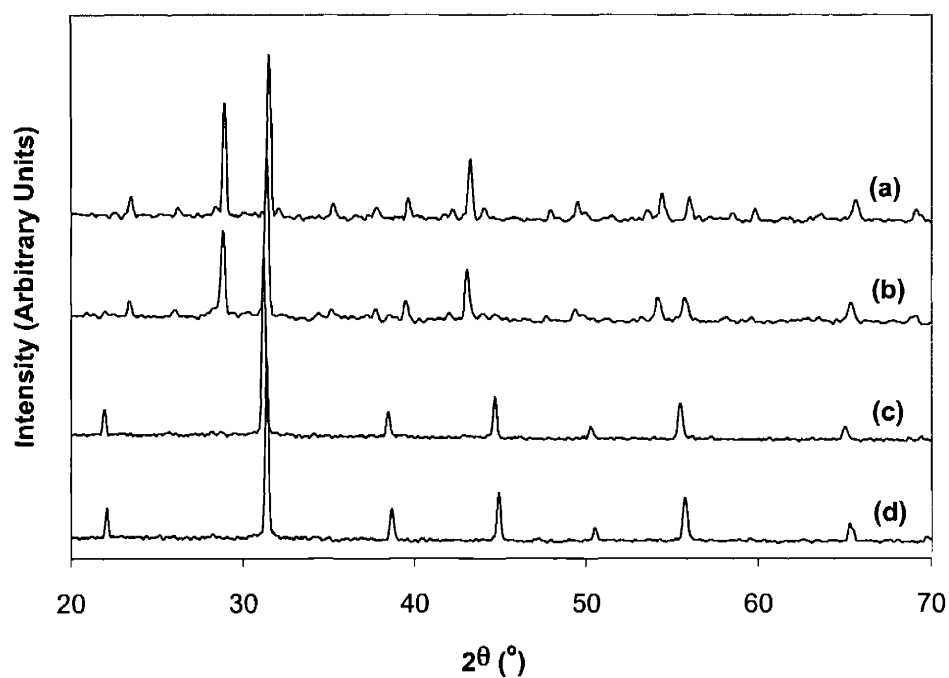
Figure 3.3. XRD patterns for $BaCo_{1-y}Fe_yO_3$ perovskites with a Fe content (y) of (a) 0.2, (b) 0.4, (c) 0.6 and (d) 0.8, after calcination at 900°C in air.
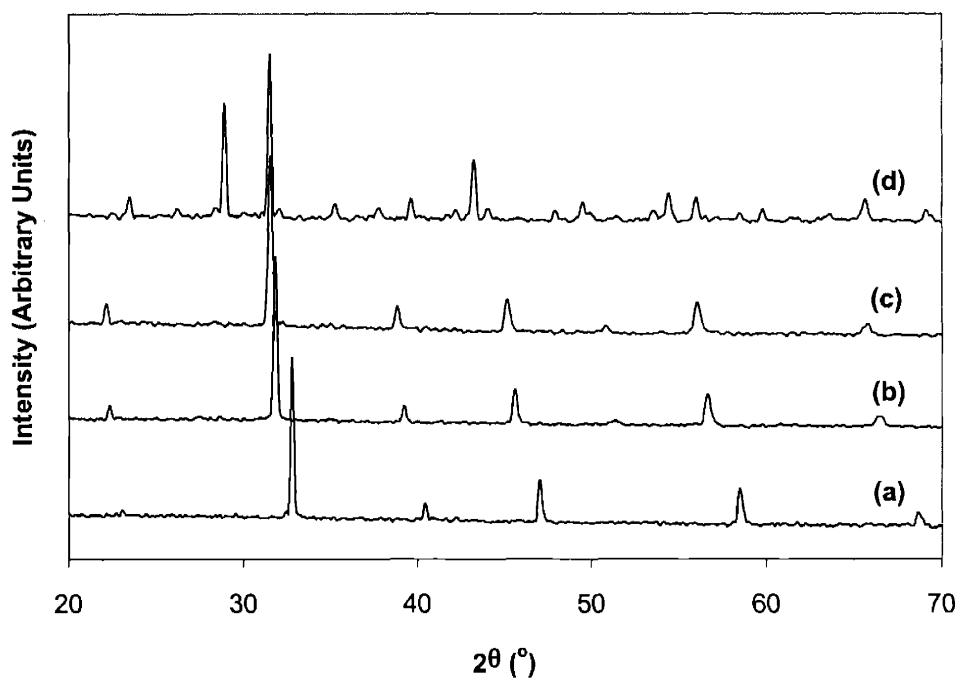
Figure 3.4. XRD patterns for $Ba_{1-x}Sr_xCo_{0.8}Fe_{0.2}O_3$ perovskites with a barium content (1-x) of (a) 0.00, (b) 0.50, (c) 0.75 and (d) 1.00, after calcination at 900°C in air.

The perovskite transformation to an ordered structure at a high barium content could be understood by examining the Goldschmidt factor, which indicated the stability of the perovskite phase through the relative sizes of the A- and B-site cations. Figure 3.5 shows the calculated Goldschmidt factors for the $Ba_{1-x}Sr_xCo_{1-y}Fe_yO_3$ system using the expression [27]:

$$Goldschmidt\ factor = \frac{(r_A + r_O)}{\sqrt{2}(r_B + r_O)} \qquad (3.1)$$

where r_A and r_B are the molar average radii of the A- and B-site cations, respectively, and r_O is the radius of an oxide ion. By replacing strontium by barium and/or iron by cobalt, the Goldschmidt factor is found to increase and deviate significantly from unity. At high barium and cobalt contents, where a phase transformation to an ordered structure is observed (Figure 3.2), the Goldschmidt factor shows its greatest deviation from unity and lies between 1.06 and 1.10. Since an ideal perovskite structure has a Goldschmidt factor equal to unity, as the Goldschmidt factor deviates from unity, the tendency to transform to a more stable structure increases. This is consistent with the XRD results that showed order-disorder phase transformation at high barium and cobalt contents.

For $Ba_2In_2O_5$ perovskites, researchers have found that substitution of indium by gallium stabilized the perovskite phase by decreasing the deviation of the Goldschmidt factor from unity [28, 29]. It was proposed that perovskites with Goldschmidt factors close to unity transformed less easily to a vacancy-ordered phase. This observation was consistent with our results for $Ba_{1-x}Sr_xCo_{1-y}Fe_yO_3$ perovskites, indicating that the intrinsic stability of the cubic phase governed its tendency to transform to an ordered structure.
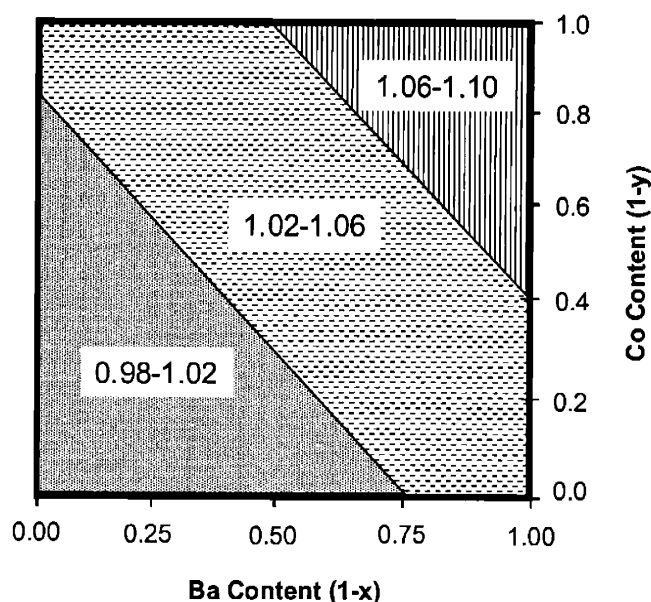
Figure 3.5. Calculated Goldschmidt factors for $Ba_{1-x}Sr_xCo_{1-y}Fe_yO_3$ perovskites.

Figure 3.6 shows the dependence of the unit cell dimension on barium content in $Ba_{1-x}Sr_xCo_{1-y}Fe_yO_3$ perovskites. The length of the unit cell vector, **a**, was calculated using the measured d-spacing of the <110> crystallographic plane. A NiO internal standard was used to correct for instrumental error in determining the peak positions. The length of the unit cell vector increased linearly with increasing barium content due to the larger ionic radius of Ba^{2+} (1.61 Å [30]) compared to that of Sr^{2+} (1.44 Å [30]) in 12-fold coordination.

Figure 3.7 shows the dependence of the unit cell dimension on cobalt content in $Ba_{1-x}Sr_xCo_{1-y}Fe_yO_3$ perovskites. As the cobalt content increased from 0.0 to 0.6, the unit cell dimension increased. The ionic size of Co^{3+} in six-fold coordination (0.55 Å [30]) was smaller than that of Fe^{3+} (0.65 Å [30]), which would suggest a lattice contraction with increasing cobalt content. However, due to the high oxygen vacancy concentration present in these perovskites (~ 15% of O^{2-} lattice sites), the B-site cations have a reduced coordination number. The preference of Fe^{3+} to adopt a four-fold coordination with a smaller ionic radius of 0.49 Å [30] might explain the observed lattice contraction on increased iron doping.
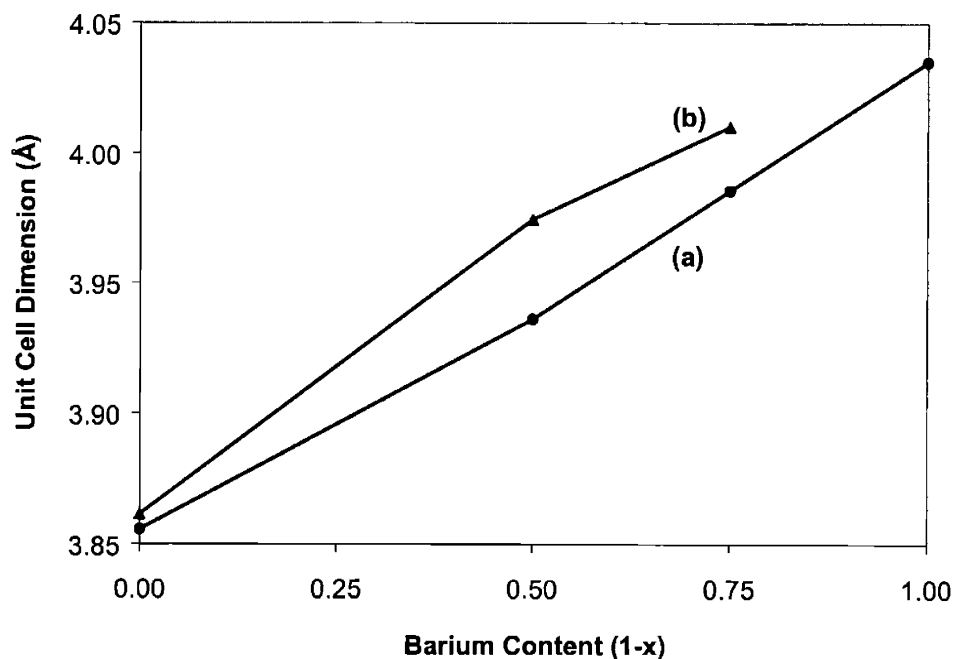
Figure 3.6. Effect of barium content on the unit cell dimension of $Ba_{1-x}Sr_xCo_{1-y}Fe_yO_3$ perovskites at a cobalt content (1-y) of (a) 0.2 and (b) 0.8, calculated using <110> XRD reflection.
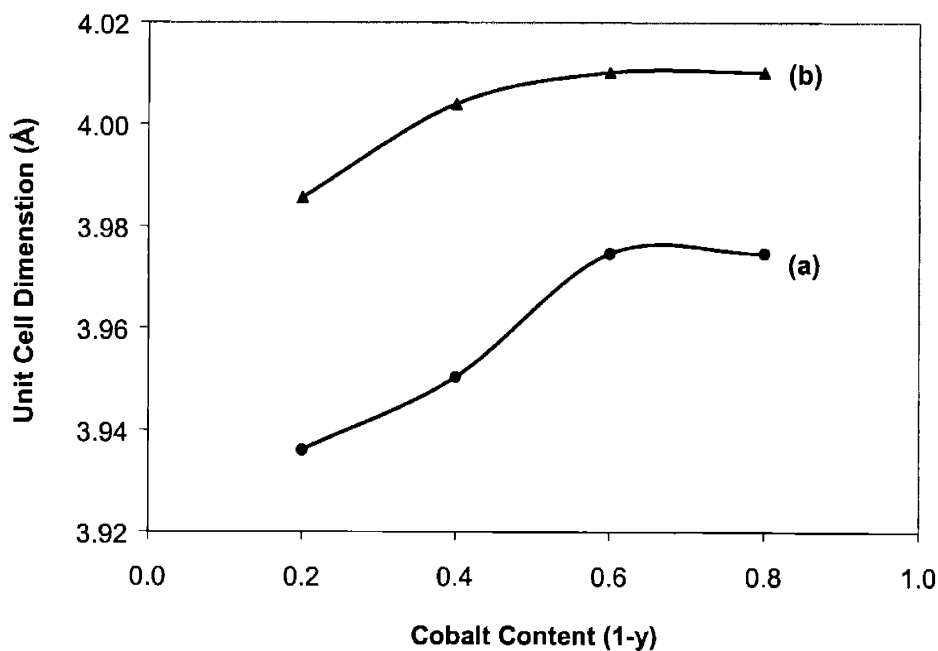
Figure 3.7. Effect of cobalt content on the unit cell dimension of $Ba_{1-x}Sr_xCo_{1-y}Fe_yO_3$ perovskites at a barium content (1-x) of (a) 0.25 and (b) 0.50, calculated using <110> XRD reflection.

Figure 3.8 shows the dependence of unit cell free volume on the $Ba_{1-x}Sr_xCo_{1-y}Fe_yO_3$ composition. The unit cell free volume was calculated by subtracting the total volume occupied by the metal cations and oxygen anions in the unit cell ($V_{occ} = \Sigma\, n_iV_i$, where n_i is the number of atoms in the unit cell and V_i is the molar average volume of the metal cations) from the total measured volume of the unit cell ($V_{tot} = a^3$). Increasing the barium content at the A site increased the unit cell free volume, since the increase in the total cell volume (implied from Figure 3.6) was greater than the increase in the occupied cell volume. Increasing the cobalt content increased the unit cell free volume, however, the change was relatively small. The unit cell free volume was expected to strongly influence the migrational activation energy of the oxide ions and the resulting oxygen flux [31, 32]. It should also be noted that there was a correlation between the decrease in perovskite stability and the increase in unit cell free volume.
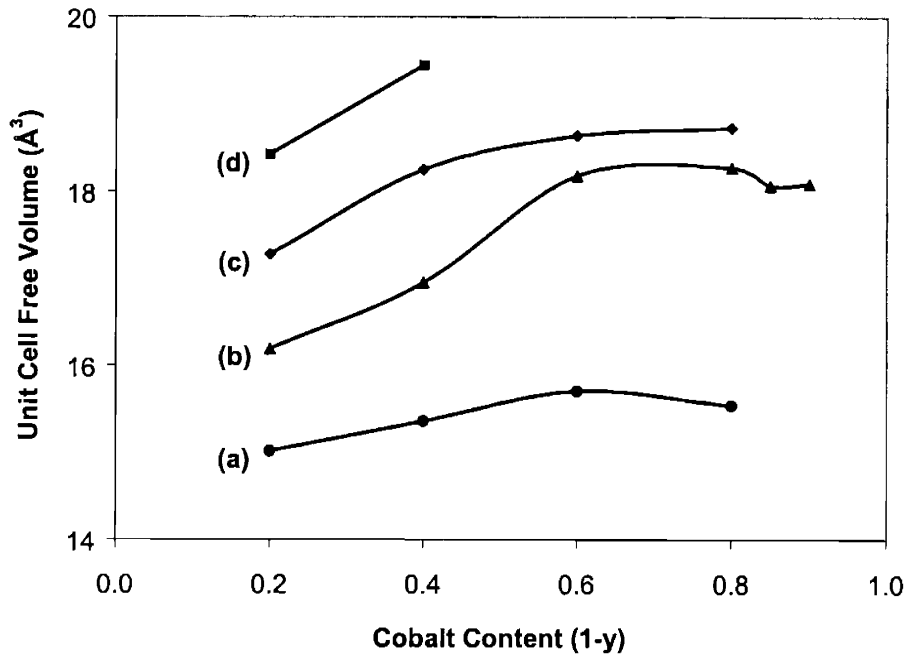
Figure 3.8. Unit cell free volume of $Ba_{1-x}Sr_xCo_{1-y}Fe_yO_3$ perovskites at a barium content (1-x) of (a) 0.00, (b) 0.50, (c) 0.75 and (d) 1.00.

3.3.2 Oxygen Flux Measurements of $Ba_{1-x}Sr_xCo_{1-y}Fe_yO_3$

$Ba_{1-x}Sr_xCo_{1-y}Fe_yO_3$ perovskite powders were sintered at $1100\text{-}1250^\circ C$ to form dense pellets with > 90% theoretical density. The oxide ion conductivity in these perovskites was characterized by measuring the oxygen flux through a 0.8 mm-thick sintered pellet at an oxygen concentration gradient between 21% (air) and 1.5% (O_2-He). The oxygen leak rate in these

experiments was < 2% of the measured oxygen flux, indicating an excellent seal between the membrane and reactor tube, and the absence of open porosity in the sintered membrane.

Figure 3.9 shows the effect of cobalt content on oxygen flux through $BaCo_{1-y}Fe_yO_3$ perovskites. At a cobalt content of 0.6 or 0.8, a dramatic decrease in oxygen flux was observed with decreasing temperature due to the phase transformation from the high-temperature perovskite phase to a low-temperature vacancy-ordered phase. This was consistent with the room-temperature XRD results that showed the formation of an ordered structure at cobalt content (1-y) of > 0.4 (Figure 3.3). The oxygen vacancies in an ordered structure were arranged along specific crystallographic directions, resulting in oxide ion conduction restricted within 2-D planes with high activation barriers associated with cross-planar migration.
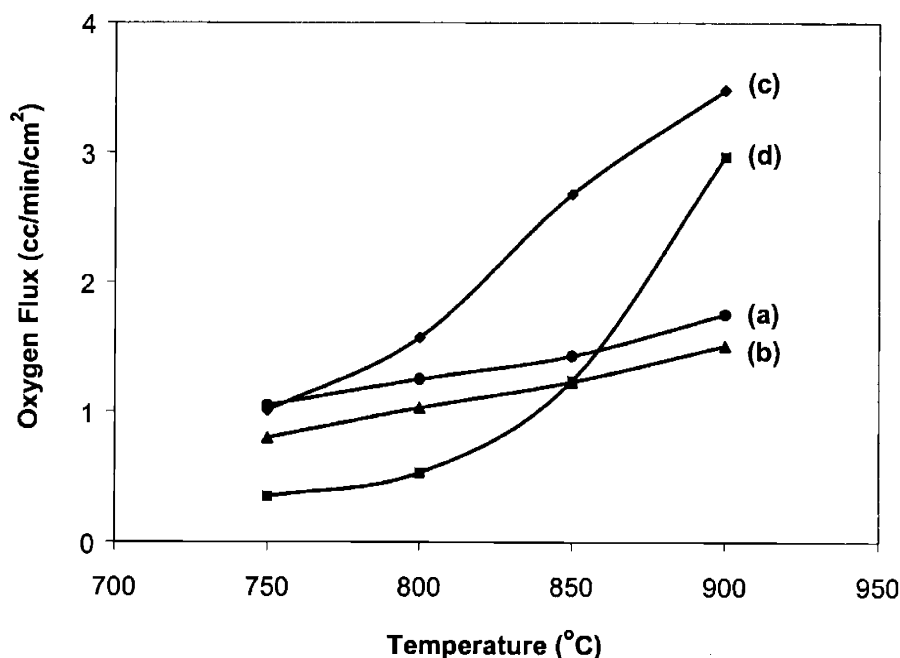
Figure 3.9. Oxygen flux of $BaCo_{1-y}Fe_yO_3$ perovskites with a cobalt content (1-y) of (a) 0.2, (b) 0.4, (c) 0.6 and (d) 0.8.

At higher iron contents (y ≥ 0.6), this phase transformation was suppressed and the presence of mobile, disordered oxygen vacancies retained the high oxygen fluxes at lower temperatures. This implied that iron acted as a "trap" for oxygen vacancies by preferentially adopting a 4-fold coordination, thereby preventing the local re-arrangement of oxygen vacancies necessary for the formation of the ordered phase. However, at temperatures above the order-disorder transition (850-900°C), the oxygen flux in $BaCo_{0.8}Fe_{0.2}O_3$ was much higher than that in $BaCo_{0.2}Fe_{0.8}O_3$, indicating a higher concentration of mobile oxygen vacancies.

Figure 3.10 shows the increase in oxygen flux with increasing cobalt content for $Ba_{0.75}Sr_{0.25}Co_{1-y}Fe_yO_3$ perovskites. Compared to $BaCo_{0.8}Fe_{0.2}O_3$, $Ba_{0.75}Sr_{0.25}Co_{0.8}Fe_{0.2}O_3$ exhibited a sharp decline in oxygen flux at lower temperatures (750-800°C). This drop in the order-disorder transition temperature with strontium doping was consistent with the increased stability of the perovskite phase (see Figure 3.4). The increase in oxygen flux with cobalt content might be due to a higher concentration of mobile oxygen vacancies and an increase in unit cell free volume (Figure 3.8). $Ba_{0.75}Sr_{0.25}Co_{0.8}Fe_{0.2}O_3$ has an oxygen flux of ~3.8 $cm^3(STP)/min/cm^2$ at 900°C, which was significantly higher than that achieved by conventional materials. For example, $La_{1-x}Sr_xCo_{1-y}Fe_yO_3$-based perovskites of similar thickness have oxygen fluxes of 0.5-2.0 $cm^3(STP)/min/cm^2$, and $CaFe_{1-x}Ti_xO_3$ and $BaCe_{1-x}Gd_xO_3$ materials have oxygen fluxes of < 0.5 $cm^3(STP)/min/cm^2$.
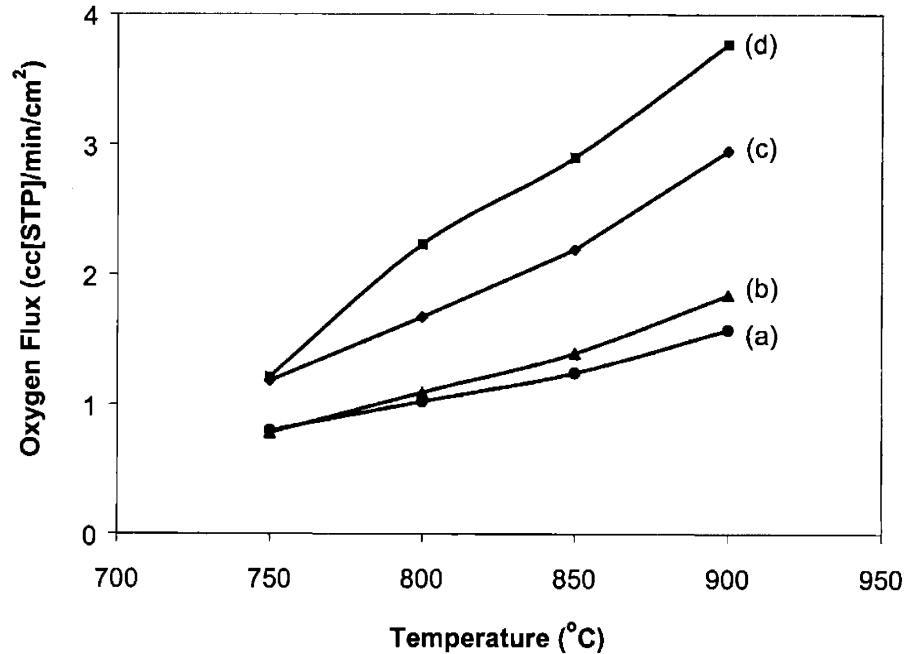
Figure 3.10. Oxygen flux of $Ba_{0.75}Sr_{0.25}Co_{1-y}Fe_yO_3$ perovskites with a cobalt content (1-y) of (a) 0.2, (b) 0.4, (c) 0.6 and (d) 0.8.

Since the kinetics of the order-disorder phase transformation could be slow [18], it was necessary to investigate the stability of the oxygen flux through the membranes at low temperatures. Figure 3.11 shows the time dependence of oxygen flux in $Ba_{0.75}Sr_{0.25}Co_{1-y}Fe_yO_3$ at 750°C. As the cobalt content increased, the decrease in oxygen flux with time became significant, indicating a slow ordering of oxygen vacancies. Thus, to design membranes with

high oxygen fluxes at 750°C, high iron concentrations were required to suppress the transformation to the vacancy-ordered phase. At higher temperatures ($\geqslant$ 800°C), no decrease in oxygen flux was observed with time, indicating that oxygen vacancies did not associate and order at these temperatures.
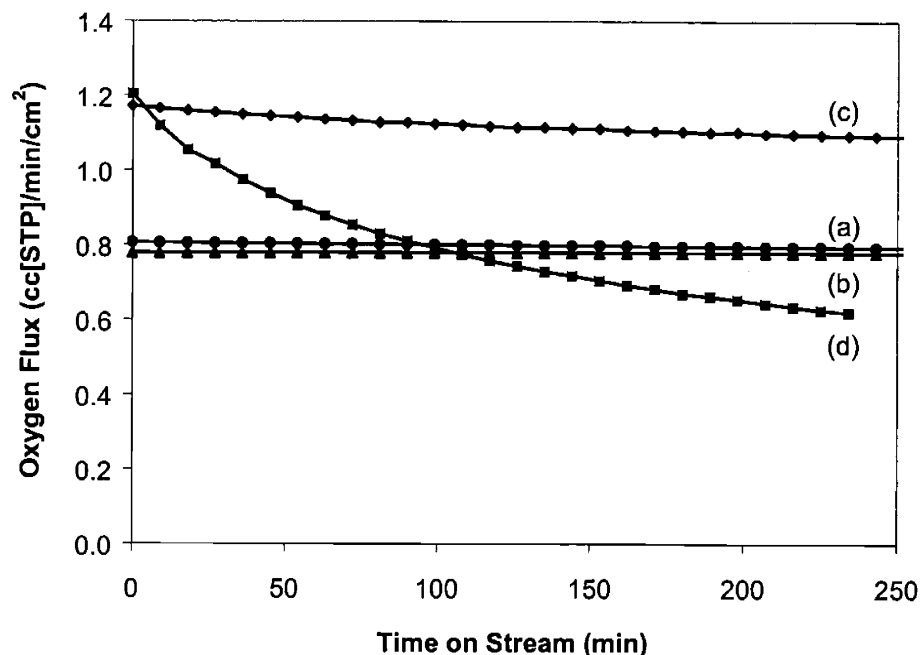
Figure 3.11. Oxygen flux of $Ba_{0.75}Sr_{0.25}Co_{1-y}Fe_yO_3$ perovskites with a cobalt content (1-y) of (a) 0.2, (b) 0.4, (c) 0.6 and (d) 0.8 at 750°C.

Figure 3.12 shows the dependence of oxygen flux on cobalt content for $Ba_{0.5}Sr_{0.5}Co_{1-y}Fe_yO_3$ perovskites. Unlike the perovskites with higher barium content, oxygen flux of $Ba_{0.5}Sr_{0.5}Co_{0.8}Fe_{0.2}O_3$ perovskite did not show any evidence of a phase transition at 750-900°C, consistent with increased perovskite phase stability with higher strontium doping. As the cobalt content was increased, the oxygen flux was found to increase till (1-y) = 0.8, followed by a reduction due to the partial phase transformation to a vacancy-ordered structure.

Figure 3.13 shows the dependence of oxygen flux on time for $Ba_{0.5}Sr_{0.5}Co_{1-y}Fe_yO_3$ perovskites at 750°C. As the cobalt concentration was increased to 0.8, the initial oxygen flux increased, but stability of the flux over time decreased. This indicated that perovskites with higher oxide conductivity, owing to their higher concentration of mobile vacancies, were more susceptible to ordering effects at lower temperatures. As the cobalt content was further increased beyond 0.8 to 0.9, a dramatic decrease in oxygen flux and stability was observed, indicating a kinetic phase transformation to an ordered structure. $Ba_{0.5}Sr_{0.5}Co_{0.8}Fe_{0.2}O_3$ demonstrated the

optimal performance at 750°C with respect to oxygen flux (~ 1.2 cc[STP]/min/cm^2) and stability, making it a viable composition for low-temperature oxygen separation.
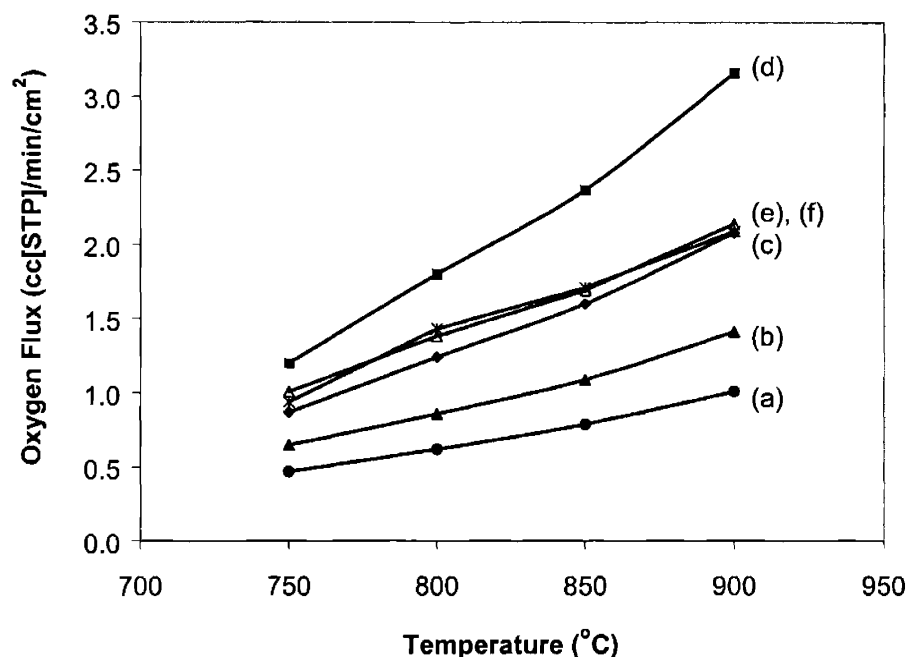
Figure 3.12. Oxygen flux of $Ba_{0.5}Sr_{0.5}Co_{1-y}Fe_yO_3$ perovskites with a cobalt content (1-y) of (a) 0.2, (b) 0.4, (c) 0.6 (◆), (d) 0.8, (e) 0.85 (△) and (f) 0.90 (*).
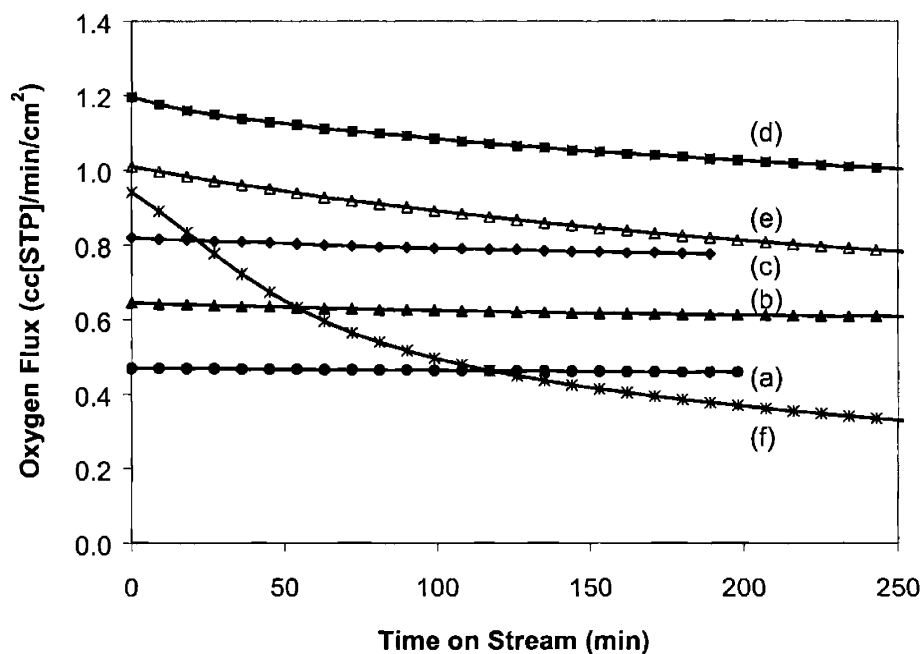
Figure 3.13. Oxygen flux of $Ba_{0.5}Sr_{0.5}Co_{1-y}Fe_yO_3$ perovskites with a cobalt content (1-y) of (a) 0.2, (b) 0.4, (c) 0.6, (d) 0.8, (e) 0.85 and (f) 0.90 at 750°C.

Figure 3.14 shows the effect of barium content on oxygen flux in $Ba_{1-x}Sr_xCo_{0.8}Fe_{0.2}O_3$ perovskites. As the barium content was increased up to 0.75, the oxygen flux increased dramatically. At $900°C$, $SrCo_{0.8}Fe_{0.2}O_3$ and $Ba_{0.75}Sr_{0.25}Co_{0.8}Fe_{0.2}O_3$ have oxygen fluxes of ~ 1.9 and ~ 3.8 $cm^3(STP)/min/cm^2$, respectively. The increase in oxygen flux was due to an expansion of the unit cell, resulting in a higher unit cell free volume (Figure 3.8), which facilitated hopping of oxide ions between lattice sites. However, at barium content > 0.75, the instability of the perovskite phase resulted in a significant decline in oxygen flux, especially at low temperatures.
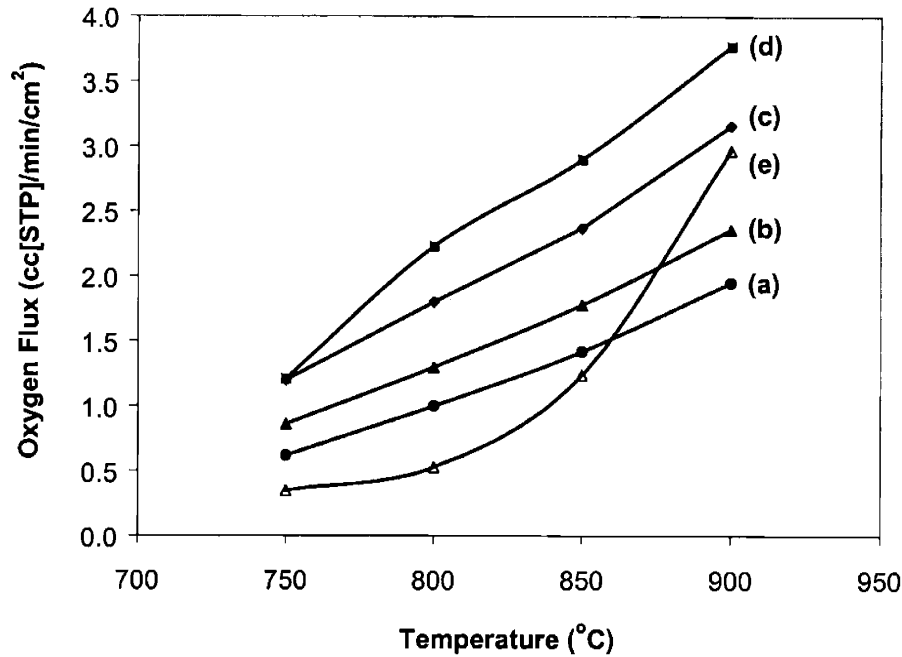
Figure 3.14. Oxygen flux of $Ba_{1-x}Sr_xCo_{0.8}Fe_{0.2}O_3$ perovskites with a barium content (1-x) of (a) 0.00, (b) 0.25, (c) 0.50, (d) 0.75 and (e) 1.00.

Figure 3.15 shows the effect of barium content on the oxygen flux in $Ba_{1-x}Sr_xCo_{0.2}Fe_{0.8}O_3$ perovskites. As with $Ba_{1-x}Sr_xCo_{0.8}Fe_{0.2}O_3$ perovskites, oxygen flux was found to increase with barium content for $Ba_{1-x}Sr_xCo_{0.2}Fe_{0.8}O_3$, but a phase transition was not observed at (1-x) = 1.00, as consistent with the phase diagram (Figure 3.2). $BaCo_{0.2}Fe_{0.8}O_3$ showed excellent stability even at $750°C$ with an oxygen flux of 1.05 $cm^3(STP)/min/cm^2$. Thus, at high barium contents, introducing high iron contents was important for stabilizing the perovskite phase to achieve high, stable oxygen fluxes.
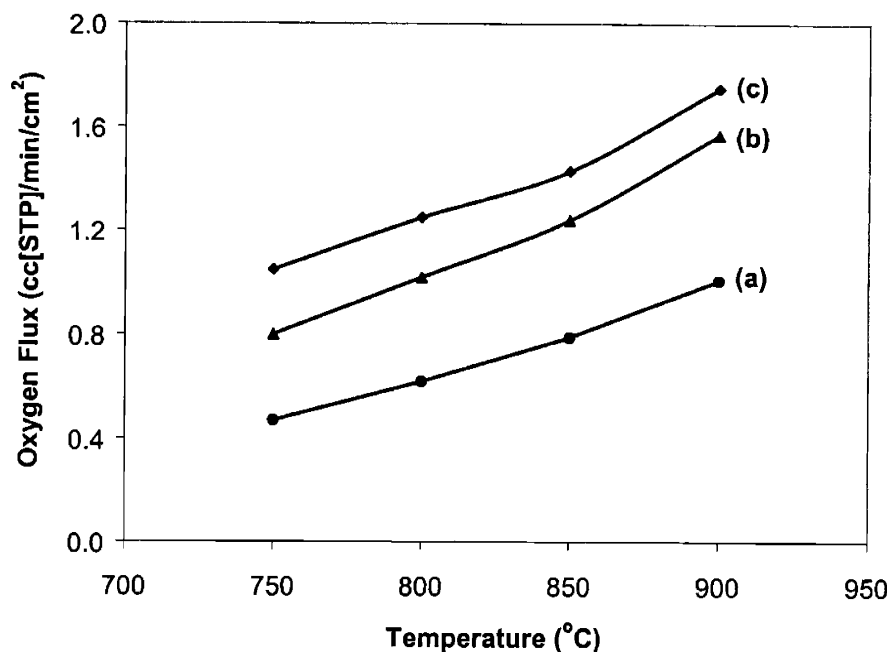
Figure 3.15. Oxygen flux of $Ba_{1-x}Sr_xCo_{0.2}Fe_{0.8}O_3$ perovskites with a barium content (1-x) of (a) 0.50, (b) 0.75 and (c) 1.00.

The overall activation energy for oxygen transfer in $Ba_{1-x}Sr_xCo_{1-y}Fe_yO_3$ perovskites is shown in Figure 3.16. Since oxygen transport occurs by thermal excitation of oxide ions from occupied to vacant oxygen sites, an Arrhenius expression can be used to relate the measured oxygen flux to temperature. The reported activation energy is a lumped quantity consisting of the intrinsic barriers for oxide ion mobility and oxygen vacancy creation. The activation energy for oxide ion mobility depends on the perovskite crystal structure, metal-oxygen bond strengths, and association/ordering of oxygen vacancies. The activation energy for oxygen vacancy creation depends on the intrinsic reducibility of the metal oxide.

At a cobalt content of 0.2, the apparent activation energy for oxygen transport was found to decrease with increasing barium content. As the barium content increased from 0.5 to 1.0, the activation energy decreased from 50 to 33 kJ/mol (Figure 3.16). This reduction in the activation barrier was consistent with the increase in lattice free volume from 16.2 to 18.4 $Å^3$ (Figure 3.8), which allowed oxide ions to diffuse more easily within the crystal structure. At a cobalt content of 0.8, as the barium content was increased from 0.0 to 0.5, the activation energy decreased from 76 to 64 kJ/mol, consistent with increasing unit cell free volume. However, as the barium concentration was increased from 0.5 to 1.0, the activation energy showed a sharp increase from 64 to 144 kJ/mol (Figure 3.16(c)). This dramatic increase in apparent activation energy was due

to the order-disorder phase transformation. Oxide ion transport in vacancy-ordered structure required overcoming barriers associated with vacancy ordering/trapping, in addition to that associated with vacancy hopping between lattice sites. The observed increase in activation energy was consistent with XRD results showing the formation of a vacancy-ordered structure (Figure 3.2), and oxygen flux measurement indicating a dramatic decrease in oxide ion conductivity (Figures 3.9 and 3.10). It will be shown in Section 3.3.4 that the oxygen vacancy concentration sharply decreased during order-disorder phase transformation, which was consistent with this increase in activation energy. $BaCo_{0.6}Fe_{0.4}O_3$ showed a lower activation energy of ~ 80 kJ/mol compared to $BaCo_{0.8}Fe_{0.2}O_3$ (144 kJ/mol), since ordering effects were less severe at a higher iron content.
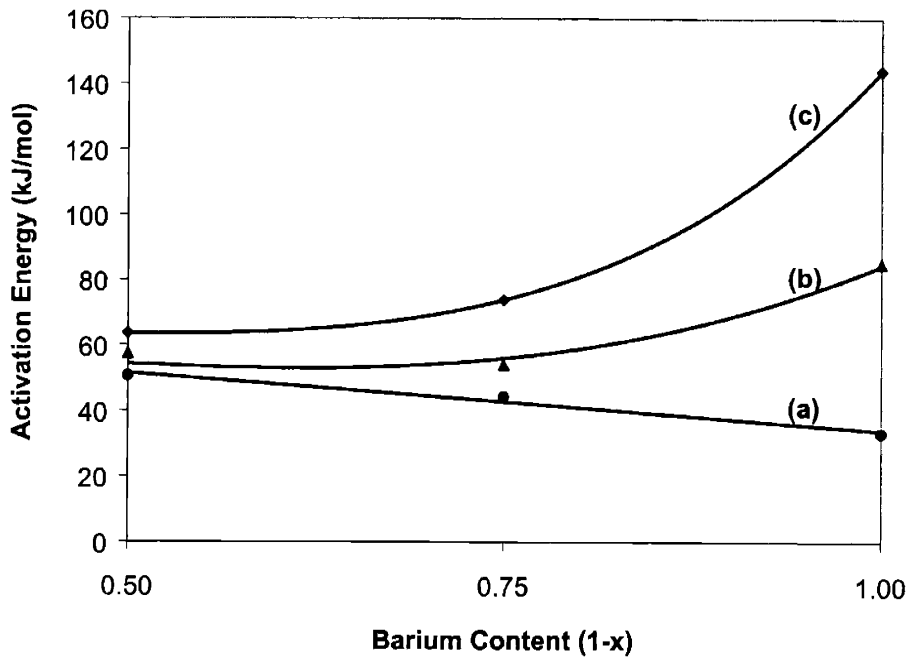
Figure 3.16. Activation energy measured for oxide ion transport in $Ba_{1-x}Sr_xCo_{1-y}Fe_yO_3$ perovskites with a cobalt content (1-y) of (a) 0.2, (b) 0.6 and (c) 0.8.

3.3.3 Crystal Structure and Oxygen Permeation of $Ba_{1-x}Sr_xCo_{1-y}Ti_yO_3$

Oxygen permeation through $Ba_{1-x}Sr_xCo_{1-y}M_yO_3$ perovskites (M = Ti, Sn and Cr) was investigated to understand the fundamental relationship between the type of stabilizer cation, and the resulting crystal structure and oxygen flux. Ti^{4+}, Sn^{4+} and Cr^{4+} were selected because these ions have 6-fold coordination radii close to Co^{3+} ($r(Ti^{4+})$ = 0.67 Å, $r(Sn^{4+})$ = 0.69 Å, $r(Cr^{4+})$ = 0.55 Å, and $r(Co^{3+})$ = 0.55 Å [10]), therefore allowing for substitution for cobalt at the B site. In

120

addition, the higher valence of these ions could locally modify the coordination preference and oxygen vacancy concentration, which might potentially disrupt the ordering of vacancies and prevent the order-disorder phase transition.

Figure 3.17 shows the XRD patterns for $Ba_{1-x}Sr_xCo_{0.8}Ti_{0.2}O_3$ perovskites after calcination at 900°C in air. Like the iron-doped perovskites, the substitution of titanium for cobalt stabilized the perovskite phase. However, the ordered phase appeared at a barium content of > 0.25, instead of > 0.75 for $Ba_{1-x}Sr_xCo_{0.8}Fe_{0.2}O_3$ perovskites. This indicated that iron was a superior dopant to titanium for stabilizing the perovskite structure. The shifting of diffraction peaks to lower angles with increasing barium content illustrated that barium was successfully introduced at the A site for significant lattice expansion.

Figure 3.18 shows the effect of increasing barium content on oxygen flux in $Ba_{1-x}Sr_xCo_{0.8}Ti_{0.2}O_3$ perovskites. It was observed that as the barium content was increased, the oxygen flux increased, reaching ~ 3.0 cm^3[STP]/min/cm^2 for $Ba_{0.25}Sr_{0.75}Co_{0.8}Ti_{0.2}O_3$. On further increase of barium content, the oxygen flux was found to decrease dramatically, which was consistent with the appearance of a segregated vacancy-ordered phase (Figure 3.17). $BaCo_{0.8}Ti_{0.2}O_3$ perovskite showed a very low oxygen flux of < 0.2 cm^3[STP]/min/cm^2 at 900°C, indicating that the order-disorder transition temperature was > 900°C. The highest oxygen flux achieved for Ti-doped perovskites of ~ 3.0 cm^3[STP]/min/cm^2 at 900°C was lower than that achieved for Fe-doped perovskites (~ 3.8 cm^3[STP]/min/cm^2 for $Ba_{0.75}Sr_{0.25}Co_{0.8}Fe_{0.2}O_3$). Since Fe was a more effective dopant for perovskite stabilization than Ti, a higher barium content could be tolerated at the A site without phase transformation.
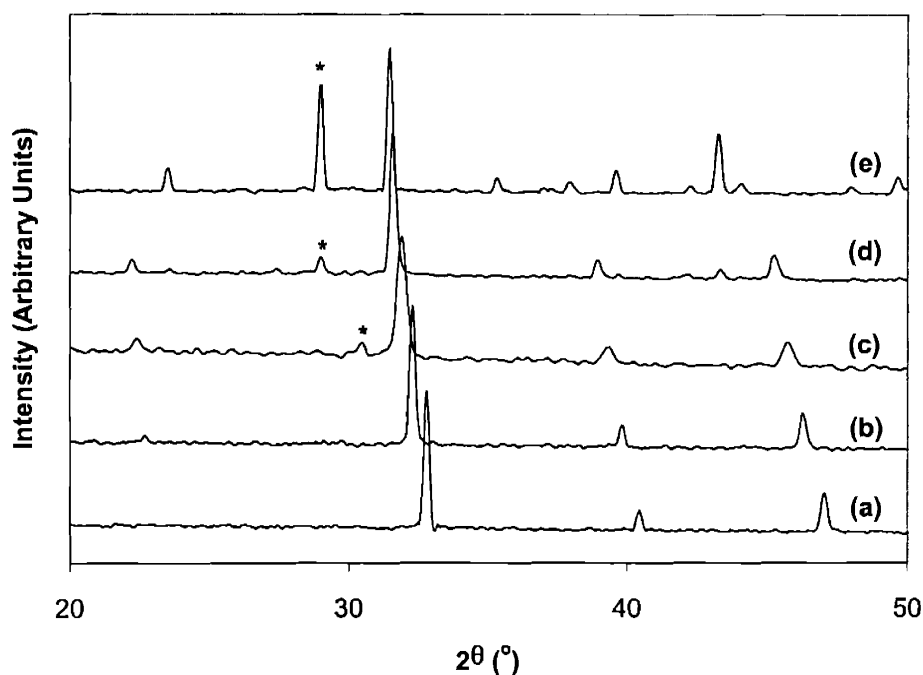
Figure 3.17. XRD patterns for $Ba_{1-x}Sr_xCo_{0.8}Ti_{0.2}O_3$ perovskites with a barium content (1-x) of (a) 0.00, (b) 0.25, (c) 0.50, (d) 0.75 and (e) 1.00, after calcination at $900°C$ in air. XRD peak denoted by "*" corresponds to the vacancy-ordered phase.
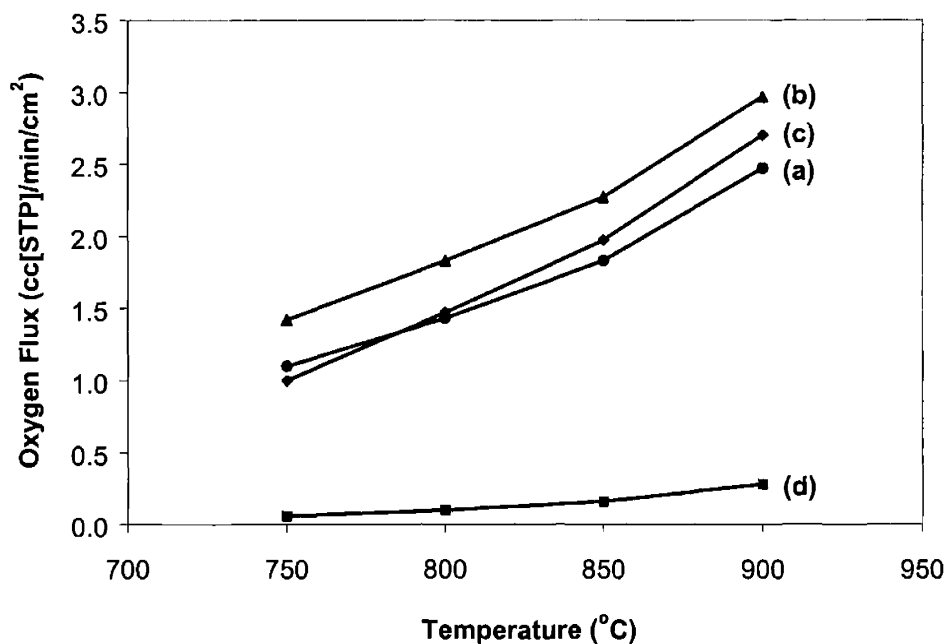
Figure 3.18. Oxygen flux of $Ba_{1-x}Sr_xCo_{0.8}Ti_{0.2}O_3$ perovskites with a barium content (1-x) of (a) 0.00, (b) 0.25, (c) 0.75 and (d) 1.00.

Figure 3.19 shows the dependence of oxygen flux on time for $Ba_{1-x}Sr_xCo_{0.8}Ti_{0.2}O_3$ perovskites at 750°C. The stability of the oxygen flux decreased with increasing barium content due to the formation of the vacancy-ordered phase. $Ba_{0.25}Sr_{0.75}Co_{0.8}Ti_{0.2}O_3$ perovskite exhibited a very high oxygen flux of ~ 1.4 $cm^3[STP]/min/cm^2$ at 750°C, with essentially no decrease over time.
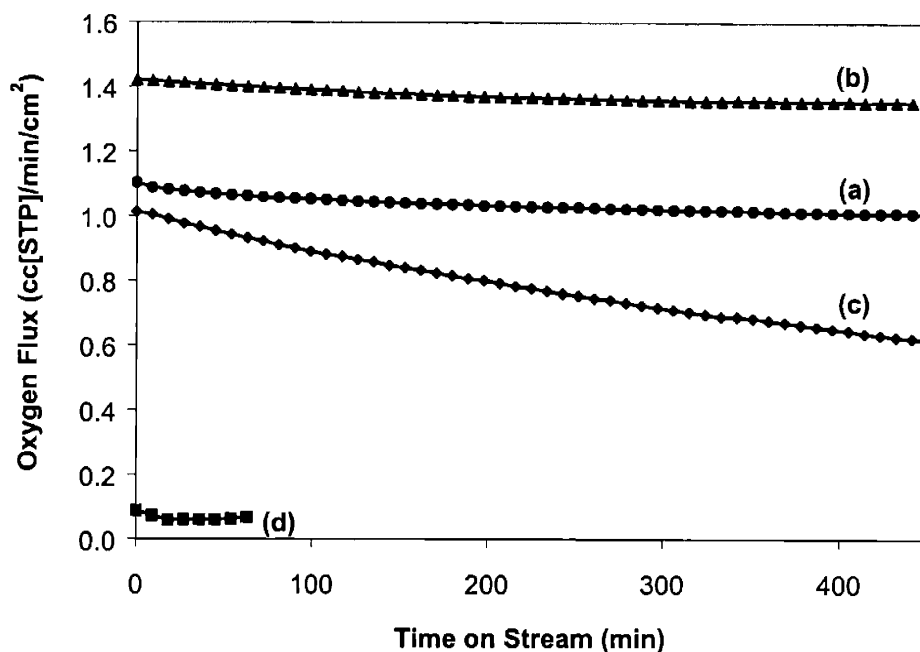
Figure 3.19. Oxygen flux of $Ba_{1-x}Sr_xCo_{0.8}Ti_{0.2}O_3$ perovskites with a barium content (1-x) of (a) 0.00, (b) 0.25, (c) 0.75 and (d) 1.00 at 750°C.

3.3.4 Crystal Structure and Oxygen Permeation of $Ba_{1-x}Sr_xCo_{1-y}Sn_yO_3$

Figure 3.20 shows the XRD patterns for $Ba_{1-x}Sr_xCo_{0.8}Sn_{0.2}O_3$ perovskites after calcination at 900°C in air. The substitution of Co^{3+} by Sn^{4+} resulted in segregation into two perovskite phases, a primary $Ba_{1-x}Sr_xCo_{1-y}Sn_yO_3$ phase and a secondary $Ba_{1-x}Sr_xSnO_3$ phase. On substitution of barium for strontium at the A site, the diffraction peaks for $Ba_{1-x}Sr_xSnO_3$ retained approximately the same relative intensity compared to those for $Ba_{1-x}Sr_xCo_{1-y}Sn_yO_3$, indicating that the overall Ba:Sr ratio did not significantly affect the degree of phase segregation. As the barium content was increased, the diffraction peaks for the $Ba_{1-x}Sr_xCo_{1-y}Sn_yO_3$ phase shifted to lower diffraction angles, indicating an increased barium content and unit cell volume. In contrast, the diffraction peaks for the $Ba_{1-x}Sr_xSnO_3$ phase showed noticeably smaller shifts to

lower diffraction angles, indicating small changes in the Ba:Sr ratio at the A site of $Ba_{1-x}Sr_xSnO_3$.
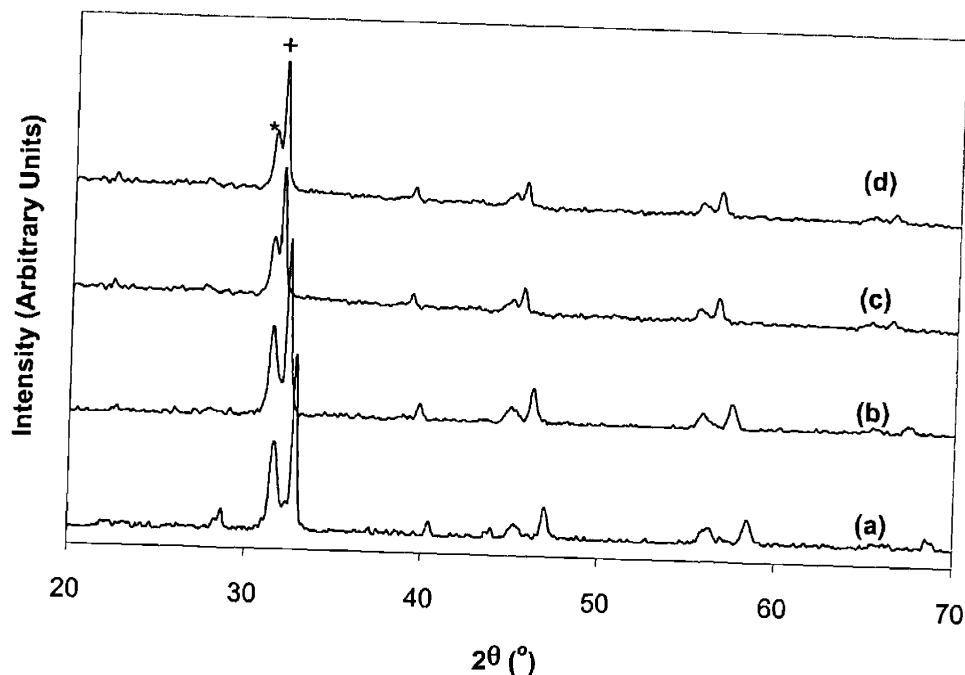
Figure 3.20. XRD patterns for $Ba_{1-x}Sr_xCo_{0.8}Sn_{0.2}O_3$ perovskites with a barium content (1-x) of (a) 0.00, (b) 0.25, (c) 0.50 and (d) 0.75, after calcination at 900°C in air. XRD peaks denoted by "*" and "+" correspond to $Ba_{1-x}Sr_xSnO_3$ and $Ba_{1-x}Sr_xCo_{1-y}Sn_yO_3$ phases, respectively.

The segregation of a secondary $Ba_{1-x}Sr_xSnO_3$ phase for $Ba_{1-x}Sr_xCo_{0.8}Sn_{0.2}O_3$ perovskites motivated the use of low Sn^{4+} doping level to prevent the formation of a two-phase perovskite mixture, and potentially avoid the order-disorder transition. Figure 3.21 shows the XRD patterns for $Ba_{0.5}Sr_{0.5}Co_{1-y}Sn_yO_3$ perovskites. As the Sn^{4+} content was lowered, the intensity of the diffraction peaks representing the $Ba_{1-x}Sr_xSnO_3$ phase decreased, verifying that the secondary perovskite phase segregation was due to excess Sn^{4+} loading. A single-phase perovskite was obtained at a tin content of ~ 0.10. For y < 0.10, the perovskite phase could no longer be stabilized to room temperature, as observed by the presence of a secondary vacancy-ordered phase. Therefore, the optimal Sn^{4+} substitution for Co^{3+} in $Ba_{1-x}Sr_xCo_{1-y}Sn_yO_3$ perovskites was determined to be $0.05 < y < 0.15$.
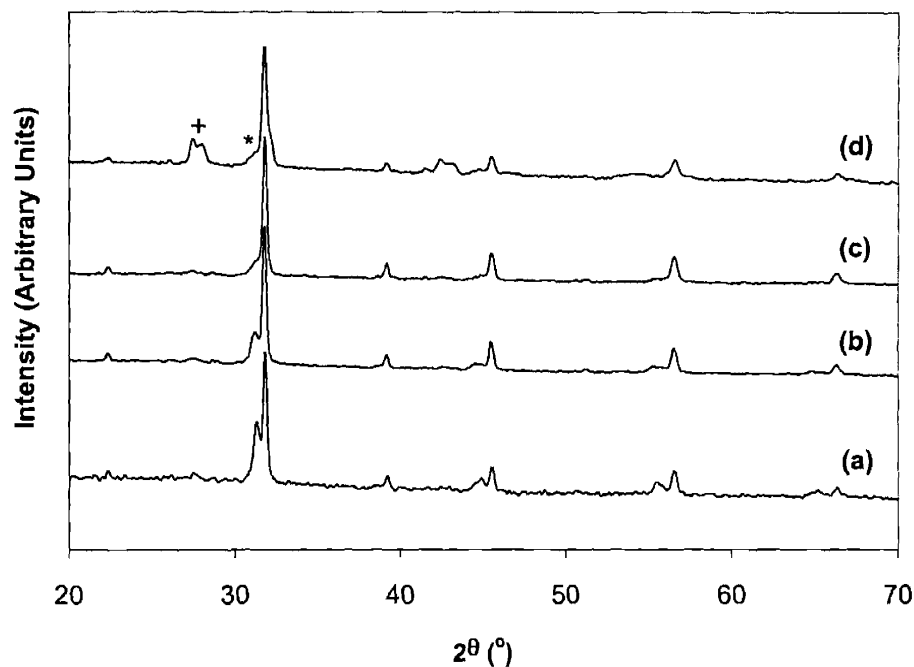
Figure 3.21. XRD patterns for $Ba_{0.5}Sr_{0.5}Co_{1-y}Sn_yO_3$ perovskites with a tin content (y) of (a) 0.20, (b) 0.15, (c) 0.10 and (d) 0.05, after calcination at $900^\circ C$ in air. XRD peaks denoted by "*" and "+" correspond to $Ba_{1-x}Sr_xSnO_3$ perovskite and $Ba_{1-x}Sr_xCo_{1-y}Sn_yO_3$ vacancy-ordered phase, respectively.

Oxygen flux measurements for $Ba_{0.5}Sr_{0.5}Co_{1-y}Sn_yO_3$ perovskites are shown in Figure 3.22. The Sn-doped perovskites exhibited oxygen fluxes of ~ 2.5 $cm^3(STP)/min/cm^2$ at $900^\circ C$. This was lower than the optimal fluxes obtained for Ti-doped perovskites (~ 3.0 $cm^3[STP]/min/cm^2$) and Fe-doped perovskites (~ 3.8 $cm^3[STP]/min/cm^2$). At $750^\circ C$, the oxygen flux increased with decreasing Sn^{4+} doping with y = 0.05 showing the highest oxygen flux of $\sim$ 1.0 $cc[STP]/min/cm^2$.
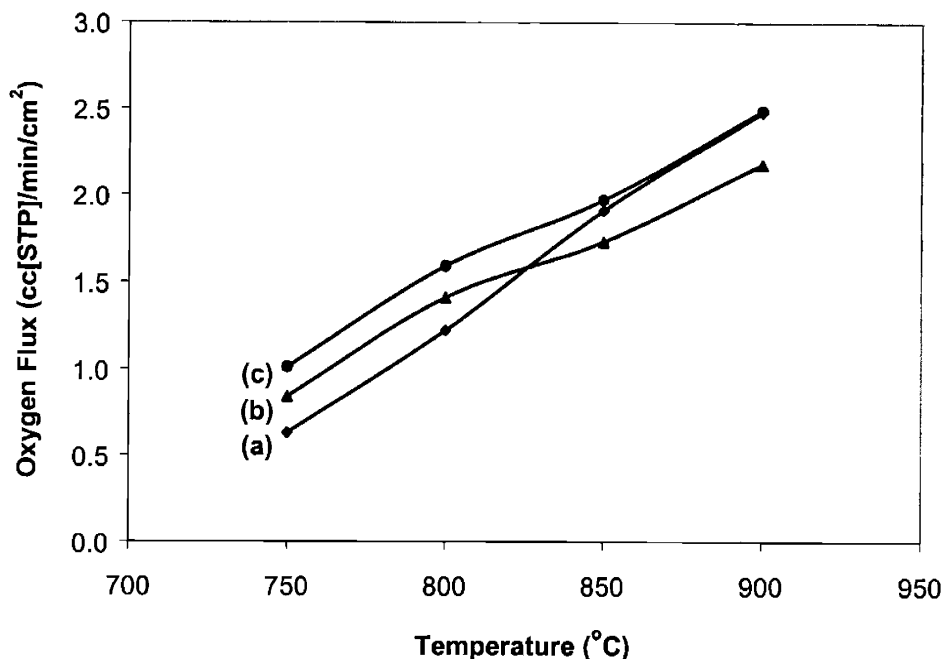
Figure 3.22. Oxygen flux of $Ba_{0.5}Sr_{0.5}Co_{1-y}Sn_yO_3$ perovskites with a tin content (y) of (a) 0.15, (b) 0.10 and (c) 0.05.

3.3.5 Crystal Structure and Oxygen Permeation of $Ba_{1-x}Sr_xCo_{1-y}Cr_yO_3$

Figure 3.23 shows the XRD patterns for $Ba_{1-x}Sr_xCo_{0.8}Cr_{0.2}O_3$ perovskites after calcination at 900°C in air. Chromium doping at the B site did not stabilize the perovskite structure at barium contents of 0-0.75. Moreover, a separate $BaCr_2O_4$ phase was observed on the addition of barium, indicating that chromium segregated to form a distinct phase, rather than replacing cobalt at the B site to stabilize the perovskite structure. It was concluded from this study that for stabilizing the perovskite phase of $Ba_{1-x}Sr_xCo_{1-y}M_yO_3$, Fe was the most effective dopant, followed by Ti, Sn and Cr. Using iron as the stabilizer dopant, the perovskite phase could be stabilized to a barium loading of 0.75, compared to only 0.25 for Ti and 0.00 for Cr, at a cobalt content of 0.80.

Figure 3.24 shows the oxygen flux for $Ba_{1-x}Sr_xCo_{0.8}Cr_{0.2}O_3$ perovskites at barium contents of 0.00 and 0.25. A sharp decrease in oxygen flux was observed on cooling, indicating a phase transformation from a highly conductive perovskite to a poorly conductive vacancy-ordered phase. The results suggested that the phase transformation occurred at ~ 800°C for $SrCo_{0.8}Cr_{0.2}O_3$, and at ~ 850°C for $Ba_{0.25}Sr_{0.75}Co_{0.8}Cr_{0.2}O_3$. As the barium content was increased, the perovskite phase became increasingly unstable, and the transformation temperature was

increased as expected. Moreover, on barium addition, the segregation of chromium into a $BaCr_2O_4$ phase resulted in a decreased chromium content at the B site, leading to a higher transformation temperature. At 900°C, $Ba_{0.25}Sr_{0.75}Co_{0.8}Cr_{0.2}O_3$ exhibited an oxygen flux of ~ 2.5 cc[STP]/min/cm^2, which was higher compared to ~ 1.5 cc[STP]/min/cm^2 for $SrCo_{0.8}Cr_{0.2}O_3$. This increase in oxygen flux with barium doping might be attributed to an increase in unit cell free volume.
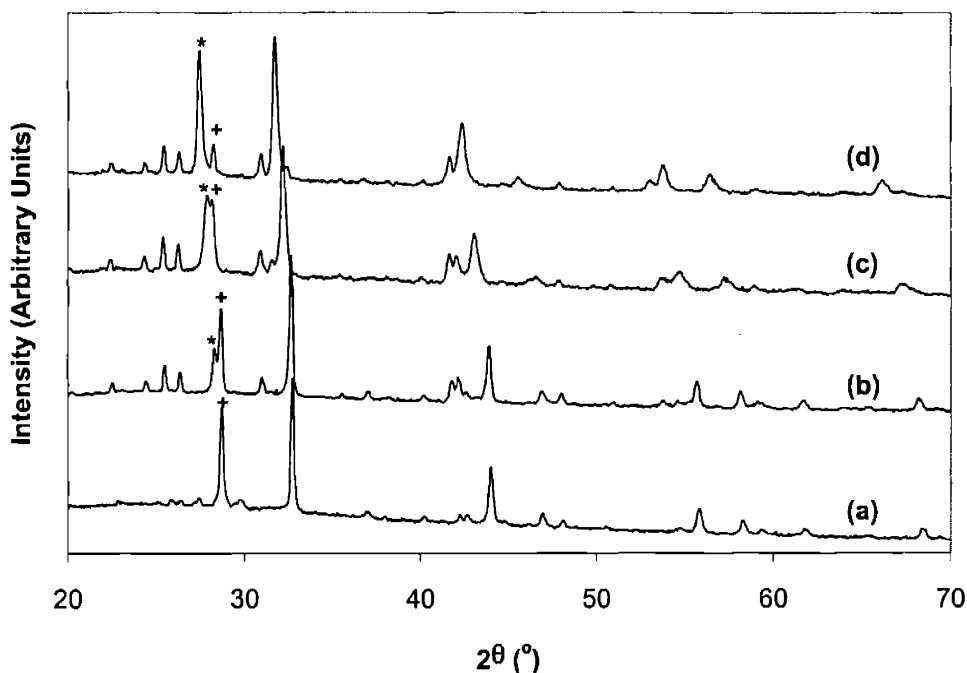
Figure 3.23. XRD patterns for $Ba_{1-x}Sr_xCo_{0.8}Cr_{0.2}O_3$ with a barium content (1-x) of (a) 0.00, (b) 0.25, (c) 0.50 and (d) 0.75, after calcination at 900°C in air. XRD peaks denoted by "*" and "+" correspond to $BaCr_2O_4$ and $Ba_{1-x}Sr_xCo_{0.8}Cr_{0.2}O_3$ vacancy-ordered phase, respectively.
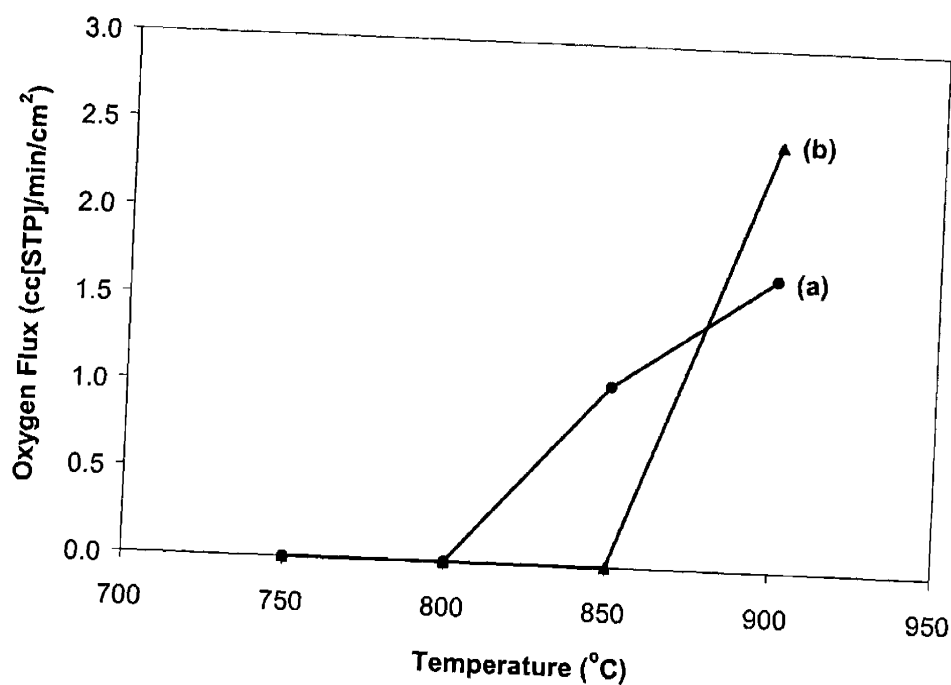
Figure 3.24. Oxygen flux in $Ba_{1-x}Sr_xCo_{0.8}Cr_{0.2}O_3$ perovskites with a barium content (1-x) of (a) 0.00 and (b) 0.25.

3.3.6 Oxygen Vacancy Concentration in $Ba_{1-x}Sr_xCo_{1-y}Fe_yO_{3-\delta}$

Oxygen vacancy concentration in $Ba_{1-x}Sr_xCo_{1-y}Fe_yO_{3-\delta}$ perovskites was measured using TGA as described in Section 3.2.3. A physical mixture of metal carbonate/oxide precursors was first calcined *in situ* to 1100-1250°C, depending on perovskite composition, to form a phase-pure, chemically homogeneous perovskite. The perovskite was then cooled at 1°C/min to determine the oxygen vacancy concentration in the desired temperature range of 600-1000°C. Figure 3.25 compares the XRD patterns of $Ba_{0.5}Sr_{0.5}Co_{0.8}Fe_{0.2}O_{3-\delta}$ perovskites prepared by *in situ* calcination of oxide/carbonate precursors in the TGA and by chemical co-precipitation followed by calcination to 900°C (as described in Chapter 2 [25]). *In situ* calcination yielded perovskite powders with excellent phase purity with the identical crystal structure as the co-precipitated powders. Therefore, the oxygen vacancy measurements performed on these powders were representative of phase-pure perovskites with controlled chemical composition.

128
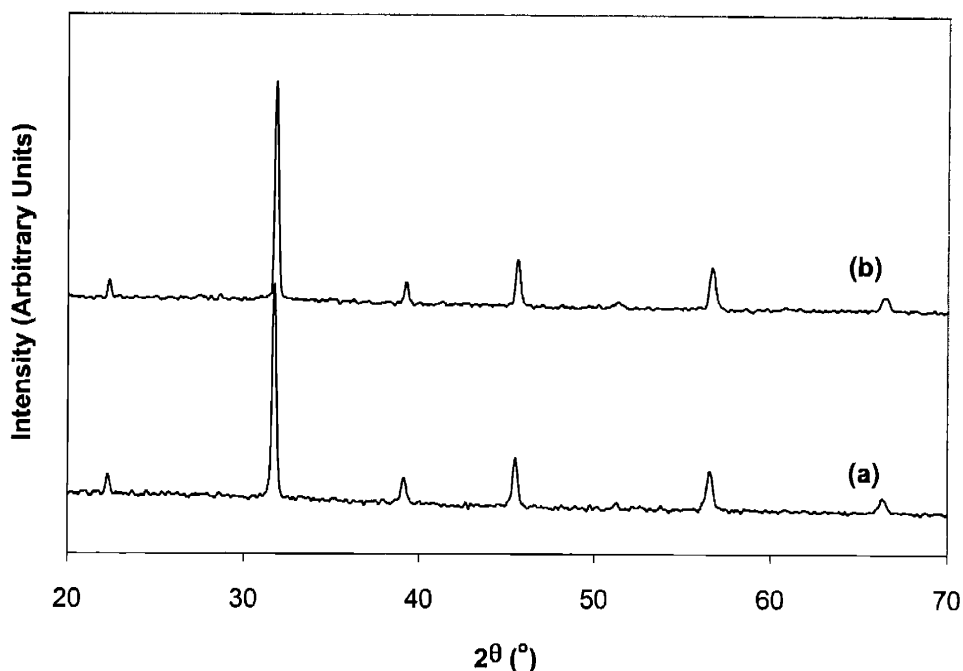
Figure 3.25. XRD patterns for $Ba_{0.5}Sr_{0.5}Co_{0.8}Fe_{0.2}O_3$ perovskite prepared by (a) *in situ* calcination of oxide/carbonate precursors in TGA at 1250°C, and (b) chemical co-precipitation followed by calcination at 900°C.

Figure 3.26 shows the dependence of oxygen vacancy concentration on barium content in $Ba_{1-x}Sr_xCo_{0.8}Fe_{0.2}O_{3-\delta}$ perovskites as a function of temperature in air. On decreasing temperature, perovskites with a barium content of 0.0 and 0.5 showed a gradual decrease in oxygen vacancy concentration. This was consistent with a thermally activated process for oxygen vacancy creation. The change in vacancy concentration with temperature could be fitted to an Arrhenius-type equation. Apparent activation energies for oxygen vacancy creation in $SrCo_{0.8}Fe_{0.2}O_{3-\delta}$ and $Ba_{0.5}Sr_{0.5}Co_{0.8}Fe_{0.2}O_{3-\delta}$ were ~ 600 J/mol and ~ 400 J/mol, respectively.

The oxygen vacancy concentration for perovskite with a barium content of 1.0 decreased dramatically at ~ 950°C, indicating a phase transformation. The vacancy concentration dropped from ~ 0.5 to ~ 0.2 on cooling from 950°C to 600°C. This suggested that the disordered $BaCo_{0.8}Fe_{0.2}O_{2.5}$ transformed to an ordered $BaCo_{0.8}Fe_{0.2}O_{2.8}$ phase. The latter has a structure with the general formula $A_nB_nO_{3n-1}$ with n = 5, which means that five perovskite-like, corner-shared BO_6 octahedra were separated by one layer of BO_4 tetrahedra stacked in a ...OOOOOTOOOOOT... sequence. The occurrence of this phase transformation on cooling $BaCo_{0.8}Fe_{0.2}O_{2.5}$ from high temperatures was consistent with the XRD results (Figure 3.4).

Figure 3.26 confirmed that the partial substitution of barium by strontium stabilized the disordered perovskite phase, and prevented long-range ordering of oxygen vacancies.
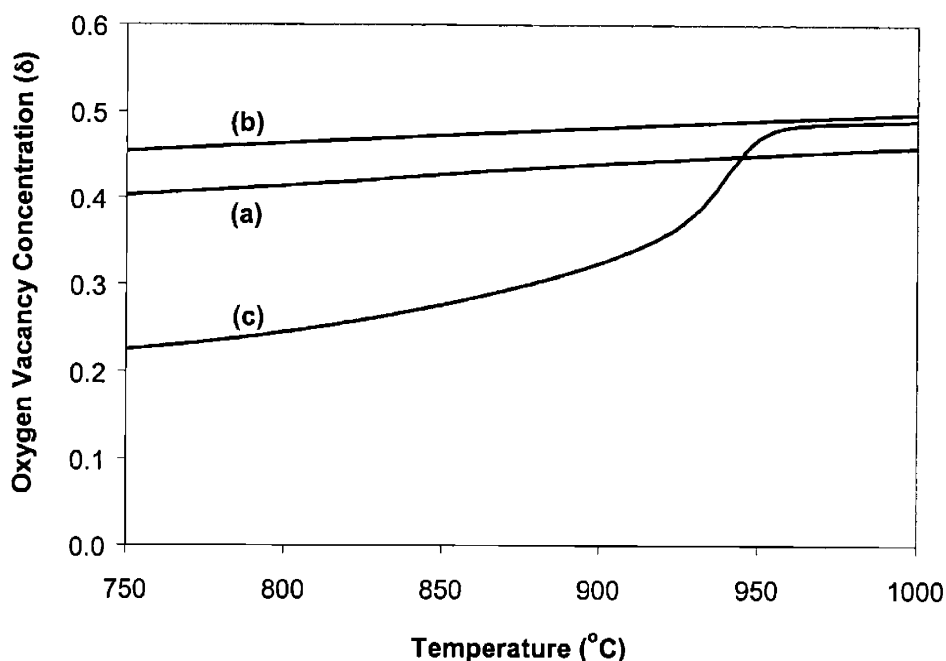
Figure 3.26. Oxygen vacancy concentration (δ) in $Ba_{1-x}Sr_xCo_{0.8}Fe_{0.2}O_{3-\delta}$ perovskites with a barium content (1-x) of (a) 0.0, (b) 0.5 and (c) 1.0.

The effect of the phase transformation on oxygen flux was shown in Figure 3.14. The dramatic decrease in oxygen flux for $BaCo_{0.8}Fe_{0.2}O_{2.5}$ on lowering the temperature could be attributed to a decrease in *both* the oxygen vacancy concentration and the mobility of these vacancies due to ordering effects. The combined effects resulted in an overall higher activation energy for oxide transport in $BaCo_{0.8}Fe_{0.2}O_{2.5}$, compared to the Sr-doped perovskites. The activation energy for oxide transport in $BaCo_{0.8}Fe_{0.2}O_{2.5}$ was equal to the sum of the activation energy for oxygen vacancy generation ($\sim$ 50 kJ/mol) and oxide ion hopping ($\sim$ 70 kJ/mol), which was in close agreement to the experimentally measured value of $\sim$ 144 kJ/mol (Figure 3.16).

Measurement of the oxygen vacancy concentration in $Ba_{1-x}Sr_xCo_{1-y}Fe_yO_{3-\delta}$ perovskites allowed for the determination of the average valence state of the B-site cations by applying a charge neutrality constraint. Since barium and strontium did not undergo changes in their +2 valence state and the oxygen vacancy concentration (δ) was known, the average charge on the Co and Fe cations can be determined. However, this method could not be used to determine how the average valence state was distributed between the Co and Fe cations.

The dependence of the average B-site valence state on barium content in $Ba_{1-x}Sr_xCo_{0.8}Fe_{0.2}O_{3-\delta}$ perovskites is shown in Figure 3.27 as a function of temperature. Mizuski *et al.* [21-24] have shown that the Co oxidation state in $La_{1-x}Sr_xCoO_{3-\delta}$ perovskites varied between +3 and +4, and approached +3 at higher temperatures (> 700°C) and at higher strontium contents (x > 0.6). This was in agreement with the results for $SrCo_{0.8}Fe_{0.2}O_{3-\delta}$ and $Ba_{0.5}Sr_{0.5}Co_{0.8}Fe_{0.2}O_{3-\delta}$, which showed an average B-site valence of about +3. However, the B-site oxidation state in $BaCo_{0.8}Fe_{0.2}O_{3-\delta}$ increased dramatically from about +3 to +3.6 on cooling from 950°C to 600°C. As oxygen ions were incorporated into the ordered structure, the average coordination number and valence state of the B-site cations would increase.
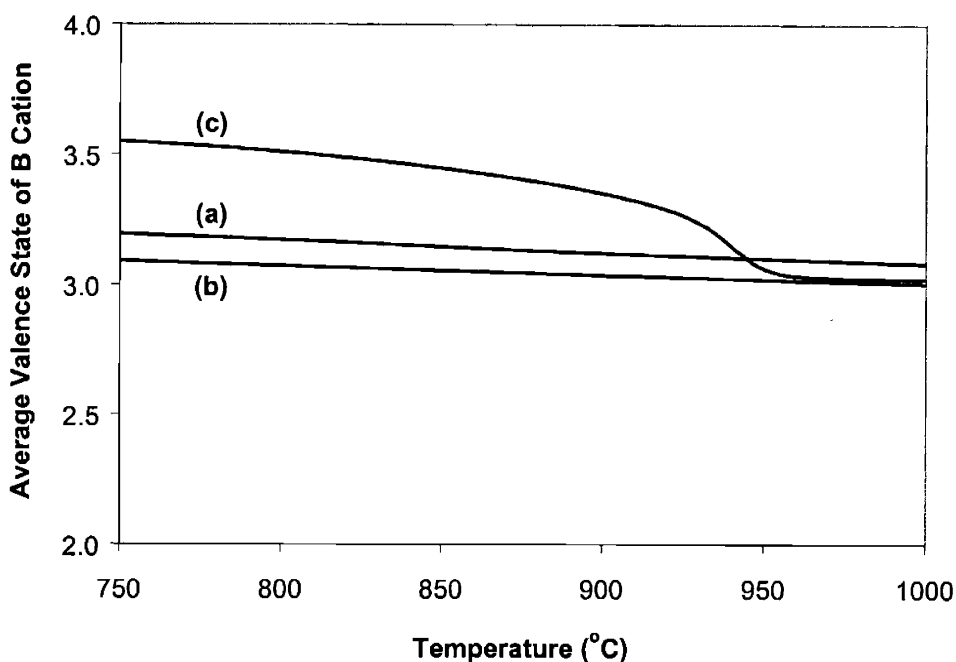
Figure 3.27. Average valence state of B cations in $Ba_{1-x}Sr_xCo_{0.8}Fe_{0.2}O_{3-\delta}$ perovskites with a barium content (1-x) of (a) 0.0, (b) 0.5 and (c) 1.0, measured in air using TGA.

Figure 3.28 shows the effect of iron content in $BaCo_{1-y}Fe_yO_{3-\delta}$ on the measured oxygen vacancy concentration. At a high iron content of ≥ 0.6, the vacancy concentration did not show a sudden decline with decreasing temperature, indicating that the disordered perovskite phase was stabilized. This result was consistent with XRD findings (Figure 3.3).

Since iron was less reducible than cobalt, it was possible that iron adopted an oxidation state of +4 in $Ba_{1-x}Sr_xCo_{1-y}Fe_yO_{3-\delta}$ perovskites. This would decrease the overall oxygen vacancy

concentration, and might provide a mechanism for stabilizing the perovskite structure. Kharton *et al.* [33, 34] reported that $SrCoO_3$ could be stabilized in the perovskite structure by partial replacement of Co^{3+} with transition metals of higher valency, such as Fe^{4+}, Cr^{4+} and Ti^{4+}; stabilization would not occur on doping with lower valency transition metals, such as Ni^{2+} and Cu^+.
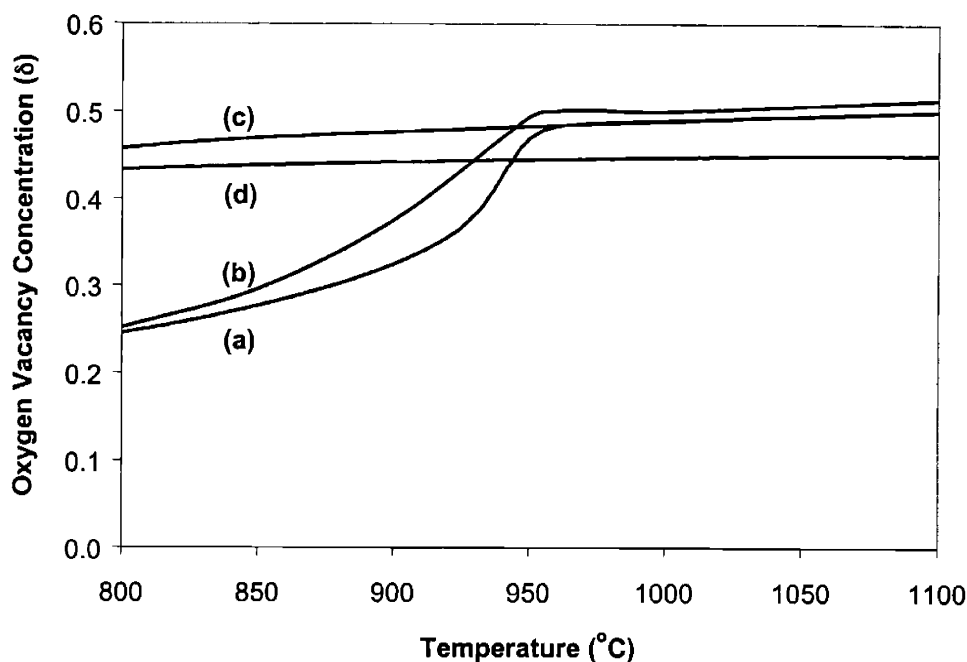
Figure 3.28. Oxygen vacancy concentration (δ) in $BaCo_{1-y}Fe_yO_{3-\delta}$ perovskites with an iron content (y) of (a) 0.2, (b) 0.3, (c) 0.6 and (d) 0.8.

The effect of iron doping on the oxygen vacancy concentration was investigated for $Ba_{0.5}Sr_{0.5}Co_{1-y}Fe_yO_{3-\delta}$ perovskites at 900°C in air (Figure 3.29). Figure 3.29 also shows the predicted oxygen vacancy concentration based on the assumption that Fe adopts a +3 or +4 oxidation state. It was clear from the experimental data that Fe cations were *not* predominantly in a +4 oxidation state, but in a +3 oxidation state upon incorporation into the $Ba_{0.5}Sr_{0.5}Co_{1-y}Fe_yO_{3-\delta}$ perovskite. Since the oxygen vacancy concentration did not decrease on iron doping, it was not a plausible mechanism for perovskite stabilization, in contrary to the results of Kharton *et al.* [33, 34]. Stabilization of the perovskite structure must be related to the local coordination preferences of iron and cobalt that disrupted the ordering of the oxygen vacancies. The contraction of the unit cell with increased iron content (Figure 3.7) suggested a 4-fold coordination preference for Fe^{3+} cations.
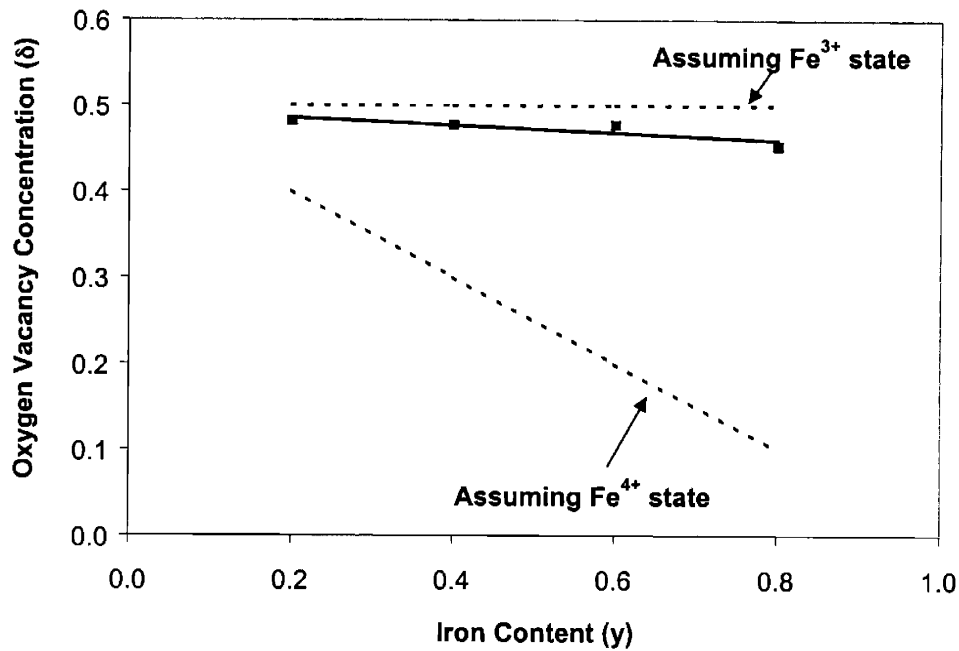
Figure 3.29. Measured (—) and predicted (---) oxygen vacancy concentration in $Ba_{0.5}Sr_{0.5}Co_{1-y}Fe_yO_{3-\delta}$ perovskites at 900°C in air.

During the phase transformation of $BaCo_{0.8}Fe_{0.2}O_{2.5}$ perovskite to $BaCo_{0.8}Fe_{0.2}O_{2.8}$ ordered phase, the vacancy concentration decreased from ~ 0.5 to ~ 0.2, as shown in Figure 3.26. This can be expressed in the form of a chemical equation as:

$$BaCo_{0.8}Fe_{0.2}O_{2.8} \quad + \quad heat \quad \leftrightarrow \quad BaCo_{0.8}Fe_{0.2}O_{2.5} \quad + \quad 0.15\ O_2 \qquad (3.2)$$

The transformation from a vacancy-ordered to a vacancy-disordered structure is an endothermic reaction, since energy is required to disrupt the energetically favored arrangement of vacancies in the ordered phase. Such a transformation generally occurs at high temperatures because the entropic contribution to the free energy becomes increasingly important with increasing temperature (since $G = H - TS$). Moreover, the movement of oxygen vacancies necessary to cause such a transformation increases with temperature, thus increasing the kinetics of such a transformation.

Figure 3.30 shows the effect of oxygen partial pressure on the order-disorder transformation of $BaCo_{0.8}Fe_{0.2}O_{3-\delta}$ perovskite. As the oxygen partial pressure decreased from 0.21 to 0.01 atm, the order-disorder transformation shifts to lower temperatures. It was important to note that the final oxygen content of the vacancy-ordered structure

$(BaCo_{0.8}Fe_{0.2}O_{2.8})$ was independent of the oxygen partial pressure. At low oxygen partial pressures, the material did not transform to an intermediate ordered phase with lower oxygen content (such as $BaCo_{0.8}Fe_{0.2}O_{2.67}$ and $BaCo_{0.8}Fe_{0.2}O_{2.75}$).
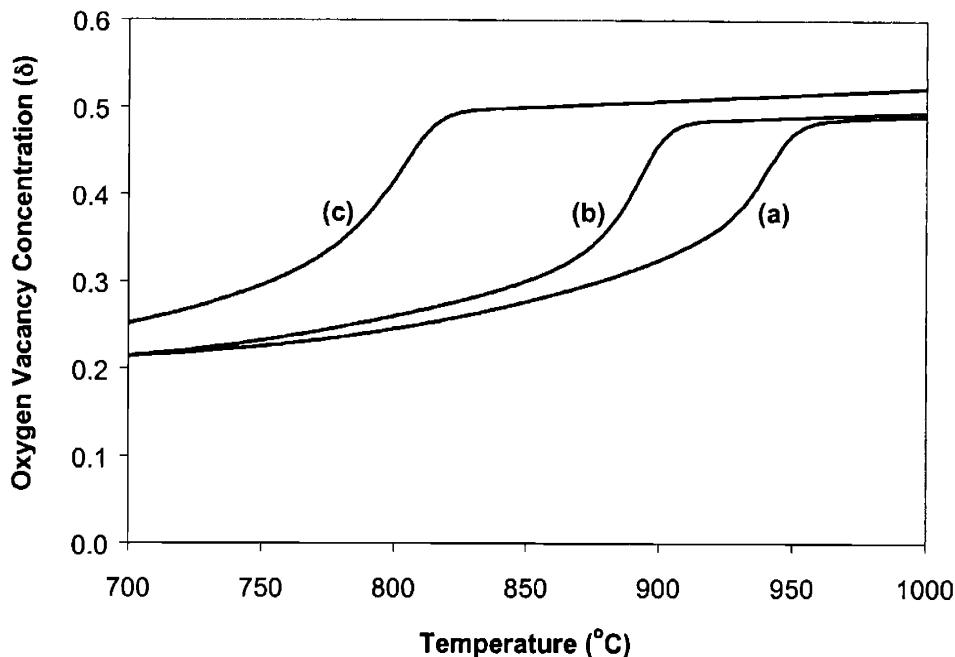
Figure 3.30. Oxygen vacancy concentration (δ) in $BaCo_{0.8}Fe_{0.2}O_{3-\delta}$ perovskite at an oxygen partial pressure of (a) 0.21, (b) 0.10 and (c) 0.01 atm, as measured by TGA.

There could be two reasons for the shifting of the order-disorder transformation to lower temperatures. As the oxygen concentration was decreased, it followed from Le Chatelier's principle that the transformation temperature should decrease, since the reaction was endothermic (Equation 3.2). This suggested that the perovskite phase was thermodynamically favored at higher temperatures and lower oxygen partial pressures. A second reason might be that the kinetics of this order-disorder transformation could be slower under oxygen-lean conditions. This was not the case, however, since the shape of the transformation curve did not suggest slower kinetics under oxygen-lean conditions.

3.3.7 Differential Thermal Analysis of Order-Disorder Transition

The transition from the perovskite phase to an ordered structure is an exothermic process due to the arrangement of vacancies in an energetically favorable configuration. This heat of

transition and the order-disorder temperature were investigated for $Ba_{1-x}Sr_xCo_{1-y}Fe_yO_{3-\delta}$ perovskites using DTA.

Figure 3.31 shows the DTA curves for $BaCo_{1-y}Fe_yO_{3-\delta}$ perovskites as a function of increasing cobalt content. These curves were measured on cooling the samples from a vacancy-disordered state at 1050 to 600°C. For an iron content of 0.4, an exothermic peak was observed at ~ 780°C with an accompanying heat of transition of -71 J/g. As the iron content was reduced to 0.2, the order-disorder transition was shifted to a higher temperature of ~ 880°C, indicating that the vacancy-ordered phase was energetically more favorable, consistent with an observed increase in the heat of transition to -91 J/g. At iron contents of 0.6 and 0.8, no transition to vacancy-ordered phase was detected, as consistent with the XRD results (Figure 3.3) and vacancy concentration profiles (Figure 3.28). This verified that the perovskite phase was stabilized by a high Fe content of ≥ 0.6 at the B site.
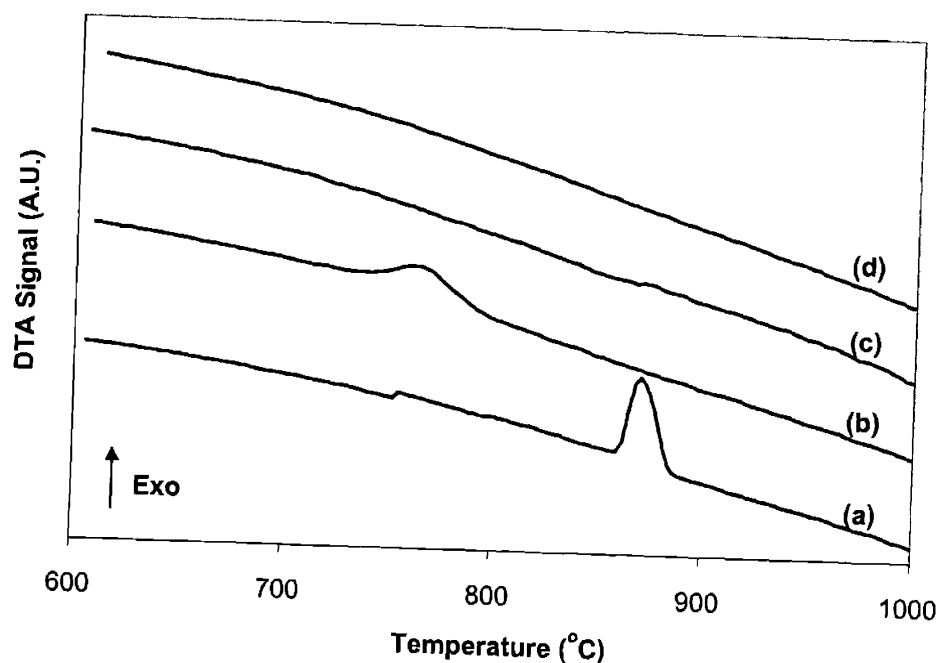
Figure 3.31. DTA curves for $BaCo_{1-y}Fe_yO_{3-\delta}$ perovskites with an iron content (y) of (a) 0.2, (b) 0.4, (c) 0.6 and (d) 0.8, on cooling from 1050 to 600°C in air.

Figure 3.32 shows the DTA curves for $Ba_{1-x}Sr_xCo_{0.8}Fe_{0.2}O_{3-\delta}$ perovskites as a function of increasing barium content. Partial substitution of strontium for barium stabilized the perovskite structure, as consistent with the XRD results (Figure 3.4) and vacancy concentration measurements (Figure 3.26). Highest oxygen fluxes were obtained with x = 0.25, while

maintaining stability of the perovskite structure. Further increase in barium content would lead to transformation to an ordered phase, resulting in lower fluxes and membrane instability.
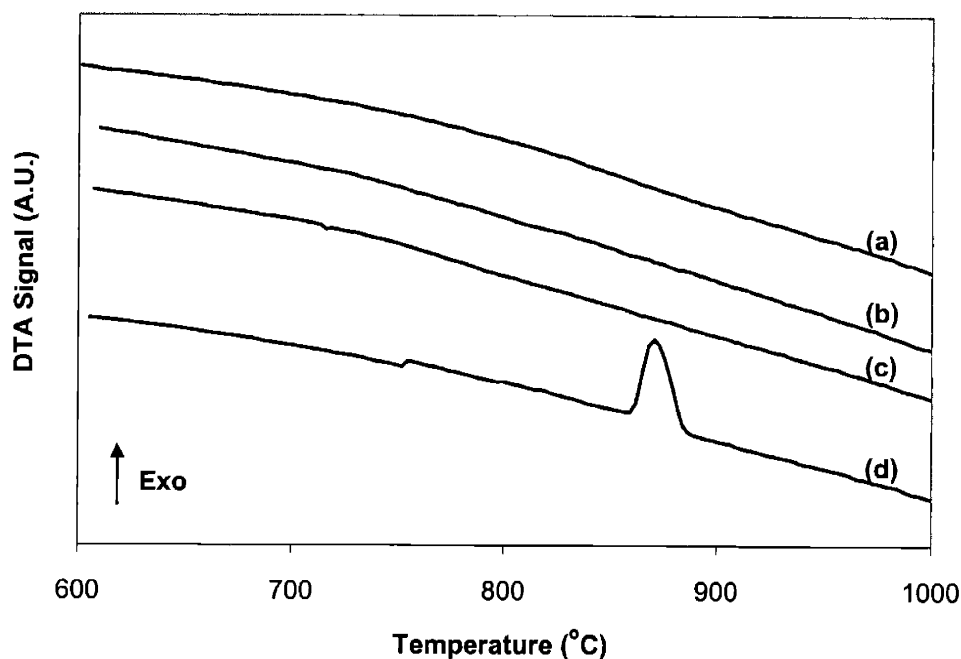
Figure 3.32. DTA curves for $Ba_{1-x}Sr_xCo_{0.8}Fe_{0.2}O_{3-\delta}$ perovskites with a barium content (1-x) of (a) 0.25, (b) 0.50, (c) 0.75 and (d) 1.00, on cooling from 1050 to 600°C in air.

3.4 Conclusions

Mixed conducting $Ba_{1-x}Sr_xCo_{1-y}M_yO_{3-\delta}$ perovskite membranes were developed for oxygen separation applications. $Ba_{0.75}Sr_{0.25}Co_{0.8}Fe_{0.2}O_{3-\delta}$ showed a very high oxygen flux of ~ 3.8 $cm^3[STP]/min/cm^2$ at 900°C. $Ba_{0.25}Sr_{0.75}Co_{0.8}Ti_{0.2}O_{3-\delta}$ exhibited an oxygen flux of ~ 1.4 $cm^3[STP]/min/cm^2$ at 750°C with excellent stability over time. These oxygen fluxes were ~ 2 times higher than those reported for the "best" existing membrane materials. As the operating temperature decreased, it became increasingly important that the perovskite structure be stabilized through compositional control. The more stable perovskites would exhibit higher oxygen fluxes at 750°C, and show the desired flux stability over time.

High oxygen fluxes were obtained by creating a high oxygen vacancy concentration (~ 15% of oxygen lattice sites) by extrinsic doping, and by increasing the unit cell free volume to allow facile oxide ion hopping. However, at high oxygen vacancy concentrations and high lattice free volumes, the perovskite structure was found to become increasingly unstable, resulting in a phase transformation to a vacancy-ordered structure. Therefore, the challenge in

developing these membranes was to prevent this phase transformation from occurring, or lower the transition temperature below the desired operating temperature range of 750-900°C. This was accomplished by doping various cations in place of Co at the B site. Iron was found to be the most effective dopant for stabilizing the perovskite phase, followed by titanium and tin. The degree of stabilization increased with increasing iron doping at the B site, and the most stable compositions were suitable for low-temperature oxygen separation.

The transformation from the perovskite phase to a vacancy-ordered phase was found to occur with the incorporation of lattice oxygen and with a release of energy. The transformation temperature was found to decrease with decreasing oxygen partial pressure, which is thermodynamically consistent. By understanding the order-disorder transformation in relation to perovskite composition, operating temperature and imposed oxygen gradient, insights into successful application of these perovskite membranes are gained.

3.5 References

[1]   Balachandran, U., Dusek, J.T., Sweeney, S.M., Poeppel, R.B., Mieville, R.L., Maiya, P.S., Kleefisch, M.S., Pei, S., Kobylinski, T.P., Udovich, C.A., and Bose, A.C., *Am. Ceram. Soc. Bull.* **74**, 71 (1995).

[2]   Tsai, C.-Y., Dixon, A.G., Ma, Y.H., Moser, W.R., Pascucci, M.R., *J. Am. Ceram. Soc.* **81**, 1437 (1998).

[3]   Pei, S., Kleefisch, M.S., Kobylinski, T.P., Faber, K., Udovich, C.A., Zhang-McCoy, V., Dabrowski, B., Balachandran, U., Mieville, R.L., Poeppel, R.B., *Catal. Lett.* **30**, 210 (1995).

[4]   Elshof, J.E., Bouwmeester, H.J.M., Verweij, H., *Appl. Catal. A.: Gen.* **130**, 195 (1995).

[5]   Nozaki, T., Fujimoto, K., *AIChE J.* **40**, 870 (1994).

[6]   Zheng, Y., Akin, F.T., Lin, Y.S., *Appl. Catal. A.: Gen.* **213**, 33 (2001).

[7]   Hibino, T., Sato, T., Ushiki, K.-I., Kuwahara, Y., *J. Chem. Soc. Faraday Trans.* **91**, 4419 (1995).

[8]   Wang, W., Lin, Y.S., *J. Mem. Sci.* **103**, 219 (1995).

[9]   Saracco, G., Specchia, V., *Catal. Rev.-Sci. Eng.* **36**, 303 (1994).

[10]   Teraoka, Y., Zhang, H.M., Furukawa, S., Yamazoe, N., *Chem. Lett.*, 1743 (1985).

[11]   Teraoka, Y., Nobunaga, T., Yamazoe, N., *Chem. Lett.*, 503 (1988).

[12] Teraoka, Y., Nobunaga, T., Okamoto, K., Miura, N., Yamazoe, N., *Solid State Ionics* **48**, 207 (1991).

[13] Teraoka, Y., Zhang, H.M., Okamoto, K., Yamazoe, N., *Mater. Res. Bull.* **23**, 51 (1998).

[14] Van Doorn, R.H.E., Kruidhof, H., Bouwmeester, H.J.M., Burggraaf, A.J., *Mater. Res. Soc. Symp. Proc.* **369**, 377 (1995).

[15] Weber, W.J., Stevenson, J.W., Armstrong, T.R., Pederson, L.R., *Mater. Res. Soc. Symp. Proc.* **369**, 395 (1995).

[16] Miura, N., Okamoto, Y., Tamaki, J., Morinag, K., Yamazoe, N., *Solid State Ionics* **79**, 195 (1995).

[17] Iwahara, H., Esaka, T., Mangahara, T., *J. Appl. Electrochem.* **18**, 173 (1988).

[18] Kruidhof, H., Bouwmeester, H.J.M., van Doorn, R.H.E., Burggraaf, A.J., *Solid State Ionics* **63-65**, 816 (1993).

[19] Qiu, L., Lee, T.H., Lie, L.-M., Yang, Y.L., Jacobson, A.J., *Solid State Ionics* **76**, 321 (1995).

[20] Liu, L.M., Lee, T.H., Qiu, L., Yang, Y.L., Jacobson, A.J., *Mater. Res. Bull.* **31**, 29 (1996).

[21] Mizusaki, J., Yoshihiro, M., Yamauchi, S., Fueki, K., *J. Solid State Chem.* **58**, 257 (1985).

[22] Mizusaki, J., Yoshihiro, M., Yamauchi, S., Fueki, K.J., *J. Solid State Chem.* **67**, 1 (1987).

[23] Mizusaki, J., Yamauchi, S., Fueki, K., Ishikawa, A., *Solid State Ionics* **12**, 119 (1984).

[24] Mizusaki, J., Mima, Y., Yamauchi, S., Fueki, K., Tagawa, H., *J. Solid State Chem.* **80**, 102 (1989).

[25] Sangar, N., Chakravorty, R., Ying, J.Y., to be submitted to *Chem. Mater.*

[26] Sangar, N., Ying, J.Y., to be submitted to *J. Catal.*

[27] Goldschmidt, V.M., *Akad. Oslo.* **A42**, 224 (1946).

[28] Yamamura, H., Yamada, Y., Mori, T., Atake, T., *Solid State Ionics* **108**, 377 (1998).

[29] Hayasi, H., Inaba, H., Matsuyama, M., Lan, N.G., Dokiya, M., Tagawa, H., *Solid State Ionics* **122**, 1 (1999).

[30] Shannon, R.D., *Acta Crystall.* **A32**, 751 (1976).

[31] Cook, R.L., Sammells, A.F., *Solid State Ionics* **45**, 311 (1991).

[32]   Sammells, A.F., Cook, R.L., White, J.H., Osborne, J.J., MacDuff, R.C., *Solid State Ionics*, **52**, 111 (1992).

[33]   Kharton, V.V., Li, S.B., Kovalevsky, A.V., Naumovich, E.N., *Solid State Ionics* **96**, 141 (1997).

[34]   Kharton, V.V., Yaremchenko, A.A., Kovalevsky, A.V., Viskup, A.P., Naumovich, E.N., Kerko, P.F., *J. Memb. Sci.* **163**, 307 (1999).

4 – Crystal Structure and Oxide Conductivity of $BaCo_{1-y}M_yO_3$-based Perovskites

4.1 Introduction

The primary challenge in the application of ceramic membranes for oxygen separation lies in developing novel compositions with high oxide conductivity and oxygen flux stability. In Chapter 3, $Ba_{1-x}Sr_xCo_{1-y}M_yO_3$ perovskites were developed with high oxygen fluxes of 3.8 cm^3[STP]/min/cm^2 at 900°C and 1.4 cm^3[STP]/min/cm^2 at 750°C [1]. These fluxes were ~ 2 times higher than the "best" oxygen fluxes achieved by existing membranes.

The strategy for increasing oxygen flux was to maximize the unit cell free volume of the perovskite structure, without causing phase transformation to an ordered structure. As the barium and/or cobalt contents were increased, the oxygen flux was found to increase, reaching a maximum at an optimal composition followed by a sharp decline due to vacancy-ordering effects. At a given temperature, the optimal composition was found to have the highest barium and cobalt contents that could be tolerated by the perovskite structure, without resulting in phase transformation. At higher temperatures where vacancy-ordering effects were minor, perovskites with high barium and cobalt contents exhibited the highest oxygen fluxes. At lower temperatures where vacancies began to associate, perovskites with higher strontium and iron contents showed the highest stable oxygen fluxes.

The role of dopants at the B site was to stabilize the perovskite structure so as to significantly increase oxygen fluxes in the desired temperature range of 750-900°C. It was found that iron was more effective than titanium, tin or chromium as the B-site dopant, stabilizing the perovskite structure while allowing higher barium doping at the A site, thereby resulting in larger unit cell free volume and higher oxygen flux [1]. High iron contents (y ≥ 0.6) were required to stabilize perovskites with barium at the A site. Oxygen fluxes for the resulting cubic perovskites were low (< 2.0 cm^3[STP]/min/cm^2 at 900°C), since the concentration of mobile oxygen vacancies was dramatically decreased at high iron contents.

From the standpoint of increasing oxygen flux by increasing unit cell free volume, it would be desirable to synthesize perovskites with barium at the A site, since it is the largest Group IIA element. It is also necessary to have a high concentration of mobile oxygen vacancies, and therefore, the concentration of any stabilizer cation(s) at B site needs to be minimized to prevent vacancy trapping. Thus, the objective of this study is to develop novel

strategies to stabilize $BaCo_{0.8}M_{0.2}O_3$ perovskites in a vacancy-disordered, cubic phase to achieve excellent oxygen fluxes.

There are currently no reports in the literature claiming a fully-stabilized, cubic $BaCo_{0.8}M_{0.2}O_3$ perovskite. Brinkman *et al.* [2] partially stabilized barium cobalite through yttrium substitution at the A site. Since yttrium has a smaller ionic radius and a higher valence state than barium, it could partially stabilize the perovskite structure. However, the measured oxygen flux for $Ba_{1-x}Y_xCoO_3$ was lower than the "best" mixed conductors reported in literature, e.g., $SrCo_{0.8}Fe_{0.2}O_3$. The presence of a poorly conductive, secondary phase lowered the overall oxide conductivity, resulting in low oxygen fluxes. Teraoka *et al.* [3-6] have investigated $La_{1-x}Ba_xCo_{0.8}Fe_{0.2}O_3$ perovskites with low Ba contents for oxygen separation. High La^{3+} loadings at the A site were required to stabilize the perovskite structure, resulting in low oxygen vacancy concentration, and therefore, low oxygen fluxes. In contrast, our approach is to stabilize barium cobalite using low doping levels ($y \leq 0.2$) of stabilizer cation(s) at the B site, thereby not significantly altering the oxygen vacancy concentration and the unit cell free volume of $BaCoO_3$, which are essential in achieving high oxygen fluxes.

The presence of oxygen vacancies in the perovskite structure must result in reduced coordination of the A- and B-site cations. Depending on the vacancy concentration, a fraction of the B-site cations may be penta- or tetrahedrally-coordinated to oxide ions, instead of octrahedrally coordinated in an ideal perovskite structure with no vacancy defects. If the oxygen vacancies are randomly arranged in the structure, the cations would have randomly reduced coordination. In general, however, transition metal or semimetal cations have preferred coordinations for their particular oxidation state, and these preferences provide an energetic driving force for ordering [7].

There are a large number of vacancy-ordering patterns for oxygen-deficient perovskites corresponding to the general formula $A_nB_nO_{3n-1}$ [8]. Compounds containing ordered vacancies are found for n = 5, 4, 3, 2, 1.5, 1.33 and 1, i.e. for overall oxygen contents of 2.8, 2.75, 2.67, 2.5, 2.33, 2.25 and 2. Perovskite systems are found to be quite specific in their tendency to form ordered structures in that only selected values of n are stable for a particular composition. This is consistent with results obtained for $BaCo_{0.8}Fe_{0.2}O_3$ perovskite, which shows transformation to an ordered structure with n = 5, without the formation of intermediate structures with n = 4 or 3 even at low oxygen partial pressures (see Section 3.3.4, [1]). Anderson *et al.* [8] have shown that

the driving force for the formation of a specific vacancy-ordered structure depends strongly upon the size and electronic configuration of the B cation, in addition to the size and coordination preference of the A-site cation. The physical and chemical differences in the A- and B-site cations from compound to compound account for the wide variety of known vacancy patterns.

Ordering of oxygen vacancies confines vacancies two-dimensionally just as though the long-range structure is of lower symmetry, which is consistent with the appearance of additional diffraction peaks for $BaCo_{0.8}Fe_{0.2}O_3$ perovskite (Figure 3.3, [1]). Since this cooperative ordering of oxygen vacancies inhibits transport, the best strategy is to develop cubic perovskites with true local random disorder. Our approach for creating local random disorder of oxygen vacancies is to synthesize perovskite compositions with local random disorder of B-site cations, with the expectation that the arrangement of oxygen vacancies will reflect this disorder. Since each transition metal has its own bond strength and coordination preference to an oxide ion, doping a variety of transition metals at the B site can potentially prevent the local ordering of oxygen vacancies. This "mixing pot" approach may frustrate the system from establishing local periodicity, which is necessary for achieving long-range ordering. For this approach to be successful in stabilizing $BaCo_{0.8}M_{0.2}O_3$ perovskites, the B-site dopants must form a solid solution and be randomly arranged without the formation of secondary phases.

Since the transformation of a vacancy-disordered perovskite to a vacancy-ordered structure is thermodynamically driven, it is necessary to examine whether this "mixing pot" approach is thermodynamically feasible. In introducing a variety of dopants at the B site, the oxide ions or oxygen vacancies coordinated to the B-site cations must have different energies. Therefore, the most stable arrangement of oxygen vacancies will have to account for these different random energies of the various oxygen sites. Hence, the most stable configuration of these vacancies may not be the one in which they are ordered along specific crystallographic directions, but may be completely or partially disordered, thereby reflecting the disorder at the B sites. In effect, the introduction of B-site dopants into the perovskite structure can potentially stabilize the disordered phase by randomly changing the energies of the oxygen sites. Since it lowers the heat of transition for vacancy ordering while keeping the entropic contribution constant, the overall free energy for the formation of an ordered phase becomes less favorable. Therefore, this "mixing pot" approach is thermodynamically feasible, and may potentially stabilize $BaCo_{0.8}M_{0.2}O_3$ perovskite in a vacancy-disordered phase.

In addition to oxygen fluxes, it is important to measure the oxide conductivity in these perovskites, since it is an intrinsic property of the material, and does not depend on specific measurement conditions. As oxygen transport in these perovskites is generally considered to occur via a vacancy hopping mechanism, the oxide conductivity σ_{ion} can be related to the oxygen vacancy concentration $[V_O]$ and vacancy diffusion coefficient D_v using the Nernst-Einstein relationship:

$$\sigma_{ion} = \frac{4F^2[V_O]D_v}{RTV_m} \tag{4.1}$$

where F is Faraday's constant, T is the absolute temperature, R is the universal gas constant, and V_m is the perovskite molar volume. The Nernst-Einstein relationship assumes that the oxygen vacancies are fully ionized and *all* contribute to transport, i.e. oxygen vacancies do not associate or interact with each other to form complex structures. Clearly, the $Ba_{1-x}Sr_xCo_{1-y}M_yO_3$ perovskites investigated in this study do not satisfy this assumption as they possess a very high oxygen vacancy concentration and have been found to form long-range ordered structures [1]. A possible modification of the Nernst-Einstein relationship to account for these interactions between oxygen vacancies would be to replace the vacancy concentration by a vacancy "activity," which is analogous to solution thermodyanmics where concentration is replaced by activity to account for non-ideal behavior. The accompanying activity coefficient would account for the deviation from ideality, including the interactions between oxygen vacancies or between vacancies and metal cations, etc. The modified Nernst-Einstein relationship can be written as:

$$\sigma_{ion} = \frac{4F^2\gamma[V_O]D_v}{RTV_m} \tag{4.2}$$

where γ represents the activity coefficient for oxygen vacancies. This approach can be further developed only if the vacancy diffusion coefficient can be independently measured, thereby allowing the determination of the activity coefficient. Several researchers [9-11] have performed tracer diffusion studies on single-crystal and polycrystalline perovskites to measure the vacancy diffusion coefficient on a limited number of perovskite compositions.

4.2 Experimental

$BaCo_{1-y}M_yO_3$ perovskites were synthesized using chemical co-precipitation followed by calcination at $900°C$ in air, as outlined in Chapter 2 [12, 13]. To determine the success of our approach in stabilizing $BaCo_{1-y}M_yO_3$ in the perovskite structure, X-ray diffraction (XRD), differential thermal Analysis (DTA), and oxygen flux measurements were employed. XRD identified the crystal structure of the metal oxide on cooling to room temperature. A Siemens D5000 θ-θ diffractometer (45 kV, 40 mA, Cu-Kα) was used. DTA (Perkin Elmer DTA7 Thermal Analyzer) was used to detect whether an order-disorder transition occurred, and determine the extent of vacancy ordering through the heat of transition (see Section 3.2.2, [1]). Oxygen flux measurements were utilized to characterize the oxide conductivity, and thereby the extent of vacancy ordering. They were performed on sintered 0.8 mm-thick membranes at 750-$900°C$ under an oxygen gradient of 0.21 to 0.01 atm, following the procedures described in Section 3.2.1 [1].

4.2.1 Measurement of Oxide Conductivity

Oxide conductivity of $Ba_{1-x}Sr_xCo_{1-y}M_yO_3$ was determined from oxygen flux measurements under integral and differential conditions. Due to the presence of transition metals at the B site, these perovskites have very high electronic conductivity. In fact, the transference number for electronic charge carriers is close to unity, indicating that the total electrical conductivity is almost equal to the electronic conductivity in these materials. Hence, it becomes very challenging to experimentally measure the relatively small oxide conductivity. Measurement of oxide conductivity is critical for establishing a relationship between the perovskite structure and associated defect chemistry to the macroscopic transport properties. Since the concentration and mobility of oxygen vacancies can depend strongly on temperature and oxygen partial pressure, it is important to measure the dependence of oxide conductivity on these operating conditions. Oxygen flux measurements, as performed in Chapter 3 [1], provide a means to characterize the average oxide conductivity in a particular perovskite, by measuring the oxygen flux under a large imposed gradient in oxygen partial pressure. This measurement does not provide information on the local variation in oxide conductivity within the membrane from changes in oxygen partial pressure.

The traditional 4-point DC method used to measure the oxide conductivity of a predominantly electronic conductor employs yttria-stabilized zirconia (YSZ) electrodes to effectively "block" the electronic current, while allowing the flow of oxide ions. The major drawback of this approach is the difficulty in effectively blocking all of the electronic current; short-circuiting paths for oxygen transport can occur, such as diffusion along the oxide surface or via the gas phase through rapid exchange, leading to overestimates of the oxide conductivity. Also, interfacial reactions can occur between the perovskite and YSZ layers, preventing the use of a co-sintering approach to suppress parasitic contributions to oxygen transport. Teraoka et al. [2-5] have performed oxide conductivity measurements on several lanthanum cobalite perovskites using a 4-point electron-blocking conductivity method.

To accurately determine the oxide conductivity contribution in $Ba_{1-x}Sr_xCo_{1-y}M_yO_3$ perovskites, oxygen flux measurements were performed on dense pellets (as described in Section 3.2.1 [8]) under isothermal, steady state conditions as a function of oxygen partial pressure. In the differential mode, the oxygen flux through the membrane was measured between a *small* imposed gradient in oxygen partial pressure. The oxide conductivity could be easily determined using the following simplified Wagner equation [14, 15]:

$$J_{O2} = \frac{-RT}{4^2 F^2 L} \int_{\ln P'_{O2}}^{\ln P''_{O2}} \sigma_{ion} \, d\ln P_{O2} \qquad (4.3)$$

This equation is derived assuming local equilibrium of defect concentrations with varying oxygen partial pressure, and a predominantly electronic conductor. Assuming that the imposed oxygen partial pressure is sufficiently small so that the oxide conductivity remains fairly constant, the Wagner equation can be simplified to:

$$\sigma_{ion}(T, P_{O2}) = \frac{-4^2 F^2 L}{RT} \frac{J_{O2}}{\ln P''_{O2} - \ln P'_{O2}} \qquad (4.4)$$

In the integral mode, the oxygen flux (J_{O2}) through the membrane was measured by fixing the oxygen partial pressure in the air chamber at 0.21 atm, while slowly decreasing the oxygen partial pressure (P_{O2}) in the helium chamber from 0.21 to 0.01 atm (see Figure 3.1). The oxide conductivity was obtained by taking the derivative of Equation 4.3 with respect to $\ln(P_{O2})$:

$$\sigma_{ion}(T, P_{O2}) = \frac{-4^2 F^2 L}{RT} \frac{\partial J_{O2}}{\partial \ln P_{O2}}\bigg|_{\ln P_{O2}} \qquad (4.5)$$

Hence, at a desired oxygen partial pressure, the oxide conductivity was determined using the slope of a plot of J_{O2} vs. $\ln(P_{O2})$.

The main challenge in using the differential and integral methods to characterize the oxide conductivity lies in accurately determining the oxygen partial pressures close to the membrane surfaces. The advantage of the differential method is that the oxygen partial pressures near the membrane surfaces can be calculated with greater accuracy compared to the integral mode since oxygen fluxes are small. However, the integral mode has the advantage of measuring the oxide conductivity under realistic oxygen gradients and oxygen vacancy drift velocities. Both methods will be employed for the measurement of oxide conductivity. It is important to note that the above equations for determining oxide conductivity do not contain any simplification/assumption based on the defect chemistry of metal oxides, and therefore can be applied to any oxide mixed conductor possessing predominantly electronic conductivity.

4.3 Results and Discussion

4.3.1 Crystal Structure and Oxygen Permeation of $BaCo_{0.8}M_{0.2}O_{3-\delta}$

$BaCo_{0.8}M_{0.2}O_{3-\delta}$ perovskites containing different dopants, including Sn^{4+}, Ti^{4+}, Fe^{3+}, Ce^{4+}, Ni^{2+}, Ga^{3+} and Zr^{4+}, were synthesized by solid-state reaction of the constituent metal oxides and/or carbonate precursors at 1050°C in air. These dopants were selected based on three desired characteristics of the stabilizer cation: (1) it should have an ionic radius larger than Co^{3+}, but not too large to prevent substitution, (2) it should adopt a higher valence state or be less reducible than Co^{3+}, and (3) it should form stable perovskites with Ba^{2+} or have Goldschmidt factors closer to unity than pure $BaCoO_3$. These criteria were established in consideration of the causes for $BaCoO_3$ instability. There is a size mismatch between barium and cobalt, which renders the resulting perovskite highly unstable. The use of a stabilizer cation having a larger ionic radius than cobalt can potentially reduce this size mismatch, provided that the dopant is not too large to give rise to phase segregation. Moreover, stabilizer cations, which form stable perovskite

structures with barium, may prefer octahedral coordination with oxide ions. Since the "ideal" coordination of B-site cations in the perovskite structure is octahedral, introducing the stabilizer cations at the B site may "force" the remaining cobalt cations to also adopt an octahedral coordination. As $BaCoO_3$ has a large oxygen vacancy concentration, significant interactions between the vacancies may result in formation of ordered structures. By introducing metal cations with different valence and reducibility at the B site, the local ordering of oxygen vacancies can potentially be disrupted. Higher valence and lower reducibility are preferred to prevent any further increase in the overall vacancy concentration, which would result in increased ordering effects.

Table 4.1 lists several physical properties of these dopants, namely, their ionic radius [16] and valence state, Goldschmidt factor of a potential $BaMO_3$ perovskite, and whether such an oxide commonly adopts a perovskite structure under the relevant temperatures and oxygen partial pressures. It can be seen that all of the selected dopants have at least one property that is consistent with the above criteria, with only Sn^{4+} adequately satisfying all three desired characteristics. $BaSnO_3$ adopts a perovskite structure, with Sn^{4+} octahedrally coordinated to the oxide ions. In addition, Sn^{4+} has a larger ionic radius and higher valence compared to Co^{3+}. Based on the criteria, the efficacy of the selected cations for stabilizing $BaCo_{0.8}M_{0.2}O_{3-\delta}$ is expected to decrease in the order: Sn > Fe ~ Zr > Ti > Ce > Ga > Ni > Co.

Figure 4.1 shows the XRD patterns for $BaCo_{0.8}M_{0.2}O_3$ perovskites after calcination at 1050°C, and cooling to room temperature in air. None of the dopants were successful in stabilizing the high-temperature vacancy-disordered phase of $BaCo_{0.8}M_{0.2}O_3$. The observed XRD patterns were representative of different ordered structures that formed on cooling to room temperature. This indicated that the local vacancy arrangement was strongly governed by the B-site cation, and could be manipulated through the appropriate selection of dopant. This was consistent with the large number of oxygen vacancy structures reported for oxygen-deficient perovskites [8].

Table 4.1. Physical properties of M dopants investigated for stabilizing $BaCo_{0.8}M_{0.2}O_3$ in a vacancy-disordered perovskite structure. Highlighted properties are not consistent with those desired for stabilizing $BaCo_{0.8}M_{0.2}O_3$.

Dopant	Ionic Radius (Å)	Valence	Goldschmidt Factor of BaMO₃	BaMO₃ Structure?
Co	0.55	3	1.091	Hexagonal
Sn	0.69	4	1.018	Perovskite
Ti	0.61	4	1.059	Perovskite
Fe	0.65	3	1.038	Orthorhombic
Ce	0.87	4	0.938	Perovskite
Ni	0.69	2	1.018	Hexagonal
Ga	0.62	3	1.054	Spinel
Zr	0.72	4	1.004	Perovskite
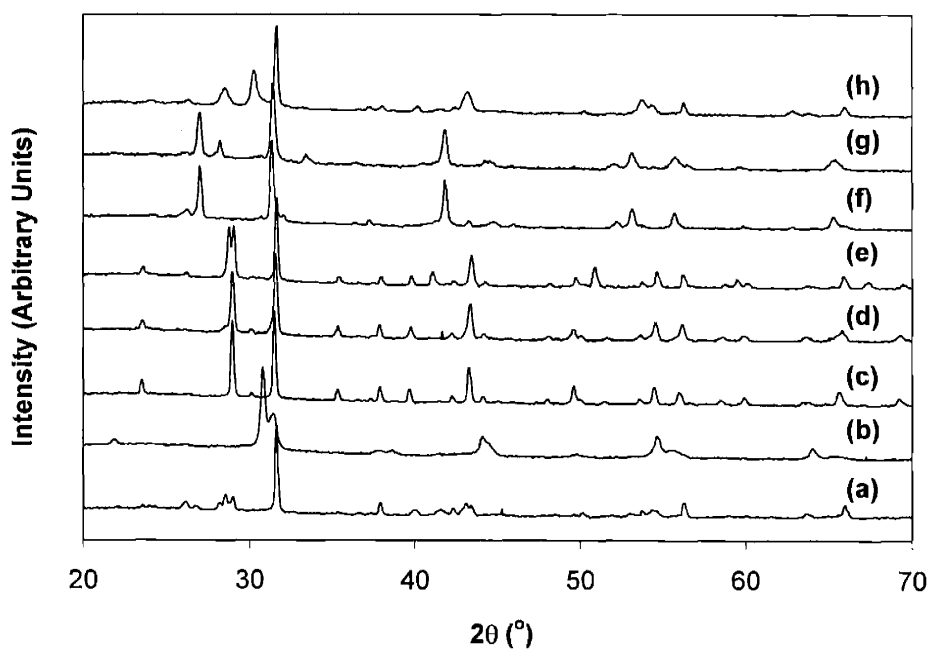
Figure 4.1. XRD patterns for $BaCo_{0.8}M_{0.2}O_3$ perovskites with various M dopants: (a) Co^{3+}, (b) Sn^{4+}, (c) Ti^{4+}, (d) Fe^{4+}, (e) Ce^{4+}, (f) Ni^{2+}, (g) Ga^{3+} and (h) Zr^{4+}, after calcination at 1050°C in air.

Although the dopants examined did not stabilize the perovskite structure to room temperature, it was of interest to determine the order-disorder temperature and the energetics of vacancy association. Figure 4.2 shows DTA results for $BaCo_{0.8}M_{0.2}O_3$ perovskites on heating from room temperature to 1050°C in air. Depending on the dopant, the order-disorder

148

temperature was found to lie between 900 and 1050°C, and increased in the order: Sn < Fe < Zr < Ga < Co < Ce < Ti < Ni. Substitution of tin, iron, zirconium or gallium at the B site resulted in a slight decrease in the order-disorder temperature compared to pure $BaCoO_3$ (960°C), indicating that these dopants stabilized the vacancy-disordered structure to a small extent. Based on the order-disorder temperature (~ 930°C), Sn was found to be the most effective dopant, which was consistent with expectations based on the three selection criteria.
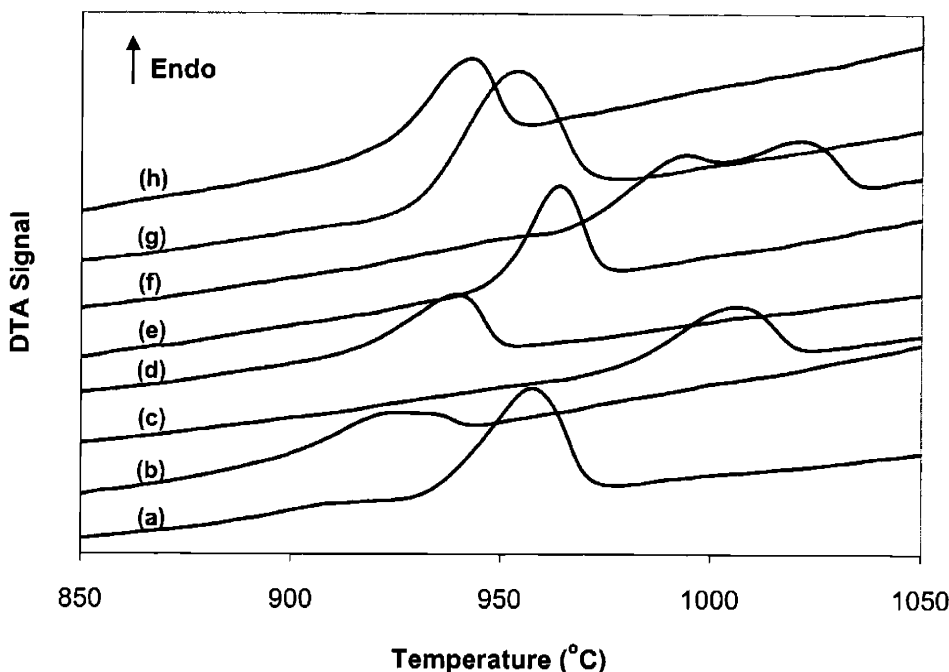
Figure 4.2. DTA of $BaCo_{0.8}M_{0.2}O_3$ perovskites with various M dopants: (a) Co^{3+}, (b) Sn^{4+}, (c) Ti^{4+}, (d) Fe^{4+}, (e) Ce^{4+}, (f) Ni^{2+}, (g) Ga^{3+} and (h) Zr^{4+}, after calcination at 900°C in air.

Since the order-disorder temperature was equal to the ratio of the changes in enthalpy and entropy on transformation, the M dopant must affect the energetics of vacancy interactions and/or the extent of vacancy disordering. The enthalpy change associated with the transformation from a vacancy-ordered to a vacancy-disordered phase is shown in Figure 4.3 for various dopants. A higher enthalpy change suggests stronger interactions between oxygen vacancies and/or a higher extent of vacancy ordering. Hence, perovskites showing higher enthalpy change during transformation are expected to possess lower oxide conductivity. The heat of transition was strongly dependent on the dopant type, varying between 35 and 148 J/g, and increased in the order: Sn < Fe < Ti < Zr ~ Ce < Co < Ni < Ga. This observed trend in the heat of transition closely resembled the predicted trend in dopant effectiveness based on the three

selection criteria. While none of the dopants investigated were able to fully stabilize $BaCo_{0.8}M_{0.2}O_3$, Sn^{4+} and Fe^{3+} were the most effective dopants based on their lower transition temperatures and considerably smaller heats of transition.
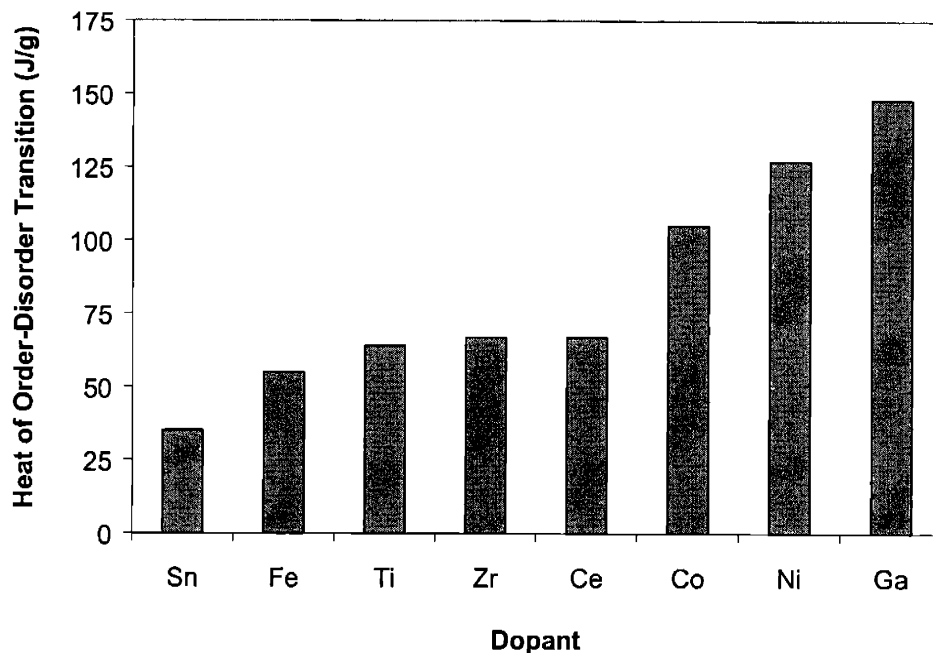
Figure 4.3. Heat of order-disorder transition measured with DTA for $BaCo_{0.8}M_{0.2}O_3$ perovskites with various M dopants.

In order to establish the effect of vacancy ordering on the oxide conductivity in $BaCo_{0.8}M_{0.2}O_3$, oxygen flux measurements were performed on three M-doped perovskites. Sn, Fe and Ti were selected because their substitution at the B site led to the lowest extent of vacancy ordering in the resulting oxide, as determined by order-disorder enthalpy changes. As a result, these doped perovskites were expected to exhibit higher oxide conductivities compared to the other systems.

Sn- and Fe-doped perovskites showed a dramatic decrease in oxygen flux on cooling (Figure 4.4), consistent with the transformation from a vacancy-disordered perovskite to a vacancy-ordered structure observed in XRD and DTA. $BaCo_{0.8}Ti_{0.2}O_3$ showed very low oxygen fluxes of < 0.3 $cm^3[STP]/min/cm^2$ even at 900°C. This was because its transition temperature was ~ 1010°C, which was above the highest temperature experienced by the membrane during an oxygen flux measurement (960°C). Sn-doped perovskite showed the highest oxygen flux, followed by Fe- and Ti-doped perovskites, consistent with the observed trend in their heat of

transition. The inability of these M dopants to fully stabilize the perovskite structure resulted in a dramatic decline in oxygen flux on cooling to lower temperatures.
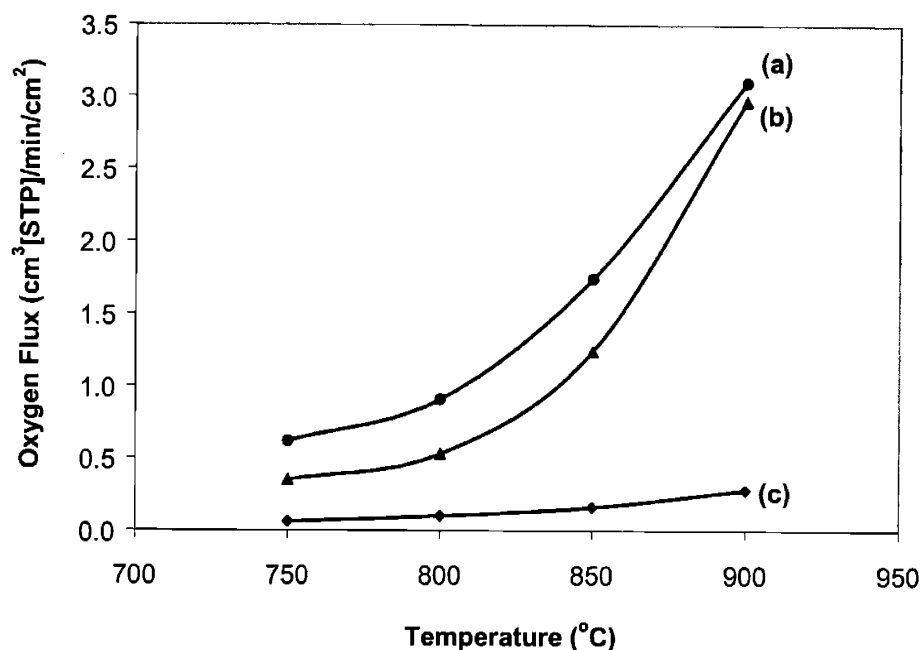
Figure 4.4. Oxygen flux of $BaCo_{0.8}M_{0.2}O_3$ perovskites doped with (a) Sn^{4+}, (b) Fe^{3+} and (c) Ti^{4+}.

In order to achieve complete stabilization of the $BaCo_{0.8}M_{0.2}O_3$ perovskite, a "mixing pot" approach was utilized, whereby a mixture of stabilizer cations were introduced at the B site to prevent the oxygen vacancies from establishing an ordered arrangement. Since Sn and Fe were found to be the most effective stabilizers from the single dopant studies, an equimolar mixture of Sn and Fe was investigated first in attempt to stabilize the $BaCo_{0.8}M_{0.2}O_3$ perovskite.

Figure 4.5 shows the effect of B-site composition on the crystal structure of $BaCo_{1-y-z}Sn_yFe_zO_3$ after calcination at 1050°C and cooling to room temperature. The perovskite phase was not stabilized using a Sn or Fe doping level of 0.2. At lower doping levels of 0.075 for both Sn and Fe, partial stabilization of the perovskite phase was observed. The cubic vacancy-disordered perovskite phase of $BaCo_{0.8}Sn_{0.1}Fe_{0.1}O_3$ was successfully stabilized to room temperature. Thus, a combination of Fe and Sn dopants was more effective than a single dopant, since this would create greater cationic disorder at the B site, thereby preventing oxygen vacancies from achieving local periodicity.

151
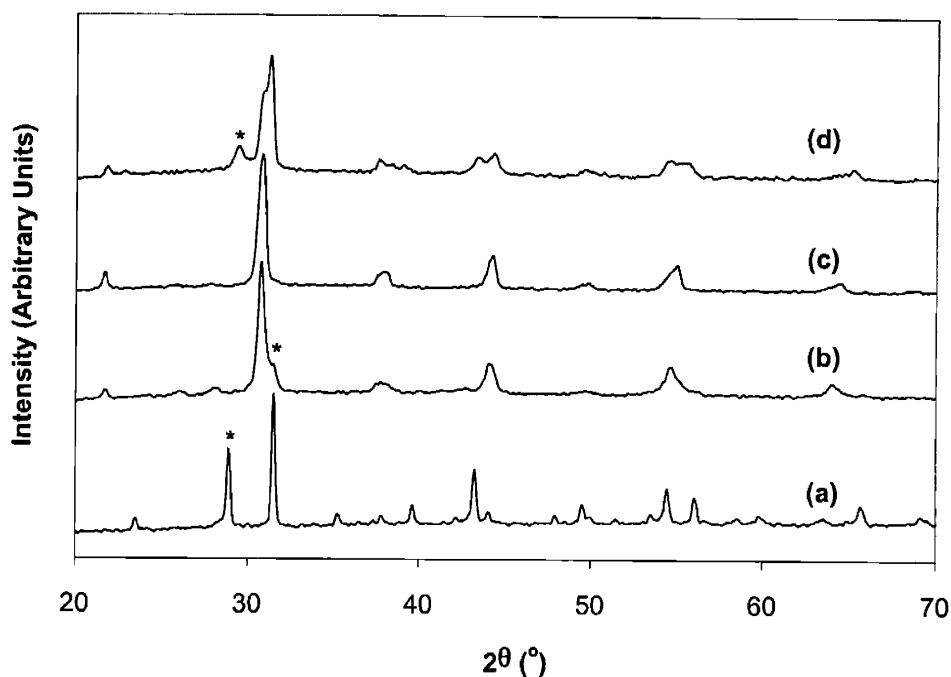
Figure 4.5. XRD patterns for $BaCo_{1-y-z}Fe_ySn_zO_3$ perovskites with (a) y = 0.2 and z = 0.0, (b) y = 0.0 and z = 0.2, (c) y = 0.1 and z = 0.1, and (d) y = 0.075 and z = 0.075, after calcination at 1050°C in air. XRD peaks denoted by "*" correspond to ordered and/or secondary phases.

Figure 4.6 shows the dependence of oxygen flux for $BaCo_{1-y-z}Sn_yFe_zO_3$ perovskites as a function of stabilizer composition. When only Fe or Sn was used as the stabilizer cation, the resulting phase transformation to an ordered structure led to a dramatic decline in oxygen flux on decreasing temperature. However, when a combination of Fe and Sn dopants was introduced at the B site, the oxygen flux increased dramatically at lower temperatures, with no sharp decline observed on cooling. This confirmed the XRD results that an order-disorder transformation was successfully suppressed. Perovskites containing a total Fe-Sn dopant content of 0.15 and 0.20 exhibited an oxygen flux of 3.5 and 3.2 $cm^3[STP]/min/cm^2$, respectively, at 900°C, and 1.2 and 1.3 $cm^3[STP]/min/cm^2$, respectively, at 750°C. These oxygen fluxes were significantly higher than those attained by existing ceramic membranes at 900°C (0.5-2.0 $cm^3[STP]/min/cm^2$).
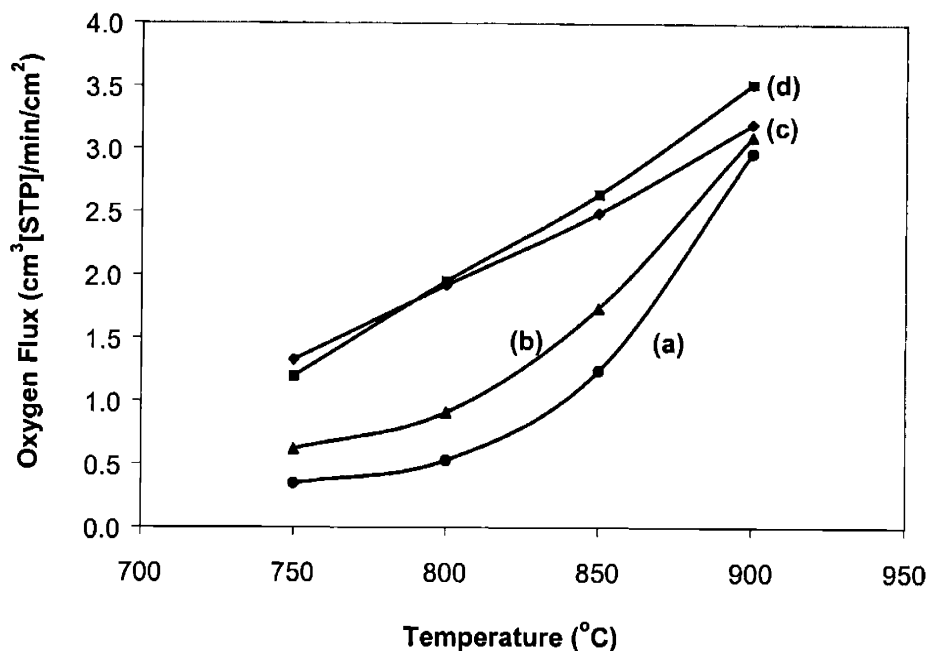
Figure 4.6. Oxygen flux of $BaCo_{1-y-z}Fe_ySn_zO_3$ perovskites with (a) y = 0.2 and z = 0.0, (b) y = 0.0 and z = 0.2, (c) y = 0.1 and z = 0.1, and (d) y = 0.075 and z = 0.075.

Figure 4.7 shows the time dependence of oxygen flux in $BaCo_{1-y-z}Sn_yFe_zO_3$ perovskites at 750°C. If the concentration of "mobile" vacancies decreased due to the formation of ordered structures, the oxygen flux would decrease over time. Substitution of only Sn or Fe for Co resulted in very low oxygen fluxes of < 0.6 cm^3[STP]/min/cm^2 at 750°C, indicating that the transformation to an ordered phase has already taken place. The oxygen flux for $BaCo_{0.8}Fe_{0.2}O_3$ remained fairly constant with time, since the concentration of mobile vacancies no longer changed after transformation, and the measured oxygen flux was due to the intrinsic oxide conductivity of the ordered phase. With a mixed Fe-Sn dopant content of 0.2, a significantly higher oxygen flux was achieved at 750°C with high flux stability over time. This confirmed that the vacancy-disordered perovskite phase was successfully stabilized in $BaCo_{0.8}Sn_{0.1}Fe_{0.1}O_3$ perovskite. In contrast, oxygen flux in $BaCo_{0.85}Sn_{0.075}Fe_{0.075}O_3$ perovskite declined significantly over time, indicating a slow decrease in the mobile vacancy concentration due to ordering effects.
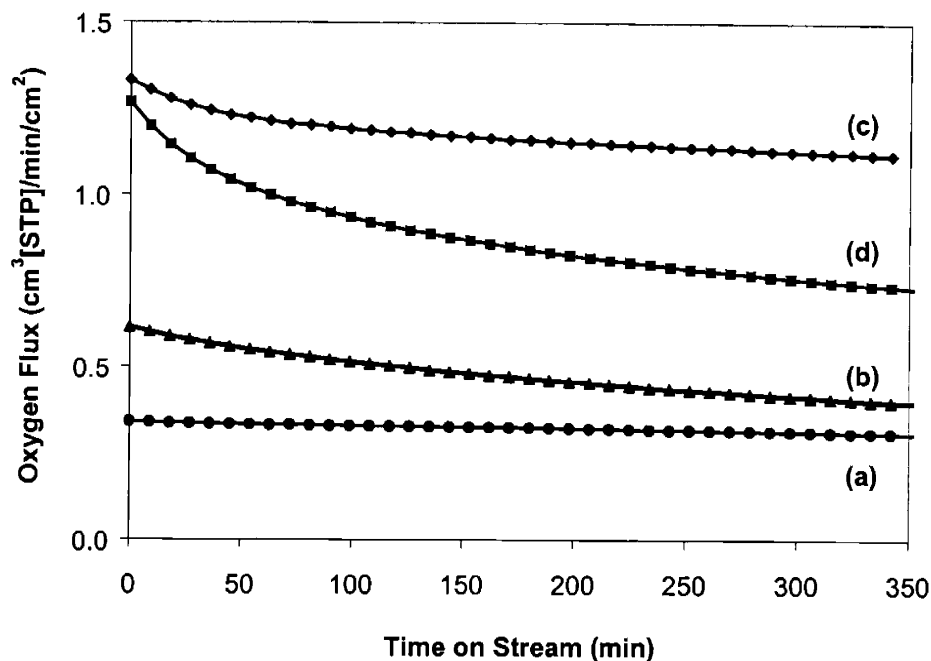
Figure 4.7. Time dependence of oxygen flux of $BaCo_{1-y-z}Fe_ySn_zO_3$ perovskites with (a) $y = 0.2$ and $z = 0.0$, (b) $y = 0.0$ and $z = 0.2$, (c) $y = 0.1$ and $z = 0.1$, and (d) $y = 0.075$ and $z = 0.075$ at 750°C.

4.3.2 Oxide Conductivity in $Ba_{1-x}Sr_xCo_{1-y}M_yO_{3-\delta}$

The contribution of oxide conductivity to the total conductivity in $Ba_{1-x}Sr_xCo_{1-y}M_yO_{3-\delta}$ perovskites was determined from integral and differential oxygen flux measurements, as described in Section 4.2.1. Figure 4.8 shows the dependence of oxygen flux in $BaCo_{0.85}Fe_{0.075}Sn_{0.075}O_{3-\delta}$ on the oxygen partial pressure of the oxygen-lean side, while keeping the oxygen partial pressure of the air chamber constant at 0.21 atm. Oxygen partial pressure in the oxygen-lean side was manipulated by changing the inlet oxygen concentration and total flowrate. The oxygen partial pressure near the membrane surface was assumed to be equal to the average of the inlet and outlet oxygen concentrations. As the oxygen partial pressure on the oxygen-lean side was decreased, the oxygen flux increased due to an increase in driving force. If the oxide conductivity remains constant, the oxygen flux should show a linear increase with decreasing $\ln(P_{O2})$ (Equation 4.3). It was observed that the oxygen flux increased non-linearly, with a decreasing slope with decreasing $\ln(P_{O2})$, indicating that the oxide conductivity decreased with decreasing oxygen partial pressure. The oxide conductivity at a desired temperature and

154

oxygen partial pressure could be calculated using the slope of the J_{O2} vs. $\ln(P_{O2})$ plot (Equation 4.5).
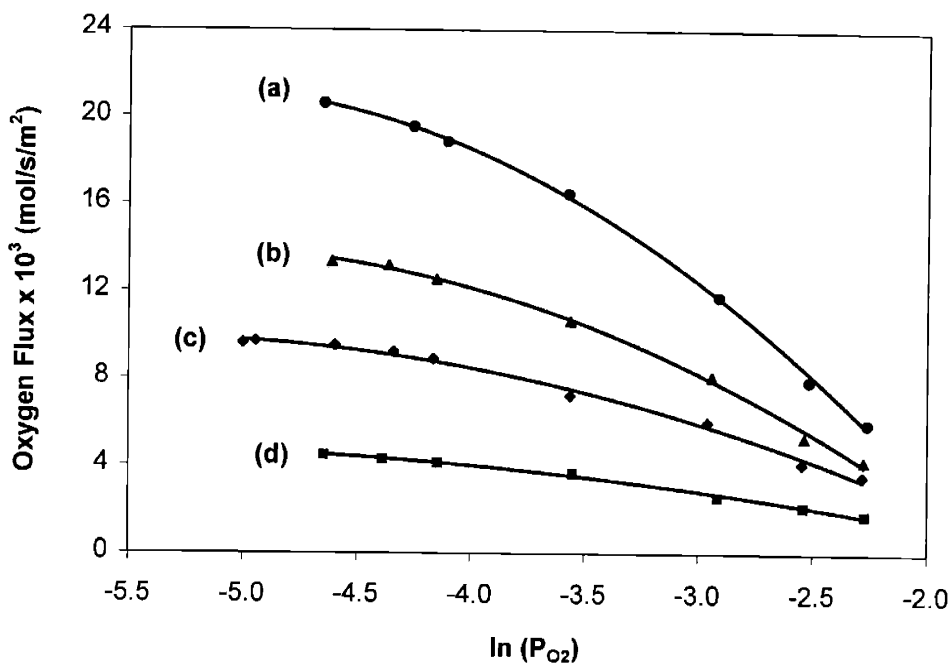
Figure 4.8. Dependence of oxygen flux of $BaCo_{0.85}Fe_{0.075}Sn_{0.075}O_3$ perovskite on oxygen partial pressure on the oxygen-lean side at (a) 900°C, (b) 850°C, (c) 800°C and (d) 750°C. Oxygen flux measurements were conducted between a fixed oxygen concentration of 21% at the air chamber and a variable oxygen partial pressure on the oxygen-lean side over a 1.09-mm thick membrane.

Figure 4.9 shows the oxide conductivity of $BaCo_{0.85}Fe_{0.075}Sn_{0.075}O_{3-\delta}$ perovskite as a function of temperature and oxygen partial pressure, determined using the integral method. The oxide conductivity at 900°C decreased from ~ 1.7 S/cm at 10% oxygen to ~ 0.4 S/cm at ~ 1% oxygen. In comparison, doped zirconia and ceria electrolytes have much lower oxide conductivities of < 0.1 S/cm at 900°C in air [12]. The observed decrease in oxide conductivity with oxygen partial pressure suggested that for oxygen separation applications, the minimum oxygen partial pressure on the oxygen-lean side should be kept above 1.5% so as to maintain a high overall oxide conductivity.

The oxygen vacancy concentration in $Ba_{1-x}Sr_xCo_{1-y}M_yO_3$ perovskites increased slightly as the oxygen partial pressure was decreased from 0.21 to 0.01 atm (Figure 3.30 [1]). It follows from Equation 4.2 that the observed decrease in oxide conductivity can result from a decrease in the vacancy diffusion coefficient, which depends primarily on the crystal structure and

perovskite composition, or from a decrease in the vacancy activity coefficient, which accounts for vacancy association/ordering effects. This suggests that the observed decrease in oxide conductivity with decreasing oxygen partial pressure is due to a decrease in the number of mobile oxygen vacancies from vacancy association/ordering effects.
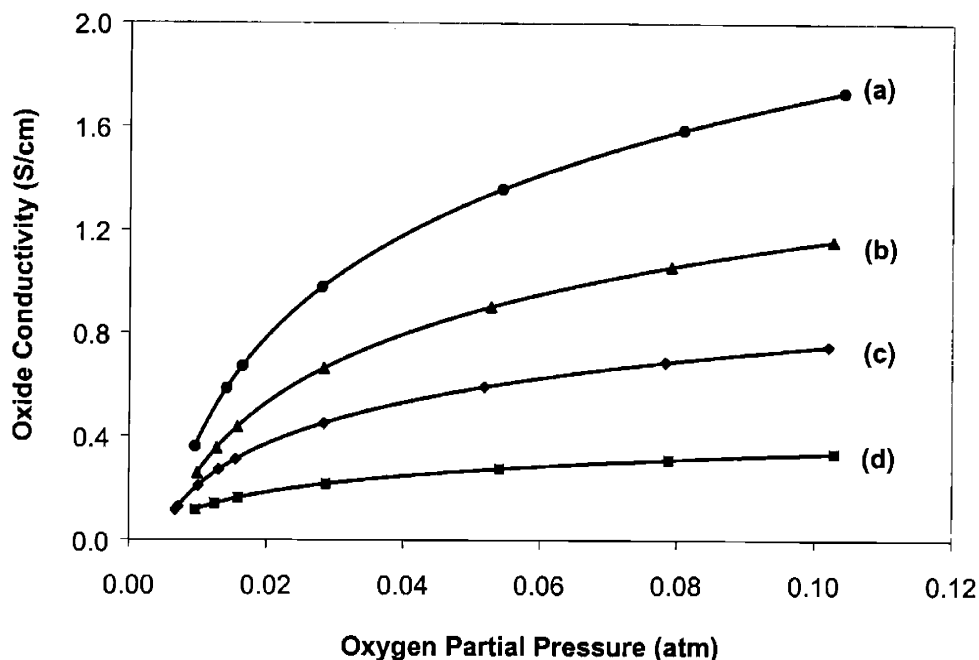
Figure 4.9. Dependence of oxide conductivity of $BaCo_{0.85}Fe_{0.075}Sn_{0.075}O_3$ perovskite on oxygen partial pressure at (a) 900°C, (b) 850°C, (c) 800°C and (d) 750°C.

Figure 4.10 shows that the oxide conductivity of $BaCo_{0.85}Fe_{0.075}Sn_{0.075}O_{3-\delta}$ perovskite decreased linearly with decreasing $\ln(P_{O2})$. Since a change in $\ln(P_{O2})$ was directly proportional to a change in chemical potential of oxygen, it followed that the oxide conductivity decreased linearly with decreasing chemical potential of oxygen (i.e. with increasing chemical potential of oxygen vacancies). As the chemical potential of oxygen vacancies increased, it became thermodynamically favorable for these vacancies to associate, and thereby decreasing the overall free energy. The resulting decrease in the concentration of mobile, unassociated vacancies would decrease the oxide conductivity. Figure 4.10 also shows that as the oxide conductivity at higher oxygen partial pressure increased with temperature, the rate of decrease of this conductivity with decreasing $\ln(P_{O2})$ also increased. This suggested that there was an equilibrium relationship between the extent of association between oxygen vacancies to form vacancy clusters, and the concentration of unassociated vacancies. The driving force of this

vacancy ordering was the increase in the chemical potential of oxygen vacancies on decreasing oxygen partial pressure.
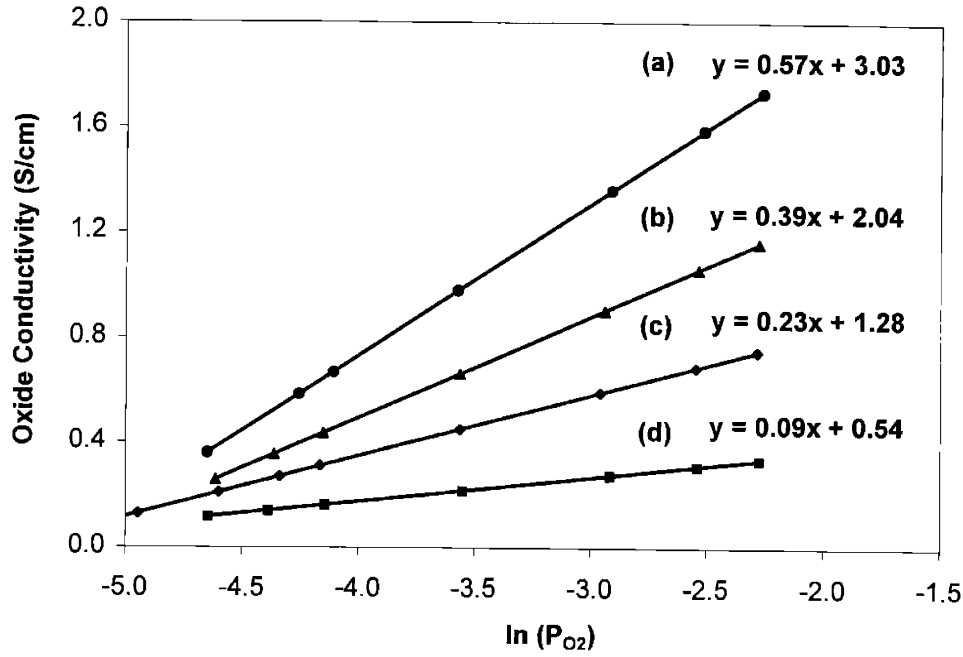
Figure 4.10. Dependence of oxide conductivity of $BaCo_{0.85}Fe_{0.075}Sn_{0.075}O_3$ perovskite on $\ln(P_{O2})$ at (a) 900°C, (b) 850°C, (c) 800°C and (d) 750°C.

Figure 4.11 shows that the oxide conductivity of $BaCo_{0.85}Fe_{0.075}Sn_{0.075}O_{3-\delta}$ has an Arrhenius dependence on temperature given by:

$$\ln(\sigma) = \ln(\sigma_o) - \frac{E_a}{RT} \qquad (5.6)$$

where E_a is the overall activation energy for oxide ion transport and σ_o is the oxide conductivity at $T \rightarrow \infty$, which is given by the hopping frequency and the equilibrium vacancy concentration at $T \rightarrow \infty$. Figure 4.11 shows a linear relationship between $\ln(\sigma)$ and $1/T$ at 800-900°C, followed by a decline on cooling from 800°C to 750°C that was more pronounced at higher oxygen partial pressures. This decrease in oxide conductivity was due to the formation of ordered vacancy structures on cooling. It is consistent with results in Chapter 3 [1] that showed $Ba_{1-x}Sr_xCo_{1-y}M_yO_3$ perovskites underwent phase transformation from a vacancy-disordered perovskite to a vacancy-ordered phase, resulting in decreased oxygen fluxes.

157
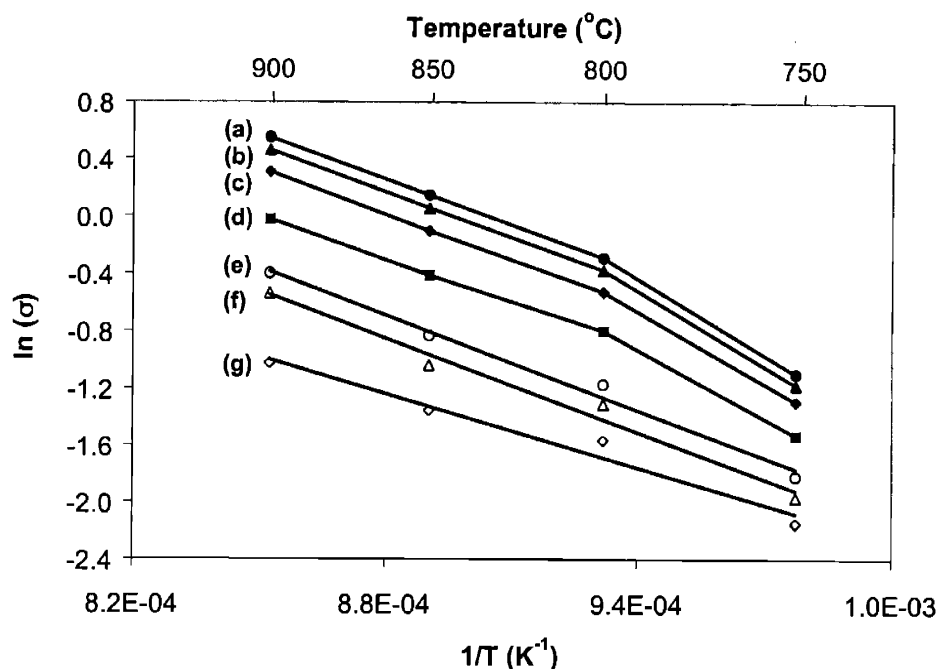
Figure 4.11. Arrhenius dependence of oxide conductivity of $BaCo_{0.85}Fe_{0.075}Sn_{0.075}O_{3-\delta}$ perovskite on temperature at oxygen partial pressures of (a) 0.100, (b) 0.080, (c) 0.055, (d) 0.028, (e) 0.016, (f) 0.013 and (g) 0.010 atm.

Figure 4.12 shows the dependence of the apparent activation energy on oxygen partial pressure, calculated using the temperature dependence of oxide conductivity. As the oxygen partial pressure decreased, the activation energy for oxide transport decreased dramatically from ~ 110 kJ/mol at 0.10 atm to ~ 70 kJ/mol at 0.01 atm. In Chapter 3 [1], an increase in activation energy from 64 to 144 kJ/mol was observed for perovskites undergoing phase transformation to a vacancy-ordered structure. The higher activation energy observed at higher oxygen partial pressures suggested that $BaCo_{0.85}Fe_{0.075}Sn_{0.075}O_{3-\delta}$ perovskite underwent phase transformation to an ordered structure more easily at higher oxygen partial pressures. This was consistent with the oxygen vacancy concentration measurements for $BaCo_{0.8}Fe_{0.2}O_{3-\delta}$ perovskite showing that the order-disorder temperature was increased on increasing oxygen partial pressure (Figure 3.30) [1]. Since this phase transformation occurred with the incorporation of lattice oxygen, higher oxygen pressures would favor this transformation, consistent with the observed higher activation energies. Moreover, the higher concentration of mobile oxygen vacancies present at high oxygen partial pressures would favor phase transformation to an ordered structure on cooling.
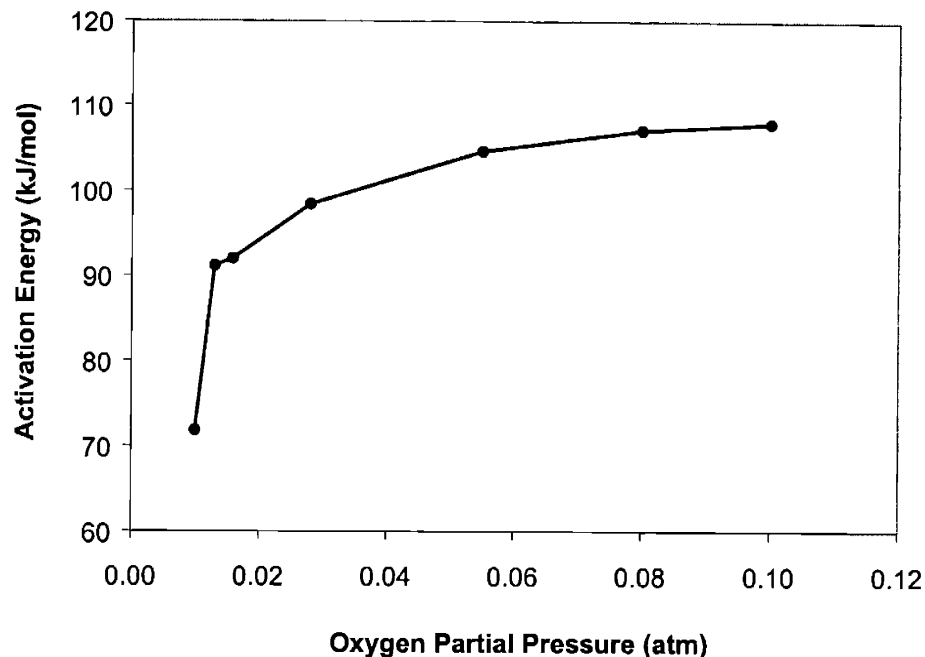
Figure 4.12. Apparent activation energy for oxide conduction in $BaCo_{0.85}Fe_{0.075}Sn_{0.075}O_{3-\delta}$, determined using oxide conductivity measurements.

The primary source of error in the measurement of oxide conductivity using the integral method aroses from the uncertainty in determining the oxygen partial pressure close to the membrane surface on the oxygen-lean side. Since oxygen fluxes were high, the oxygen partial pressure could vary considerably from the inlet and outlet gas concentrations. To more accurately determine the oxygen concentration close to the membrane surface, oxide conductivity was measured using the differential method. Figure 4.13 compares the oxide conductivity of $Ba_{0.5}Sr_{0.5}Co_{0.8}Fe_{0.2}O_{3-\delta}$ perovskite measured using both the integral and differential methods. The dependence of oxide conductivity on oxygen partial pressure was in close agreement for the integral and differential methods, with an average conductivity of ~ 0.95 and ~ 0.85 S/cm, respectively, at 900°C. These values were consistent with the average conductivity of ~ 0.94 S/cm for $Ba_{0.5}Sr_{0.5}Co_{0.8}Fe_{0.2}O_{3-\delta}$ from oxygen flux measurements at 900°C (Chapter 3 [1]).
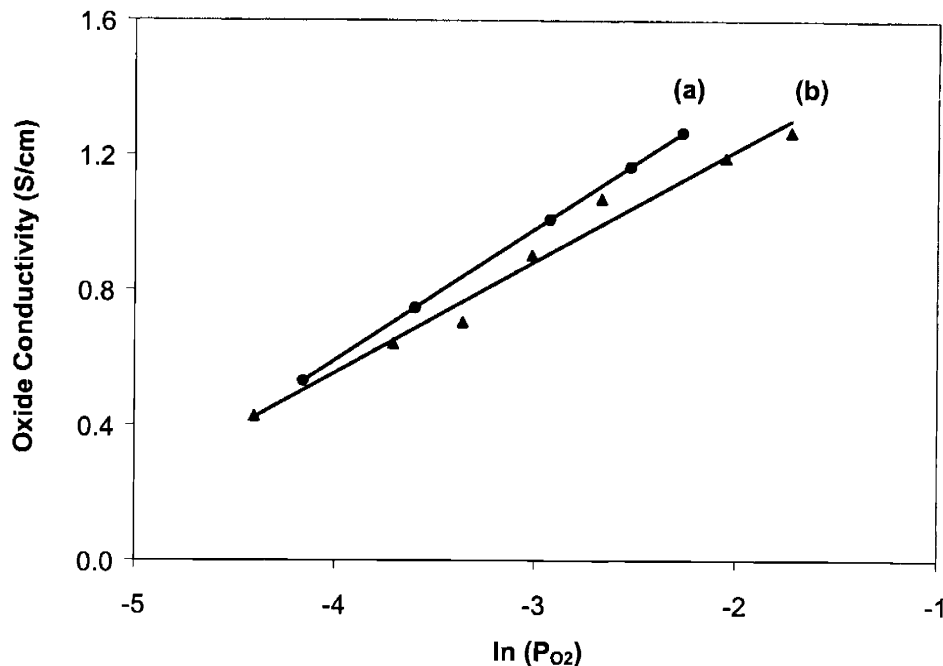
Figure 4.13. Dependence of oxide conductivity of $Ba_{0.5}Sr_{0.5}Co_{0.8}Fe_{0.2}O_{3-\delta}$ on $\ln(P_{O2})$ at 900°C, measured using (a) integral and (b) differential methods.

Figure 4.14 shows the dependence of oxide conductivity on oxygen partial pressure for $Ba_{1-x}Sr_xCo_{1-y}M_yO_3$ perovskites at 900°C. A decrease in oxide conductivity with decreasing oxygen partial pressure was observed for various perovskite compositions. The oxide conductivity decreased linearly with $\ln(P_{O2})$ for most perovskites, which could be related to an increase in the chemical potential for oxygen vacancies. Perovskite compositions that showed very high oxide conductivity at high oxygen partial pressures also exhibited the highest rate of decrease in oxide conductivity with decreasing $\ln(P_{O2})$. This indicated that the extent of vacancy association was proportional to the initial concentration of mobile oxygen vacancies. As the perovskite composition was varied, the concentration of mobile oxygen vacancies would change, even though the overall oxygen vacancy concentration remained nearly constant. This resulted in markedly different oxide conductivities at high oxygen partial pressures. Perovskites containing high stabilizer concentrations showed low oxide conductivities due to the association of oxygen vacancies with stabilizer cations (vacancy trapping). A lower concentration of mobile oxygen vacancies resulted in a slower rate of decline in oxide conductivity with decreasing $\ln(P_{O2})$.
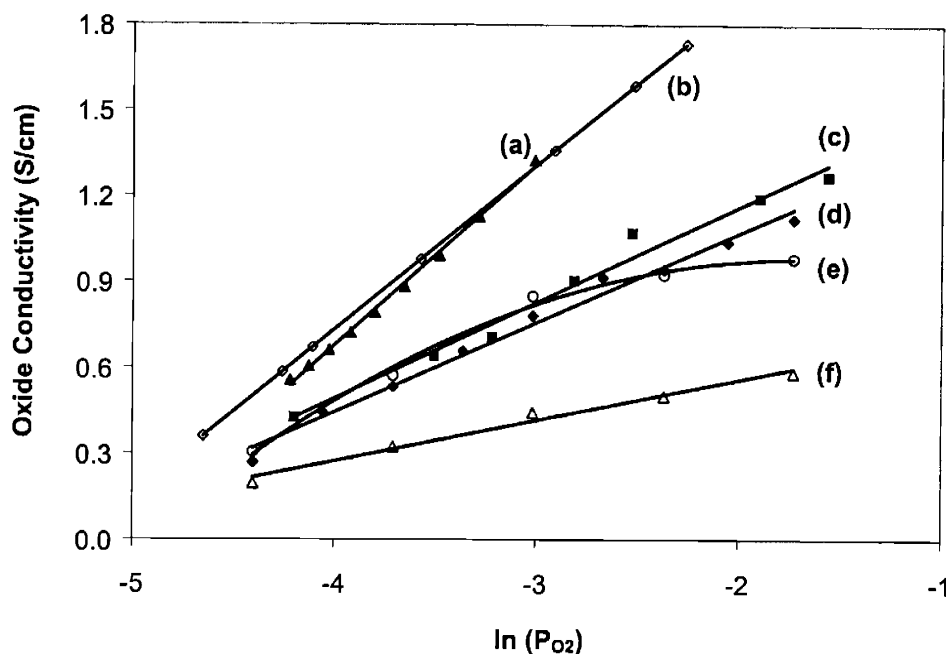
Figure 4.14. Dependence of oxide conductivity of $Ba_{1-x}Sr_xCo_{1-y}M_yO_{3-\delta}$ perovskites on $\ln(P_{O2})$ at 900°C for (a) $BaCo_{0.85}Ni_{0.05}Fe_{0.05}Sn_{0.05}O_{3-\delta}$ (▲), (b) $BaCo_{0.85}Fe_{0.075}Sn_{0.075}O_{3-\delta}$ (◇), (c) $Ba_{0.5}Sr_{0.5}Co_{0.8}Fe_{0.2}O_{3-\delta}$ (■), (d) $Ba_{0.5}Sr_{0.5}Co_{0.9}Fe_{0.1}O_{3-\delta}$ (◆), (e) $BaCo_{0.8}Fe_{0.2}O_{3-\delta}$ (○), and (f) $Ba_{0.5}Sr_{0.5}Co_{0.2}Fe_{0.8}O_{3-\delta}$ (△).

Figure 4.15 shows the correlation between the initial oxide conductivity, measured at high oxygen partial pressures, and its subsequent rate of decrease with decreasing oxygen partial pressure. A linear relationship was found to exist between the slope of the σ vs. $\ln(P_{O2})$ plot and its intercept at $\ln(P_{O2}) = 0$ for the various $Ba_{1-x}Sr_xCo_{1-y}M_yO_3$ perovskites investigated in this study. Although these perovskites have nearly the same overall oxygen vacancy concentration and similar crystal structures, their oxide conductivity and dependence on oxygen partial pressure were varied due to difference in the concentration of mobile vacancies. Association of oxygen vacancies with stabilizer cations (vacancy trapping) or with other vacancies (vacancy ordering) can decrease oxide conductivity. Perovskites containing a higher concentration of mobile oxygen vacancies would exhibit a higher tendency for vacancy ordering, resulting in a higher rate of decrease in oxide conductivity with decreasing oxygen partial pressure (i.e. easier transformation to ordered structures).
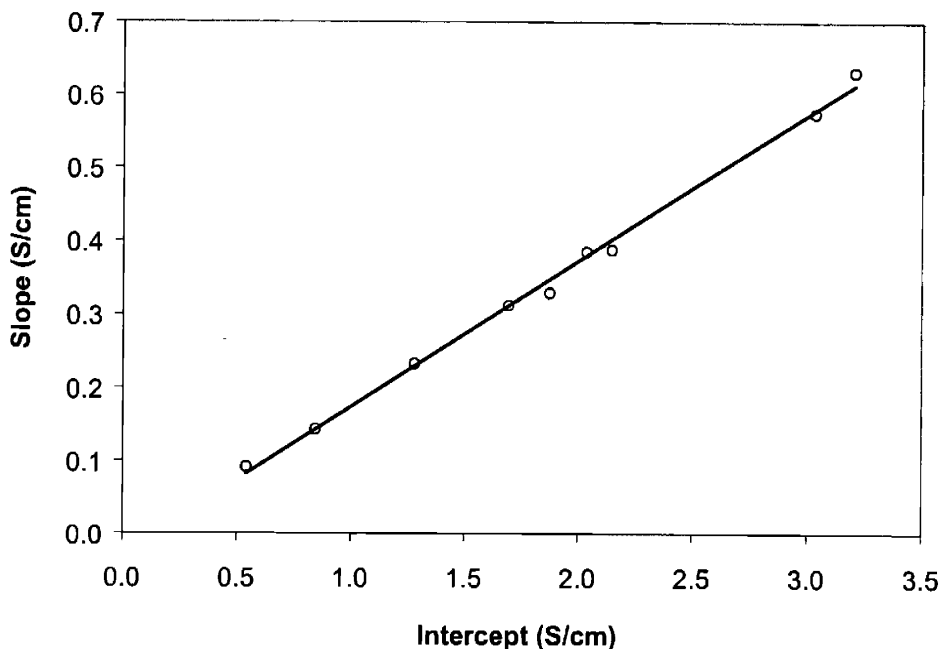
Figure 4.15. Relationship between the rate of decrease in oxide conductivity with decreasing $\ln(P_{O2})$ (slope) and the initial oxygen flux at high oxygen partial pressures (intercept) for $Ba_{1-x}Sr_xCo_{1-y}M_yO_3$ perovskites at 750-900°C.

Figure 4.16 shows the dependence of oxide conductivity on oxygen partial pressure for two compositions with different oxygen vacancy concentrations. The oxygen vacancy concentration in $Ba_{0.5}Sr_{0.5}Co_{0.8}Fe_{0.2}O_{3-\delta}$ of ~ 0.482 (at 900°C in air) was decreased to ~ 0.420 by 20% substitution of La^{3+} at the A site. These oxygen vacancy concentrations were measured using TGA, as discussed in Section 3.2.3 [1]. Lanthanum was chosen since it has a higher, stable valence state of +3 compared to strontium or barium (+2), and comparable ionic radius (1.36 Å) as an equimolar strontium-barium mixture (1.53 Å). Lowering the overall oxygen vacancy concentration decreased the oxide conductivity, since the number of mobile oxygen vacancies also decreased. The oxide conductivity in $La_{0.2}(Ba_{0.5}Sr_{0.5})_{0.8}Co_{0.8}Fe_{0.2}O_{2.6}$ initially remained fairly constant with decreasing oxygen partial pressure, then underwent a decline at very low oxygen partial pressures, while the conductivity in $Ba_{0.5}Sr_{0.5}Co_{0.8}Fe_{0.2}O_{2.5}$ showed a continuous decline with decreasing oxygen partial pressure. Since vacancy association/ordering effects were expected to decrease with decreasing overall vacancy concentration, a smaller dependence of oxide conductivity on oxygen partial pressure was expected, which was consistent with the observed results.
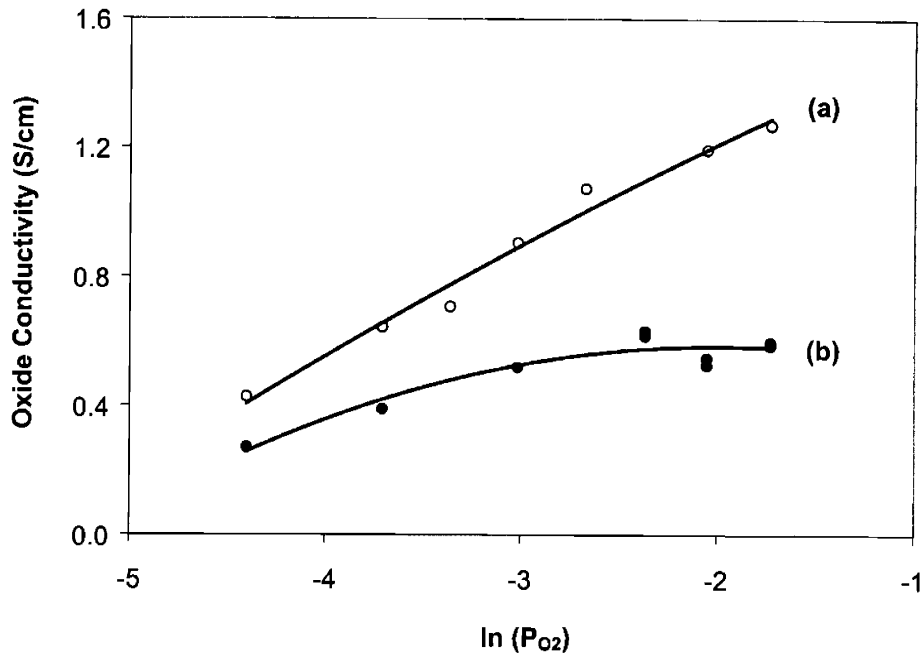
Figure 4.16. Dependence of oxide conductivity on oxygen partial pressure for (a) $Ba_{0.5}Sr_{0.5}Co_{0.8}Fe_{0.2}O_{3-\delta}$ and (b) $La_{0.8}(Ba_{0.5}Sr_{0.5})_{0.2}Co_{0.8}Fe_{0.2}O_{3-\delta}$ perovskites at 900°C.

Using the dependence of oxide conductivity on oxygen partial pressure and temperature, the oxygen flux was predicted for $Ba_{1-x}Sr_xCo_{1-y}M_yO_3$ perovskites using Equation 4.3. Figure 4.17 shows an excellent agreement between the predicted oxygen fluxes and the experimentally measured oxygen fluxes for these perovskites as reported in Chapter 3 [1] and Section 4.3.1. This indicated that the observed dependence of oxide conductivity on oxygen partial pressure and temperature was accurate. This approach can be very useful in designing oxygen separation systems, since it allows for prediction of oxygen flux as a function of varying process conditions.
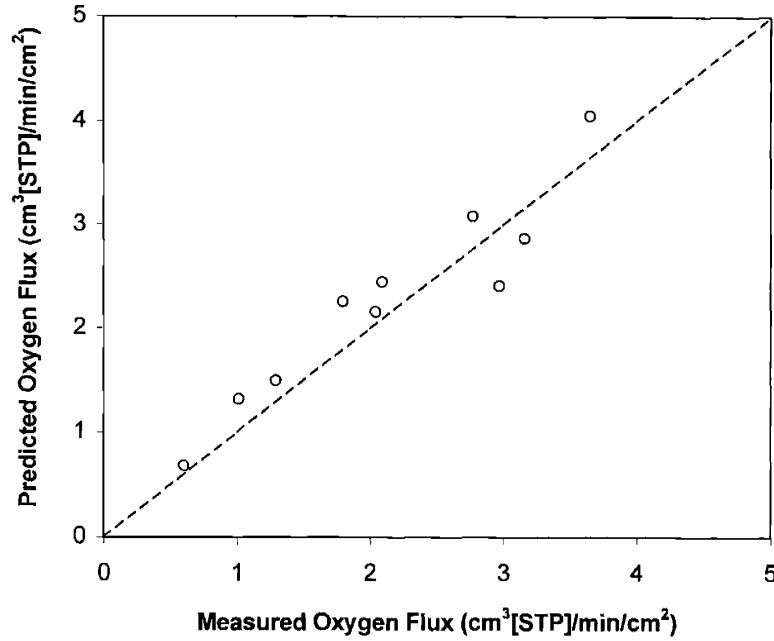
Figure 4.17. Comparison of the experimentally measured oxygen flux in $Ba_{1-x}Sr_xCo_{1-y}M_yO_3$ membranes (Chapter 3 [1] and Section 4.3.1) and the predicted oxygen flux determined by using the dependence of oxide conductivity on oxygen partial pressure and temperature.

Since the dependence of oxide conductivity on oxygen partial pressure is known, the spatial profile of the oxygen partial pressure along the diffusion direction can be calculated, assuming local equilibrium of defect concentrations. The governing equation for one-dimensional transport of oxide ions is given by:

$$\frac{d}{dx}\left[\sigma \, \frac{d\mu_{O2}}{dx}\right] = \frac{d}{dx}\left[\sigma \, \frac{d\ln(P_{O2})}{dx}\right] = 0 \qquad (4.7)$$

where μ_{O2} is the chemical potential of gas-phase oxygen in equilibrium with oxide ions. The dependence of oxide conductivity on oxygen partial pressure (shown in Figure 4.14) can be approximated as:

$$\sigma = a\ln(P_{O2}) + b \qquad (4.8)$$

where a and b are the slope and intercept, respectively, for a specific perovskite composition. Combining Equations 4.7 and 4.8 results in a second-order, non-linear ordinary differential equation:

$$(ay+b)\frac{d^2y}{dx^2}+a\left(\frac{dy}{dx}\right)^2 = 0 \qquad\qquad (4.9)$$

where $y = \ln(P_{O2})$ is used to simplify the differential equation. The non-linearity of the differential equation arises from $a \neq 0$, which represents the dependence of the oxide conductivity on oxygen partial pressure. Assuming fast surface exchange kinetics, two boundary conditions need to be satisfied at the membrane surfaces:

$$At \ x = 0, \ y = y_1 = \ln(P_1) \qquad\qquad (4.10)$$

$$At \ x = L, \ y = y_2 = \ln(P_2) \qquad\qquad (4.11)$$

where L is the membrane thickness, and P_1 and P_2 are the oxygen partial pressures on the oxygen-rich and oxygen-lean sides of the membrane, respectively. The non-linear differential equation, subject to the above boundary conditions, was solved using Mathematica[®] for y(x):

$$y(x) = \frac{1}{a}\left[-b + \sqrt{(b^2 + 2aby_1 + a^2y_1^2) - (2aby_1 + a^2y_1^2 - 2aby_2 - a^2y_2^2)\frac{x}{L}}\,\right] \qquad (4.12)$$

Figure 4.18 shows the profile of $\ln(P_{O2})$ within the membrane for various perovskite compositions, as defined by their unique a and b parameters (from Figures 4.14 and 4.15). It was shown in Figure 4.15 that a linear relationship existed between a and b parameters for various perovskite compositions, and therefore, only one parameter could be independently varied. The a parameter was found to vary between 0.5 and 3.5, with the more stable perovskite compositions having low a values. Oxygen partial pressures on the oxygen-rich and oxygen-lean sides were fixed at 0.21 and 0.01 atm, respectively.
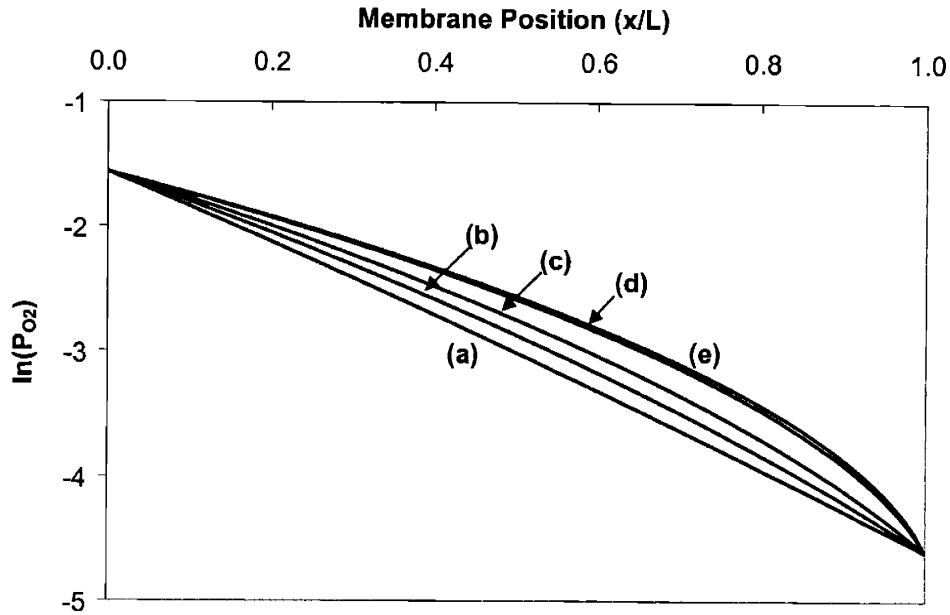
Figure 4.18. Dependence of $\ln(P_{O2})$ on membrane position, as given by Equation 4.12, for perovskite compositions with an a parameter of (a) 0.01, (b) 0.04, (c) 0.1, (d) 1 and (e) 10.

As the a parameter was increased, the $\ln(P_{O2})$ profile became increasingly non-linear, consistent with the increasing dependence of oxide conductivity on oxygen partial pressure. As the oxide conductivity decreased with decreasing oxygen partial pressure, higher gradients in $\ln(P_{O2})$ were required in order to keep the oxygen flux constant across the membrane. The sharpest decline in $\ln(P_{O2})$ was observed near the oxygen-lean side of the membrane, which could provide useful insights into the failure mechanisms of the perovskite membrane. Failure is typically observed when an imposed oxygen gradient causes changes in the crystal structure (phase transformation, change in vacancy concentration, etc.) along the membrane thickness, resulting in crack formation and membrane disintegration [17, 18]. Hence, from the standpoint of structural stability, a linear decrease in $\ln(P_{O2})$ is desirable, since any changes in crystal structure or microstructure will occur more gradually. The more stable perovskite compositions (with low a values) show a nearly linear dependence on $\ln(P_{O2})$. In contrast, less stable compositions (with high a values) exhibit sharp gradients in $\ln(P_{O2})$ near the oxygen-lean side, making them more susceptible to structural failure. Therefore, a trade-off exists between achieving high oxygen fluxes, and maintaining structural and chemical stability of the membrane.

4.4 Conclusions

A novel approach was developed to stabilize the vacancy-disordered perovskite phase of $BaCo_{0.8}M_{0.2}O_3$ on cooling to room temperature, so that significantly higher oxygen fluxes at lower temperatures could be achieved with excellent stability over the desired temperature range of 750-900°C. When a single type of dopant cation was introduced at the B site, the vacancy-disordered phase could not be fully stabilized, resulting in phase transformation to an ordered structure and low oxygen fluxes. These dopants were selected based on their ionic radius, valence state, and ability to form stable perovskites with barium. The endothermic heat for the order-disorder transition was found to vary considerably with the dopant type, indicating that the extent of vacancy ordering could be significantly affected by manipulating the B-site composition. Dopants that matched the selection criteria most closely (i.e. Sn^{4+} and Fe^{3+}) exhibited smaller heats of transition and lower order-disorder temperatures, suggesting they were indeed most effective in stabilizing the perovskite phase. A "mixing pot" approach was then utilized to successfully stabilize the perovskite phase in $BaCo_{0.8}Sn_{0.1}Fe_{0.1}O_3$ to room temperature, by introducing both Sn^{4+} and Fe^{3+} at the B site. Substituting a mixture of stabilizer cations created more cationic disorder at the B site, which together with their coordination preferences and valence states, prevented the oxygen vacancies from forming an ordered structure. This resulted in higher oxygen fluxes, and excellent flux stability even at 750°C. The stabilized $BaCo_{1-y-z}Sn_yFe_zO_3$ perovskites exhibited very high oxygen fluxes of ~ 3.5 and ~ 1.3 $cm^3[STP]/min/cm^2$ at 900°C and 750°C, respectively, which were substantially higher than those attained by conventional perovskite membrane compositions.

The oxide conductivity of $Ba_{1-x}Sr_xCo_{1-y}M_yO_3$ perovskites was characterized as a function of temperature and oxygen partial pressure. The oxide conductivity obtained using oxygen flux measurements in integral and differential methods were in good agreement, indicating that the measurement procedure was accurate and reproducible. At a fixed temperature, the oxide conductivity was found to decrease linearly with decreasing $\ln(P_{O2})$ for most perovskite compositions. The more stable perovskite compositions, which contained a higher strontium content and/or the appropriate stabilizer dopant(s), showed a lower dependence of oxide conductivity on oxygen partial pressure, compared to the less stable perovskite compositions. An excellent correlation was observed between the slope (a parameter) and the intercept (b parameter) of the σ vs. $\ln(P_{O2})$ plot for all perovskite compositions investigated. This suggested

that perovskites with an initially higher "mobile" oxygen vacancy concentration has a higher tendency to associate with each other and form ordered structures, resulting in a higher rate of decrease in oxide conductivity with decreasing oxygen partial pressure.

The measured dependence of oxide conductivity on oxygen partial pressure and temperature was used to predict oxygen fluxes in these membranes at a specified temperature and imposed oxygen partial pressure gradient. These predicted oxygen fluxes were found to be in excellent agreement with experimentally measured oxygen fluxes reported in Chapter 3 [1] and Section 4.3.1. Combining the oxide conductivity with transport equations, the oxygen concentration profile within these membranes was calculated for various perovskite compositions. Perovskites with a higher strontium content and/or the appropriate stabilizer dopant(s) showed nearly linear dependence of $\ln(P_{O2})$ with membrane thickness, while less stable compositions displayed a non-linear dependence with a sharp decline in $\ln(P_{O2})$ near the oxygen-lean side, making these membranes more susceptible to structural failure.

4.5 References

[1]   Sangar, N., Ying, J.Y., to be submitted to *J. Am. Ceram. Soc.*

[2]   Brinkman, H.W., Kruidhof, H., Burggraaf, A.J., *Solid State Ionics* **68**, 173 (1994).

[3]   Teraoka, Y., Zhang, H.M., Furukawa, S., Yamazoe, N., *Chem. Lett.*, 1743 (1985).

[4]   Teraoka, Y., Nobunaga, T., Yamazoe, N., *Chem. Lett.*, 503 (1988).

[5]   Teraoka, Y., Nobunaga, T., Okamoto, K., Miura, N., Yamazoe, N., *Solid State Ionics* **48**, 207 (1991).

[6]   Teraoka, Y., Zhang, H.M., Okamoto, K., Yamazoe, N., *Mater. Res. Bull.* **23**, 51 (1998).

[7]   Alder, A., Russek, S., Reimer, J., Fendorf, M., Stacy, A., Huang, Q., Santoro, A., Lynn, J., Baltisberger, J., Werner, U., *Solid State Ionics* **68**, 193 (1994).

[8]   Anderson, M.T., Vaughey, J.T., Poeppelmeier, K.R., *Chem. Mater.* **5**, 151 (1993).

[9]   Yamauchi, S., Ishigaki, T., Mizusaki, J., Fueki, K., *Solid State Ionics* **9&10**, 997 (1983).

[10]   Ishigaki, T., Yamauchi, S., Mizusaki, J., Fueki, K., Tamura, H.J., *J. Solid State Chem.* **54**, 100 (1984).

[11]   Ishigaki, T., Yamauchi, S., Kishio, K., Mizusaki, J., Fueki, K., *J. Solid State Chem.* **73**, 179 (1988).

[12]   Sangar, N., Chakravorty, R., Ying, J.Y., to be submitted to *Chem. Mater.*

[13]   Sangar, N., Ying, J.Y., to be submitted to *J. Catal.*

[14]   Wagner, C., *Progr. Solid State Chem.* **10**, 3 (1975).

[15]   Bouwmeester, H.J.M., Burggraaf, A.J., in "The CRC Handbook of Solid State Electrochemistry," (P.J. Gellings and H.J.M. Bouwmeester, Eds.), p. 481, CRC Press, New York, 1996.

[16]   Shannon, R.D., *Acta Crystall.* **A32**, 751 (1976).

[17]   Balachandran, U., Dusek, J.T., Sweeney, S.M., Poeppel, R.B., Mieville, R.L., Maiya, P.S., Kleefisch, M.S., Pei, S., Kobylinski, T.P., Udovich, C.A., Bose, A.C., *Am. Ceram. Soc. Bull.* **74**, 71 (1995).

[18]   Pei, S., Kleefisch, M.S., Kobylinski, T.P., Faber, K., Udovich, C.A., Zhang-McCoy, V., Dabrowski, B., Balachandran, U., Mieville, R.L., Poeppel, R.B., *Catal. Lett.* **30**, 210 (1995).

5 – Recommendations for Future Work

We have shown that multicomponent perovskites ($La_{1-x}A_xMn_{1-y}B_yO_3$) are excellent catalysts for methane oxidation at low temperatures, due to their high intrinsic catalytic activity and nanocrystalline microstructure. Due to their ability to activate methane at low temperatures, these perovskites may be effective catalysts for converting methane to methanol/formaldehyde and/or for oxidative coupling of methane to ethane/ethylene. The activity and selectivity of these reactions depend greatly on the amount and nature of adsorbed oxygen species on the catalyst surface, which can be manipulated by varying A- and B-site composition. B-site dopants (such as Ce, Al, Ga and Bi), which favor p-type electronic conductivity at low oxygen partial pressures, are expected to enhance selectivity by decreasing the amount of non-selective, electrophilic oxygen species on the catalyst surface. Highly basic A-site dopants (such as Sr, Ba, Na and K) should increase catalyst activity by increasing the rate of hydrogen abstraction from methane.

Mixed conducting $Ba_{1-x}Sr_xCo_{1-y}M_yO_{3-\delta}$ perovskite membranes were developed for oxygen separation applications with high oxygen fluxes and excellent separation selectivity. Oxygen flux can be further increased by decreasing membrane thickness through the fabrication of dense, ultrathin ($\sim 10 \ \mu m$) perovskite membranes. These films can be synthesized using electrophoretic deposition of nanocrystalline perovskite powders on porous supports, followed by high-temperature sintering. Initial studies have shown promising results; dense perovskite films (10-50 μm) have been obtained by optimization of electrophoretic deposition conditions, support pore size and composition, perovskite particle size, and sintering conditions. Electrophoretic deposition can also be used to synthesize membranes with graded compositions in order to optimize oxide conductivity with respect to oxygen partial pressure, and increase membrane stability under reducing conditions.

The development of mixed-conducting membranes for oxygen delivery applications has interested researchers with the possibility of using these membranes for the production of chemicals with higher selectivity, with the additional advantage of combining reaction and separation in a single unit operation. The ability to control the nature of the oxygen species by balancing the rates of diffusion and reaction on the membrane surface can potentially lead to higher selectivities for partial oxidation reactions, such as oxidative coupling of methane.

6 – Conclusions

Nanocrystalline perovskites ($La_{1-x}A_xMn_{1-y}B_yO_3$) were successfully synthesized using chemical co-precipitation with higher surface area and smaller grain size compared to conventional synthesis techniques, resulting in superior catalytic performance. The chemical stoichiometry and phase purity of these multicomponent oxides depended greatly on precipitation conditions.

The catalytic activity of these perovskites was investigated for different A- and B-site substitutions. Among $LaBO_3$ perovskites, the catalytic activity was found to decrease in the order: Mn > Fe ~ Ni > Co, with $LaMnO_3$ showing the lowest light-off temperature of 420°C. The intrinsic catalytic activity at 650°C decreased in the order: Ni > Co > Fe > Mn, with $LaNiO_3$ showing the highest intrinsic rate. Substitution of Group IIA metals for La^{3+} was found to increase reaction rate of $La_{1-x}A_xMnO_3$, while higher valency dopants did not change or decreased catalyst activity. In the case of Ca^{2+} and Sr^{2+} dopants, intrinsic activity of $La_{1-x}A_xMnO_3$ was found to increase with doping level until x = 0.4 and 0.6, respectively. $La_{0.4}Sr_{0.6}MnO_3$ exhibited the lowest light-off temperature of 380°C, with a reaction rate that was 2.5 times higher than $LaMnO_3$. Methane TPR experiments showed that methane oxidation over the perovskites occurred by methane adsorption on the catalyst surface via hydrogen abstraction. Substitution of Group IIA metals for La^{3+} enhanced catalytic activity by increasing the rate of methane activation, but lowered activity at high doping levels due to slow carbonate decomposition.

Mixed conducting $Ba_{1-x}Sr_xCo_{1-y}M_yO_{3-\delta}$ perovskite membranes were developed for oxygen separation applications. $Ba_{0.75}Sr_{0.25}Co_{0.8}Fe_{0.2}O_{3-\delta}$ showed a very high oxygen flux of ~ 3.8 cm^3[STP]/min/cm^2 at 900°C. $Ba_{0.25}Sr_{0.75}Co_{0.8}Ti_{0.2}O_{3-\delta}$ exhibited an oxygen flux of ~ 1.4 cm^3[STP]/min/cm^2 at 750°C with excellent stability over time. These oxygen fluxes were ~ 2 times higher than those reported for the best existing membrane materials. High oxygen fluxes were obtained by creating a high oxygen vacancy concentration (~ 15% of oxygen lattice sites) via extrinsic doping, and by increasing the unit cell free volume to allow facile oxide ion hopping. The challenge in developing these membranes was to prevent the phase transformation of vacancy-disordered perovskite to a poorly conductive vacancy-ordered structure in the desired temperature range of 750-900°C. This was accomplished by doping various cations in place of Co at the B site. Iron was found to be the most effective dopant for stabilizing the perovskite phase, followed by titanium and tin.

A novel approach was developed to stabilize the vacancy-disordered perovskite phase of $BaCo_{0.8}M_{0.2}O_3$ on cooling to room temperature, so that significantly higher oxygen fluxes could be achieved at low temperatures with excellent stability. When a single type of dopant cation was introduced at the B site, the vacancy-disordered phase could not be fully stabilized, resulting in phase transformation to an ordered structure and low oxygen fluxes. Dopants that satisfied the selection criteria most closely (i.e. Sn^{4+} and Fe^{3+}) corresponded to smaller heats of transition and lower order-disorder temperatures. A "mixing pot" approach was utilized to stabilize the perovskite phase to room temperature by introducing both Sn^{4+} and Fe^{3+} at the B site. Substituting a mixture of stabilizer dopants created more cationic disorder at the B site, which together with their coordination preferences and valence states, successfully prevented the oxygen vacancies from forming an ordered structure. This resulted in higher oxygen fluxes, and excellent flux stability even at a relatively low temperature of 750°C. The stabilized $BaCo_{1-y-z}Sn_yFe_zO_3$ perovskites exhibited impressive fluxes of ~ 3.5 and ~ 1.3 $cm^3[STP]/min/cm^2$ at 900°C and 750°C, respectively, which were substantially higher than those achieved by conventional perovskite membrane compositions.